BERGISCHE
UNIVERSITÄT
WUPPERTAL

Dissertation zur Erlangung des akademischen Grades eines Doktors der Naturwissenschaften

Measurement of the charged-current Drell-Yan single- and double-differential cross-sections at high transverse masses at $\sqrt{s} = 13\,\text{TeV}$ with the ATLAS detector

Frederic Schröder
geboren in Lübbecke

2022

Fachbereich Mathematik und Naturwissenschaften
Fachgruppe Physik
Bergische Universität Wuppertal

Erstgutachter:	Priv. Doz. Dr. Frank Ellinghaus (Bergische Universität Wuppertal)
Zweitgutachter:	Prof. Dr. Eram Rizvi (Queen Mary University of London)
Abgabedatum:	06.05.2022
Prüfungsdatum:	15.07.2022

Abstract

In this thesis, the measurement of the single- and double-differential cross-sections for the charged-current Drell-Yan process in the leptonic decay into an electron and an electron neutrino, $q\bar{q} \to W \to e\,\nu_e$, is presented. The analysed dataset is recorded by the ATLAS experiment at the Large Hadron Collider during pp-collisions of the full Run 2 at a centre-of-mass energy of $\sqrt{s} = 13\,\text{TeV}$. In contrast to former measurements, where the cross-section at the peak of the W boson mass is measured, this thesis focuses on W boson masses up to $\mathcal{O}(1\,\text{TeV})$, where the cross-sections are measured for the first time. One of the key ingredients for this measurement is the estimation of the multijet background, originating from fake electrons. The multijet background is estimated based on the data-driven Matrix Method. Occurring issues of data-driven methods that depend on the transverse missing momentum are described and a corresponding systematic uncertainty is assigned. Another crucial aspect is the unfolding of the analysed dataset in a phase space, where a high amount of migrations is expected. The measured data distribution is unfolded to the born level using the Iterative Bayesian Unfolding. Its iterative procedure is well-suited to correct bin-by-bin migrations. The single-differential cross-section as a function of the transverse mass of the W boson, $m_{\text{T}}^{W} \in [200, 2000]$ GeV, and the double-differential cross-section as a function of the transverse mass of the W boson and the absolute value of the electron's pseudorapidity, $m_{\text{T}}^{W} \otimes |\eta(e)| \in [200, 2000]\,\text{GeV} \otimes [0.0, 2.4]$, are presented. The differential cross-sections for both charges of the W boson, i.e. in the e^+ and e^- channel, are measured separately. The corresponding statistical and systematic uncertainties are reported as well. The unfolded single- and double-differential cross-sections are compared to the theoretical prediction from Powheg Box v1 and pythia 8, where an overall reasonable agreement within the uncertainty is found.

Contents

1 Introduction

For centuries, researchers all over the world have been dealing with the question of what the universe is made of. Already in the 5th century before Christ, Democritus and Leucippus postulated that the universe and all matter consist of several unique indivisible particles, that build up all known matter. Back in time, the first candidate for an indivisible particle were atoms, i.e. the chemical elements like e.g. hydrogen. Although we know nowadays that atoms consist of varying quantities of protons, neutrons and the most commonly known electrons, the idea to search for the smallest pieces of matter remained.
From all the searches and studies performed in order to identify the building blocks of our universe throughout the past centuries, elementary particle physics developed. Besides the electron, which has been observed as the first elementary particle in 1897 by J.J.Thompson [1], a large variety of new particles were discovered at several different experiments in the 1950s and 1960s.
In the 1970s, the Standard Model of Particle Physics (SM) [2–5] has been formulated representing the current knowledge about elementary particles and their interactions. The SM is a well-established model successfully predicting experimental behaviour and has been tested extensively, passing every test so far. Nevertheless, there are unexplained phenomena as well. Neutrino oscillation, the matter-antimatter asymmetry, dark matter, or the gravitational interactions are not described by the SM.
The testing and validation of the SM as well as the exclusion or limitation of other models and their parameters is a main part of a large variety of different studies performed in elementary particle physics. The prerequisite for observing, measuring, and testing theories of subatomic particles is their creation in a well-known environment. A great opportunity offers the production by particle accelerators, where e.g. electrons or protons can be brought to collision at high energies. As the spacial resolution of particle accelerators is the inverse of the collisions' energy, higher and higher energies are required to probe smaller and smaller structures. The most powerful particle accelerator in the world is the Large Hadron Collider [6] (LHC) located close to Geneva at the '**C**onseil **e**uropéen pour la **r**echerche **n**ucléaire' (CERN). Four large experiments are located at the LHC, namely: ATLAS [7], CMS [8], LHCb [9] and ALICE [10]. While the ALICE experiment focuses on heavy-ion physics based on lead ion collisions, the LHCb experiment is dedicated to studies based on the beauty (or b quark) by exploiting the region close to the particle beam. The ATLAS and CMS experiments are so-called multi-purpose detectors covering especially the possibilities of precise measurements of known particles and their properties and the search for new particles. The knowledge about the SM and its parameters is improved at these experiments by searches for new physics e.g. extending the SM, which could resolve remaining open questions, and precise measurements e.g. constraining fundamental SM parameters.
In this thesis, the single-differential and double-differential cross-sections of the charged-current Drell-Yan (ccDY) process, consisting of the production of a W boson from a quark and anti-quark annihilation, which decays into an electron and an electron-neutrino,

$q\bar{q} \to W \to e\,\nu_e$, are measured. While the cross-section is very well known at the peak of the W boson mass, the cross-sections focusing on W boson masses up to $\mathcal{O}(1\,\text{TeV})$ are measured for the first time.
In this phase space, differential cross-sections of the ccDY itself represent a key result allowing to investigate the agreement between precise theoretical predictions and the experimental data and, subsequently, for further interpretations: On one hand, the ccDY process provides the possibility to constrain the density functions describing the partonic content of the proton based on the measured differential cross-sections and precise theory predictions of this process. These density functions can not be calculated directly from theory, thus they are obtained from experimental data only. The precise knowledge of these density functions is crucial to precisely predict SM physics.
On the other hand, the differential measurement of the cross-section from W boson masses in the TeV range allows for the interpretation of the differential cross-sections in an effective field theory (EFT). An EFT is a model-independent tool to probe new physics. Assuming that new physics appears at a high mass scale M, far above the energies that can be directly probed nowadays, the influence of this new physics would be detectable for energies E that are much smaller than the mass scale M. In the case of the ccDY production, the SM could be extended by a hypothetical new fermion or vector boson at a mass scale M as explained in detail in Reference [11]. Such new particles would change the high energy behaviour of the SM gauge bosons, such as the W boson, and would lead to small deviations of the cross-section as a function of the W boson mass. The authors of Reference [11] conclude that the expected sensitivities for the data set that is recorded starting from 2022 at the LHC could exceed even the high accuracies obtained by the Large Electron-Positron (LEP) experiment.

This thesis is organised as follows: In Chapter 2, a brief introduction to the SM of particle physics is presented. Then, the LHC and the ATLAS experiment are described in Chapter 3. While an overview of the strategy for the measurement is given in Chapter 4, a theoretical introduction to unfolding is provided in Chapter 5. After the analysed dataset and the Monte Carlo simulations used are presented in Chapter 6, the event reconstruction and the signal extraction is explained in Chapter 7 and 8, respectively. While the detailed description of the background estimation is addressed in Chapter 9, a comparison of signal and background events with the data events is presented in Chapter 10. Afterwards, the systematic uncertainties are explained in Chapter 11. The unfolding, in order to obtain the differential cross-sections, is explained in Chapter 12 and the unfolded results are discussed in Chapter 13. Finally, the conclusions are drawn and a brief outlook is given in Chapter 14.

2 The W boson in the Standard Model

The theoretical model describing the elementary particles and their interactions at the subatomic scale is the so-called Standard Model of Particle Physics (SM). The SM [2–5] describes the dynamics and interactions of the elementary particles based on three of the four fundamental forces. It consists of fermions, the particles that are the building blocks of matter, the gauge bosons representing the weak, strong and electromagnetic force that mediate the fundamental interactions of particles with other particles, themselves or fields and the Higgs boson, which is a smoking gun for the explanation of how the masses of the elementary particles are generated.
The SM is a well-established theoretical model, developed during the 1960's and 1970's, which represents the current state of knowledge and successfully predicts experimental behaviour in a huge amount of experiments. Nevertheless, the matter-antimatter asymmetry or the absence of dark matter are examples for the deficits of the SM. In addition, the inclusion of the gravitational interactions into the SM has not been achieved so far. The incorporation of gravity to the SM would in fact require an additional gauge boson as force carrier that has not been observed so far and, consequently, strong limits on the expected coupling have been set [12]. Due to the expected very weak coupling of gravity to elementary particles, gravitational interactions are neglected.

2.1 Matter particles

In Figure 2.1, the fundamental particles of the SM and their properties are illustrated. The fundamental particles that build up our matter are so-called fermions f which carry a half-integer spin s and can be subdivided into quarks q and leptons ℓ. Both classes of fermions are further grouped into three generations based on their mass. The lightest (heaviest) particles are assigned to the first (third) generation. In our universe, stable matter consists of first generation fermions, while quarks and charged leptons of the second and third generation are unstable. Each fermion has a partner which is called anti-fermion[1] $\bar{f}$. Antiparticles occur with the same mass, but opposite quantum numbers in contrast to particles.
Quarks are represented by six different eigenstates, called flavours. Besides the categorisation into three generations, quarks are subdivided into up-type and down-type based on their electrical charge. The up u, charm c and top t quark are up-type quarks which carry an electrical charge of $+\frac{2}{3}\,e$ and the down d, strange s and bottom b quark are down-type quarks which carry an electrical charge of $-\frac{1}{3}\,e$. An additional property of quarks is the colour charge, where red, blue and green[2] are defined as three independent states.

[1] In the following, f refers to particles and antiparticles, unless stated otherwise.
[2] Antiparticles carry the corresponding anti-colours.

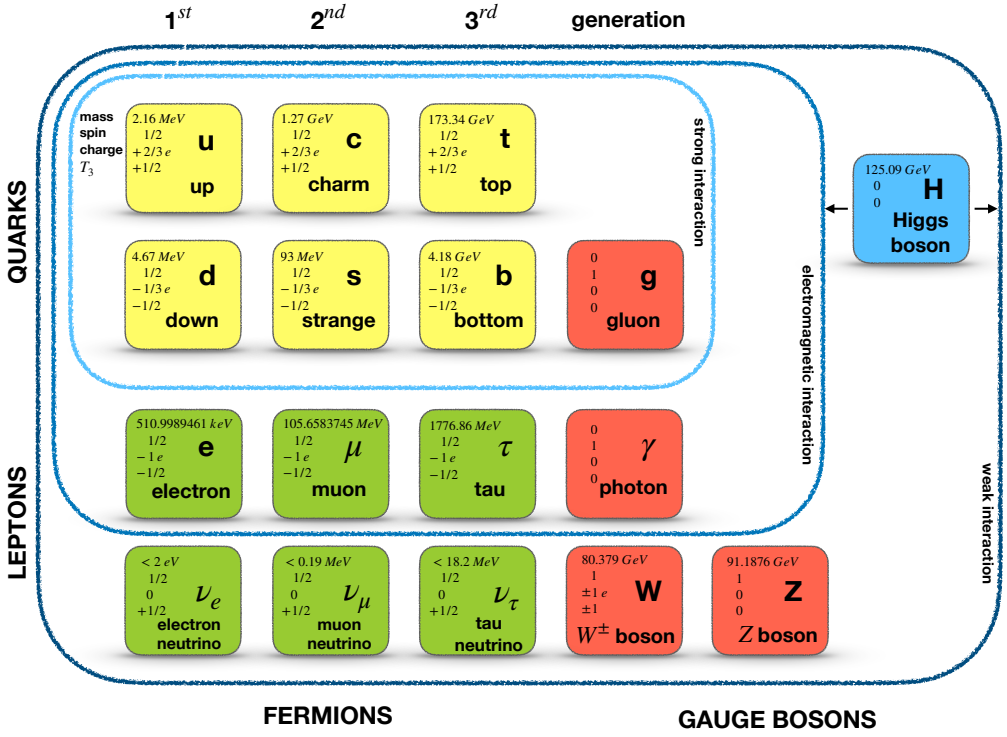

Figure 2.1: A schematic overview of the fundamental particles described by the SM. The mass, spin, charge and third component of the weak isospin is shown for each particle. The mass of the top quark was determined in Reference [13], the Higgs boson mass is taken from Reference [14] and the remaining masses can be found in Reference [15]. Three fundamental forces are indicated by the three blue boxes, which are related to the force carriers γ, $W^{\pm}$, Z and g. The connection between the electromagnetic and weak interaction by spontaneous symmetry breaking is indicated by arrows besides the Higgs boson. Further details can be found in the description below.

Leptons occur in six different flavours, where in each generation a lepton is associated to a lepton neutrino. The electron[3] e, the muon μ and the tau τ represent the charged leptons whereas the electron neutrino ν_e, muon neutrino ν_μ and the tau neutrino ν_τ are electrically uncharged. Although neutrinos are massless in the SM, a non-zero mass is expected from experimental physics point of view due to the observation of neutrino oscillations [16, 17].

2.2 Gauge bosons and fundamental forces

The theoretical model of the SM is a relativistic, renormalizable quantum field theory that is invariant under the symmetry group $SU(3)_C \times SU(2)_L \times U(1)_Y$. This group is composed of the symmetry group of the strong force $SU(3)_C$ and the electroweak interaction

[3] The anti-electron is usually called positron. In the following, electron refers to both, the electron e^- and positron e^+, unless stated otherwise.

$SU(2)_L \times U(1)_Y$, where the electroweak interaction summarises the electromagnetic and weak interaction in a unified theory.
Generally, in a field theory approach, particles are related to so-called fields, which are functions of space-time. Field theories constitute dynamics of a certain field represented by Lagrangian densities L. Each Lagrangian density can be subdivided into several terms describing e.g. mass terms of the fermions or interactions of the fermion field and a gauge field. Each fundamental interaction in the SM is described by a Lagrangian density and needs to satisfy their corresponding symmetry group.
In the SM, gauge bosons mediate the fundamental interactions. The strong interaction is mediated by the gluons g, the electromagnetic interaction by the photon γ and the weak interaction by the $W^{\pm}$[4] and the Z bosons. Each gauge boson couples to certain quantum numbers which therefore defines which particles participate in the corresponding interaction. In addition, the coupling strength of each fundamental interaction is energy-dependent, often referred to as 'running couplings'. The 'running' of each coupling is described in detail in the following.
The strong interaction is described by Quantum Chronodynamics (QCD) and is invariant under the non-abelian symmetry group $SU(3)_C$, where the quantum number C refers to the colour charge in the gauge group representation. The eight generators of $SU(3)$ are identified with the eight massless gluon fields g. The mediator of the strong interaction, the gluon, carries and couples to colour and anti-colour charge only. For this reason, gluons couple to the colour charge of quarks and to themselves. The strength of the QCD coupling constant α_S depends on the momentum Q exchanged in particle interactions. The average obtained by the Particle Data Group for the coupling with an exchanged momentum of $Q = M_Z$ is $a_S(M_Z^2) = 0.1179 \pm 0.0010$ [15], where M_Z refers to the mass of the Z boson. At smaller energies, corresponding to large distances, the coupling strength increases, which is called confinement. As a result, quarks can not occur as single particles but in colourless bound states, classified as mesons $q\bar{q}$ and baryons qqq. Mesons and baryons are summarised as hadrons and the process of building colourless states is called hadronisation. In contrast, the coupling constant strength decreases for higher energies, corresponding to small distances, where quarks are asymptotically free. While the outcome of QCD interactions can be calculated perturbatively (pertubative QCD) for small coupling constants, it is not possible for large values of α_S, corresponding to small energies, i.e. exchanged momenta.
The electromagnetic interaction is described by an abelian gauge theory, the Quantum Electrodynamics (QED), and is mediated by the photon γ. The photon is massless and carries no charge itself. Furthermore, it couples to electrically-charged particles only. The coupling strength of the electromagnetic interaction increases for larger energies, referring to small distances, and reaches a plateau at $\alpha_{EM} = \frac{1}{137}$.
The weak interaction is mediated by the gauge bosons W and Z. The W boson is electrically-charged, while the Z boson is electrically-neutral. The quantum number of the weak interaction is the weak isospin I_3. Because all fermions carry a weak isospin of $\pm\frac{1}{2}$, the weak interaction is the only force acting on all elementary fermions. The masses of the W boson $m_W = 80.379 \pm 0.012\,\text{GeV}$[5] [15] and the mass of the Z boson $m_Z = 90.1876 \pm 0.0021\,\text{GeV}$ [15] are much higher compared to most of the other elementary particles. Since massive gauge

[4] In the following, W boson refers to both, the W^- and W^+, unless stated otherwise
[5] In this thesis $c \equiv 1$ is used.

fields violate the gauge invariance of the SM, the gauge bosons are not massive from the beginning in the electroweak gauge theory. Due to their large masses, the coupling strength of the weak interaction is small compared to the strong and electromagnetic interaction. Although it is of the order of $\alpha_{weak} \approx \frac{1}{30}$ at the energy of the W and Z boson masses, it decreases for large energies.

2.3 Peculiarities of the weak interaction

The weak interaction allows for a neutral- and a charged-current interaction. The neutral-current interaction is mediated by the electrically neutral Z boson. For the coupling of the Z boson to charged leptons and quarks, the neutral-current interaction involves components similar to the corresponding electromagnetic interaction. The only process consisting completely of $SU(2)_L$ neutral-current components is the scattering of neutrinos. Furthermore, flavour-changing neutral-currents (FCNCs) are forbidden at tree level in the SM and suppressed at loop level by the GIM mechanism [18].
The charged-current interaction is mediated by the W bosons, each carrying an electric charge of ± 1. One of the most famous properties of the weak interaction, that has not been observed for the strong or electromagnetic interaction, is the violation of parity. Parity is a transformation which refers to the mirror symmetry. In 1957, parity violation in the weak interaction was shown by the experiment of C.S. Wu [19]. In the SM it is mathematically incorporated in the charged-current weak interaction by the following vertex factor modifying the coupling of the W boson to quarks and leptons.

$$\frac{-i\alpha_{weak}}{2\sqrt{2}}\gamma^{\mu}(1-\gamma^{5}) \tag{2.1}$$

The vertex factor consists of the coupling constant of the weak interaction α_{weak} and Dirac matrices γ^{μ} with $\mu \in [0,1,2,3]$. While the single γ^{μ} leads to a so-called *vector* coupling that is invariant under parity transformation, the $\gamma^{\mu}\gamma^{5}$ displays the so-called *axial vector* coupling, which violates parity due to an additional sign under the parity transformation. The composed structure of *vector* and *axial vector* coupling is the so-called $V-A$ coupling. The $V-A$ coupling characterises the charged-current weak interaction by restricting the coupling of the W bosons to left-handed particles and right-handed antiparticles. The so-called 'chirality' determines whether a particle is left- or right-handed based on its transformation under the symmetry group. For massless particles, chirality is the same as helicity. The helicity determines the handedness of a particle based on spin and momentum. A particle with right-handed helicity is defined as a parallel alignment of spin and momentum, while a particle with left-handed helicity is defined as an anti-parallel alignment.
In addition to the parity transformation, $\mathcal{P}$, there is also the charge transformation, $\mathcal{C}$, where charges and magnetic moments are reversed, i.e. particles are interchanged by their antiparticles. The combination of $\mathcal{C}$ and $\mathcal{P}$, denoted as $\mathcal{CP}$, was believed to be conserved for a long time until it was proven to be violated in neutral kaon decays [20].
Another unique property of the charged-current weak interaction for quarks is given by flavour-changing charged-currents (FCCC). For leptons, W bosons couple to each generation separately, where cross-generational couplings, i.e. for example $e^{+} \rightarrow W^{+} + \bar{\nu}_{\mu}$, are not

allowed. In case of quarks, those cross-generational couplings, for example $s \to d + W^-$, exist. A first concept describing the mixing of quarks has been proposed in 1963 by Cabibbo, who introduced the Cabibbo angle θ_C, which has been extended in 1970 by Glashow, Iliopoulus and Maiani (GIM) to the Cabibbo-GIM scheme for two quark generations[6]. In 1974, Kobayashi and Maskawa introduced the CKM matrix [21], V_{ij}, based on the Cabibbo-GIM scheme. The CKM matrix relates the weak eigenstates (d', s', b') to the mass eigenstates of quarks under the strong interaction (d, s, b), where the weak eigenstates are represented by the superposition of the mass eigenstates weighted with the Cabibbo angle.

$$\begin{pmatrix} d' \\ s' \\ b' \end{pmatrix} = \begin{pmatrix} V_{ud} & V_{us} & V_{ub} \\ V_{cd} & V_{cs} & V_{cb} \\ V_{td} & V_{ts} & V_{tb} \end{pmatrix} \begin{pmatrix} d \\ s \\ b \end{pmatrix} \tag{2.2}$$

From a theoretical point of view this matrix can not be predicted by the SM and has to be determined experimentally.

2.4 Electroweak unification

The electromagnetic and weak interactions are summarised in a unified theory: the electroweak interaction. During the 1950s and 1960s Glashow, Weinberg and Salam described the GWS model [2, 3, 22]. The symmetry group representation of the electroweak interaction is $SU(2)_L \times U(1)_Y$. The $SU(2)_L$ provides three massless gauge bosons, W^i with $i \in [1, 2, 3]$, coupling via the weak isospin T_3. In addition, the generator of the $U(1)_Y$ is the massless gauge boson B, coupling to the weak hypercharge $Y_{\text{weak}} = 2(Q - T_3)$, composed of the electric charge Q and the weak isospin T_3.
The superpositions of the four gauge bosons in the GWS model can be measured as

$$W_\mu^\pm = \frac{1}{\sqrt{2}} \left(W_\mu^1 \pm i W_\mu^2 \right), \tag{2.3}$$

$$Z_\mu = -\sin(\theta_W) B_\mu^0 + \cos(\theta_W) W_\mu^3 \tag{2.4}$$

$$\text{and } A_\mu = \cos(\theta_W) B_\mu^0 + \sin(\theta_W) W_\mu^3 \tag{2.5}$$

in experiments, where the weak mixing angle θ_W is defined as $\cos(\theta_W) = \frac{m_W}{m_Z}$. Nevertheless, all four gauge bosons remain massless in the GWS model, although masses are experimentally observed for the W and Z bosons. In the following section, the mechanism generating the masses for SM particles will be explained.

2.5 Higgs mechanism

In 1964, the Higgs mechanism was proposed by Brout, Englert and Higgs [23–25] in order to resolve the inconsistency of experimentally observed particle masses of the W and Z bosons and the massless gauge bosons as described in the gauge theory of the SM. In the Higgs

[6] At that time, the third generation of quarks wasn't discovered.

mechanism, the concept of spontaneous symmetry breaking (SSB) allows the gauge bosons to obtain their masses as explained in the following. A proof for the Higgs mechanism was found in 2012, when the Higgs boson, which represents an excitation of the Higgs field, was discovered at the ATLAS experiment [26] and the CMS experiment [27].
The Higgs field is represented by a complex scalar field of the symmetry group $SU(2)_L$

$$\phi(x) = \begin{pmatrix} \phi^+ \\ \phi^0 \end{pmatrix} \tag{2.6}$$

with a spin $s = 0$. The corresponding Lagrangian density of the Higgs field consists of a kinematic term and the potential $V(\phi)$. The kinematic term introduces the coupling of the Higgs field to the W^i_μ and B_μ gauge fields of the unified electroweak interaction. The potential

$$V(\phi) = \mu^2(\phi^\dagger\phi) + \lambda(\phi^\dagger\phi)^2 \tag{2.7}$$

leads to the famous shape often referred to as 'mexican hat potential' for $\mu^2 < 0, \lambda > 0$. In addition, the potential provides an infinite number of minima at the so-called vacuum expectation value (VEV) $\nu \approx 246\,\text{GeV}$. The SSB is achieved, if one of the minima of the potential is adopted.
The non-zero VEV breaks the symmetry of the electroweak interaction, while the electromagnetic and strong symmetry groups remain unbroken. In that way, the W and Z bosons obtain their mass through the absorption of three degrees of freedom of the Higgs field after electroweak symmetry breaking, while the gluon and photon remain massless. The overall symmetry group of the SM is broken down to $SU(3)_C \times U(1)_{EM}$.
Additionally, the mass terms of the fermions can be explained by the Yukawa coupling

$$Y = \sqrt{2}\frac{m_F}{\nu} \tag{2.8}$$

of the fermion fields ψ to the Higgs field via the vacuum expectation value ν.

2.6 Predictions of the Standard Model

Theoretical predictions of the SM or of physics beyond the SM are a key ingredient for the precise measurement or for the search for new physics. The comparison of theoretical predictions and the measured data allows to conclude whether or not a particular theory describes what can be observed in data. In the following, a brief description of the calculation of theoretical predictions based on the SM is given, where the focus lies on proton-proton (pp) collisions at particle colliders. This case corresponds to the origin of the data analysed in this thesis.
In collider physics, the investigation of a specific process is characterised by the final state X. The common measure, in order to compare the theoretical predictions to measured data, is the number of expected events for such a final state, which is defined as

$$N_{exp} = \mathrm{L} \cdot \sigma(pp \to Q) \cdot \mathcal{BR}(Q \to X)\,, \tag{2.9}$$

with the cross-section σ, the luminosity L and the branching ratio $\mathcal{BR}$. The integrated luminosity L describes the total number of particles that pass a unit area. The cross-section σ describes the probability per unit area for a certain particle Q to be produced in the collision of two protons and the branching ratio is defined as $\mathcal{BR}(Q \to X) = \frac{\Gamma_X}{\Gamma_{\text{total}}}$. The decay width Γ_i describes the probability of a certain decay and the sum of all possible decays n is defined as the total decay width $\Gamma_{\text{total}} = \sum_{i=1}^{n} \Gamma_i$. While the integrated luminosity is measured at the corresponding particle collider, the cross-section σ and its branching ratio $\mathcal{BR}$ have to be predicted.

The theoretical prediction of a process $pp \to Q \to X$, described by the cross-section and branching ratio, is characterised by the initial and final state. Here, the initial state is determined by the two protons. A proton is a baryon that is composed of three valence quarks, two up-type quarks u and one down-type quark d. The valence quarks are bound by the strong force, which is mediated by gluons. The exchanged gluons can split into $q\bar{q}$ pairs, building the so-called sea quarks. Additionally, a gluon or quark can radiate further gluons. For this reason, the sea quarks are dynamically changing. However, the gluons, valence- and sea-quarks are summarised as partons of the proton.
During inelastic pp collisions, the so-called *hard scattering* process occurs between partons of the protons. As an example, consider two colliding protons with momentum p_A and p_B leading to a hard scattering of the partons a and b, each of which carry a fraction x_a and x_b of the respective protons momentum. The probability for these partons carrying the indicated momenta is described by the parton distribution functions (PDF) $f_{a|A}$ and $f_{b|B}$. A sketch depicting the hard scattering process of the partons and indicating where perturbative QCD (pQCD) can be applied is presented in Figure 2.2.

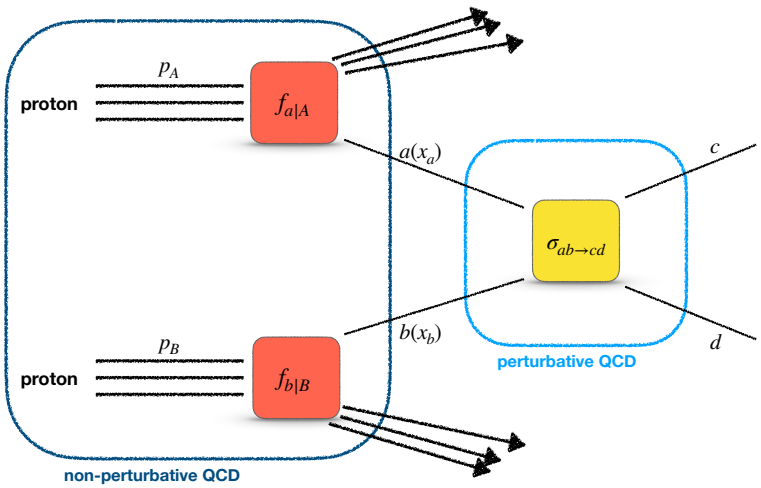

Figure 2.2: A sketch of the hard scattering process $ab \to cd$ with the cross-section $\sigma_{ab\to cd}$. The incoming protons p_A and p_B interact inelastically via the partons a and b with a momentum of x_a and x_b, respectively. The corresponding probability for a parton a (b) with a momentum fraction x_a (x_b) is given by the PDFs $f_{a|A}$ ($f_{b|B}$). In addition, the region for perturbative (non-perturbative) QCD calculations is indicated by the light (dark) blue boxes.

Based on the initial state consisting of the proton, a difficulty in the calculation of a cross-section arises from the composite structure of the proton. As stated in Chapter 2.2, the outcome of QCD, i.e. the cross-section of a process under the strong interaction, can not be calculated by perturbation theory for large coupling constants, corresponding to small energies/exchanged momenta. For this reason, it is not possible to calculate the cross-section directly, as the partons interact at several energies. The factorisation theorem [28] allows to separate the non-perturbative QCD interactions, i.e. the PDFs, and the pQCD interactions, i.e. the partonic cross-section $\hat{\sigma}$, at a certain factorisation scale μ_F. According to the factorisation theorem the cross-section σ from protons p_A and p_B for a final state $c\,d$ is defined as

$$\sigma_{p_a p_b \to cd} = \sum_{a,b} \int dx_a dx_b f_{a|A}(x_a, \mu_F^2) f_{b|B}(x_b, \mu_F^2) \cdot \hat{\sigma}_{ab\to cd}(\hat{s}, \mu_F^2)\,, \tag{2.10}$$

which is the convolution of the partonic cross-section $\hat{\sigma}$ and the PDFs $f_{a|A}$ ($f_{b|B}$).

The partonic cross-section can be calculated based on Feynman rules for pQCD depending on the order of perturbation theory. The theoretical calculation of a cross-section requires the matrix-element[7] $\mathcal{M}$ and the available phase-space. A matrix-element is calculated based on Feynman diagrams [29], a visual representation of the processes of interest. The calculation of the matrix element of all contributing Feynman diagrams can often not be performed easily, which is why subsets of the Feynman diagrams, e.g. depending on the order of perturbative series in α_S, are used. A leading order (LO) cross-section is therefore obtained from LO contributions of Feynman diagrams, while higher order cross-section, e.g. the next-to-leading order (NLO) cross-sections, take into account further Feynman diagrams. Higher orders contribute with decreasing impact to the total cross-section, where all Feynman diagrams are considered.
The cross-section is calculated by integrating the matrix-element over the available phase space. The phase space factor consists of kinematic terms, e.g. particle momenta or masses. Divergences in the calculation of the cross-section occur if higher order contributions are considered. A finite value is obtained by renormalisation depending on the renormalisation scale μ_R, which is an arbitrary energy scale.

In contrast, PDFs can not be calculated directly from theory, but have to be obtained by global fits of functional forms to data from a large variety of experiments and measurements. The necessary steps in order to determine PDFs are briefly discussed in the following: PDFs depend on the Bjorken-x, the momentum fraction x_a of a parton a and the evolution with the scale, Q^2. Since only the evolution with the scale can be derived from theory, functional forms at a starting scale Q_0 are used for the parametrisation in order to obtain the x-dependence. Common parametrisations are defined as

$$F_i(x, Q_0^2) = A_i x_i^B (1-x)^{C_i} P_i(x)\,, \tag{2.11}$$

where the index i refers to the considered parton ($u, \bar{u}, d, \bar{d}, s, \bar{s}, c, \bar{c}, b, \bar{b}, g$) and A, B and C are free parameters. The term $P_i(x)$ can be described by a smooth function such as e.g.

[7] also called amplitude

Chebyshev or Bernstein polynomials. The starting scale Q_0 is usually chosen in the order of 1 GeV, while the parameters A, B and C have to be estimated by global fits to measured experimental data. The Dokshitzer-Gribov-Lipatov-Altarelli-Parisi (DGLAP) equations, also known as QCD evolution equations, allow to evolve these estimated functional forms from the starting scale to any desired scale Q.

Before the building of the Large Hadron Collider, data from deep inelastic scattering (DIS) performed at the HERA accelerator played a crucial role in the determination of PDFs. Nowadays, the HERA data are still important due to the high precision achieved in the measurements. Nevertheless, there are areas in the $x - Q^2$ plane that can only be measured at the LHC. In Figure 2.3, the overall approximated sensitivity of data is visualised in the $x - Q^2$ plane. For the Large Hadron Collider, a particle with mass M and a rapidity of y is assumed to be produced at a centre-of-mass energy $\sqrt{s} = 13$ TeV, and the data from

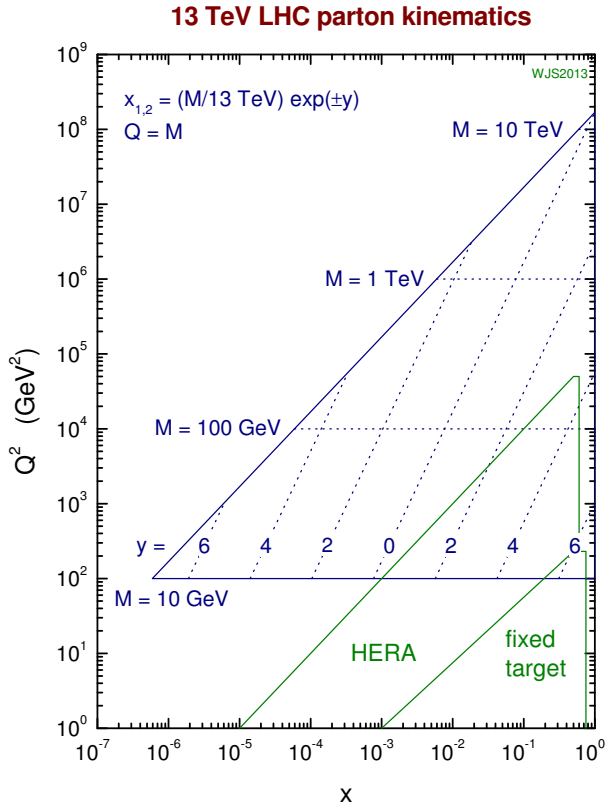

Figure 2.3: Representation of the momentum x of the parton and the transferred momentum Q^2 shown for a generated particle with the mass M and a rapidity y at the LHC collider at $\sqrt{s} = 13$ TeV (blue). The $x-Q^2$-plane is investigated at fixed target experiments and at the HERA experiment [30].

the HERA collider and further fixed target experiments are also depicted. While the data from the HERA collider contribute especially at smaller scales Q^2 for lower momenta x and the fixed target experiments are sensitive to smaller scales Q^2 with higher momenta x, the most interesting region for the LHC consists of larger Q^2 and a broad area in the parton momentum x. In these areas, the data from the LHC collider will be able to provide additional insights on the PDFs of the proton.
An example for the x-dependence at two scales of one of the most recent PDFs, NNPDF3.1 that corresponds to next-to-next-to-leading order (NNLO), is given in Figure 2.4. It can be observed that the valence quarks u_v, d_v carry a large momentum fraction of the proton at small scales Q^2, while the sea quarks carry only a very small fraction of the protons momentum. However, the fraction of the protons momentum from the sea quarks and gluon radiations are more relevant for increasing Q^2.

The convolution of the estimated PDFs and calculated partonic cross-section, each provided at a certain accuracy in pQCD, allows to calculate the number of expected events as defined in Equation 2.9. In turn, PDFs of a certain process can be determined, if the cross-section is known.

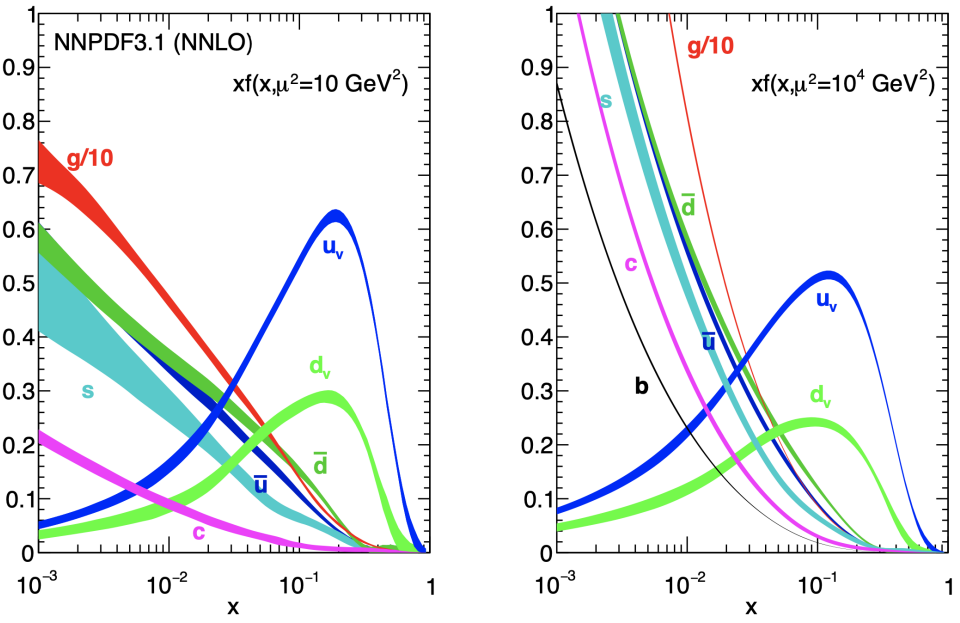

Figure 2.4: Parton distribution functions as a function of the parton momentum x from the NNPDF group (showing NNPDF3.1) at a scale $Q^2 = \mu^2 = 10\,\mathrm{GeV}^2$ (left) and $Q^2 = \mu^2 = 10^4\,\mathrm{GeV}^2$ (right) [31].

3 The ATLAS experiment at the Large Hadron Collider

Although nuclear reactors and cosmic rays offer possibilities to produce and measure elementary particles, the most central tools predominantly used in particle physics are particle accelerators. At the Large Hadron Collider, protons are accelerated almost to the speed of light and brought to collision. Various particles produced in these collisions are precisely measured by one of the central detection systems: the ATLAS detector. In the following, the production and acceleration of protons at the Large Hadron Collider and the composition of the ATLAS detector will be discussed in detail.

3.1 Large Hadron Collider

The **L**arge **H**adron **C**ollider (LHC) [6], placed near Geneva at the '**C**onseil **e**uropéen pour la **r**echerche **n**ucléaire' (CERN), is a circular particle accelerator and collider with a circumference of 27 km, a design centre-of-mass energy of $\sqrt{s} = 14\,\text{TeV}$ and a design luminosity of $L = 10^{34}\,\text{cm}^{-2}\text{s}^{-1}$. The LHC was built in the time of 1998-2008 and since then, it is the largest and most powerful particle accelerator in the world.
The beam pipe, several superconducting magnets and the accelerating structure of the LHC has been installed approximately a hundred meters underground in the tunnel of the Large Electron-Positron (LEP) collider, which has been dismantled in November 2000. At the LHC, two proton beams, each in a separated beam pipe, are accelerated. In order to avoid interactions of the protons with gas molecules, the beam pipes are evacuated and operated at very low pressures, corresponding to an ultrahigh vacuum. A system of several superconducting magnets, operated at a temperature of 1.9 K, is installed along the beam pipes to bend and control the particle beams. The cooling of the magnets to such low temperatures is achieved using liquid helium. Over a thousand dipole magnets, 15 meters long, deflect the particle beam on the circuit. In addition, quadrupole, sextupole, octapole and decapole magnets are used in order to focus and adjust the position of the particle beam. Eight radio-frequency (RF) cavities provide the acceleration of the particles. A RF cavity provides a field operated with an oscillating voltage at a radio-frequency of 400 MHz at a temperature of 4.5 K. The frequency is tuned such that protons that achieved their maximum energy are not accelerated further.
Before a proton is guided into the beam pipe of the LHC, multiple pre-acceleration steps are performed. An illustration of the particle accelerators at CERN is shown in Figure 3.1. Protons are obtained by ionising hydrogen and are then accelerated in the Linear Accelerator, `LINAC2`. With an energy of approximately 50 MeV they enter the circular collider `Booster`, where an energy of 1.4 GeV is reached. Then, the protons are transferred to the `Proton Synchrotron` (PS) and subsequently to the `Super Proton Synchrotron` (SPS), where the

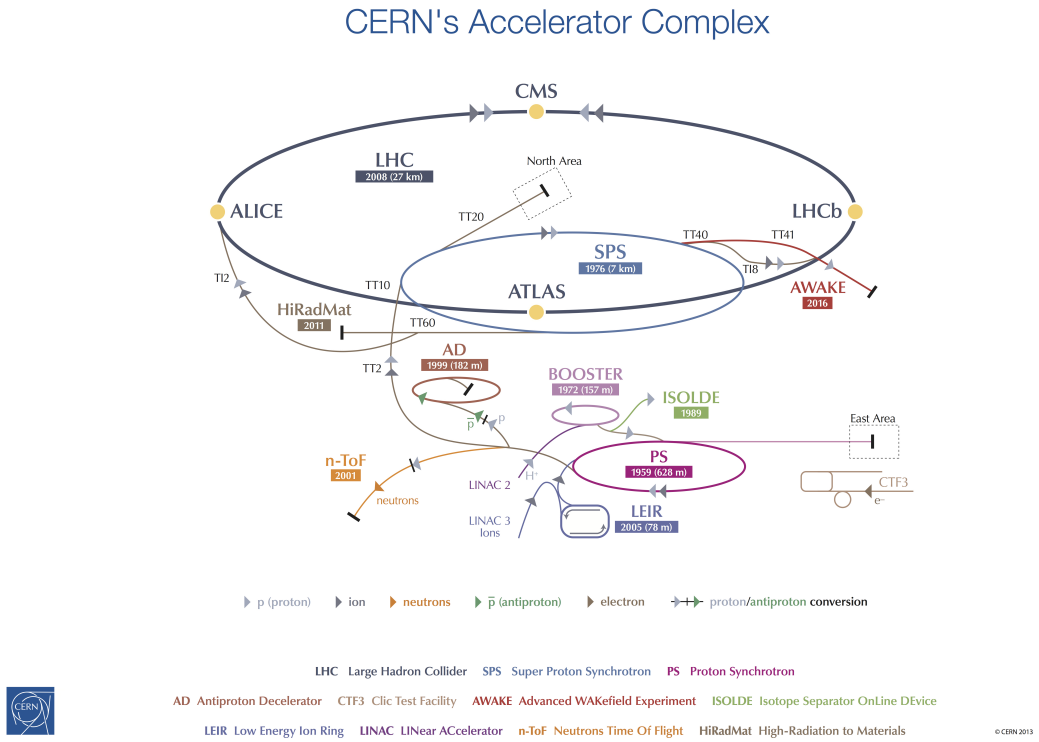

Figure 3.1: Illustration of the accelerator complex at CERN [32].

proton energy is increased further to 25 GeV and 450 GeV, respectively. Finally, the pre-accelerated protons are injected into the LHC pipes. The highest proton beam energy at which the LHC has been operated, is 6.5 TeV per beam. As a result, the centre-of-mass energy in a pp collision is $\sqrt{s} = 13\,\text{TeV}$. The beam at the LHC is composed of bunches with 10^{11} protons on average and with a bunch spacing of 25 ns, according to a collision frequency of 40 MHz. The particle bunch collisions are induced at four interaction points along the beam pipe, where the experiments ATLAS [7], CMS [8], LHCb [9] and ALICE [10] are located.

Two of the experiments, ATLAS and CMS, are general purpose detectors dedicated to two broad categories relevant to particle physics. This comprises precise measurements of SM predictions and parameters, in particular those of the Higgs boson, as well as the general search for new particles beyond the SM. While most of the experiments are following different aims, it has been intended to build these two experiments with a similar structure in order to provide independent measurements, where one experiment can confirm the results of the other. Another experiment at the LHC is LHCb, where precision measurements of B-hadrons are performed. These B-hadrons allow the investigation of $\mathcal{CP}$ violation, which is a key element in order to understand the matter-antimatter symmetry in the universe. And finally, there is the ALICE experiment, which focuses on the investigation of the quark-gluon plasma providing the expected representation of the universe shortly after the Big Bang. The quark-gluon plasma is produced during special heavy-ion runs at the LHC, where mostly

lead ions are accelerated and collided.
Over the past years, data-taking periods under different conditions have been provided. During Run 1, data corresponding to an integrated luminosity of $\int \mathrm{L}\,\mathrm{d}t = 4.5$ fb^{-1} and 20.3 fb^{-1} were recorded in 2011 at a centre-of-mass energy of $\sqrt{s} = 7\,\mathrm{TeV}$ and in 2012 at $\sqrt{s} = 8\,\mathrm{TeV}$, respectively. Then, a long shutdown took place in 2013 and 2014, where upgrades have been installed at the beam pipe and the experiments. Furthermore, short and long shutdowns are used for maintenance of the LHC. In Run 2, between 2015 and 2018, the centre-of-mass energy was further increased to $\sqrt{s} = 13\,\mathrm{TeV}$ and a total amount of data corresponding to 139 fb^{-1} was recorded. Since 2019, the second long shutdown is taking place at the LHC. The data-taking of Run 3 is planned to start during 2022, where the expected integrated luminosity is approximately 300 fb^{-1}. In the long shutdown starting in 2025, the LHC is upgraded to the High-Luminosity LHC (HL-LHC) [33] with a five times higher luminosity $L \approx 5 \times 10^{34}\,\mathrm{cm}^{-2}\mathrm{s}^{-1}$ compared to the LHC.

3.2 ATLAS detector

The largest detector of the four major experiments built around one of the interaction points along the beam pipe of the LHC belongs to the ATLAS[1] experiment [7]. ATLAS is a general purpose detector and has a layered, cylindrical structure with a length of 46 m and a diameter of 25 m and is composed of several subdetectors: The Inner Detector is closest to the beam pipe and used to precisely measure the tracks of charged particles. Furthermore, a calorimeter system is used to measure the energy of electrons, photons and hadrons. Finally, the outermost detector is the muon spectrometer, where the tracks of muons are measured. Muons are the only elementary particles, besides neutrinos, that are able to pass the calorimeter system. An overview of the ATLAS detector is presented in Figure 3.2.
Some of the detector components are immersed with magnetic fields used in order to bend the trajectory of charged particles, allowing to measure the momentum and electric charge of the particle. Lastly, a so-called Trigger and Data Acquisition system is used in order to reduce the huge amount of data by finding and selecting interesting events. In the following, each component of the ATLAS detector is described and explained in detail.

3.2.1 Coordinate system

The geometry of the ATLAS detector is described based on a right-handed coordinate system, where the nominal interaction point and the origin of the coordinate system coincide. The positive x-axis points from the nominal interaction point to the centre of the LHC ring, the y-axis points upwards to the earth surface and the z-axis is directed along the beam pipe. Due to the structure of the ATLAS detector, cylindrical coordinates with the radius r, the azimuthal angle ϕ and the polar angle θ are commonly used. As a consequence, the angles ϕ and θ cover the x-y-plane and the y-z-plane, respectively. The range of $\phi \in [-\pi, \pi]$ is defined such that $\phi = 0$ corresponds to the direction of x-axis and therefore, the upper (lower) half

[1] ATLAS is short for A Toroidal LHC ApparatuS

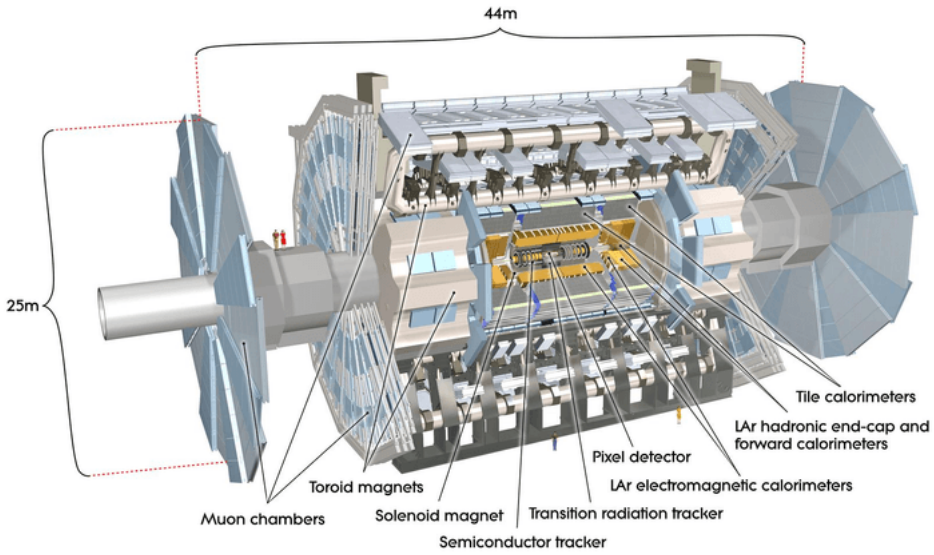

Figure 3.2: The structure of the ATLAS detector [7].

plane of the detector is described by the range of $\phi \in [0, \pi]$ ($\phi \in [-\pi, 0]$). Another definition of the polar angle, the pseudorapidity η defined as

$$\eta = -\ln(\tan(\theta/2)) \,,$$

is commonly used in order to provide a similar particle flow in each $\Delta\eta$-interval. The range of η is defined as $\eta \in [0, \infty]$, where $\eta = 0$ points along the y-axis, transverse to the beam pipe and $\eta = \infty$ is parallel to the beam pipe. The pseudorapidity is used for the definition of the coverage of all detector components.
In addition, a further set of variables is defined in the x-y plane, which is also referred to as the transverse plane since it covers the transversal motion with respect to the beam direction. The transverse momentum p_T and the transverse energy E_T are defined as:

$$p_T = p \times \sin(\theta) = \sqrt{p_x^2 + p_y^2} \,,$$
$$E_T = E \times \sin(\theta) = \sqrt{p_T^2 + m^2} \,.$$

It can be observed that for particles with masses $m = 0$ the transverse momentum and transverse energy are equal. Since the x- and y-coordinates of a collision at a hadron collider are known to be zero, the transverse momentum is conserved. The missing transverse momentum E_T^{miss} is defined as the negative sum of the transverse momenta of all visible particles

$$E_{\mathrm{T}}^{\mathrm{miss}} = -\sum p_T \,.$$

Given that the initial transverse momentum in a collision is zero, a non-zero value[2] after the collision suggests that undetected particles have been present. Furthermore, angular distances $\Delta R = \sqrt{\Delta\eta^2 + \Delta\phi^2}$ are measured in the x-y-plane.

[2]Referring to sizeable values beyond the point of resolution.

3.2.2 Inner Detector

The detector component closest to the interaction point is the Inner Detector [7, 34, 35] dedicated to the precise measurement of tracks from charged particles and the reconstruction of vertices. In the central region it has a cylindrical structure with a length of 6.2 m, a diameter of 2.1 m and end-caps in the forward regions. Furthermore, it is immersed in the 2 T magnetic field provided by the surrounding superconducting solenoid magnet. Due to the magnetic field in the Inner Detector, electrically-charged particles are deflected, which allows to measure the momentum and the sign of the electric charge of the particle from the curvature of the track. The momentum resolution relies on the precise measurement of the curvature of a track. As a consequence, it decreases in case of particles with high momenta, because their tracks are less curved.
The Inner Detector mainly conists of the Pixel Detector, the Semiconductor Tracker and the Transition Radiation Tracker. A cut-away view of the Inner Detector and its sub-detectors with their distance to the beam pipe is shown in Figure 3.3, which will be described in more detail in the following.

The innermost sub-detector, with a distance of 33.25 mm to the beam pipe, is the Pixel detector. It consists of silicon pixel modules arranged in four layers in the central region and three end-cap disks in the forward region. The sensor of each pixel module is a semiconductor detector. In the layers at a distance of $R = 50.5\,\text{mm}, 88.5\,\text{mm}, 122.5\,\text{mm}$ to the beam pipe their common size is usually $50 \times 400\,\mu\text{m}^2$. Importantly, each of the layers provides an independent measurement. The semiconductor detectors are composed of a p and n-doped region. Due to the recombination of free electrons from the n-doped region and free holes from the p-doped region, a depletion zone arises at the border of the two regions. In order

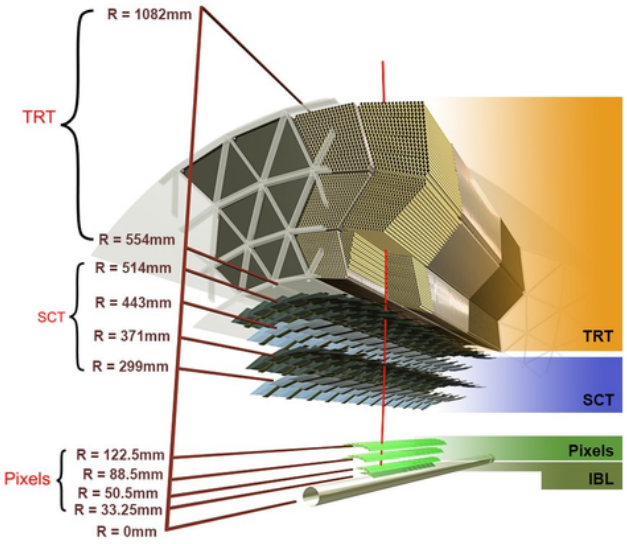

Figure 3.3: A cut-away view of the ATLAS Inner Detector [36] composed of the Insertable B-Layer (IBL), the Pixel Detector, the Semiconductor Tracker (SCT) and the Transition Radiation Tracker (TRT) and their distance to the beam pipe. The red line indicates a charged particle with $p_{\text{T}} = 10\,\text{GeV}$ passing through the detector.

to further increase the natural depletion zone, silicon detectors are cooled down and an external voltage in reverse direction is applied. If a particle traverses the detector, free electron-hole pairs are produced in the depletion zone. Then, the free electrons and holes are attracted by the anode or cathode and their movement can be measured as a current. The Insertable B-Layer (IBL) [37, 38], installed during the shutdown of the LHC after Run 1, is the innermost layer of the pixel detector. This additional, fourth layer consists of semiconductor detectors with a size of $50 \times 250\,\mu m^2$ and is especially suited to measure secondary vertices, which is important for the identification of hadronised b quarks.

The Semiconductor Tracker (SCT) is the second layer of the Inner Detector placed at radii of 299 mm to 514 mm around the Pixel detector. The SCT is a silicon microstrip detector, which is composed of microstrips with a size of $80\,\mu m \times 6.4\,cm$ and ultimately based on semiconductors as the Pixel detector. It is divided into four layers in the barrel region and nine disks in each of the end-cap regions. Each layer of the SCT is composed of a two-sided detector module, combining two silicon layers with 768 strips each. The two strip layers of the detector module are tilted by 40 mrad. Therefore, the coordinate of a traversing particle can be measured in the $R-\phi$ and z plane. Overall, 6.3 million read-out channels are used to typically measure eight hits for each traversing particle corresponding to four space-points.

The outermost part of the pixel detector is the Transition Radiation Tracker (TRT) composed of straw tubes with a diameter of 4 mm. It is located at radii of 554 mm to 1082 mm to the beam pipe and covers a region of $|\eta| < 2.0$. Each straw tube consists of a gold-plated tungsten wire and a filling of either argon gas or a mixture of xenon-based gases. A voltage is applied between the wire and the wall of the tube in order to attract electrons to the anode that were produced by the ionisation of the gas from traversing particles. As a result, a signal can be measured for a traversing particle. While straw tubes of a length of 144 cm are parallel to the beam pipe in the barrel region, straw tubes with a length of 38 cm are perpendicular to the beam pipe in the end-caps. In the forward region of the Inner detector, wheels are obtained by the radial arrangement of straw tubes. The 351000 read-out channels provide an average number of 36 hits per track, which is high compared to the Pixel detector and the SCT.
In addition to the measurement of the space points of traversing particles, the TRT provides the opportunity to identify certain particles. A charged relativistic particle that traverses the TRT generates transition radiation due to the different absolute permittivity of the materials. The transition radiation differs based on the mass of traversing particles and therefore allows to distinguish e.g. between electrons and pions, the lightest mesons.

3.2.3 Calorimeter system

The ATLAS calorimeter system [7, 39] is placed around the Inner Detector covering in total a region of $|\eta| < 4.9$ and can be subdivided into the electromagnetic (EM) and the hadronic calorimeter (HCAL). A sketch of the calorimeters is presented in Figure 3.4.
The main goal of the calorimeter system is to identify and measure the energy of several particles originating from the pp collisions. All calorimeters are so-called sampling calorimeters consisting of alternating layers of absorber plates and active material. Absorber plates consist of high density material such that when a particle originating from a collision passes through, it loses its energy by inducing particle showers until it gets stopped eventually. The

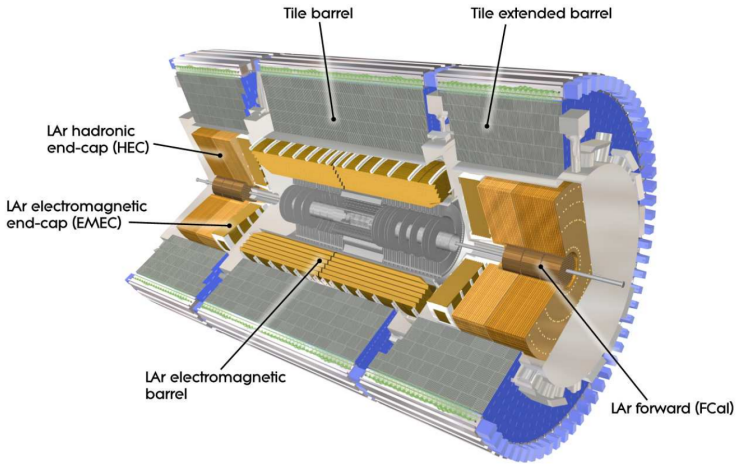

Figure 3.4: A cut-away view of the ATLAS calorimeters [7].

active material is then read-out in order to measure the particle shower and its corresponding energy. These showers are mostly produced via bremsstrahlung and pair production in the EM calorimeter for electrically charged particles. As strongly interacting particles deposit only a small fraction of their energy in the EM calorimeter, several processes are involved within the hadronic particle showers leading to energy depositions in the HCAL. While the electromagnetically interacting particles, like electrons and photons, deposit all their energy in the EM calorimeter, strongly interacting particles deposit most of their energy in the HCAL where they are then stopped.

The EM calorimeter measures the energy of electromagnetically interacting particles in the region of $|\eta| < 3.2$. It can be subdivided into the barrel region for $|\eta| < 1.475$ and the end-caps in the range of $1.375 < |\eta| < 3.2$. The end-caps can be further subdivided into the outer and inner wheel for the region of $1.375 < |\eta| < 2.5$ and $2.5 < |\eta| < 3.2$, respectively.
The EM calorimeter consists of liquid argon (LAr) as the active material with kapton electrodes and lead absorber plates. In order to ensure a full ϕ coverage of the calorimeter, an accordian-shape for the lead absorber plates and the kapton electrodes is chosen. In the same way, a good electron resolution in the full calorimeter is obtained by the variation of the thickness of lead in the absorber plates depending on $|\eta|$.
The calorimeter is divided into a different number of sections in depth and various granularities. Due to the highest resolution and availability of tracking information from the Inner Detector, the region dedicated to precision physics is represented by $|\eta| < 2.5$. The calorimeter is divided into three sections in depth in this region and into two sections in depth for the inner wheel of the end-cap. Usually, the overlap of the detectors in the region between barrel and end-cap is removed due to the large amount of material in front of the calorimeter. In Figure 3.5, an overview of the three different layers and their granularity in the $|\eta| - \phi$-plane of the EM calorimeter at $\eta = 0$ is depicted. First, the presampler of one thin layer of LAr with a granularity of 0.025×0.1 in $\Delta\eta \times \Delta\phi$ is positioned upstream of the EM calorimeter in order to correct for energy losses of incoming particles due to the interaction with the material of the Inner Detector. The first layer of the calorimeter in the barrel region, the so-called strip-layer, consists of a fine segmentation made up by strips with

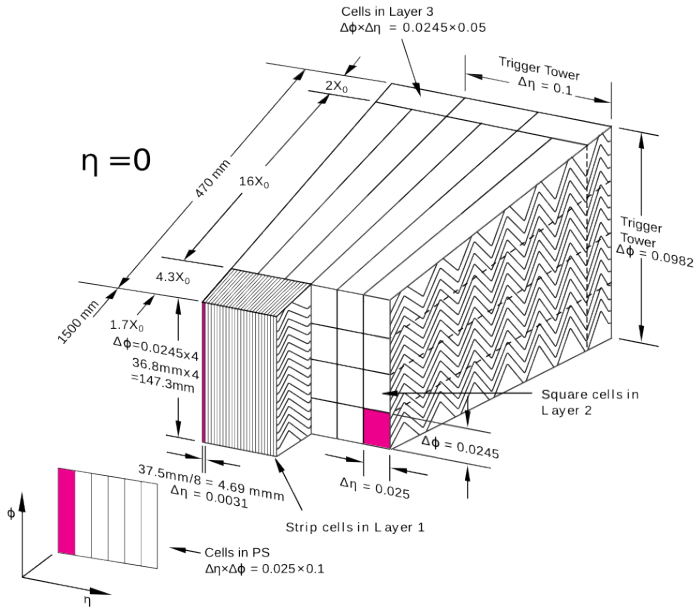

Figure 3.5: A sketch of the structure and granularity of the three different layers of the ATLAS EM calorimeter and the presampler in the barrel region [40].

a coverage of $\Delta\eta = 0.0031$ and $\Delta\phi = 0.1$. The strip-layer provides a precise measurement of the position of the incoming particle. The first layer of the EM calorimeter corresponds to a radiation length of approximately 4.3 X_0 at $|\eta| = 0$, where one radiation length corresponds to the mean distance reducing the energy of an electron to $1/e$ of its initial energy. In addition, the second layer has a coarser granularity of 0.025×0.0245 in $\Delta\eta \times \Delta\phi$. The main goal of the second layer is to measure most of the incoming particles energy. Consequently, it is thicker compared to the first layer, corresponding to approximately $16\,\mathrm{X}_0$ at $|\eta| = 0$. Finally, the third layer is characterised by an even coarser granularity with a cell size of 0.05×0.0245 in $\Delta\eta \times \Delta\phi$. It has a thickness of approximately $2\,\mathrm{X}_0$ at $|\eta| = 0$, which is devoted to the measurement of the tails of the particle showers induced by the incoming particles. These measurements are used for the correction of energy leakage into the HCAL and for triggering purposes.

The main goal of the HCAL is the energy measurement of hadronically interacting particles. It is subdivided into the Tile calorimeter in the region of $|\eta| < 1.0$ and the two extended barrels $0.8 < |\eta| < 1.7$ with a granularity of 0.1×0.1 in $\Delta\eta \times \Delta\phi$ in the first two layers. A coarser granularity of 0.2×0.1 in $\Delta\eta \times \Delta\phi$ is used for the last layer. It consists of scintillating tiles as the active material and steel absorbers. A traversing particle interacts with the scintillator tiles, leading to excited states in the tiles. The subsequent deexcitation into the ground state results in photons which are then read-out. In addition, the hadronic end-caps (HEC) are segmented into two rings covering the region of $1.5 < |\eta| < 3.2$, where LAr as the active material alternates with copper absorber plates. The granularity is 0.1×0.1 in $\Delta\eta \times \Delta\phi$ for $1.5 < |\eta| < 2.5$ and 0.2×0.2 in $\Delta\eta \times \Delta\phi$ for $2.5 < |\eta| < 3.2$.

The Forward Calorimeter (FCAL) is placed between the end-caps of the calorimeter and the beam pipe, covering $3.2 < |\eta| < 4.9$. All three sections of the FCAL are based on LAr as the

active material. Its first section, devoted to the energy measurement of electromagnetically interacting particles, uses copper absorbers. In contrast, the second and third section, dedicated to the energy measurement of hadronically interacting particles, is based on LAr alternating with tungsten absorbers.

3.2.4 Muon Spectrometer

Muons interact only rarely with the detector material and deposit almost no energy traversing the calorimeter system. For this reason, the identification and measurement of the momenta of muons is performed by the outermost detector component, the Muon Spectrometer (MS) [7, 41], where a combination of trigger and high-precision tracking chambers is used. The MS can be subdivided into the barrel region and two end-caps, with muon chambers placed cylindrically around the interaction point and the two large wheels orthogonal to the beam pipe, respectively. All in all, the MS covers the region of $|\eta| < 2.7$. In addition, a superconducting barrel toroid magnet is used in the region of $|\eta| < 1.4$ and two endcap magnets are used in the range of $1.6 < |\eta| < 2.7$. The corresponding magnetic field, which deflects electrically-charged particles and therefore bends muon trajectories in the η-plane, allows to estimate the sign of the electric charge and the momentum of the muon. A cut-away view of the MS with its sub-detectors is shown in Figure 3.6.
The measurement of the muon momentum is based on high-precision tracking chambers, namely of Monitored Drift Tubes (MDTs) and Cathode Strip Chambers (CSCs). Although MDTs are dominantly used over the full region of $|\eta| < 2.7$, the innermost layer in the range of $2.0 < |\eta| < 2.7$ consists of CSCs. In the central region of the detector at $|\eta| \approx 0$ the MS is interrupted by services for the calorimeter system, inner detector and solenoid magnet. Additionally, measurement inefficiencies are expected at certain values in the $\eta - \phi-$plane due to the support structure of the ATLAS detector.
MDTs are composed of multiple drift tubes filled with Ar/CO_2 gas, each with a diameter of 30 mm and a length of $0.85 - 6.5$ m. When muons traverse a drift tube, the gas gets ionised, leading to the production of free electrons and ions. The produced particles are collected at wires, allowing the measurement of one space coordinate of the initial interaction. CSCs are multiwire proportional chambers that are filled with Ar/CO_2 and CF_4 gas and that consist of cathode planes segmented into strips and anode wires. The cathodes and anodes are arranged perpendicular to each other. If the gas of the CSCs is ionised and free electrons and ions are produced, electrons get attracted to the anode wires, while the positively charged ions are collected at the cathode. As a result, two coordinates are obtained for each particles traversing the CSC, due to the orthogonal arrangement of anodes and cathodes.
Furthermore, a system of trigger chambers is set up consisting of Resistive Plate Chambers (RPCs) in the region $|\eta| < 1.05$ and Thin Gap Chambers (TGCs) in the range of $1.05 < |\eta| < 2.4$. RPCs are built of two parallel plates with high resistance in a distance of 2 mm, where a gas mixture mainly consisting of $C_2H_2F_4$ is filled into the gap between the two plates and a voltage is applied to create an electric field of 5 kV/mm. A traversing muon ionises the gas and the free electrons are then accelerated to the plate corresponding to the anode. In contrast, TGCs are multiwire proportional chambers filled with a gas mixture of CO_2 and n-C_5H_{12}, with a similar principle of operation as CSCs.

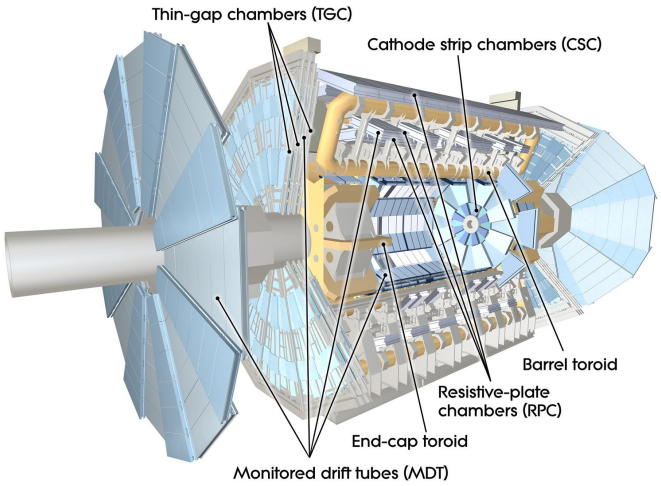

Figure 3.6: A cut-away view of the ATLAS muon spectrometer [7].

3.2.5 Trigger and Data Acquisition system

A bunch spacing of 25 ns has been used for pp collisions during the data-taking of Run 2, corresponding to an event rate of 4×10^7 events per second. The amount of data produced per second is too large to be stored. The decision, whether or not an event should be selected and stored, is made by the Trigger and Data Acquisition (TDAQ) [42] system. Each event has to be accepted by the two-level trigger system to be read-out completely and stored permanently.
The hardware-based Level-1 (L1) trigger is the first stage of the trigger system and can be subdivided into the L1 Calorimeter Trigger, the L1 Muon Trigger and the L1 Central Trigger. The information provided by the L1 Calorimeter and Muon Trigger are based on simple detector signatures in the calorimeter system and the MS, respectively. One part of the Central Trigger is the L1 topological processor. It combines the information of the L1 Calorimeter and Muon Trigger and provides more complex quantities like invariant masses. The final decision in the first stage is performed by the L1 trigger processor, which therefore defines a region-of-interest (RoI). Those events, that are accepted by the L1 trigger, account to 1×10^5 events per second and are subsequently buffered in the read-out system (ROS).
The second stage of the trigger system is the software-based high-level trigger (HLT). The decision of the HLT is based on simplified reconstruction algorithms, where the full event information obtained by the ROS and the L1 trigger ROI are used as inputs. The reconstruction algorithms depend on the different types of objects specific to the trigger that is considered. The HLT reduces the event rate to 1000 events per second. Finally, the information of each event accepted by the HLT is stored permanently.

4 Strategy for the measurement of the cross-section

The charged-current Drell Yan (ccDY) process [43, 44], $q\bar{q} \to W \to \ell\nu_\ell$, based on data from pp collisions recorded by the ATLAS experiment at the LHC is investigated. In this thesis, the cross-section in the electron channel, $\ell = e$, is measured. In parallel, another thesis addresses the cross-section measurement in the muon channel, $\ell = \mu$, where first results can be found in Ref. [45]. In a collaborative effort, further details for both channels are documented in Ref. [46].

The analysed data is recorded during inelastic collisions, where only partons of the proton interact. The ccDY process is characterised by the production of a W boson from the annihilation of a quark and anti-quark, where each quark originates from one of the colliding protons. The cross-section is measured for both electric charges of the W boson separately. The W^+ (W^-) boson is dominantly generated by the annihilation of up-quark u (down quark d) and anti-down quark $\bar{d}$ (anti-up quark $\bar{u}$) in order to conserve the electric charge, while cross-generational quark pairs, e.g. up quark (anti-up quarks) and anti-bottom quark (bottom quark)[1] are suppressed by the CKM matrix. In pp collisions, the production rate of a positively charged W boson is higher compared to a negatively charged W boson. The difference can be traced back to the composition of partons in the proton, which consists of one down valence quark and twice as many up valence quarks. Although sea quarks might contribute to the W boson production as well, the different production rates remain.
Due to the short lifetime of the W boson, it decays into hadrons with a branching ratio of $\mathcal{BR}(W \to \text{hadrons}) = \frac{2}{3}$ and into leptons with a branching ratio of $\mathcal{BR}(W \to \ell\nu_\ell) = \frac{1}{3}$, where each lepton flavour contributes with a fraction of $\frac{1}{3}$. As a consequence of the short lifetime, only the decay products of the W boson are measured in the detector. In this thesis, the W^- (W^+) boson decay into an electron e^- (a positron e^+) and electron anti-neutrino $\bar{\nu_e}$ (electron neutrino ν_e), as displayed in the Feynman diagram with $\ell = e$ in Figure 4.1, is investigated. The leptonic decay with an electron in the final state benefits from the precise

[1] A similar argument holds true for production via the strange-quark.

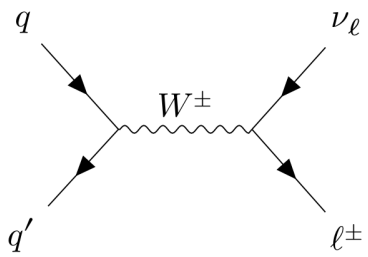

Figure 4.1: The Feynman diagram of the charged-current Drell-Yan process. In this thesis, the electron channel with $\ell = e$ is investigated.

electron reconstruction and very good energy resolution in the ATLAS detector. In contrast, it is much more difficult to measure hadronic final states due to the hadronisation of quarks in the detector. On the other side, neutrinos leave the detector unseen and instead only the missing transverse momentum $E_{\mathrm{T}}^{\mathrm{miss}}$ can be reconstructed, where the energy resolution is worse.
The W boson is usually reconstructed from the electron and the electron neutrino. Due to the missing information of the neutrino at detector level, only the transverse mass of the W boson defined as

$$m_{\mathrm{T}}^{W} = \sqrt{2 \cdot p_{\mathrm{T}}(e) \cdot E_{\mathrm{T}}^{\mathrm{miss}} \cdot (1 - \cos(\phi(e, E_{\mathrm{T}}^{\mathrm{miss}})))} \tag{4.1}$$

can be calculated, where the transverse momentum of the electron, the missing transverse momentum, and the angle between the electron and the missing transverse momentum are used. In general, the W boson mass amounts to $m_W = 80.379 \pm 0.012\,\mathrm{GeV}$ [15] and is described by a Breit-Wigner distribution with a width of $\Gamma_W = 2.046 \pm 0.049\,\mathrm{GeV}$ [15]. As a consequence of its width, W bosons are produced not only on-shell, referring to produced W boson masses close to the resonant W boson mass, but also off-shell, referring to W boson masses far off the resonant W boson mass.

As introduced in Chapter 2.6, the cross-section provides a probability of the amount of expected, produced particles per unit area. While the cross-section of the W boson mass is well-known close to the peak of $m_W \approx 80\,\mathrm{GeV}$, the cross-section as a function of the transverse mass of the W boson distribution dominantly generated by off-shell W bosons is measured up to $\mathcal{O}(1\,\mathrm{TeV})$. Additionally, the cross-section as a function of the transverse mass of the W boson and the absolute value of the electrons' pseudorapidity $|\eta(e)|$ is measured. A sketch of the W boson mass distribution, represented by the blue line, and the targeted phase space for the cross-section measurement, indicated by the turquoise lines, is visualised in Figure 4.2.

A search for an additional heavy gauge boson [47], the so-called W' boson, has been performed in the phase space of high transverse masses of the W bosons by the ATLAS

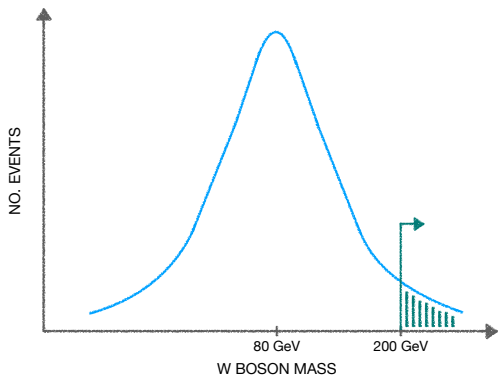

Figure 4.2: A sketch of the number of events as a function of the W boson mass distribution in blue. The area indicated by the turquoise lines refers to the region where the cross-section measurement is performed.

collaboration. As a result, no significant excess over the SM expectation is observed and masses of the hypothetical W' boson up to 6.0 TeV are excluded. The W' search is used for cross-checks and the corresponding event selection has been used as a starting point of the measurement in this thesis. A similar search has been performed at the CMS experiment, as described in Reference [48], where exclusion limits of up to $m_{W'} = 5.7$ TeV are set.
These searches are not designed for high precision as in this measurement but aim for the exclusion of a peak upon the continuous SM prediction. Importantly, small deviations of the cross-section as targeted by effective field theories (EFT) are not excluded.

In the following, the ccDY process will be referred to as *signal*. Other processes with a similar or identical final state contribute as *backgrounds* to the measurement. The background in the electron channel consists of real electron and of so-called *multijet* contributions. Real electron contributions, i.e. electrons produced in electroweak processes, are described by Monte Carlo (MC) simulations, as described in Chapter 6. In contrast, the multijet (MJ) background, where objects measured in the detector are misidentified as real electrons, is estimated by the data-driven Matrix Method, as described in Chapter 9.
Data events are compared to the estimated signal and background contributions, including the statistical and systematic uncertainties, as described in Chapter 10 and Chapter 11. The measured data distribution is unfolded in order to remove detector effects and be able to compare to theoretical predictions directly. Although a large variety of methods for the unfolding procedure are available, only the so-called *Bin-by-Bin Unfolding* and the *Iterative Bayesian Unfolding* are considered. Further details on the theoretical background of unfolding procedures and the extraction of the cross-section are described in Chapter 5 and 12, respectively.

A combination of the measured cross-sections in the electron and muon channel is intended, which provides an important consistency check of the separate measurements, because the results are expected to agree within statistical and systematic uncertainties, due to lepton universality. This combination is not part of this thesis.

5 At a glance: Mathematical formulation of unfolding

The following chapter is dedicated to a general introduction and the mathematical formulation of unfolding, which is based on Ref. [49, 50], and the description of two selected unfolding techniques commonly used in elementary particle physics, namely *bin-by-bin Unfolding* and the *Iterative Bayesian Unfolding*.

Modern elementary particle physics is often performed at powerful particle accelerators and colliders with complex detectors, build around the interaction point of the collider. Produced particles are measured by detectors and a large number of different variables is investigated by researchers, such as mass or the momentum of a particle. Distributions of the measured data and theoretical predictions are usually compared in binned variables, where the theoretical predictions are mostly obtained by MC simulations. A MC simulation subsequently simulates the hard scattering process at parton level, the hadronisation or showering of particles and the detector response of a given process. The distribution after the detector simulation, including the reconstruction and calibration of events, corresponds to the reconstructed level. The step-by-step approach in the creation of MCs allows to access the particles' properties at parton level as well as at reconstructed level. Because every detector differs slightly from each other, the comparability of results, e.g. to other experiments, in the measured, binned variable is non-trivial. Furthermore, several detector effects lead to inefficiencies of the measured quantity from data events, which are often unique for each detector.
In general, the relation of the true distribution $f(t)$ of the true variable t and the measured distribution $g(s)$ of the measured variable s is described by a so-called response function $R(s,t)$, which accounts for the measurement process. As indicated above, the *direct* process from the true distribution $f(t)$ to the measured distribution $g(s)$ is simulated in the MC sample, i.e. the true distribution is folded with the detector simulation. The *inverse* process, where the true distribution $f(t)$ is obtained from the measured distribution $g(s)$, is called *unfolding* in particle physics. Mathematically, it is defined as a Fredholm integral equation of the first kind

$$\int_{\Omega} R(s,t) \cdot f(t)\, dt + b(s) = g(s)\,, \tag{5.1}$$

where a potential background distribution $b(s)$, contributing to the distribution $g(s)$ is considered additionally. For binned distributions, the Fredholm integral equation is discretised and can be expressed [1] by

$$A \cdot x = y \tag{5.2}$$

with the vector x of size n and the vector y of size m, representing $f(t)$ and $g(s)$ respectively, and the $m \times n$ matrix A, representing $R(s,t)$.

[1] The background contributions are removed for simplicity and readopted at a later stage.

An illustration of the challenge in the unfolding procedure is presented in Figure 5.1. A hypothetical continuous true distribution [2] $f(t)$ is compared to a hypothetical corresponding measured distribution $g(s)$, which is shown as a histogram y. Four typical effects that affect

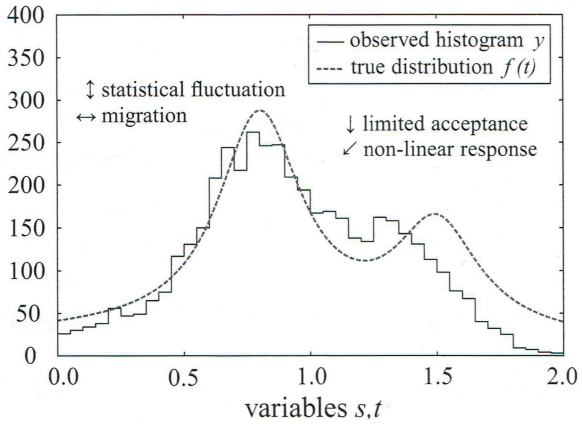

Figure 5.1: Visualisation of the hypothetical true distributions $f(t)$ for a variable t and the corresponding measured, binned histogram y representing the distribution $g(s)$ and the interplaying effects of the two distributions, namely: migration, statistical fluctuation, limited acceptance, non-linear response [49].

the measured distribution are shown. First, *statistical fluctuations*, following a Poisson distribution in case of counted events, occur in all bins. Then, *migrations* refer to events that are generated and reconstructed in different bins for the true and measured distribution. *Acceptance effects* reduce the number of measured events and a *non-linear response* leads to a shift between the two distributions. All these effects are typical for a detector response and make it difficult to estimate the true distribution from a measured distribution. The estimation of the true distribution $f(t)$ via an unfolding procedure allows to compare to (other) theoretical predictions or other experiments directly and further interpretations, e.g. the estimation of PDFs, can be performed.

In the following, *bin-by-bin* unfolding and Iterative Bayesian Unfolding are explained. The theoretical concept and the advantages of each unfolding procedure are discussed.

The most basic unfolding procedure is the *bin-by-bin* unfolding. This simple approach is based on a bin-wise efficiency correction applied to a binned distribution of measured data. If the matrix A in Equation 5.2 is assumed to be diagonal and symmetric it can be interpreted as the efficiency. The inverse A^{-1} is multiplied to the vector y in order to estimate the vector x. Importantly, a symmetric and diagonal matrix can be inverted easily. The calculation of an inclusive cross-section σ from data events, i.e. measured in a single bin, is illustrated by the equation

$$\sigma = \frac{N_{\text{data}} - N_{\text{background}}}{\mathcal{L} \cdot \mathcal{BR} \cdot \epsilon} \tag{5.3}$$

with the number of expected data events N_{data} and the number of potential background events $N_{\text{background}}$. All signal and background processes contribute to the measured data

[2] In practice and in this thesis, usually binned distributions for the true distribution are used.

distribution, where the composition of signal and background processes is unknown. The subtraction of predicted background events from MC from the number of expected data events ensures to measure the cross-section of the signal process only. Furthermore, the branching ratio $\mathcal{BR}$, the integrated luminosity $\mathcal{L}$ of the analysed dataset and the efficiency $\epsilon = \frac{N_{\text{reconstructed}}}{N_{\text{parton}}}$ are required. The efficiency, known from MC simulation, is calculated as the ratio of the theoretical predicted number of events at the reconstructed and the parton level.
The single-differential cross-section

$$\frac{d\sigma}{dx_i} = \frac{N_{\text{data, i}} - N_{\text{background, i}}}{\Delta x_i \cdot \mathcal{L} \cdot \mathcal{BR} \cdot \epsilon_i}\,, \tag{5.4}$$

i.e. the cross-section as a function of a variable x, can be obtained by applying bin-by-bin unfolding for each bin i of the binned distribution.
The bin-by-bin unfolding is restricted to the same amount and size of bins for the true and measured distribution and is only valid for negligible migrations. Nevertheless, a reasonable approximation can be obtained in case of non-negligible migrations, if the migrations are overall small enough.

A more complex approach widely accepted and used in the ATLAS community and beyond, is the Iterative Bayesian Unfolding (IBU), as described by D'Agostini, where all details can be found in Ref. [51]. The bayesian approach relies on Bayes Theorem, known from probability theory and relates measured and true distribution to probabilities and the response function to a conditional probability. The mathematical definition is based on causes C_i, i.e. events in bin i of the true distribution, and effects E_j, i.e. events in bin j of the measured distribution. The probability for a cause C_i and an effect E_j is described by $P(C_i)$ and $P(E_j)$, respectively. The conditional probability for the i-th cause C_i to produce the j-th effect E_j is given by $P(E_j|C_i)$.
By focusing on the application in the field of experimental particle physics, the true and measured distributions are assumed to be binned. The number of bins n_E and n_C correspond to the number of bins in the true and measured distribution, respectively. Consequently, n_C corresponds to the number of causes and n_E to the number of effects.
Then, Bayes' Theorem allows to estimate the probability of a cause C_i given a certain effect E_j based on $P(E_j|C_i)$ and $P_0(C_i)$ as defined in

$$P(C_i|E_j) = \frac{P(E_j|C_i) \cdot P_0(C_i)}{\sum_{l=1}^{n_C} P(E_j|C_l) \cdot P_0(C_l)}\,, \tag{5.5}$$

where $P_0(C_i)$ is the initial distribution of the probability $P(C_i)$. As seen in Equation 5.5, the observation of a certain event in bin j of the measured distribution, i.e. an effect, corresponds to the probability of the event in bin i of the true distribution, i.e. a cause i, multiplied with the conditional probability that the true event i produced the measured event j, i.e. $P(E_j|C_i)$. The corresponding denominator ensures a normalised probability by summing up the probabilities of each cause to produce the effect.
In experimental particle physics, the conditional probability $P(E_j|C_i)$ is usually referred to as response matrix because it describes the detector response. The probabilities of $P(E_j|C_i)$ can be estimated based on MC simulations and are not changed during the unfolding. In

contrast, the initial probability $P_0(C_i)$ changes after the first iteration of the IBU.
In order to estimate the true number of events from the number of measured events $N(E)$, taking into account bin-by-bin migrations via the response matrix, the estimator for the number of true events

$$\hat{N}(C_i) = \frac{1}{\epsilon_i} \sum_{j=1}^{n_E} N(E_j) \cdot P(C_i|E_j), \text{ where } \epsilon \neq 0, \tag{5.6}$$

is defined, where the efficiency ϵ_i corresponds to the number of events in the true distribution that are not reconstructed in the detector. Subsequently, an estimator for probability of the true distribution is defined as

$$\hat{P}(C_i) = \frac{\hat{N}(C_i)}{\sum_{i=1}^{n_C} \hat{N}(C_i)}\,. \tag{5.7}$$

The estimator $\hat{P}(C_i)$ relies in particular on the initial distribution $P_0(C_i)$, where the estimated number of events lays between the initial distribution and the true distribution. As a consequence, an iterative procedure in order to obtain the final true distribution is performed, where the (initial) distribution is replaced by the estimator $\hat{P}(C_i)$ in each iteration. The optimisation of the number of iterations is specific for each analysis and will be discussed in Chapter 12 for this measurement.
According to the theoretical basis of the IBU, the single-differential cross-section is defined as

$$\frac{d\sigma}{dx_j} = \frac{1}{\Delta x_j \cdot \mathcal{L} \cdot \mathcal{BR}} \frac{1}{\epsilon_j} \sum_i R_{ji}^{-1} f_{\text{in}}^i \cdot (N_{\text{data}}^i - N_{\text{background}}^i)\,. \tag{5.8}$$

In Equation 5.8, the bin widths Δx_j for each bin j of the true distribution, the integrated luminosity $\mathcal{L}$ and the branching ratio $\mathcal{BR}$ ensure the conversion into a single-differential cross-section according to Equation 2.9. Furthermore, the efficiency ϵ_j per bin j of the true distribution as well as the inverse of the response matrix R_{ji} are required, where the response matrix can be related to the matrix A defined in Equation 5.2. Then, the number of measured events from the signal process is incorporated by the difference of data and MC events, $(N_{\text{data}}^i - N_{\text{background}}^i)$. Finally, another correction factor f_{in}^i per bin i of the measured distribution allows to remove the fraction of measured events, which are not part of the true distribution and for this reason, would not be described by the response matrix.
Overall, the IBU provides a theoretically well-defined procedure that can be applied for binned distributions, where a different number of bins of the true and measured distribution, are possible. Besides the ability to unfold one-dimensional distributions, the IBU allows to unfold multidimensional distributions as well. Furthermore, unfolded distributions are corrected for migration, inefficiencies and smearing effects. Nevertheless, a realistic guess about the initial true distribution, i.e. the initial probability of the causes $P_0(C_i)$, is needed.

6 Data and Monte Carlo samples

A subset of data events, that were recorded by the ATLAS detector, is described and denoted as analysed dataset in the following. In addition, the properties of simulated MC samples are presented. The MC simulations provide a precise prediction of the particles' generation for a defined process at particle colliders and the corresponding cross-section at a specific order of perturbation theory with its kinematics. Additionally, the detector response can be simulated. The process of interest is called the signal, while the contributions from other processes are summarised as backgrounds.

6.1 Analysed datasets

The datasets used in this measurement consists of data events produced from pp collisions at the LHC at a centre-of-mass energy of $\sqrt{s} = 13\,\text{TeV}$ and was collected by the ATLAS detector during Run 2 between 2015 and 2018. The integrated luminosity as a function of time is presented in Figure 6.1a. The full luminosity delivered by the LHC is represented by the green area, whereas the luminosity recorded by the ATLAS detecor is indicated by the yellow area. The fraction of data events intended for physics, i.e. which have been recorded under good conditions, is a subset of the recorded dataset, and corresponds to an integrated luminosity $\mathcal{L} = 139.0 \pm 2.4\ \text{fb}^{-1}$ [52].
In Figure 6.1b the average number of interactions per bunch crossing regarding to the full Run 2 dataset, recorded at the ATLAS experiment in pp collisions between 2015 and 2018, is presented. Due to the high number of protons in each of the colliding pp bunches, several additional collisions, so-called pile-up, occur besides the process of interest. The dataset is

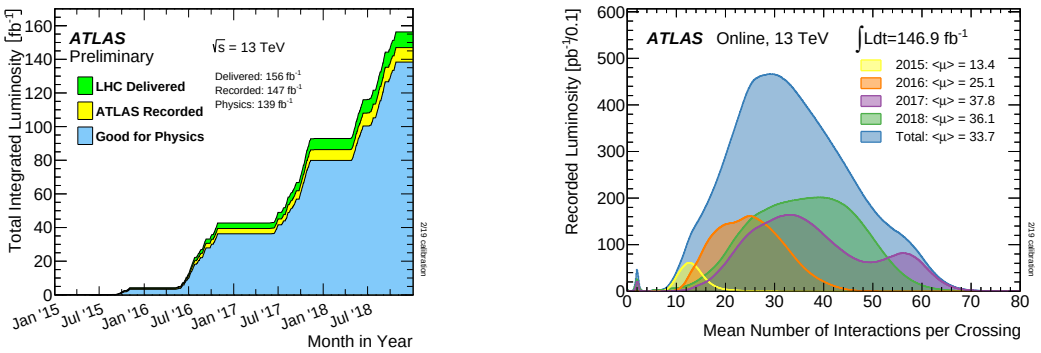

(a) (b)

Figure 6.1: The total integrated luminosity of the LHC and the average number of interactions per bunch crossing during Run 2 taken from Reference [53].

composed of four subsets, that are recorded under different conditions, where the average number of interactions is 13.4, 25.1, 37.8 and 36.1 in the years 2015, 2016, 2017 and 2018, respectively.

6.2 Event generation at the Large Hadron Collider

In experimental particle physics, the theoretical predictions based on the SM or models beyond are provided by MC simulations. The generation of a MC sample [54] can be subdivided into the hard scattering process, initial and final state radiation (ISR/FSR) from QCD, additional parton-parton interactions, the hadronisation of final state particles, the decay of unstable hadrons and the QED radiations. Each of the steps is visualised in Figure 6.2 and discussed shortly in the following.

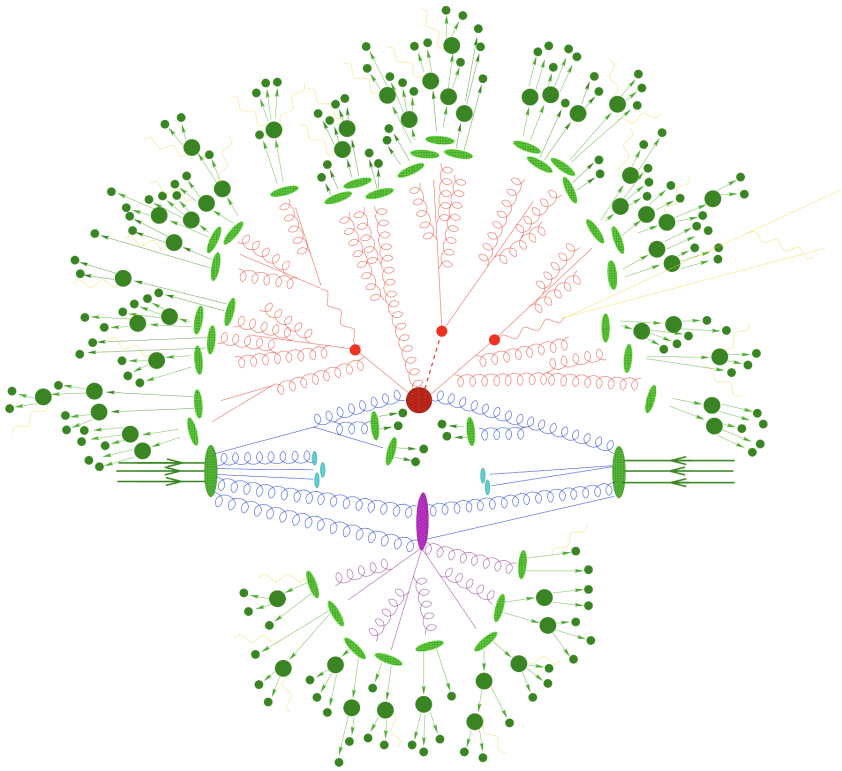

Figure 6.2: Illustration of the relevant aspects for an exemplary pp collision [55]. The protons are represented by large, dark green ovals and the partons of the proton, that correspond to the initial state, by the blue lines. The large (small) red circle corresponds to the hard scattering process (further decay vertices of generated particles during the hard scattering) and the red lines visualise the final state radiation from QCD. Additional parton-parton interactions are shown as a large purple oval and the corresponding lines. The hadronisation of final state particles is represented by the small, light green ovals and the decay of hadrons by dark green circles. QED radiations, that can occur at any stage, are shown as yellow lines.

As discussed in Chapter 2.6, the factorisation theorem allows to separate perturbative and non-perturbative QCD interactions, i.e. the description of the hard scattering process and the distribution of partons in the proton. While PDFs are provided by several different working groups, the probability distribution of the hard scattering process, which corresponds to the square of the matrix-element, have to be calculated by Feynman rules via perturbation theory. Both, PDFs and probability distribution, are used as ingredients to the calculation of the convolution integral depending on the available phase space, following Equation 2.10. The convolution integral is solved numerically by MC generators based on the random sampling via the MC method, which is eponymous for the simulation. MC generators are used to generate the first step of MC samples, so-called LHE files, consisting of the four momenta of the particles participating in the hard scattering process and depending in particular on a certain order of perturbation theory, the factorisation scale μ_F and the renormalisation scale μ_R.
Additional radiations from QCD and QED interactions are considered in order to approximately account for higher orders of perturbation theory. In case of QCD radiations, the inital state and partons produced in the final state are coloured objects, where gluons can split into quark anti-quark pairs and quarks can radiate gluons. All these interactions can be described via *parton shower algorithms* down to approximately $\mathcal{O}(1\,\text{GeV})$ by pQCD. Again, the factorisation theorem allows to separate effects from perturbative and non-perturbative interactions. Non-perturbative effects of confinement, where pQCD breaks down and partons form hadrons, become relevant if the parton momentum decreases induced by multiple parton splittings. Two different approaches, the string model [56] and the cluster model [57], are commonly used. Furthermore, additional QED radiation is described by parton shower algorithms as well and might occur at any stage.
Additional parton-parton interaction, which are referred to as *underlying event* (UE), can occur between the remnants of the proton besides the hard scattering process in order to regain a colourless state. Typically, low energy hadrons are formed as a consequence of the UE where phenomenological models that are tuned to data are used.
Hadrons originating from the hard scattering process or additional parton-parton interactions are not stable. Consequently, their decays need to be simulated as well, where dedicated algorithms based on theoretical calculations and measured hadron decays are used.
In the end, each of the simulated events is passed trough a detector simulation in order to obtain the corresponding detector signals. Each MC sample provides on one hand the events after the detector simulation, corresponding to the reconstructed level, and on the other hand, the true particles generated during the hard scattering process, corresponding to the MC truth level.

6.3 Simulated signal and background samples

In the following, an overview of the MC samples used for the theoretical prediction of signal and background processes in this thesis is provided. First, general properties of the MC samples are summarised and subsequently the properties of the signal and each of the background samples is described. Background contributions from top quark production, including top anti-top production, $t\bar{t}$, and single top production, the neutral-current Drell-

Yan (ncDY) process $Z \to \ell\ell$ with $\ell \in \tau, e$, additional ccDY decay channels $W \to \tau\nu_\tau$ and furthermore the diboson production of WW, WZ and ZZ are considered.
Every MC sample is passed through the detector simulation based on `GEANT4` [58], where a more detailed, full detector simulation, called FullSim (FS), or a fast detector simulation, called AtlasFast 2 (AF2) [59], can be performed. All MC samples used in this thesis, except specific samples only used for the estimation of uncertainties, are based on FS. After the transition from particles to detector signals, the same software for the object reconstruction, described in Chapter 7, is used for MC simulation and the analysed dataset.
The generation of a MC sample relies on the matrix-element generator with its PDF and the parton shower program with its PDF. Commonly, a single program is used to model the parton shower, hadronisation and the UE. The simulation of the parton shower program can often be improved by the usage of tuned parameter sets. Finally, the generation of pile-up events is modelled by the overlay of the hard scattering event with inelastic pp collisions that where simulated with Pythia 8.186 [60] using the PDF NNPDF2.3LO [61] and the A3 tune [62].

The nominal signal MC, corresponding to the ccDY process $W \to e\nu_e$, is generated using Powheg Box v1 [63–65] and the CT10 [66] NLO PDF at NLO in pQCD. The parton shower, hadronisation and the UE is modelled with pythia 8.186 [67] using the `AZNLO tune` [68] and the CTEQ 6 PDF [69]. Additional QED radiations are simulated by Photos [70].
In this thesis, the transverse mass of the W boson is studied up to $\mathcal{O}$(TeV). Since an inclusive sample without any restrictions concerning the phase space consists dominantly of events at low masses of the W boson and less statistics is expected for higher and higher masses of the W boson. As a consequence, an inclusive sample and a set of samples sliced in the invariant mass of the W boson is used. The inclusive sample is used in the range of invariant masses of the W boson $m_{\text{inv}}^W < 120\,\text{GeV}$. A slicing procedures ensure high statistics by restricting the phase space to a small range of the invariant mass in the MC event generation. In total, 18 different MC samples, that cover all-together a range of the invariant mass $m_{\text{inv}}^W \in [120, 5000]$ GeV and one additional sample covers the region of $m_{\text{inv}}^W > 5000\,\text{GeV}$. In order to avoid double-counting and restrict the inclusive sample to events with an invariant W boson mass $m_{\text{inv}}^W < 120\,\text{GeV}$, an adequate upper cut is applied on the MC truth level invariant mass for the inclusive sample. The full list of simulated signal samples and their respective cross-sections are shown in Appendix A.
A mass-dependent k-factor, centrally provided within the ATLAS collaboration, allows to apply further corrections improving the accuracy of the signal MC sample. A precision of NNLO in pQCD, where the CT14 NNLO PDF [71] set is used for the matrix-element generation, and electroweak corrections at NLO are achieved. Similarly, a mass-dependent k-factor for the ncDY and $W \to \tau\nu_\tau$ processes is used.

Since the nominal signal MC does not provide theoretical systematic uncertainties and another MC sample is required as well for the systematic variation of the matrix-element generation and parton shower, alternative signal MC samples are generated. Two different approaches are followed for their generation: One of the MC samples is generated using Powheg-Box v2 [63–65] at NLO in pQCD, where the showering is provided by Herwig 7 [72, 73]. The PDF set CT18NNLO [74] is used. The validation of this MC sample was performed as a part of this thesis and is briefly discussed in Chapter 6.4. Another alternative MC sample is simulated with the SHERPA 2.2.11 [75] generator. The PDF set

NNPDF3.0 NNLO [76] is used. Final states with zero, one or two additional partons and final states with three, four or five additional partons achieve an accuracy of NLO and LO in pQCD, respectively.

The $t\bar{t}$ background, consisting of the production of a top-anti-top pair, is generated with Powheg Box v2 at NLO in QCD using the NNPDF3.0 NNLO PDF, the parton shower is simulated by Pythia 8 using the A14 set of tuned parameters [77].
Alternative $t\bar{t}$ samples are used for the evaluation of systematic uncertainties concerning the parton shower and the matrix-element generator. For this reason, two additional MC samples are used, where in one MC sample the matrix-element generator is replaced by MadGraph5_AMC@NLO v2.6.0 [78] and in the other MC sample the parton shower is modelled by Herwig 7. These samples are only available in AF2.
The single top background consists of three contributions, covering the production of a top quark in association with a W boson (tW) and the single top t- and s-channel processes. The tW samples are generated with Powheg Box at NLO in pQCD using the NNPDF3.0 NLO PDF sets. The digram removal scheme [79] is used to remove interference and overlap with $t\bar{t}$ production. The t-channel contribution is modelled with Powheg Box at NLO in pQCD and the NNPDF3.0 NLO nf4 PDF sets, while the s-channel contribution is simulated with Powheg Box at NLO in pQCD using the NNPDF3.0 NLO PDF sets. The parton shower and hadronisation is based on Pythia 8 with the A14 tune for all three MC samples.
The ncDY background, $Z/\gamma^* \to \ell\ell$, is generated with Powheg Box v1 interfaced with Pythia 8.186 for the parton shower and hadronisation processes. The PDF CT10 NLO and the AZNLO tune are used. The ncDY process is divided into a single inclusive and 18 sliced samples as described for the ccDY process.
Another ccDY decay channel, $W \to \tau\nu_\tau$, is simulated based on the same generator and showering as for the simulated signal MC sample and contributes as a background. Subsequent decays of the τ lepton into electrons are the reason for the contribution.
The diboson background is splitted into several samples, covering WW, WZ and ZZ, which are modelled with Sherpa 2.2.1 or Sherpa 2.2.2 [75]. The final state consists especially of the leptonic contribution originating from the decay of the bosons, where an accuracy of NLO in pQCD is achieved for final states with zero or one additional parton and two or three additional partons in the final state are generated at LO in pQCD. All diboson MC samples are based on the NNPDF3.0 NNLO PDFs and a dedicated set of tuned parton-shower parameters developed by the Sherpa authors.
The dijet process consists of multiple slices, where each MC sample is generated based on LO pQCD matrix-elements from Pythia 8, which where matched to the parton shower. Additionally, the modelling of the parton shower and the hadronisation were performed by Pythia 8 using the A14 tune. For both, the matrix-element generation and the parton shower, the PDF set NNPDF2.3 LO was used.

6.4 Validation of alternative Monte Carlo samples

Since the generation of a MC sample requires a substantial amount of computing resources, it is crucial to check the validity of newly generated events before. This procedure is usually based on a small sample generated for the purpose of the validation. The alternative MC sample is based on an updated version of POWHEG BOX and a different showering provided by HERWIG 7. A common approach for the validation of a new MC sample relies on comparisons at MC truth level, where the validation MC sample is compared to an established MC generator. Usually, a large amount of variables is investigated in such validation procedures and potentially occuring differences have to be investigated.
In Figure 6.3, two of the distributions that differ most between the nominal POWHEG+PYTHIA 8 MC sample and the POWHEG+HERWIG 7 validation sample are presented. The comparison of the transverse momentum of the W boson p_{T}^{W} and the rapidity of the W boson y_W is performed at MC truth level. Additionally, a separate validation sample, where the parameter *ptsqmin* is varied to 0.8 in the POWHEG+HERWIG 7 generation is shown. For the transverse momentum of the W boson differences between the two MC generators close to $p_{\mathrm{T}}^{W} \approxeq 2\,\mathrm{GeV}$ can be observed. These differences are expected and can be traced back to the special tune that is only available for PYTHIA 8. The variation of the *ptsqmin* parameter targets an improved agreement, which can not be observed. As a result, the parameter is chosen to be $ptsqmin = 1.0$. Besides the large differences for low transverse momenta of the W boson, a good agreement as a function of the rapidity of the W boson can be found between POWHEG+HERWIG 7 and POWHEG+PYTHIA 8.

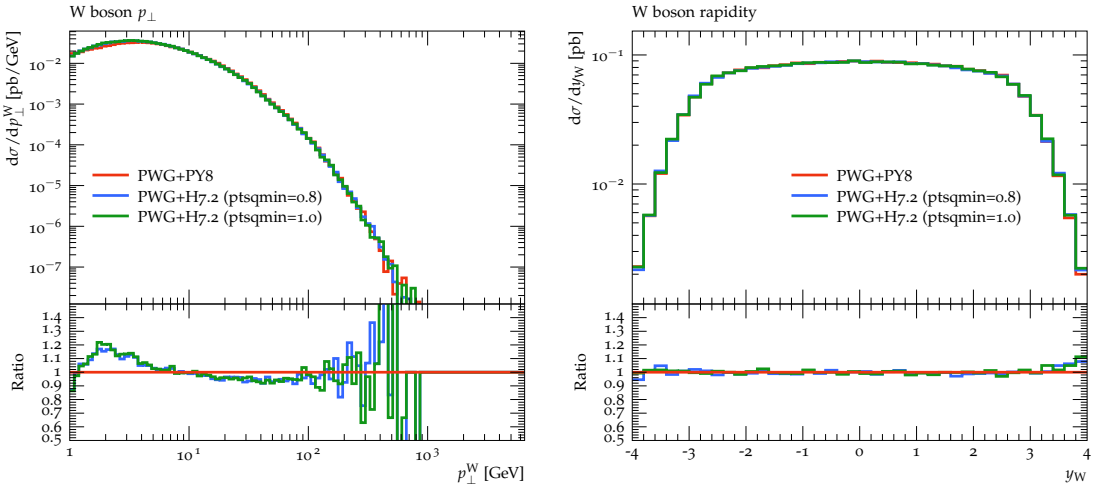

Figure 6.3: Comparison of the transverse momentum p_{T}^{W} and the rapidity y_W of the W boson m_W for the MC samples POWHEG+PYTHIA8, denoted as PWG+PY8, and POWHEG+HERWIG 7.2, denoted as PWG+H7.2 on MC truth level. Two variations of the parameter $ptsqmin \in [0.8, 1.0]$ are shown for the PWG+H7.2 MC sample.

7 Event reconstruction with the ATLAS detector

Different objects that are generated during *pp* collisions are measured and identified with the ATLAS detector. Dedicated algorithms, based on the information recorded by the various detector components, are used for the identification of certain particle types. The identification procedure is the same for the collected data and the MC simulations.
Depending on the multiplicity of each single object the final state of an event is defined. The final state of the signal process consists of one electron and one electron neutrino. For this reason, the reconstruction of electrons and of the missing transverse momentum, providing a measure for undetected particles, i.e. neutrinos, are described in detail. Additionally, the reconstruction of muons and jets are discussed. Finally, the overlap removal procedure is explained.

7.1 Trigger

Electron triggers [80] are used to recover events with electrons from the huge amount of data produced at the LHC. The ATLAS trigger system consists of a level-1 and a high-level trigger as explained in Chapter 3.2.5. The workflow of the electron triggers and their peculiarities are described in the following.
As described in Chapter 3.2.5, an EM region of interest in the central region $|\eta| < 2.5$ is identified by the L1 trigger. A first energy measurement within the RoI is performed and requirements on that energy measurement are denoted e.g. as *EM20*, where a transverse energy threshold of $E_T > 20\,\text{GeV}$ is passed. Additionally, there are three optional requirements at the L1: First, the usage of a η dependent energy threshold is denoted by the letter "V". Second, a veto for hadronic activity might be applied. In this case, its application is indicated by the letter "H". Lastly, an EM isolation of the electron, denoted as "I", might be required.
Subsequently, a fast and a precise reconstruction are performed for electrons in the HLT. One of the main requirements in the fast reconstruction is based on the matching of a track, obtained from a fast track reconstruction in the RoI, to an energy cluster of the electron candidate. The precise reconstruction consists of additional matching requirements between track and energy cluster, the electron identification using a multivariate technique, and the application of isolation requirements. The electron identification and isolation requirements provide a measure for the likeliness that a real electron, with a low event activity around the electron candidate, has been measured. More details are described below in Chapter 7.2.3. Although the demanded electron identification and isolation in the precision reconstruction of the trigger is designed to be as close as possible to the requirements that are applied in the offline reconstruction, a few exceptions are made. Consequently, the trigger requirements are slightly less strict with respect to the offline reconstruction.

Single electron triggers, as used in this thesis, are characterised by their energy, identification and isolation requirements. A certain transverse energy of the electron, e.g. $E_T > 24\,\text{GeV}$, denoted as *e24*, is required. In addition, the multivariate technique used for the electron identification offers the so-called *lhloose*, *lhmedium* and *lhtight* working points. An additional requirement can be demanded for each of the working points, where the information about the transverse impact parameter[1] relative to the beam-line d_0 might be used in the identification procedure. The application of a d_0 requirement especially allows to prevent inefficiencies related to bremsstrahlung. Finally, an optional track-only isolation, denoted as *ivarloose* might be required.
The single electron triggers, separated by the different years of data-taking, are summarised in the Tab. 7.1.

Table 7.1: List of single electron triggers used in this measurement.

Year	Trigger
2015	HLT_e24_lhmedium_L1EM20VH
	HLT_e60_lhmedium
	HLT_e120_lhloose
2016-2018	HLT_e26_lhtight_nod0_ivarloose
	HLT_e60_lhmedium_nod0
	HLT_e140_lhloose_nod0

7.2 Electron selection

The electron reconstruction and energy calibration, the identification and isolation requirements for electrons and the efficiency corrections applied for MC simulations are explained in this section. Only electrons in the central region of the detector fulfilling $|\eta(e)| < 2.4$ are considered.

7.2.1 Reconstruction

The electron reconstruction [81] is composed of the reconstruction of tracks, the clustering of energy depositions in the calorimeter cells and their matching to track-cluster pairs, which are denoted as superclusters. In general, tracks represent the path of a charged particle through the inner detector. In the following, the reconstruction of electron tracks is described only. Additionally, clusters of energy depositions allow to obtain an estimate of the energy of the electron.

The reconstruction of a track [81, 82] starts by collecting hits that are measured in the pixel and the SCT detector. These hits are assembled in order to built so-called space-points, corresponding to the position of the interaction of the measured particle with the active material of the inner detector. In case of the SCT, both sides of the two-sided module are

[1] Referring to the shortest distance between the particle's trajectory and the z-axis.

combined for a single space-point, whereas in the pixel detector one cluster allows to define one space-point. In order to obtain a track seed, three space-points from the pixel and the SCT detector are required. At this point, a pattern recognition algorithm is applied in order to obtain track candidates, which are extended to additional space points. If no track candidates can be extrapolated, a more advanced pattern recognition algorithm that relies on a Kalman filter is used. In this case, the energy losses, due to the material in the detector, of up to 30% are taken into account. Afterwards, track candidates with a transerverse momentum of at least 400 GeV are fitted using a global χ^2 track fitter, including hits in the TRT. At the same time, a dedicated algorithm is used to resolve ambiguities of tracks that partially rely on the same hits.

The second part of the electron reconstruction is the formation of superclusters [81] from the energy depositions in the calorimeter. A supercluster is a dynamical, variable-size object improving the offline reconstruction with respect to former fixed-size cluster approaches, because the algorithm is able to adjust the cluster size if needed. First, topological clusters (topo-cluster) are formed based on energy depositions in the EM and hadronic calorimeter cells, where the cell energy $E_{\text{cell}}^{\text{EM}}$ at the EM scale[2] fulfils $E_{\text{cell}}^{\text{EM}} \geq 4\sigma_{\text{noise, cell}}^{\text{EM}}$ with the expected cell noise $\sigma_{\text{noise, cell}}^{\text{EM}}$. Neighbouring cells are subsequently added to the topo-cluster if the energy threshold of two, instead of four, is exceeded. Afterwards, further neighbouring cells, where no energy threshold has to be fulfilled, are added. The EM energy of topo-clusters is based on EM calorimeter cells for electrons in $0 \leq |\eta(e)| \leq 2.4$, where the energy deposited in the presampler and scintillator are added in the region $1.37 \leq |\eta(e)| \leq 1.63$. Clusters are discarded for EM energies smaller than 400 MeV and EM fractions f_{EM}, which relies on the ratio of the EM energy and the total cluster energy, of less than 0.5. The remaining topo-clusters are referred to as EM topo-clusters in the following.
The superclusters are built for electrons and photons separately, while overlap is removed at a later stage. The supercluster reconstruction consists of two steps: Potential seeds for building superclusters are identified based on the E_T-sorted list of EM topo-clusters. Clusters with a transverse energy $E_T \geq 1$ GeV and an associated track with four hits in the SCT are identified as electron supercluster seeds. Subsequently, the EM topo-clusters next to the electron supercluster seeds are marked as potential satellite cluster candidates, which might originate e.g. from bremsstrahlung. A satellite cluster candidate becomes a satellite of the associated seed cluster in one of the two following cases. On the one hand, the satellite fulfils $\Delta\eta \times \Delta\phi = 0.0075 \times 0.125$ around the barycenter of the seed cluster. On the other hand, the satellite is also added in the range of $\Delta\eta \times \Delta\phi = 0.125 \times 0.300$ around the barycenter of the seed cluster if the track is the best-matched track for the seed cluster. The combination of a seed cluster and its associated satellites is called supercluster.

Finally, the combination of an electron supercluster and a matched track is called electron candidate. As mentioned above, the electron and photon candidates are reconstructed separately, which is why ambiguities have to be resolved. Afterwards, reconstructed electrons are obtained and their energy has to be calibrated as explained in the following.

[2]Refers to the basic signal scale that corresponds to the energy depositions of EM showers in the calorimeter.

7.2.2 Energy calibration

The energy calibration [81, 82] for electron candidates relies on the deposited energy in the EM calorimeter. Although the electron shower is usually fully contained in the EM calorimeter and the energy is expected to be measured precisely by the energy deposits, a fraction of the electron energy is usually lost before the calorimeter or outside of the reconstructed supercluster.
The calibration procedure [83] is performed step-wise: First, a MC-based calibration for electrons is applied. This calibration relies on a multivariate regression algorithm targeting the correction of energy losses in bins of the pseudorapidity η and the transverse energy E_T based on the description of the detector material in the detector simulation. So-called uniformity corrections, accounting for non-simulated variations of the detector response in specific regions, and an intercalibration, correcting for the different scales in each of the longitudinal EM calorimeter layers, are applied. The final energy calibration is performed based on $Z \to ee$ events, where the electron response in data is calibrated to reflect the electron response in the MC simulation. In this step, differences in the energy resolution between data and MC simulations are corrected by applying scale factors to the MC simulation. More details on energy calibrations based on the energy response are conceptually described in Chapter 7.4. Lastly, the calibrated electron energy scale is validated for electrons originating from the $J/\Psi \to ee$ process.

7.2.3 Identification and isolation requirements

Due to the similarity of energy depositions from electrons, jets and photons, the electron identification [82] plays a crucial role in the suppression of reconstructed electrons that are e.g. truly jets or converted photons. The identification efficiency of real electrons has to remain high at the same time. For this reason, a likelihood discriminant d_L is defined as the natural logarithm applied to the likelihood of the signal and background, L_S and L_B respectively. The likelihoods $L_{S(B)}$ are evaluated from probability density functions combining a selection of discriminating variables in order to distinguish signal and background. The considered variables are based on the electron track, the development of the shower in the calorimeters and the compatibility of the electron track and reconstructed cluster. The probability distribution functions are obtained by a tag-and-probe method that relies on data events recorded in 2015 and 2016. Events from $Z \to ee$ and $J/\Psi \to ee$ production, corresponding to different ranges of E_T, are used. Further details can be found in Reference [84].
Three operating points covering different signal efficiencies for various physics analysis needs are considered in this thesis. The *LooseAndBLayer*, *Medium* and *Tight* likelihood operating points are defined by the requirement of certain thresholds on the likelihood discriminant that are optimised in bins of the pseudorapidity η and bins of transverse energy E_T.

An additional isolation criterion, quantified by the activity in a cone around the electron candidate, allows to further reduce e.g. contributions from electrons originating from hadronic jets. The electron isolation is defined by one of the following requirements: On one hand by the number of tracks with a certain transverse momentum corresponding to other charged particles close to the electron track, *track isolation*, and on the other hand by the amount of energy depositions close to the electron candidate, *calorimeter isolation*.

The track isolation relies on the variable $p_{\mathrm{T}}^{\mathrm{cone}\Delta R_{\mathrm{max}}}$, where the transverse momenta of all selected tracks in a fixed-size ΔR cone around the track of the electron candidate are summed up. For heavy particles or high-momentum particles that decay into much lighter particles besides an electron, usually ΔR between the electron and other decay products is very small. In this case, an isolation requirement with e.g. a fixed-size $\Delta R = 0.2$ would reject the event.
Another common definition is based on a variable cone size, where the ΔR cone shrinks with increasing transverse momentum of the electron candidate. The variable cone size

$$\Delta R = \mathsf{min}\left(\frac{10}{p_T(e)}, \Delta R_{\mathrm{max}}\right)$$

is used for the definition of the variable $p_T^{\mathrm{varcone}\Delta R_{\mathrm{max}}}$, with a typical value of $\Delta R_{\mathrm{max}} = 0.2$. The calorimeter isolation depends on the variable $E_T^{\mathrm{cone}\Delta R_{\mathrm{max}}}$ which consists of the sum of the *raw* transverse energies of topo-clusters at the EM scale in a ΔR cone around the electron candidate and the core, pile-up and leakage corrections. First, the core correction excludes contributions in $\Delta\eta \times \Delta\phi = 0.0125 \times 0.175$ around the barycentre of the electron cluster. Afterwards, so-called energy leakage, describing the energy that leaks from the electrons shower development into the isolation cone, is corrected. Finally, pile-up effects are removed by a correction function based on the number of reconstructed primary vertices. As a result, the calorimeter isolation is defined as

$$E_T^{\mathrm{cone}\Delta R_{\mathrm{max}}} = E_{T,\mathrm{raw}}^{\mathrm{cone}\Delta R_{\mathrm{max}}} - E_T^{\mathrm{core}} - E_T^{\mathrm{leakage}} - E_T^{\text{pile-up}}\,.$$

7.2.4 Efficiency correction

The probability to measure a real electron differs for events from MC simulation and data. For this reason, an efficiency for the electron $\epsilon_{\text{total, ele}}$ depending on each individual step is defined as

$$\epsilon_{\text{total, ele}} = \epsilon_{\text{reco}} \times \epsilon_{\text{ID}} \times \epsilon_{\text{isol}} \times \epsilon_{\text{trig}} \times \epsilon_{\text{MisID}}\,, \tag{7.1}$$

where the reconstruction efficiency ϵ_{reco}, the identification efficiency ϵ_{ID}, the isolation efficiency ϵ_{isol}, the trigger efficiency ϵ_{trig} and the additional charge-misidentification efficiency ϵ_{misID} are considered.
The former four efficiencies correspond to the procedures discussed already. The charge mis-identification efficiency accounts for the amount of electron events, where the charge of the electron is not reconstructed correctly, i.e. misidentified, at the detector level.
The efficiencies are obtained separately for MC simulations and data based on the well-known neutral-current DY, $Z \to ee$, the charged-current DY, $W \to e\nu_e$ and the J/Ψ process, $J/\Psi \to ee$. The estimation relies on the tag-and-probe method. Each estimated efficiency for MC simulation, e.g. $\epsilon_{ID,MC}$, and data, $\epsilon_{ID,Data}$, corresponds to a so-called scale factor (SF)

$$\mathrm{SF}_{\mathrm{ID}} = \frac{\epsilon_{ID,Data}}{\epsilon_{ID,MC}}\,,$$

which is applied as multiplicative weights to the event weight. Electron SFs are centrally provided within ATLAS [85].

In this thesis, electrons with a transverse momentum $p_T(e) > 20\,\text{GeV}$ and a pseudorapidity $|\eta(e)| < 2.4$, excluding $1.37 < |\eta(e)| < 1.52$, fulfilling the *LooseAndBLayer* identification criteria are considered. Additionally, the compatibility of the electron originating from the primary vertex is ensured requiring $|z_0 \sin(\theta)| < 0.5\,\text{mm}$ and $|d_0|/\sigma_{d_0} < 5$ based on the longitudinal and transverse impact parameters, z_0 and d_0. Finally, electrons originating from a *bad* calorimeter cluster are vetoed.

7.3 Muon selection

The muon reconstruction [86] relies on tracks in the inner detector and the muon system, where each detector component is used to reconstruct tracks of muon candidates separately. Afterwards, a matching between the MS tracks and the inner detector tracks or the MS tracks and the interaction point is performed. The reconstruction of tracks in the inner detector is based on a similar strategy as described for electron candidates. This section is dedicated to the description of the track reconstruction in the MS. In addition, the identification and isolation requirements of muons are discussed.

The reconstruction of muon track candidates is based on hit patterns in the MS. A Hough transform [87] is performed and used to search for hits that are aligned on a bended trajectory. The obtained hits in different layers are fitted, starting in the middle layer of the MS, in order to obtain a muon track candidate.
Afterwards the combination of tracks from the inner detector and the MS are refitted, optimised by adding (removing) certain hits to (from) the trajectory and classified as combined muons (CB). A set of additional algorithms can be used to reconstruct e.g. extrapolated muons, where muons are reconstructed based on MS tracks in combination with a loose requirement on originating from the interaction point.
The identification of muons aims for the selection of real muons and suppression of muons originating from the decay of hadrons, where several working points are provided, namely: loose, medium, tight, low-p_{T} and high-p_{T}. Muons that satisfy the loose, medium and tight identification are subsets of each other. In this thesis, only muons fulfilling a medium identification are considered and discussed in the following. The medium working point relies on CB and extrapolated tracks, where the latter are restricted to the region of $\eta(\mu) \in [2.5, 2.7]$. Consequently, only CB muons are considered because leptons are only investigated up to $|\eta(\ell)| \leq 2.4$ in this measurement. CB tracks are required to consist of three hits in at least two MDT layers for $0.1 < |\eta(\mu)| \leq 2.4$ and at least one MDT layer and a maximum of one MDT hole[3] layer for $|\eta(\mu)| < 0.1$. Furthermore, a loose compatibility of the measurement in the inner detector and MS has to be fulfilled.
Finally, the muon isolation, separated into track-based and calorimeter-based isolations, provides a strong background rejection against muons that e.g. originate from the decay of hadrons. The track-based isolation p_T^{varcone} is defined as the scalar sum of transverse momenta

[3] A hole refers to a missing hit in an active sensor along the particle's trajectory.

in a variable ΔR cone and the calorimeter-based isolation E_T^{topocone} as the transverse energy of topo-clusters in a fixed size ΔR cone.

In this thesis, muons with a transverse momentum $p_T(\mu) > 20\,\text{GeV}$ and an absolute value of the pseudorapidity $|\eta(\mu)| < 2.4$ fulfilling the medium identification quality are considered. Additionally the longitudinal and transverse impact parameters have to fulfil, $|z_0 \sin(\theta)| < 0.5\,\text{mm}$ and $|d_0|/\sigma_{d_0} < 3$.

7.4 Small-R jet selection

Jets are the result of the hadronisation of partons due to confinement. At the ATLAS experiment, the most common jet definition is based on the $anti-k_t$ [88] algorithm with a radius parameter $R = 0.4$, corresponding to so-called small-R jets. The small-R jet reconstruction [89] is described in the following.
Topological clusters are built from the calorimeter cells using a nearest-neighbour algorithm [90]. The total energy of topo-clusters corresponds to the EM scale, which is based on the measurement of energy depositions from EM showers. Furthermore, topo-clusters, i.e. jet candidates, are corrected to be compatible with the primary vertex of the hard scattering process, also known as *origin correction*.
So-called EMTopo jets, the primary jet definition until the end of Run 2 at the ATLAS experiment, are reconstructed based on origin-corrected EM scale topo-clusters. A more advanced approach that includes information from the tracking system besides information from the calorimeter is called particle flow (PFlow) jet. The PFlow algorithm [91] is the current primary jet definition used at the ATLAS experiment and aims for the approximate identification of individual particles. Charged particles and their energy depositions in the calorimeter can be identified, which allows to subtract the charged particle's energy from the topo-cluster and instead consider the tracks' momenta matched to the topo-cluster. The advantages of PFlow jets are improved energy and angular resolution, reconstruction efficiencies and pile-up stability.

The estimation of the jet energy, performed after the jet reconstruction, is based on a jet energy scale (JES) calibration that is applied stepwise:

1. Pile-up corrections
2. Absolute MC-based calibration
3. Global sequential calibration
4. Residual in-situ calibration

Effects from pile-up are corrected in two consecutive steps, where the first depends on the jet p_T-density and jet area and the second removes residual dependencies. Details can be found in Reference [89].
Then, a MC-based calibration is applied to account for detector-related effects, e.g. the non-compensating calorimeter response. The energy scale of the reconstructed jet is corrected to the jet energy at MC truth level. For this reason, a truth-matching of the reconstructed to the geometrically closest MC truth level jet is performed. The truth-matching depends

on the angular distance $\Delta R = 0.3$, as defined in Chapter 3.2.1 and allows to define the average jet energy response $\mathcal{R}$ as the mean of the Gaussian fit to the ratio of the energy at reconstructed level E^{reco} and MC truth level E^{truth}. Typical jet energy responses are presented in Figure 7.1, where the average jet energy response for PFlow small-R jets as a function of the pseudorapidity η and the reconstructed jet energy E^{reco} is shown. In each of the plots, one of the variables is shown on the x-axis and the other one corresponds to the differently coloured distributions. It can be observed that the average jet responses increase for higher reconstructed energies and smaller absolute pseudorapidities. In order to correct the absolute energy scale for the jet candidates, the inverse of the average jet energy response is applied to the reconstructed jet energies. After the application of the absolute MC-based calibration, deviations from unity of the average jet energy response are in the order of several percent.
Afterwards, the global sequential calibration (GSC) step is focused on corrections concerning the flavour and energy distribution of the constituent particles, the average particle composition and shower shape of the jet, and the particle type that initiated the hadronisation resulting in the reconstructed jet. Especially differences between quark- and gluon-initiated jets can be observed. Multiple multiplicative correction steps are applied throughout the GSC improving the jet energy resolution and reducing fluctuations due to the aforementioned effects. The GSC relies on the p_T response defined as the ratio of transverse momenta of the jet at reconstruction and MC truth level.
Finally, the in situ jet calibration is applied in order to account for differences per jet between data and MC simulations that occur dominantly due to imperfect simulation, e.g. of the involved physics processes such as jet formation. Here, the final correction is applied to data based on a ratio of separately derived jet responses from data and MC simulations.
Another aspect of the jet reconstruction is the estimation of the jet energy resolution (JER), where a detailed discussion of its measurement can be found in Reference [89]. In this thesis, JER plays a role because jets are considered in the determination of the missing transverse momentum $E_{\text{T}}^{\text{miss}}$. Especially a precise measurement of the transverse momentum of the jet is required in order to obtain a reasonable $E_{\text{T}}^{\text{miss}}$ resolution.

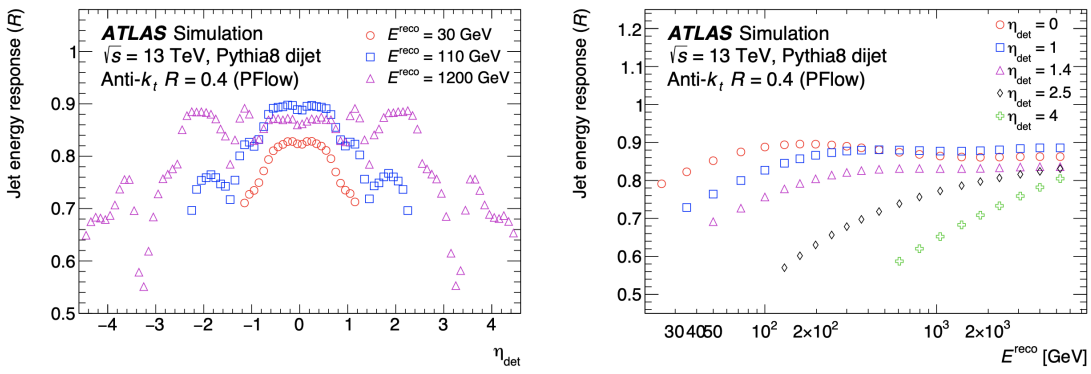

Figure 7.1: The average jet energy response depending on the pseudorapidity of the jet η and the reconstructed jet energy E^{reco} for PFlow jets [89].

In this thesis, small-R jet candidates, identified with the PFlow algorithm, have to fulfil a transverse momentum $p_T(j) > 25\,\text{GeV}$ and an absolute value of the pseudorapidity $|\eta(j)| < 2.5$. A jet cleaning algorithm is applied in order to further increase the quality of selected jets.

7.5 Missing transverse momentum $E_{\text{T}}^{\text{miss}}$

Since neutrinos do not interact with the ATLAS detector, an alternative measure is needed. For this reason, the missing transverse momentum $E_{\text{T}}^{\text{miss}}$ is determined by exploiting the momentum conservation in the transverse plane. The colliding protons' transverse momentum is approximately zero and, for this reason, the vectorial sum of the transverse momenta of all final state particles has to be zero as well. Due to momentum conservation it is possible to measure particles that leave the detector unseen by the missing momentum in the collision. In the following, the reconstruction of the missing transverse momentum [92, 93] is discussed. The missing momenta $E_{x,y}^{\text{miss}}$ in the x- and y-plane are defined as

$$E_{x,y}^{\text{miss}} = E_{x,y}^{\text{miss},e} + E_{x,y}^{\text{miss},\gamma} + E_{x,y}^{\text{miss},\tau} + E_{x,y}^{\text{miss,jets}} + E_{x,y}^{\text{miss},\mu} + E_{x,y}^{\text{miss,soft}} \,, \tag{7.2}$$

where the calibrated momenta of all electrons, photons, taus, jets, muons and the soft term is summed. In this measurement, photons and τ leptons are not considered in the $E_{\text{T}}^{\text{miss}}$ calculation. There are different approaches to account for objects that have not been matched in one of the particle reconstruction steps. The track-based soft term (TST) $E_{\text{T}}^{\text{miss}}$ relies on tracks in the inner detector, while the calorimeter-based soft term (CST) $E_{\text{T}}^{\text{miss}}$ takes calorimeter signals as input. Depending on the choice of soft term, the $E_{\text{T}}^{\text{miss}}$ performance and uncertainties associated to $E_{\text{T}}^{\text{miss}}$ differ. Only the TST $E_{\text{T}}^{\text{miss}}$ is considered in the following.
As described above, it is only possible to account for missing momenta in the transverse plane. For this reason, the missing momenta $E_{x,y}^{\text{miss}}$ are used to define the missing transverse momentum, $E_{\text{T}}^{\text{miss}}$, and the associated angle, ϕ^{miss}, in the x-y-plane of the ATLAS detector.

$$E_{\text{T}}^{\text{miss}} = \sqrt{\left(E_x^{\text{miss}}\right)^2 + \left(E_y^{\text{miss}}\right)^2} \tag{7.3}$$

$$\phi^{\text{miss}} = \arctan\left(\frac{E_y^{\text{miss}}}{E_x^{\text{miss}}}\right) \tag{7.4}$$

7.6 Overlap removal

The object reconstruction of all particles discussed in this section is based on tracking and calorimeter information. Due to independent reconstructions of various particle types an overlap may occur, where e.g. the same energy deposition is associated to two different particles. The overlap removal procedure is used to avoid these double-counting effects, which is crucial in order to correctly estimate the missing transverse momentum $E_{\text{T}}^{\text{miss}}$ of an event.

Table 7.2: Criteria for the overlap removal procedure.

Reject	Against	Criteria
Muon	Electron	is *calorimeter* muon and shared Inner Detector track
Electron	Muon	shared Inner Detector track
Jet	Electron	$\Delta R < 0.2$
Electron	Jet	$\Delta R < 0.4$
Jet	Muon	$N_{\texttt{track}} < 3$ and (ghost-associated or $\Delta R < 0.2$)
Muon	Jet	$\Delta R < 0.4$

A summary of the consecutively performed steps of the overlap removal procedure is given in Tab. 7.2. All presented requirements are used in the following, unless stated otherwise.

A *calorimeter* muon is rejected if it shares an Inner Detector track with an electron. In the next step, remaining electrons with a shared track with a muon are discarded. While jets geometrically matched within $\Delta R < 0.2$ to an electron are removed, electrons geometrically overlapping within $\Delta R < 0.4$ with a jet are rejected afterwards. Jets with less than three associated tracks N_{track} and either within $\Delta R < 0.2$ to a muon or with a ghost-associated[4] track in the Inner Detector are discarded. Finally, muons within $\Delta R < 0.4$ of a jet are rejected.
Usually, another requirement targeting the overlap of two electrons is part of the overlap removal procedure. In this case, electrons with a shared track are investigated. The electron candidate with the lower transverse momentum $p_{\text{T}}(e)$ is removed. In this thesis, its application was intended, but this was prevented by a technical issue.

[4] A muon is ghost-associated to a jet, if the muons track is identified with a ghost track of the jet. A ghost track of a jet is characterised by the same direction of the ghost track and the jet, while the transverse momentum of the ghost track is approximately zero.

8 Signal extraction

The identification of specific particle types depends on the detector signature of each particle candidate and allows to distinguish different final states. The selection of events that corresponds to a desired final state is performed by placing requirements on each event, where e.g. a certain number of electrons are required. This procedure is the so-called event selection and discussed in Chapter 8.1. Furthermore, the fiducial event selection that is required at the MC truth level defines the so-called fiducial volume. The fiducial event selection is described in Chapter 8.2. Subsequently, the optimised binning of the variables, where the single-differential and double-differential cross-sections are measured in, are defined in Chapter 8.3.

8.1 Selection criteria at reconstructed level

The goal of the event selection is the identification of ccDY events in the huge amount of data recorded by ATLAS during Run 2. The analysed data set is composed of a mixture of several different processes, where the signal process is a fraction only. The event selection defines the so-called signal region and, for this reason, is designed such that the final state of the signal process is dominantly selected, where the enhancement of the number of selected signal events with respect to the number of selected background events is pursuit. Importantly, the number of signal region events has to remain as high as possible in order to avoid high statistical uncertainties in the measurement.

The event selection is subdivided into a pre-selection and a primary selection. The pre-selection ensures that the events are recorded under good run conditions of the LHC, detected under good conditions of the detector and have a primary vertex corresponding to the hard scattering process. These requirements have been outlined in Chapter 6.1 and Chapter 7. In addition, events are required to fire at least one of the single electron triggers that are described in Chapter 7.1. The pre-selection is summarised in Tab. 8.1.

Table 8.1: Definition of the pre-selection defined in order to ensure good conditions of the accelerator and detector before the primary selection is performed.

Pre-Selection
Good run conditions of the LHC
Good detector conditions of ATLAS
Primary vertex of the event
Fire at least one single electron tigger

The primary selection focuses on the identification of the of ccDY process, where the final state consists of a single electron and its corresponding neutrino. The electron from the W boson decay is expected to satisfy high identification and isolation requirements. Both, additional electrons and electrons that fulfil only low identification and isolation requirements should be rejected. For this reason, two working points for the identification and isolation of electrons, labelled as *loose* and *tight* level, are defined. The *loose* level is required to fulfil the `LooseAndBLayerLH` identification criteria, which is used to ensure basic electron requirements. Furthermore, the track- and calorimeter-isolation requirement `FCLoose`, which is defined as $E_T^{\text{cone20}} < 0.20 \cdot p_T$ and $p_T^{\text{varcone20}} < 0.15 \cdot p_T$, has to be fulfilled. In addition to the requirements on the *loose* level, the *tight* level requires `TightLH` identification criteria and the calorimeter-isolation criteria `FCHighPtCaloOnly`, defined as $E_T^{\text{cone20}} < \texttt{max}\,(0.015 \cdot p_T, 3.5\,\text{GeV})$.
Based on these definitions, exactly one tight level electron with $p_{\text{T}}(e) > 65\,\text{GeV}$ is required and in order to reduce background contributions, additional muons, as defined in Chapter 7.3, and electrons with a transverse momentum of $p_{\text{T}}(e) > 20\,\text{GeV}$ fulfilling the *loose* level are vetoed. Since a single electron is expected in the final state of ccDY, the electron veto is demanded on the *loose* level, where more events are suppressed compared to the *tight* level. Furthermore, selected events with exactly one tight electron have to fulfil a trigger match, where the object that fired the trigger initially has to be in the event, after the electron specific selection steps are performed.

Only electrons with an absolute value of the electron's pseudorapitidy $|\eta(e)| < 2.4$ are considered. Although the electron measurement until $|\eta(e)| < 2.47$ is possible, it is limited to an absolute value of the pseudorapidity of 2.4, because the single muon trigger in the muon measurement can not be used beyond. This muon channel requirement has been adapted in order to ensure that a combination of both channels does not suffer from binning effects or extrapolations. Anyway, only a negligible fraction of electrons are in the range of $2.4 < |\eta(e)| < 2.47$.

Besides the electron, the final state is characterised by missing transverse momentum from the electron neutrino, which is accounted for by requiring $E_{\text{T}}^{\text{miss}} > 85\,\text{GeV}$. A higher value compared to the transverse momentum of the electron is required for three reasons: First, $E_{\text{T}}^{\text{miss}}$ allows to suppress multijet events characterised by small missing transverse momenta. Then, migration effects are reduced for high $E_{\text{T}}^{\text{miss}}$ requirements. Lastly, an asymmetric selection criteria of p_T and $E_{\text{T}}^{\text{miss}}$ reduces edge effects in the theoretical calculation of the transverse mass.

Finally, the targeted phase space for the measurement is defined by a transverse mass of the W boson $m_{\text{T}}^W > 200\,\text{GeV}$. Nevertheless, the unfolding procedure benefits from the knowledge about the number of events in an additional bin in the range of $m_{\text{T}}^W \in [150, 200]\,\text{GeV}$. Further details are provided in Section 12. The transverse mass of the W boson is composed of p_T and $E_{\text{T}}^{\text{miss}}$, thus their selection requirements impact m_{T}^W. As an additional motivation, the p_T and $E_{\text{T}}^{\text{miss}}$ requirements approximately add up to a transverse W boson mass of $m_{\text{T}}^W \approx 150\,\text{GeV}$, which is equivalent to the lower limit of the m_{T}^W bin edge. As a consequence, reasonable statistics is expected for $m_{\text{T}}^W \in [150, 200]\,\text{GeV}$.
The two electron identification and isolation working points and the primary event selection are summarised in Tab. 8.2.

Table 8.2: Definition of the two electron working points with different identification and isolation requirements and the corresponding event selection.

Primary-Selection	
Criteria	Requirement
loose level	`LooseAndBLayerLH` ID
	`FCLoose` isolation
tight level	`TightLH` ID
	`FixedCutHighPtCaloOnly` isolation
Final state	== 1 tight level electron + $E_{\mathrm{T}}^{\mathrm{miss}}$
Veto	Loose level electrons and muons
$\lvert\eta(e)\rvert$	< 2.4
$p_{\mathrm{T}}(e)$	$> 65\,\mathrm{GeV}$
$E_{\mathrm{T}}^{\mathrm{miss}}$	$> 85\,\mathrm{GeV}$
m_{T}^{W}	$> 200\,\mathrm{GeV}$

8.2 Selection criteria at truth level

The unfolding procedure, as outlined in Chapter 5, allows to estimate the number of events at truth level based on the number of events at reconstructed level, i.e. removes effects introduced by the measurement process of data events in the detector. While the event selection defines the phase space considered at reconstructed level, this section is dedicated to the definition of the phase space at truth level. The fiducial selection, i.e. event selection at the truth level, defines the so-called *fiducial* volume.
The fiducial volume plays a crucial role in the determination of several unfolding effects, e.g. in the estimation of events that migrate from a certain bin at fiducial level into another bin at reconstructed level. Furthermore, the unfolded cross-sections can be compared to theoretical predictions in the fiducial volume. In the following, the truth level definitions of the electron and the fiducial selection are discussed.
Multiple states of the electron are provided in the truth level record of the MC, which can be accessed before the particles are passed through the detector simulation. Depending on the selected state of the truth level electron, the truth level is referred to as

- born level, if the lepton before FSR,
- bare level, if the lepton after FSR,
- or dressed level, if the bare lepton and all photons originating from the same decay vertex in a cone of $\Delta R(e, \gamma) < 0.1$ are added,

is selected. A comparison of the three truth level distributions in the transverse mass of the W boson can be found in Fig. F.1 in Appendix F, where small differences between the three distributions are observed. In this thesis, electrons that correspond to the born level are used only.
In particle physics, the fiducial selection is usually defined similar to the event selection at

reconstructed level. In case of substantial differences in the definition of the two levels, either extrapolations or correction factors that rely on the MC sample are required. Since the MC sample can not be perfect, such corrections should be minimised. The fiducial selection at born level is summarised in Tab. 8.3.
Events at fiducial level have to fulfil the following selection steps: At born level, a pseudorapidity of the electron $|\eta(e_{\text{born}})| < 2.4$ and a transverse momentum of the electron $p_T(e_{\text{born}}) > 65\,\text{GeV}$ are required. In addition, the transverse momentum of the neutrino, has to fulfil $p_T(\nu_e^{\text{born}}) > 85\,\text{GeV}$. Both, the electron and the electron neutrino are used to calculate the transverse mass of the W boson at born level $m_T^W(\text{born}) > 200\,\text{GeV}$.

Table 8.3: Definition of fiducial selection performed at the born level.

Fiducial Selection	
Criteria	Requirement
$\|\eta(e_{\text{born}})\|$	< 2.4
$p_T(e_{\text{born}})$	$> 65\,\text{GeV}$
$p_T(\nu_e^{\text{born}})$	$> 85\,\text{GeV}$
$m_{\text{T}}^W(e_{\text{born}}, \nu_e^{\text{born}})$	$> 200\,\text{GeV}$

8.3 Definition of variables for the cross-section measurement

The double-differential cross-section as a function of the transverse mass of the W boson m_{T}^W and the absolute value of the pseudorapidity of the electron $|\eta(e)|$ is measured in this thesis. In addition, the single-differential cross-section as a function of the transverse mass of the W boson is investigated. The variables, m_{T}^W and $m_{\text{T}}^W \otimes \eta(e)$, in which the differential cross-sections are measured, are denoted as measured variables in the following. Besides their definition, it is necessary to define a suitable binning for the variables at fiducial level and at reconstructed level. Several criteria are considered for the definition of the binning at reconstructed level:

1. Experimental resolution of the reconstructed objects.
2. Bin-wise migration caused by the reconstruction.
3. Statistical uncertainty in the data.

The binning at fiducial level is defined close to the binning of the measured variables at reconstructed level.
Since two of the three criteria depend on the bin size, the binning is optimised based on an iterative process. A preliminary binning is chosen and varied until the following requirements are fulfilled: The size of the bin has to be larger than the experimental resolution in the muon channel, which is worse compared to the electron channel. Furthermore, a compromise between large bins in order to reduce statistical uncertainties of the data events and as many bins as possible have to be made. In the end, the purity, which is defined in the following subsection, of at least 50% is required.

The final binning for the single-differential cross-section measurement of the transverse mass of the W boson at reconstructed level is defined as

$$m_{\mathrm{T}}^{W} = [(150,)\, 200, 250, 300, 350, 425, 500, 600, 750, 900, 1100, 1400, 2000]\,\mathrm{GeV}, \tag{8.1}$$

where one additional bin below $m_{\mathrm{T}}^{W} = 200\,\mathrm{GeV}$ is added. At a later stage, the low m_{T}^{W} bin is exploited to improve the unfolding, as outlined in Chapter 8.1.
The final binning of the fiducial level is chosen to be identical to the binning defined at reconstructed level.

In addition, the binning for the double-differential cross-section measurement is defined as

$$m_{\mathrm{T}}^{W} = [(150,)\, 200, 300, 425, 600, 900, 2000]\,\mathrm{GeV}, \tag{8.2}$$

where the number of m_{T}^{W} bins is reduced with respect to the binning of the single-differential cross-section measurement in order to increase the number of events per m_{T}^{W} bin, i.e. reduce the statistical uncertainty. The introduction of an additional binning in $|\eta(e)|$ reduces the number of events per $m_{\mathrm{T}}^{W} \otimes |\eta(e)|$, i.e. enlarges the statistical uncertainty, and is defined as

$$|\eta(e)| = [0.0,\ 0.2,\ 0.4,\ 0.6,\ 0.8,\ 1.0,\ 1.2,\ 1.37,\ 1.52,\ 1.8,\ 2.0,\ 2.2,\ 2.4] \tag{8.3}$$
for the first three m_{T}^{W} bins,

$$|\eta(e)| = [0.0,\ 0.4,\ 0.8,\ 1.37,\ 1.52,\ 2.0,\ 2.4] \tag{8.4}$$
for the fourth and fifth m_{T}^{W} bins,

$$|\eta(e)| = [0.0,\ 0.6,\ 1.37,\ 1.52,\ 2.4] \tag{8.5}$$
for the sixth m_{T}^{W} bins.

The angular resolution in the pseudorapidity is very good, thus the statistical uncertainty plays the most important role in the definition of the binning. Six bins in m_{T}^{W} are chosen such that the bin edges in the single-differential and double-differential cross-section measurement match. As a consequence, comparisons between the single-differential and double-differential cross-sections are easily possible. The absolute value of the pseudorapidity is binned equidistantly with a size of $\Delta\eta(e) = 0.2$ in the first three m_{T}^{W} bins, with an exception in the range of $|\eta(e)| \in [1.37, 1.52]$, where the events in the transition region of the barrel and end-cap of the LAr calorimeter are vetoed. Similarly, the $|\eta(e)|$ binning is chosen for the last three m_{T}^{W} bins, where a broader bin size of $\Delta\eta(e) = 0.4(0.6)$ is used.
The corresponding final binning at the fiducial level is identical as a function of the transverse mass. In contrast, the $|\eta(e)|$ binning is defined as

$$|\eta(e)|_{\mathrm{fiducial}} = [0.0,\ 0.2,\ 0.4,\ 0.6,\ 0.8,\ 1.0,\ 1.2,\ 1.4,\ 1.6,\ 1.8,\ 2.0,\ 2.2,\ 2.4] \tag{8.6}$$
for the first three m_{T}^{W} bins,

$$|\eta(e)|_{\mathrm{fiducial}} = [0.0,\ 0.4,\ 0.8,\ 1.2,\ 1.6,\ 2.0,\ 2.4] \tag{8.7}$$
for the fourth and fifth m_{T}^{W} bins,

$$|\eta(e)|_{\mathrm{fiducial}} = [0.0,\ 0.6,\ 1.2,\ 1.8,\ 2.4] \tag{8.8}$$
for the sixth m_{T}^{W} bins,

where a strictly equidistant binning is chosen in order to avoid that peculiarities such as the transition region of the barrel and end-cap of the LAr calorimeter are reflected in the measured cross-sections.
Each of the different criteria that have been used for the definition of the optimised binning of the measured variables is presented in the following subsections.

8.3.1 Experimental resolution

First, the experimental resolution, defined by the ATLAS detector, which provides a measure for how accurately a variable at reconstructed level is determined concerning its true value. The estimation of the experimental resolution relies on the W MC sample and is visualised for the transverse momentum of the electron in Figure 8.1. Technically, a two-dimensional distribution of the distribution at reconstructed level and the MC truth level, as shown in Figure 8.1a, is used to obtain the projection of the distribution at reconstructed level for a range at truth level, as shown in Figure 8.1b. The RMS is calculated for each projection and used as a measure for the resolution. The experimental resolution as a function of the transverse momentum of the electron and the missing transverse momentum is estimated and shown in Figure 8.2. The estimated RMS is at several GeV for small values of the transverse momentum of the electron and the missing transverse momentum. It increases continuously up to 40 GeV as a function of $p_{\mathrm{T}}(e)$ and to 60 GeV as a function of $E_{\mathrm{T}}^{\mathrm{miss}}$ at approximately 1000 GeV. Overall, similar behaviour as a function of $p_{\mathrm{T}}(e)$ and $E_{\mathrm{T}}^{\mathrm{miss}}$ is observed.
In addition, the experimental resolution for the transverse mass of the W boson m_{T}^{W} is calculated and compared to the muon channel as displayed in Figure 8.3. The experimental resolution as a function of m_{T}^{W} is shown in Figure 8.3a, where the trends observed for the experimental resolution of $p_{\mathrm{T}}(e)$ and $E_{\mathrm{T}}^{\mathrm{miss}}$ can be found as well. While the RMS is approximately 20 GeV at small m_{T}^{W}, the largest RMS of 100 GeV is observed at high m_{T}^{W}.
In order to consistently measure the cross-section, the same binning for the electron and

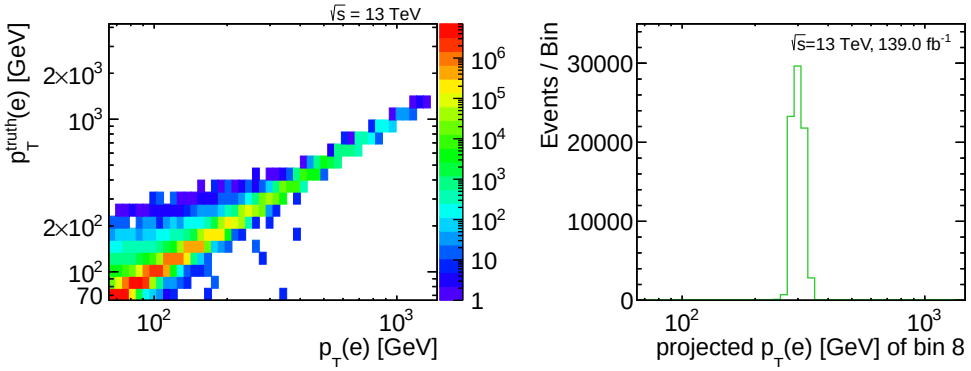

(a) (b)

Figure 8.1: Two-dimensional distribution of the electron's transverse momentum at truth level and at reconstructed level. Exemplarily, a projection of the reconstructed distribution in the eights bin, i.e. for a given truth level value between $p_{\mathrm{T}}^{\mathrm{truth}}(e) = 280$ GeV and $p_{\mathrm{T}}^{\mathrm{truth}}(e) = 330$ GeV, used for the calculation of the RMS is shown.

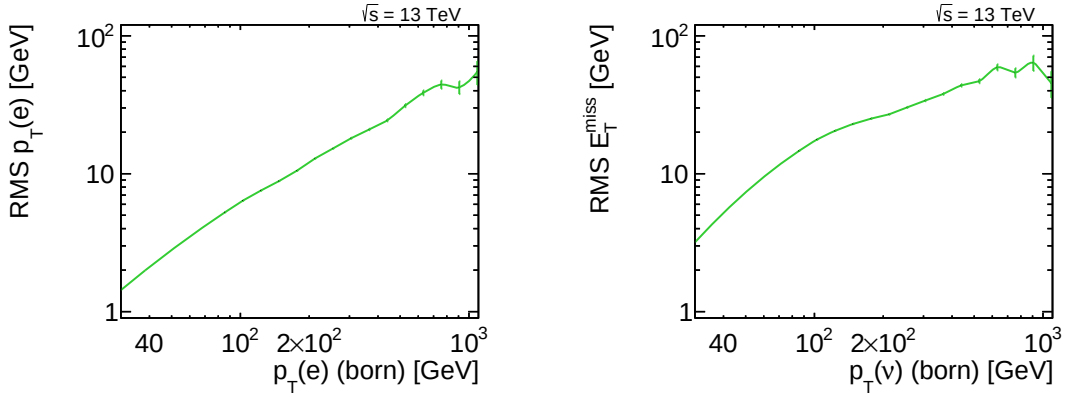

(a) (b)

Figure 8.2: Experimental resolution as a function of the (a) transverse momentum of the electron and (b) transverse momentum of the electron neutrino at truth level corresponding to $E_{\mathrm{T}}^{\mathrm{miss}}$ at reconstructed level.

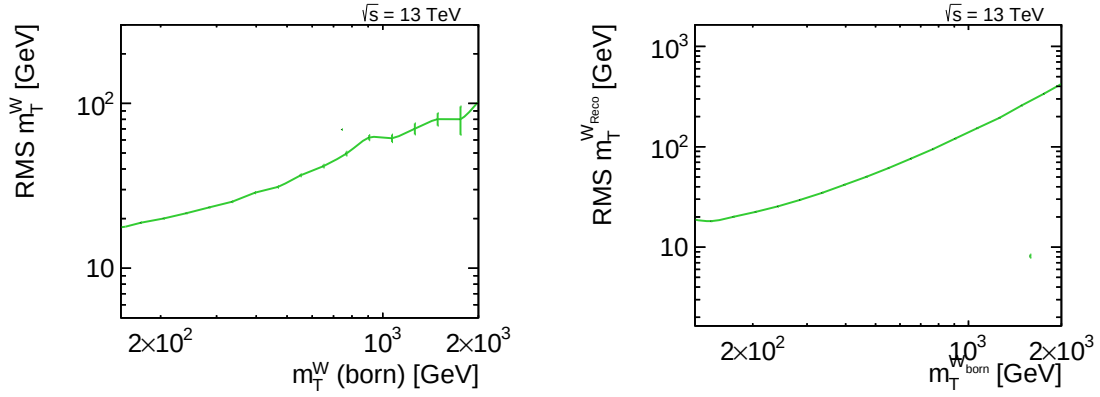

(a) (b)

Figure 8.3: Experimental resolution as a function of the transverse mass of the W boson for a) the electron channel and b) the muon channel at truth level. The experimental resolution for the muon channel is taken from Reference [46].

muon channel is chosen. Importantly, it has to be taken into account that the experimental resolution at high m_{T}^{W} is expected to be better in the electron channel compared to the muon channel. In Figure 8.3b, the experimental resolution of the transverse mass of the W boson in the muon channel, taken from Reference [46], is shown. At $m_{\mathrm{T}}^{W} = 150\,\mathrm{GeV}$ a similar resolution with respect to the electron channel is found. In contrast, the experimental resolution gets worse with increasing m_{T}^{W}, where an RMS of up to 400 GeV at high m_{T}^{W} is observed. The experimental resolution at high m_{T}^{W} is driven by the experimental resolution of high transverse momenta of the muon. The momentum of the muon is determined track-based. At high $p_T(\mu)$, the tracks are less curved and the uncertainty of the momentum measurement increases. As a result, the experimental resolution of the muon channel is worse compared to the electron channel and, for this reason, was used for the optimisation of the binning of the measured variables.

8.3.2 Migration

Migrations are events that are generated and reconstructed in different bins of the true and measured distribution, as introduced in Chapter 5. Two main sources are distinguished in the following: First, migrations across bins at high m_{T}^{W} are expected due to the reconstruction of particles or events, where e.g. a transverse momentum of the electron is measured too small. As a result, the event is found in a different bin at truth level and at reconstructed level. Second, migrations from on-shell W bosons are expected due to the steeply falling distribution of the transverse mass of the W boson above the mass peak at $m_W \approx 80\,\mathrm{GeV}$, which favors the appearance of migration effects.
The migration of events is described by the migration matrix M_{ij} that provides the amount of events generated at MC truth level in bin i and reconstructed in bin j. Each bin j of the reconstructed distribution is normalised to unity and afterwards scaled in order to provide the percentage of events migrating for each of the bins i. The over- and underflow is considered in the normalisation. Furthermore, the so-called *purity* describes the events that are generated and reconstructed in the same bin, i.e. which fulfil $i = j$. Overall, the calculation of the migration matrix relies on the W MC sample, since the true and reconstructed distributions are required.
In Figure 8.4, the two-dimensional migration matrix M_{ij} as a function of the transverse mass of the W boson at born level and at reconstructed level in the e^- channel is shown. The binning of the migration matrix corresponds to the final single-differential cross-section

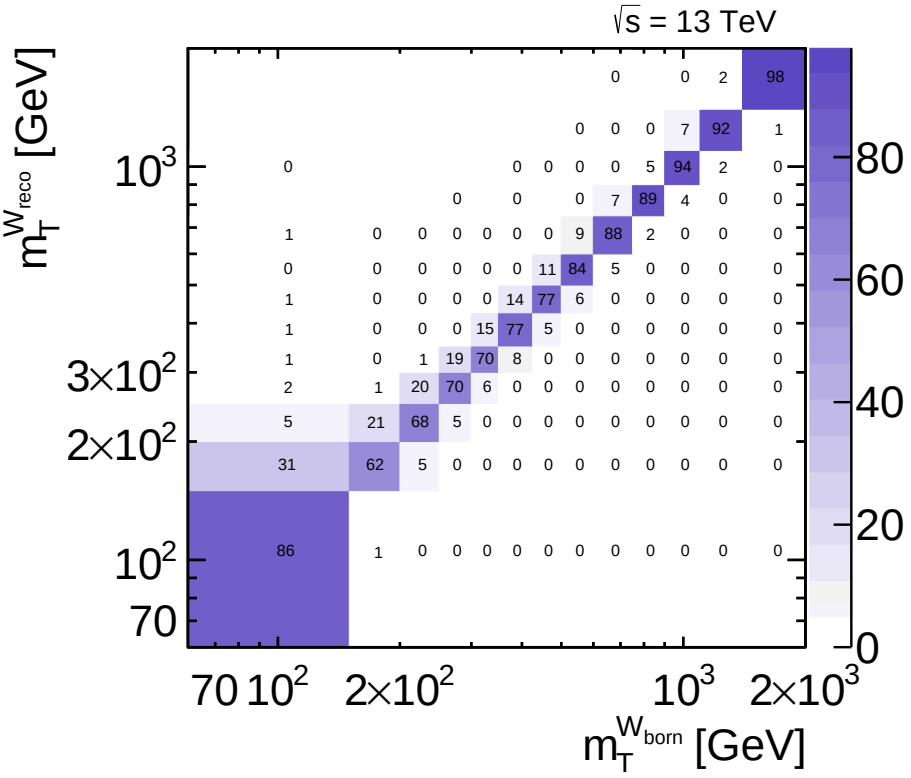

Figure 8.4: Migration matrix $M_{reco,born}$ for the $W^- \to e^-\nu$ signal process. The given numbers are in percent, while under- and overflow bin are considered in the normalisation.

measurement binning, where a bin at $m_{\mathrm{T}}^{W} \in [60, 150]\,\mathrm{GeV}$ is added. The additional m_{T}^{W} bin targets the visualisation of the second source of migrating events that originate from on-shell W bosons. All events that fulfil the nominal event selection, where the m_{T}^{W} requirement is exceptionally lowered to $m_{\mathrm{T}}^{W} = 60\,\mathrm{GeV}$, are considered. Importantly, the fiducial selection is not applied.
The smallest purity of 62% can be observed for $m_{\mathrm{T}}^{W} \in [150, 200]\,\mathrm{GeV}$ and increases up to 98% for high transverse masses. In general, the purities are clearly higher than 50%, because the same requirement is used for the binning in the muon channel, where smaller purities are obsered. Non-zero migrations occur in bins next to the diagonal that mainly originate from the first source of migrations, i.e. migrations which are induced by the measurement process. The second source, where the migrations originate from on-shell W bosons, is visible in the non-zero entries in the first column of the migration matrix. These events are generated with a transverse mass around 80 GeV, the peak of the W boson mass distribution, and a non-negligible fraction are reconstructed up to several hundred GeV. Nevertheless, these events migrate predominantly into bins at low reconstructed m_{T}^{W}.
The migration matrix for the e^{+} channel is very similar to the one discussed here and, for this reason, shown in Appendix F.
Migrations for the absolute value of the pseudorapidity of the electron $|\eta(e)|$ are known to be very small because the experimental resolution in $|\eta(e)|$ is very good. Consequently, a minor impact on the measurement binning for the double-differential measurement of the cross-section is expected.

8.3.3 Data statistical uncertainty

The last criteria considered in the optimisation of the measurement binning is the statistical uncertainty of data events. The binning is adjusted to provide a reasonable small statistical uncertainty, which can be achieved by increasing the bin sizes, where an increasing amount of events is selected. However, in order to introduce as much bins in the measurement as possible, the bin size has to be kept small at the same time.
In general, data events fulfil a Poisson statistics, where the statistical uncertainty is provided by the square root of the number of events $\sqrt{N}$. The corresponding relative statistical uncertainty, where the statistical uncertainty is shown relative to the number of events $\frac{\sqrt{N}}{N}$, is presented in Figure 8.5 as a function of m_{T}^{W} and $m_{\mathrm{T}}^{W} \otimes |\eta(e)|$. The statistical uncertainties corresponding to the amount of data events fulfilling the event selection, as defined in Chapter 8.1, are discussed in the following. In Figure 8.5a and Figure 8.5b, the statistical data uncertainty is presented as a function of the transverse mass of the W boson in the e^{+} and e^{-} channel. The first bin in both distributions is marked with a grey coloured shadow, which indicates that these bins do not correspond to the signal region. It can be observed that the statistical uncertainty monotonously increases as a function of m_{T}^{W}, i.e. the number of data events decreases, where the largest value of about 11% (17%) can be found in the last bin for the e^{+} (e^{-}) channel. The statistical uncertainty is larger in the e^{-} channel, because the cross-section for W^{-} bosons in pp collisions is lower compared to W^{+} bosons.
The statistical uncertainty of data events in the double-differential measurement binning for the e^{+} and e^{-} channel is shown in Figure 8.5c and Figure 8.5d. Here, the binning for the double-differential cross-section measurement is represented by one single distribution of $m_{\mathrm{T}}^{W} \otimes |\eta(e)|$, where the $|\eta(e)|$ distributions of each m_{T}^{W} bin are shown side-by-side.

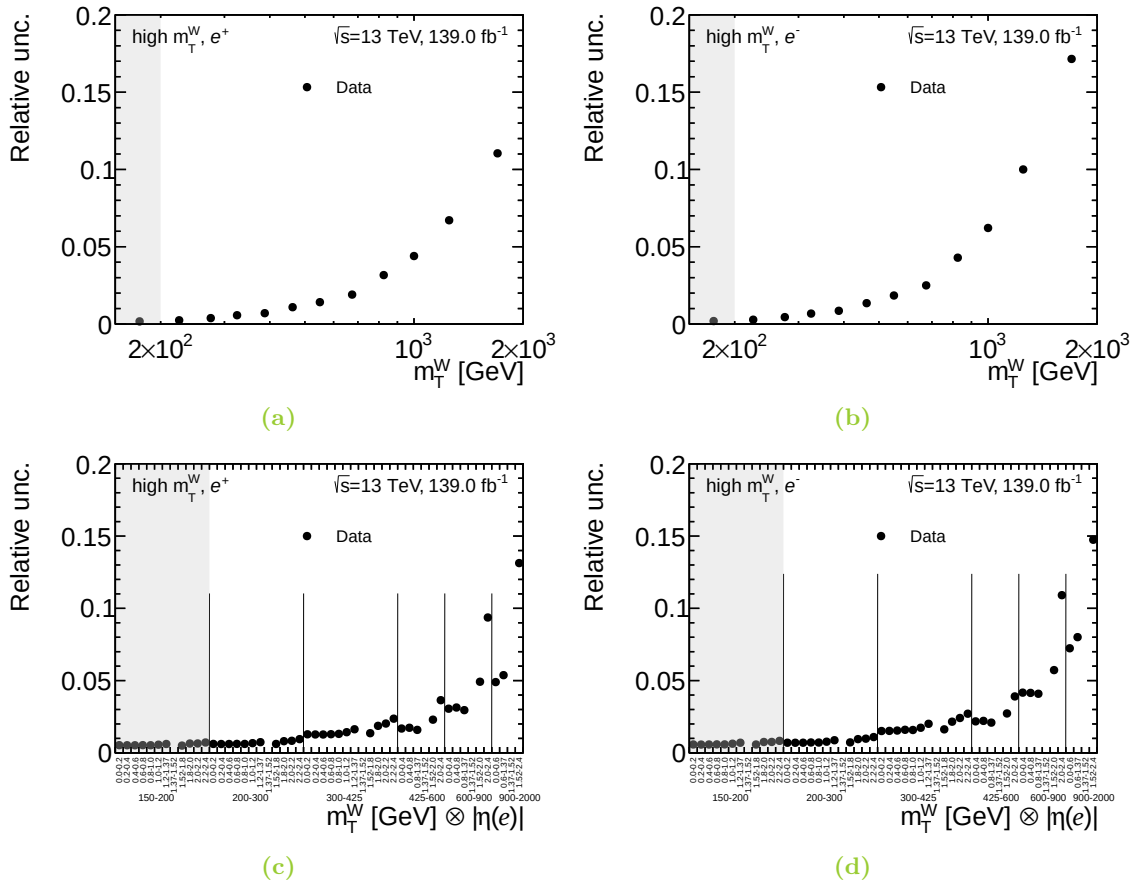

Figure 8.5: Relative statistical uncertainty of the analysed dataset as a function of m_{T}^W for (a) in the e^+ and b) the e^- channel. In addition, the relative statistical uncertainty as a function of $|\eta(e)| \otimes m_{\mathrm{T}}^W$ for (c) the e^+ and d) the e^- channel.

Furthermore, perpendicular black lines at the bin borders of m_{T}^W are added. The binning in $|\eta(e)|$ can be found at the x-axis and the binning in m_{T}^W is given below. Since transverse masses below 200 GeV are not measured, the corresponding area is filled with a grey coloured shadow.

The distribution of the statistical uncertainty in $|\eta(e)|$ is approximately flat for the first and second m_{T}^W bin, where for the third and following m_{T}^W bins, the uncertainty increases within $|\eta(e)|$. The event topology of the ccDY changes as a function of m_{T}^W, where larger transverse masses of the W boson are produced at smaller absolute rapidities y_W, i.e. more central. As a consequence, the electron is produced more central in the detector, i.e. the forward region is less populated, which refers to a higher statistical uncertainty. Furthermore, the same increase of the statistical uncertainty in m_{T}^W as in the one-dimensional binning is observed. Overall, the largest statistical uncertainties as a function of $m_{\mathrm{T}}^W \otimes |\eta(e)|$ are approximately 13% (15%) in the e^+ (e^-) channel, while the statistical uncertainties are much smaller otherwise.

9 Background estimation

After the event selection, as discussed in Chapter 8.1, has been applied to the analysed data, the events are composed of electrons originating from the signal process or the background processes. Each background process contributes due to a similar final state or due to e.g. inefficiencies in the detector. As an example, the ncDY process, where a Z boson is produced from two quarks and decays into two leptons $\ell^+\ell^-$, contributes for $\ell = e$ in the final state. The same final state as for the signal process is present, if one of the electrons is missed, for example in the region of $1.37 < |\eta(e)| < 1.52$. The expected number of background events, characterised by real electron final states, is well-described by the MC samples and estimated by requiring the nominal event selection for each of the processes.
The multijet background is characterised by multiple jet events. Although the event selection requires the electron to fulfil the *tight* level, which refers to well-defined electrons, a small fraction of events can originate from jets. A jet can be misidentified as an electron because of a deposition of the jet energy in the electromagnetic calorimeter together with a mismatch of a charged particle track onto this energy deposition. Due to the strong requirements on well-defined electrons, the fraction of jets that are able to 'fake' a real electron is very small. However, the cross-section of multijet events is much higher than the cross-section of the signal process and, for this reason, the contribution is sizeable. The estimation of multijet background is performed based on a data-driven method, because the small fraction of electron misidentifications in generated jet events is not sufficient for the generation of a MC sample.
In the following, the theoretical basis of the Matrix Method is described. Subsequently, detailed studies concerning the $E_{\mathrm{T}}^{\mathrm{miss}}$ modelling in data-driven background estimates is performed. Then, the estimation of the MJ background, the evaluation of the systematic uncertainties corresponding to the MJ estimate and the modelling of the estimated background is discussed.

9.1 Matrix Method

The Matrix Method is a data-driven approach estimating the number of misidentified, so-called *fake*, electrons. One of the main sources for fake electrons are multijet events where one of the jets is misidentified as an electron. Further contributions originate from events where e.g. pions are produced in the hadronisation of a jet that further decay in two electrons and a photon.
The key element of the Matrix Method is based on relaxing the electron identification and isolation requirements of the *tight* level and then determining the efficiencies for a loose object, i.e. real or fake electron to become a measured tight electron. The *tight* and *loose* level, where the latter refers to the relaxed level, as defined in Section 8.1 are used. The

number of loose and tight level electrons is related to the number of real and fake electrons by using the corresponding efficiencies for real and fake electrons as represented by the equation

$$\begin{pmatrix} N_T \\ N_L \end{pmatrix} = \begin{pmatrix} \epsilon_R & \epsilon_F \\ 1-\epsilon_R & 1-\epsilon_F \end{pmatrix} \begin{pmatrix} N_R \\ N_F \end{pmatrix} , \tag{9.1}$$

where the number of real (fake) electrons N_R (N_F), the number of tight (loose) electrons N_T (N_L) and the real (fake) efficiencies ϵ_R (ϵ_F) are used. The real (fake) efficiency is defined as the number of real (fake) electrons passing the tight level $N^T_{R(F)}$ divided by the number of real (fake) electrons passing the loose level $N^L_{R(F)}$:

$$\epsilon_{R/F} = \frac{N^T_{R/F}}{N^L_{R/F}} . \tag{9.2}$$

Consequently, the real (fake) efficiencies provide the fraction of real and fake objects fulfilling the loose and tight level. While the real efficiencies are typically obtained from MC simulations, the fake efficiencies are not well-described in MC simulations and have to be estimated in a region enriched with fake electrons, which are generally not described by MC. Inverting the matrix in Equation 9.1 leads to an estimate for the number of fake leptons, which are contributing to the tight level, i.e. the measurement level. The corresponding equation is based on the number of loose and tight level electrons and the real and fake efficiencies in the following way:

$$\epsilon_F N_F = \frac{\epsilon_F}{\epsilon_R - \epsilon_F}[\epsilon_R(N_L + N_T) - N_T] . \tag{9.3}$$

Importantly, the variables N_L and $N^L_{R/F}$ differ. While the former is defined as the number of loose level electrons that do not fulfil the tight level N_L, the latter refers to all loose level electrons independently of whether or not being identified as tight level electrons. In Equation 9.3, N_L and N_T are accessible in data and ϵ_R and ϵ_F can be measured. Finally, the multijet estimate, i.e. number of fake electrons measured at the tight level, is obtained by the multiplication of the following event weights

$$w^T_{MM} = \frac{\epsilon_F(\epsilon_R - 1)}{\epsilon_R - \epsilon_F} \tag{9.4}$$

$$w^L_{MM} = \frac{\epsilon_F \epsilon_R}{\epsilon_R - \epsilon_F} \tag{9.5}$$

to a dataset at the loose level, where the application of the respective weight depends on whether a loose or a tight level electron is identified in each event. A key element for a good modelling of the multijet background is the precise estimate of the real and fake efficiencies.

9.2 Dependence on the choice of objects in the $E_{\mathrm{T}}^{\mathrm{miss}}$ calculation

The estimate of the multijet background via the Matrix Method relies on two main requirements: The variation of identification and isolation working points and the estimation of

real and fake efficiencies. These efficiencies are estimated in specific phase spaces, that are typically orthogonal to the signal region.
As a consequence, the objects present at each working point and in each phase space can differ. Since the various objects are used for the calculation of the missing transverse momentum, deviations in $E_{\mathrm{T}}^{\mathrm{miss}}$ are expected at different working points. In Chapter 7.5, the event reconstruction including electrons, jets, muons, and tracks is discussed, where the energy and momentum of each object is estimated differently.
In the following, objects used as the input for the calculation of $E_{\mathrm{T}}^{\mathrm{miss}}$, their energy calibration and implications on the $E_{\mathrm{T}}^{\mathrm{miss}}$ are presented.

9.2.1 Different energy calibrations of objects and implications on $E_{\mathrm{T}}^{\mathrm{miss}}$

Object calibration: Out of the numerous different objects that are used as inputs to the calculation of $E_{\mathrm{T}}^{\mathrm{miss}}$, the focus will be on electrons and jets in this section. Both leave electromagnetic showers in the calorimeter system, thus fake electrons are expected to dominantly originate from jets. Although both, the electron and jet energy calibration rely on the response, the estimated energy includes substantial additional correction factors for jets. In order to correctly estimate the energy of a fake electron, the true object, which could be an electron or jet, has to be known. In a data-driven approach, the truth quantities are not known. Consequently, the energy calibration of fake electron candidates is investigated in MC under two assumptions: a true electron or a true jet. In order to meet the expected topology of jets *faking* electrons, a dijet MC, as introduced in Chapter 6.3, is used and events are selected based on an electron specific selection, where the requirements of

- at least one electron $N_e = 1$,
- a transverse momentum of the electron $p_{\mathrm{T}}(e) > 30\,\mathrm{GeV}$,
- electron identification criteria
  - loose object: `LooseAndBLayerLH`
  - tight object: `TightLH`

have to be fulfilled. Another change has to be applied to the common overlap removal procedure as explained in Sec 7.6. To be able to compare the energy calibration of jets and electrons, it is necessary to disable the requirement of $\Delta R(e, jet) > 0.4$. Since the same object in the calorimeter should be studied, exactly the desired overlap would be removed by the overlap removal requirement. Apart from these modifications the same object reconstruction as described in Chapter 7 is applied.
The response $\mathcal{R}$ is the measure to evaluate the fraction of reconstructed energy measured in the detector with respect to the generated energy and is defined as

$$\mathcal{R} = < \frac{p_T(\text{measured object})}{p_T(\text{truth object})} > , \tag{9.6}$$

where the mean of the transverse momentum of the measured object divided by the transverse momentum of the truth object is calculated. This is a measure that is commonly used in a jet energy calibration, as described in Chapter 7.4. While the transverse momentum of the

measured object is accessible in the MC prediction on reconstructed level, the estimation of the truth objects' transverse momentum relies on the MC truth level. In order to ensure the same object is used on both levels, a truth matching procedure is necessary. An overview of the truth matching requirements are shown in Tab. 9.1. In both cases, the truth matching

Table 9.1: Overview of the truth matching requirement applied for electrons or jets.

Object	Truth matching requirements
Electron	- choose measured electron with highest transverse momentum - match truth jet, with highest transverse momentum, to the measured electron fulfilling $\Delta R < 0.1$
Jet	- choose measured electron with highest transverse momentum - select measured jet fulfilling $\Delta R < 0.1$ - match truth jet, with highest transverse momentum, to the measured jet fulfilling $\Delta R < 0.1$

starts from the measured electron with the highest transverse momentum. In case of a measured electron it is possible to directly match the measured electron to the truth object, which is a jet, in the MC by requiring that the jet agrees geometrically in $\Delta R < 0.1$. If multiple candidates fulfil the truth matching, the highest transverse momentum truth jet is chosen.
In order to ensure that strictly the same objects in the calorimeter are used, the truth matching procedure for a measured jet starts from the measured electron as well. First, the selected, measured electron is matched[1] to the closest measured jet, fulfilling $\Delta R < 0.1$. If multiple candidates fulfil the requirement, the object with the highest transverse momentum is chosen. Afterwards, the same geometrical truth matching of the measured jet to the closest truth jet is applied.

The response for the same calorimeter object, identified as a jet or an electron for *loose* electrons after the event selection are presented in Figure 9.1. A two-dimensional distribution of the transverse momentum of the reconstructed jet, $p_{\mathrm{T}}(j_{e-match})$, that is ΔR-matched to the reconstructed electron, divided by the truth-matched jets' transverse momentum, $p_{\mathrm{T}}(j_{truthmatch})$, is presented as a function of the transverse momentum of the jet $p_{\mathrm{T}}(j_{e-match})$ in Figure 9.1a. Calculating the mean of the ratio of the two tansverse momenta in the two-dimensional distribution allows to show the jet response, defined in Equation 9.6, as a function of the transverse momentum of the jet $p_{\mathrm{T}}(j_{e-match})$, as shown in Figure 9.1b. It can be observed that the two-dimensional distribution in Figure 9.1a is populated the most close to unity and the corresponding jet response is close to unity as a consequence. Furthermore, the largest number of the events are found at small transverse momenta, which is expected from the evolution of the cross-section of dijet events, decreasing with increasing transverse momentum of the jet.
Since the full jet energy calibration is applied, the response is expected to approximately agree with unity. In general, the energy of a jet, based on the shower reconstruction in the electromagnetic and hadronic calorimeters, is measured too small, due to the potentially

[1] This step of the truth matching is only possible if the corresponding overlap removal is disabled.

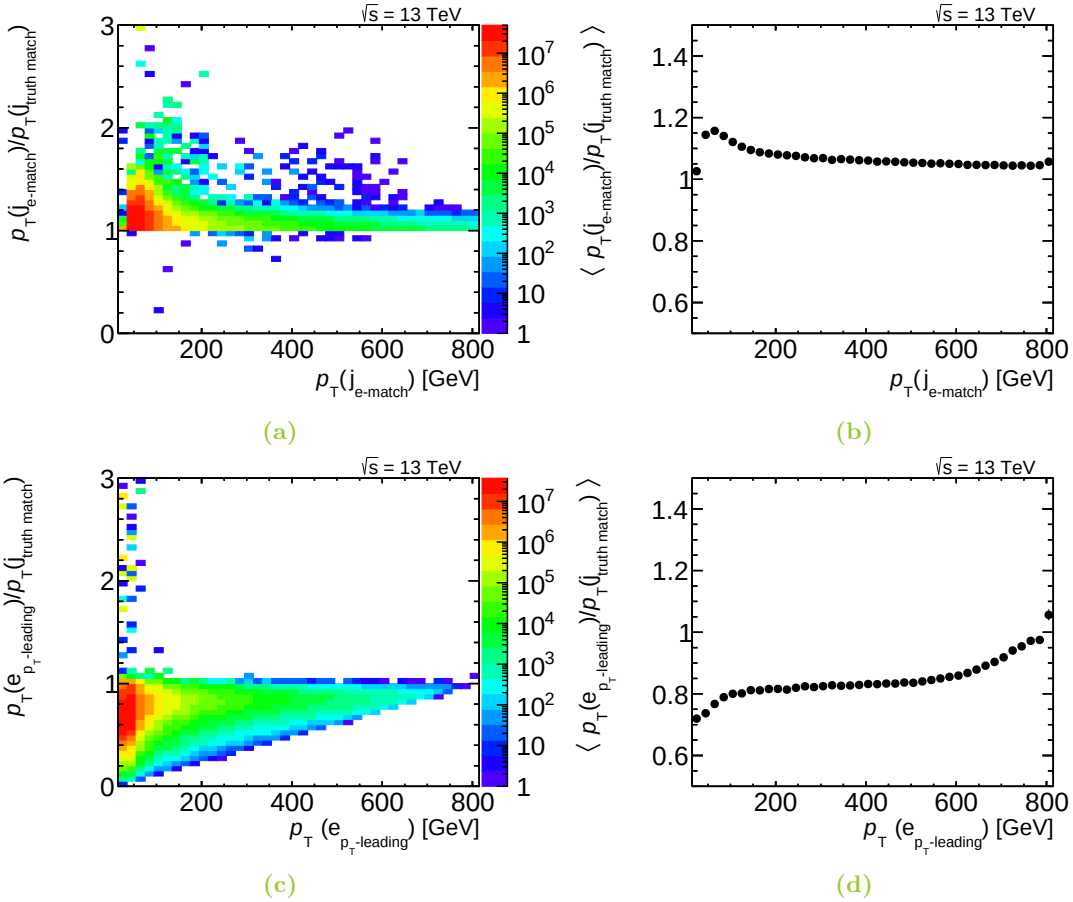

Figure 9.1: The response of the same calorimeter object identified as a jet or an electron after requiring at least one `LooseAndBLayerLH` electron is presented in the upper and lower row, respectively. Plots are shown as two-dimensional heat map as well as profile.

ambiguous assignment of certain energy depositions to a specific jet. Additionally, because not all decay particles of the jet can be measured. In order to account for these effects, a so-called calibration constant, as described in Chapter 7.4, is applied to reconstructed jet candidates. As a result, the jet energy response after the jet energy calibration is approximately at unity.

Although deviations from unity are in general in the order of less than a percent for jet candidates, differences in the jet energy response shown in Fig 9.1b are expected to be larger. A higher response is possible if the selected objects in the calculation of the calibration constant differ from the selected jet objects that are investigated. The following has to be considered: A *typical* jet deposits a fraction of its energy in the electromagnetic and hadronic calorimeter each, whereas an electron deposits its energy almost completely in the electromagnetic calorimeter. A jet, that is likely to be misidentified as an electron as it is investigated here, deposits usually a higher fraction of its energy in the electromagnetic calorimeter compared to a *typical* jet, increasing the similarity between jets and electrons. The calibration constants are estimated based on a jet specific selection, where ideally a *typical* jet is represented. In the distributions shown here, only jets that might be misidentified

as electrons are selected. Their energy deposited in the electromagnetic calorimeter is higher compared to *typical* jets, but the same calibration constant is used. As a consequence, the response of an electron-matched jet is expected to be above unity, which can be observed in Figure 9.1b.
In addition, the two-dimensional distribution of the ratio of the transverse momenta of the electron on reconstructed level and the jet on MC truth level as a function of the p_T of the reconstructed electron with the highest transverse momentum, $e_{p_T-leading}$, and the corresponding energy response are shown in Figure 9.1c and Figure 9.1d, respectively. Again, most events are populated at transverse momenta $p_T \in [30, 60]$ GeV as for the jet events, due to the decreasing cross-section of dijet events. Apart from this, the two-dimensional distribution as well as the energy response are notably different compared to the ones where a jet is reconstructed. The reconstruction of the electron energy does not include a calibration constant as for jets, since its energy is almost completely deposited in the electromagnetic calorimeter. As a result, the energy reponse is mostly distributed in a range of $\mathcal{R} \in [0, 1]$. The energy response is approximately $\mathcal{R} = 0.7$ for $p_T = 30\,\text{GeV}$, increases to $\mathcal{R} = 0.8$ and is mostly flat for intermediate transverse momenta $p_T \in [60, 600]$ GeV and is the highest for $p_T > 600\,\text{GeV}$. Overall, a similar energy response as used in the jet energy calibration shown in Figure 7.1 can be observed.
The same overview of the jet and electron energy responses for selected *tight* electrons is displayed in Figure 9.2. The two-dimensional distributions and the energy responses are very similar to the results in case of the selected *loose* electrons. In Figure 9.2b, the jet energy response is above unity, due to the application of calibration constants on jets selected based on their ability to fake an electron, as explained for Figure 9.1. Now, stricter identification criteria are required for electrons selected from the dijet MC, where an overall smaller number of selected events and even higher similarities between electrons and jets are expected. Although such a jet selection could provide an even higher amount of reconstructed energy in the electromagnetic calorimeter and subsequently yields a bigger difference with respect to unity in the energy response, only small differences between Figure 9.1b and Figure 9.2b can be observed.
In Figure 9.2, similar trends of the electrons as for *loose* objects in Figure 9.1 are visible. A selected, measured electron that originates from a truth jet provides a very similar energy response that does not rely on fulfilling the loose or the tight electron identification criteria, presented in Figure 9.1d and Figure 9.2d. A slightly different response is observed in the region of low transverse momenta $p_T < 150\,\text{GeV}$, whereas the energy response for *loose* and *tight* electrons agree approximately otherwise.
Finally, it can be concluded that the object calibration which is studied based on the energy response for the same object in the calorimeter differs for being identified as a jet or an electron. Two effects can be distinguished: First, a large difference in the energy response is observed if the same object measured in the calorimeter, representing a potential fake electron, is identified as an electron or a jet. Second, a very small difference is observed if the investigated object is identified as a *loose* or *tight* electron in the selection.
The estimated energy of the object and, subsequently, the $E_{\text{T}}^{\text{miss}}$ in the corresponding event will depend on taking the object into account as a jet or an electron, because the objects energy is an input to the estimation of $E_{\text{T}}^{\text{miss}}$.

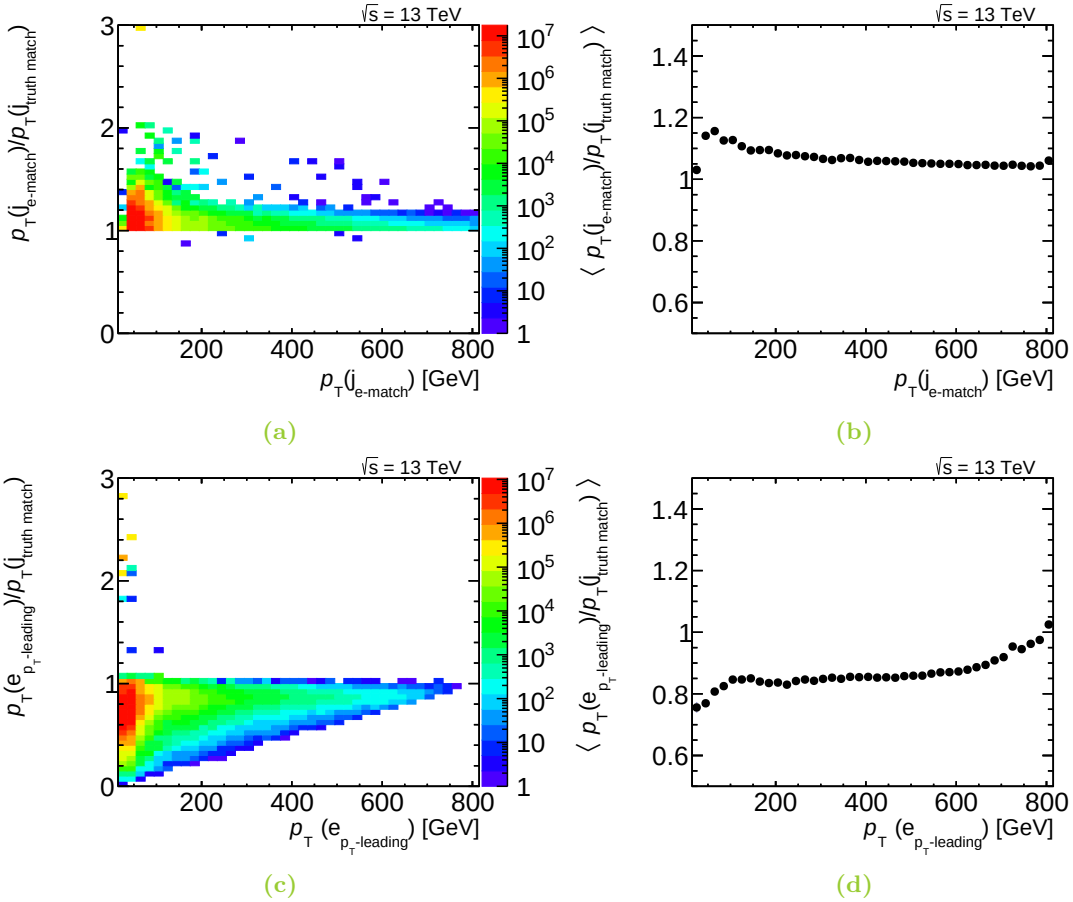

Figure 9.2: The response of the same calorimeter object identified as a jet or an electron after requiring at least one `TightLH` electron is presented in the upper and lower row, respectively. Plots are shown as two-dimensional heat map as well as the profile.

Comparison of $E_{\mathrm{T}}^{\mathrm{miss}}$ working points: In order to study the implications on $E_{\mathrm{T}}^{\mathrm{miss}}$, concluded from the previous studies on object calibrations, two working points are defined. Objects identified as *tight* electrons are considered as real electrons for both working points, while objects identified as *loose* electrons are treated differently in the $E_{\mathrm{T}}^{\mathrm{miss}}$ calculation:

- `loose` $E_{\mathrm{T}}^{\mathtt{miss}}$: Consider objects identified as *loose* electron candidates as electrons.
- `tight` $E_{\mathrm{T}}^{\mathtt{miss}}$: Consider objects identified as *loose* electron candidates as jets, where the jet calibration is applied.

Importantly, both working points will provide the same $E_{\mathrm{T}}^{\mathrm{miss}}$ if a selection requires *tight* electrons only and will only be different as soon as a $E_{\mathrm{T}}^{\mathrm{miss}}$ selection requirement is used together with *loose* electrons as in the multijet estimation via the Matrix Method.

In Figure 9.3, the `loose` and `tight` $E_{\mathrm{T}}^{\mathtt{miss}}$ are compared for the W MC, and for data events after the same *loose* selection as defined for the object calibration studies. In contrast, the requirement that the electron, fulfilling the *loose* identification criteria, does not pass the *tight* identification criteria is added in order to separate effects from *loose* and *tight* electrons.

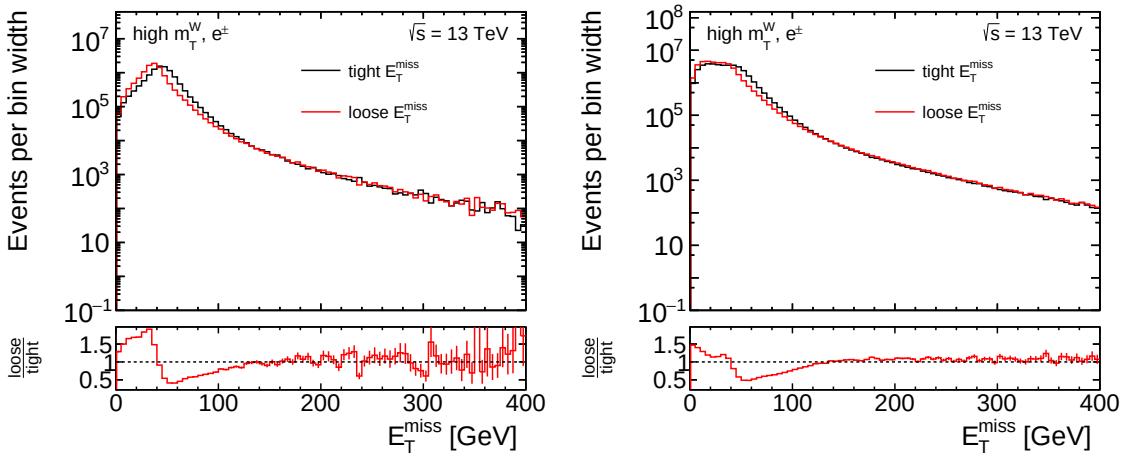

Figure 9.3: The loose and tight $E_{\mathrm{T}}^{\mathrm{miss}}$ for electrons fulfilling the `LooseAndBLayerLH` identification and isolation is compared. Only events that are not passing the tight identification requirements are shown for a) W MC and b) data.

For the W MC, shown in Figure 9.3a, the distribution of the `loose` $E_{\mathrm{T}}^{\mathrm{miss}}$ working point increases until its maximum value around $E_{\mathrm{T}}^{\mathrm{miss}} \approx 40\,\mathrm{GeV}$ and decreases towards higher values, as it is expected in case of a true on-shell W boson produced in the simulated event. The maximum of the `tight` $E_{\mathrm{T}}^{\mathrm{miss}}$ distribution is shifted to higher values. The $E_{\mathrm{T}}^{\mathrm{miss}}$ in both working points is approximately the same for $E_{\mathrm{T}}^{\mathrm{miss}} \geq 125\,\mathrm{GeV}$. The shift of the `tight` $E_{\mathrm{T}}^{\mathrm{miss}}$ distribution is induced by the application of the jet calibration, which is applied to the *loose* electrons that do not pass the *tight* identification criteria. Since the W MC consists of true electrons only, the jet calibration leads to an overestimated energy of the *loose* electron and consequently[2] a larger $E_{\mathrm{T}}^{\mathrm{miss}}$.
The same comparison of the two working points for data events is presented in Figure 9.3b. Differences between the `loose` $E_{\mathrm{T}}^{\mathrm{miss}}$ and the `tight` $E_{\mathrm{T}}^{\mathrm{miss}}$ can be observed, where the `tight` $E_{\mathrm{T}}^{\mathrm{miss}}$ distributions is slightly shifted to larger $E_{\mathrm{T}}^{\mathrm{miss}}$. However, a similar trend of both distribution is visible. In contrast to Figure 9.3a, no clear maximum of the distribution can be found. While the true objects are known in the MC, this is not possible in data events. For this reason, the shape of the data distribution can not be interpreted as easily as for the MC and different behaviour of `loose` and `tight` $E_{\mathrm{T}}^{\mathrm{miss}}$ can not be traced back to the true object and its calibration.

The `loose` and `tight` $E_{\mathrm{T}}^{\mathrm{miss}}$ are compared as well after the *tight* selection as defined for the calibration studies in Figure 9.4. No differences of the two working points are found for *tight* electrons simulated by the W MC or originating from data events, per definition.

[2]It is assumed that the produced $E_{\mathrm{T}}^{\mathrm{miss}}$ dominantly originates from the decay products of the W boson.

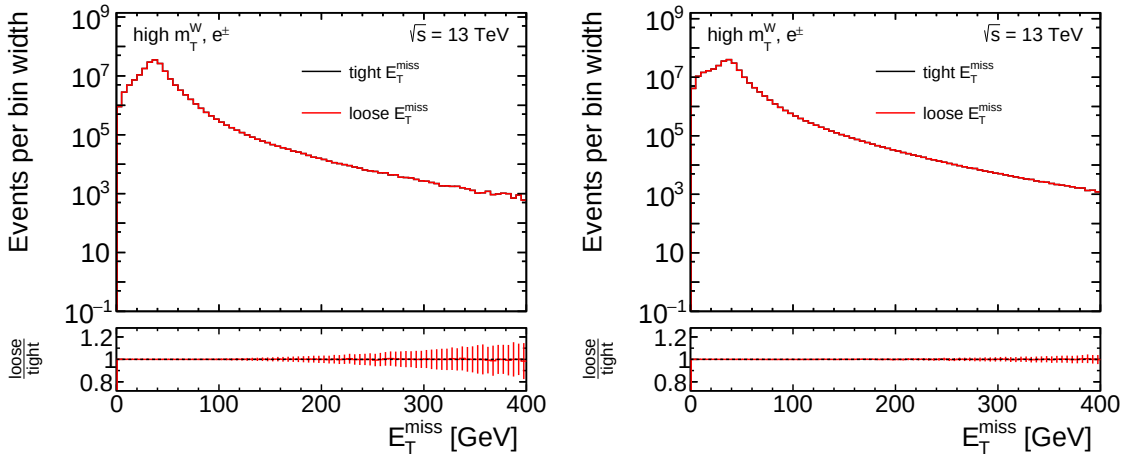

Figure 9.4: The loose and tight $E_{\mathrm{T}}^{\mathrm{miss}}$ for electrons fulfilling the `TightLH` identification and isolation are shown for a) W MC and b) data.

Predicting the composition of real and fake electrons: The remaining aspect, after studying the effects from object calibrations and implications on $E_{\mathrm{T}}^{\mathrm{miss}}$, is the composition of events with respect to real and fake electrons in the phase-space measured in this thesis. An estimate of the composition of data events, i.e. the fraction of real electrons and electron fakes dominantly originating from jets, is investigated based on a comparison of MC events and data, because the composition is not known in data a priori. The modelling of MC events is assumed to correctly predict the contribution of real electrons from the MC-based processes. Data and MC are compared after the *loose* selection defined for the object calibration study, where two requirements are added: First, electrons are not allowed to fulfil the *tight* identification requirements, because differences are expected to contribute to the *loose* identification level only. In addition, the electron is required to pass $p_{\mathrm{T}}(e) > 65\,\mathrm{GeV}$ in order to increase the similarity to the selection in the signal region. The comparison of data and MC events as a function of $E_{\mathrm{T}}^{\mathrm{miss}}$, based on the `loose` $E_{\mathrm{T}}^{\mathtt{miss}}$ definition, is shown in Figure 9.5. The analysed dataset is compared to the stacked contributions from all simulated MC-based processes, where no multijet estimate is taken into account on purpose. Importantly, the visualisation corresponding to the `loose` $E_{\mathrm{T}}^{\mathtt{miss}}$ definition represents a choice only at this point. The MC-based processes are assumed to describe the real electron fraction of data events, while the remaining difference, i.e. data subtracted by the sum of all MCs, refers to the fraction of fake electrons.
However, it can be observed in the ratio between data and MC that the fraction of electron fakes is more than three times higher compared to the fraction of real electron in the region of $E_{\mathrm{T}}^{\mathrm{miss}} \leq 60\,\mathrm{GeV}$. In contrast, the fraction of real electrons becomes dominant for approximately $E_{\mathrm{T}}^{\mathrm{miss}} > 90\,\mathrm{GeV}$. In the transition region, a decreasing fraction of electron fakes is visible.

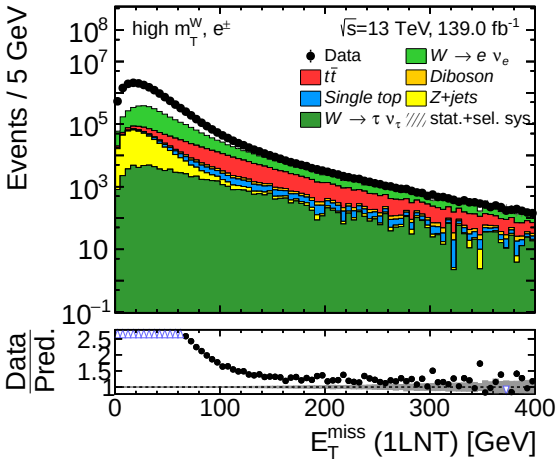

Figure 9.5: MC-Data comparison is shown for $E_{\mathrm{T}}^{\mathrm{miss}}$ for electrons fulfilling the *loose* identification but not the *tight* identification, denoted as loose-not-tight (LNT). The `loose` $E_{\mathrm{T}}^{\mathtt{miss}}$ definition is used.

Summary and conclusions on the $E_{\mathrm{T}}^{\mathrm{miss}}$ working point: In the studies presented in this section it has been shown that assumptions on the particle type in the region where the fake electron background is estimated and the respective calibration applied for these particles leads to differences in the $E_{\mathrm{T}}^{\mathrm{miss}}$ calculation.
It can be concluded that loose objects that are truly real electrons are well-described by using the `loose` $E_{\mathrm{T}}^{\mathtt{miss}}$ working point, whereas loose objects that are truly jets are well-described by `tight` $E_{\mathrm{T}}^{\mathtt{miss}}$. But neither the `loose` $E_{\mathrm{T}}^{\mathtt{miss}}$ nor the `tight` $E_{\mathrm{T}}^{\mathtt{miss}}$ provides an optimal estimate for the full phase space. In this thesis, the fake background estimation relies on inverting the $E_{\mathrm{T}}^{\mathrm{miss}}$ requirement. Consequently, a difference in the $E_{\mathrm{T}}^{\mathrm{miss}}$ is expected for the region, where the fake background is estimated and the signal region because the fraction of real and fake electrons in data differs substantially. Nevertheless, it is expected that the `tight` $E_{\mathrm{T}}^{\mathtt{miss}}$ (`loose` $E_{\mathrm{T}}^{\mathtt{miss}}$) provides a more reasonable estimate of the true missing energy in the region where the fake background is estimated (in the signal region), because it is fake (real) electron enriched. However, the $E_{\mathrm{T}}^{\mathrm{miss}}$ working point should not be changed depending on the phase space, because it would be inconsistent, i.e. the same events would be handled differently. Nevertheless, the studied dependence on the choice of objects in the $E_{\mathrm{T}}^{\mathrm{miss}}$ has to be taken into account.
In this thesis, the `loose` $E_{\mathrm{T}}^{\mathtt{miss}}$ WP is used due to its more reasonable energy estimation in the signal region, i.e. $E_{\mathrm{T}}^{\mathrm{miss}} > 85\,\mathrm{GeV}$, where the measurement is performed. In order to describe the expected differences originating from the composition of real and fake electrons another $E_{\mathrm{T}}^{\mathrm{miss}}$ WP as described in the following section and applied consistently as a systematic uncertainty.

Although the discussion has been restricted to differences observed in the $E_{\mathrm{T}}^{\mathrm{miss}}$ calculation related to the Matrix Method, it has to be pointed out that alternative methods are affected as well. For example, the template method also relies on inverting identification criteria and therefore have to be considered affected as well.

9.2.2 Estimation of object- and phase-space dependent $E_{\mathrm{T}}^{\mathrm{miss}}$

In the following, another $E_{\mathrm{T}}^{\mathrm{miss}}$ working point taking into account the dependence on the real and fake electron composition and the selected phase space is defined. The so-called `mixed` $E_{\mathrm{T}}^{\mathtt{miss}}$ is estimated as the weighted sum of `loose` $E_{\mathrm{T}}^{\mathtt{miss}}$ and `tight` $E_{\mathrm{T}}^{\mathtt{miss}}$ fractions, where the weighting relies on the real and fake electron fractions.
The estimation of real electron fractions, i.e. the part of events well-described by the `loose` $E_{\mathrm{T}}^{\mathtt{miss}}$, and subsequently the estimation of the `mixed` $E_{\mathrm{T}}^{\mathtt{miss}}$ working point are described in the following. In the end, the `mixed` $E_{\mathrm{T}}^{\mathtt{miss}}$ working point will be used as a systematic uncertainty.

Calculation of real and fake electron fractions: The pre-requisite for an estimation of the `mixed` $E_{\mathrm{T}}^{\mathtt{miss}}$ working point is the knowledge of the weights required for adding the `loose` $E_{\mathrm{T}}^{\mathtt{miss}}$ and `tight` $E_{\mathrm{T}}^{\mathtt{miss}}$ estimates proportionally. The fractions depend on the phase space and, for this reason, need to be estimated for each region where the multijet corresponding to the `mixed` $E_{\mathrm{T}}^{\mathtt{miss}}$ working point should be estimated. The calculation of the `loose` $E_{\mathrm{T}}^{\mathtt{miss}}$ fractions obtained in the signal region is described exemplarily as a function of the transverse momentum $p_{\mathrm{T}}(e)$ in Figure 9.6.

Here, the comparison of the stacked MC-based processes and the data events are compared, similarly as in Figure 9.5 in Chapter 9.2.1. The events are selected following the full signal region selection, except for the tight identification requirement of the electron. Instead, only the loose identification requirement needs to be passed. The $E_{\mathrm{T}}^{\mathrm{miss}}$ requirement refers to the `loose` $E_{\mathrm{T}}^{\mathtt{miss}}$ working point in order to consistently use the same working point as for the nominal estimation. It should be stated that it could not be validated that the `loose` $E_{\mathrm{T}}^{\mathtt{miss}}$ provides, in fact, the most reasonable choice at the timeline of this thesis.

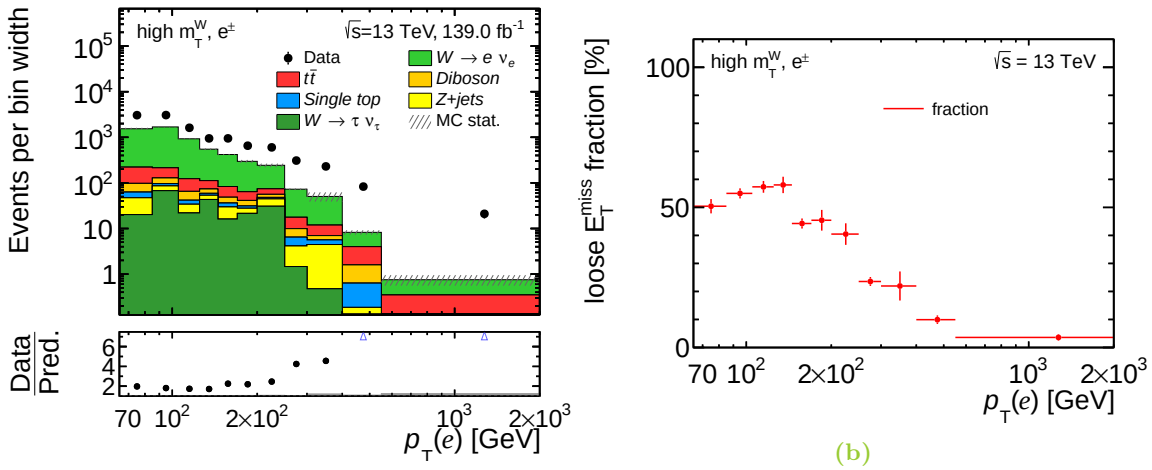

Figure 9.6: Distribution of the transverse momentum $p_{\mathrm{T}}(e)$ shown as a) MC-Data comparison, where the electron fulfils the loose identification criteria only and b) the corresponding `loose` $E_{\mathrm{T}}^{\mathtt{miss}}$, i.e. real electron, fraction in the signal region.

In Figure 9.6, approximately twice as much data are observed with respect to the sum of all MC processes for low transverse momenta $p_{\mathrm{T}}(e)$. The ratio of data and the sum of MC events increases for increasing transverse momenta of the electron.
In order to quantify the fraction of events well-described by `loose` $E_{\mathrm{T}}^{\mathtt{miss}}$ and `tight` $E_{\mathrm{T}}^{\mathtt{miss}}$ from the MC-Data comparison, the following equations are used

$$f_{\mathrm{loose}} = \frac{1}{\mathrm{Data/Pred.}}\,, \tag{9.7}$$

$$f_{\mathrm{tight}} = 1 - \frac{1}{\mathrm{Data/Pred.}}\,, \tag{9.8}$$

where the fraction f_{loose} corresponds to events from real electrons that are well-described by the usage of the `loose` $E_{\mathrm{T}}^{\mathtt{miss}}$ working point and the fraction f_{tight} refers to events from fake electrons that are well-described using the `tight` $E_{\mathrm{T}}^{\mathtt{miss}}$ working point. As an example, in case of twice as much data as MC it is assumed that half of the data events are originating from real electrons, i.e. `loose` $E_{\mathrm{T}}^{\mathtt{miss}}$ is more suitable. And subsequently half of the data originates from fake electrons, i.e. `tight` $E_{\mathrm{T}}^{\mathtt{miss}}$ is more suitable. The calculated `loose` $E_{\mathrm{T}}^{\mathtt{miss}}$ fractions following Equation 9.7 are shown in Figure 9.6b. It can be observed that the inverse behaviour as for the data and MC ratio, where the `loose` $E_{\mathrm{T}}^{\mathtt{miss}}$ fraction is approximately at 50% in the beginning and decreases for increasing transverse momenta.
The same procedure is performed in a three-dimensional binning depending on the transverse momentum $p_{\mathrm{T}}(e)$, absolute value of the pseudorapidity $|\eta(e)|$ and the absolut value of the angle between the electron and missing transverse momentum $|\Delta\phi(e, E_{\mathrm{T}}^{\mathrm{miss}})|$ and the result is shown in Figure 9.7. A strong dependency can be observed in all three variables in Figure 9.7. Overall, large values of the `loose` $E_{\mathrm{T}}^{\mathtt{miss}}$ fractions are observed for low and intermediate transverse momenta, whereas small values of the `loose` $E_{\mathrm{T}}^{\mathtt{miss}}$ fractions are found for high transverse momenta of the electron. As a consequence, the `loose` $E_{\mathrm{T}}^{\mathtt{miss}}$ fractions indicate that more and more fake electrons are found at larger and larger $p_{\mathrm{T}}(e)$. Furthermore, the `loose` $E_{\mathrm{T}}^{\mathtt{miss}}$ fractions decrease for electrons in the forward region and increase for smaller angles between the electron and missing transverse momentum.

Estimation of the `mixed` $E_{\mathrm{T}}^{\mathtt{miss}}$: The `mixed` $E_{\mathrm{T}}^{\mathtt{miss}}$ is calculated as the weighted sum of the `loose` $E_{\mathrm{T}}^{\mathtt{miss}}$ and `tight` $E_{\mathrm{T}}^{\mathtt{miss}}$, where the weights are determined based on the `loose` $E_{\mathrm{T}}^{\mathtt{miss}}$ fractions defined in the previous paragraph. In the following, the Matrix Method is used to determine the contribution from multijet events. A full, separate multijet estimate for the `loose` $E_{\mathrm{T}}^{\mathtt{miss}}$ and `tight` $E_{\mathrm{T}}^{\mathtt{miss}}$ working point is performed. This is required as a starting point in order to obtain the `mixed` $E_{\mathrm{T}}^{\mathtt{miss}}$.
The estimation of the multijet background corresponding to the `mixed` $E_{\mathrm{T}}^{\mathtt{miss}}$ working point, MJ(`mixed` $E_{\mathrm{T}}^{\mathtt{miss}}$), relies on the following formula:

$$\mathrm{MJ}(\mathtt{mixed}\ E_{\mathrm{T}}^{\mathtt{miss}}) = \sum_{i=0}^{N_{\mathrm{events}}} f_{\mathrm{loose}}^{i} \cdot \mathrm{MJ}^{i}(\mathtt{loose}\ E_{\mathrm{T}}^{\mathtt{miss}}) + \sum_{j=0}^{N_{\mathrm{events}}} f_{\mathrm{tight}}^{j} \cdot \mathrm{MJ}^{j}(\mathtt{tight}\ E_{\mathrm{T}}^{\mathtt{miss}})\,, \tag{9.9}$$

where per event the fractions f_{loose} and f_{tight} as described in Equation 9.7 and Equation 9.8 and the estimated multijet of the `loose` and `tight` $E_{\mathrm{T}}^{\mathtt{miss}}$, MJ(`loose` $E_{\mathrm{T}}^{\mathtt{miss}}$) and MJ(`tight` $E_{\mathrm{T}}^{\mathtt{miss}}$), as described in Equation 9.4 are used. It can be seen that the fractions

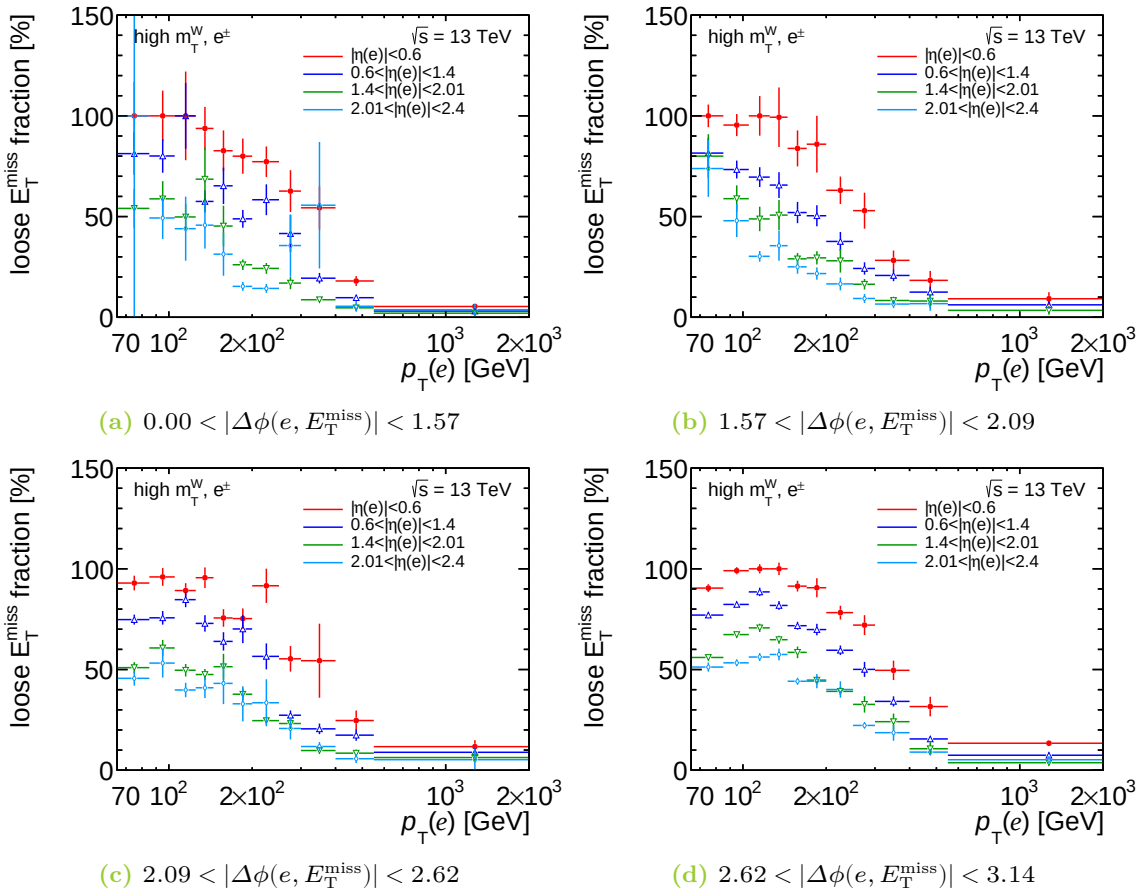

(a) $0.00 < |\Delta\phi(e, E_T^{miss})| < 1.57$

(b) $1.57 < |\Delta\phi(e, E_T^{miss})| < 2.09$

(c) $2.09 < |\Delta\phi(e, E_T^{miss})| < 2.62$

(d) $2.62 < |\Delta\phi(e, E_T^{miss})| < 3.14$

Figure 9.7: `Loose` E_T^{miss}, i.e. real electron, fractions in the signal region binned three-dimensionally in the transverse momentum of the electron $p_T(e)$, the absolute value of the pseudorapidity $|\eta(e)|$ and $|\Delta\phi(e, E_T^{miss})|$ obtained from MC-Data comparisons, where the electron fulfils the loose identification criteria only.

are effectively used as weights. These weights are applied for each event i and j in separate estimations of the multijet. Afterwards, both reweighted multijet estimates are summed up. Two edge cases have to be considered for f_{loose} and f_{tight}: First, the nominal estimate of the `loose` E_T^{miss} working point is used in case of $f_{\text{loose}} \geq 100\,\%$, i.e. where more real electrons described by the MC than data events are present. Second, the nominal estimate of the `tight` E_T^{miss} working point is used in case of $f_{\text{loose}} \leq 0\,\%$, i.e. where no contributions from real electrons are available, corresponding to a maximal uncertainty with respect to `loose` E_T^{miss}.
Finally, the two per-event weighted summands are added together and represent the estimated multijet contribution of the `mixed` E_T^{miss}. Here, the phase space and the composition of objects, based on the MC-Data comparisons of loosely identified electrons only, are taken into account. As aforementioned, the `mixed` E_T^{miss} working point will be used as a systematic uncertainty, while the `loose` E_T^{miss} is used nominally. In the following, the nominal multijet estimate via the Matrix Method will be discussed further.

9.3 Measurement of the real efficiencies

The pre-requisite for the application of the Matrix Method is the knowledge of the real and fake efficiencies. For the estimation of the real electron efficiency, a phase space with a high fraction of real electrons is required. The event selection defined in Chapter 8.1 is adjusted in the following way:

- A truth matching of the reconstructed tight level electron to the born level electron is added. The geometrical distance is restricted to $\Delta R(e, e_{\text{born}}) < 0.1$.
- No $E_{\text{T}}^{\text{miss}}$ and m_{T}^{W} requirements.

Since the $E_{\text{T}}^{\text{miss}}$ requirement is removed, the estimation of the real efficiency does not depend on the `loose` or `tight` $E_{\text{T}}^{\texttt{miss}}$ working point[3]. The real efficiency is measured based on the signal MC, where the necessary information corresponding to the reconstructed and MC truth level are available and a very high fraction of real electrons is ensured. In Figure 9.8, the real efficiency, calculated based on Equation 9.2 in a binned distribution, is shown as a function of $p_{\text{T}}(e)$ and $|\eta(e)|$.

The binning of the real efficiency is motivated based on two requirements: On the one hand, it should reflect the dependency in $p_{\text{T}}(e)$ and $|\eta(e)|$ precisely. On the other hand, large statistical uncertainties should be minimised, because of their impact on the precision of the measurement. Four $|\eta(e)|$ bins, where two bins are used in the central region until the transition region of the barrel and end-cap of the LAr calorimeter and two bins are used in the forward region, and eight $p_{\text{T}}(e)$ bins per $|\eta(e)|$ bin are defined.
Overall, the real efficiency is close to unity fulfilling $\varepsilon_R > 0.9$ in most $p_{\text{T}}(e)$ bins. A single statistical fluctuation can be observed in the bin $p_{\text{T}}(e) \in [500, 800]$ GeV and $|\eta(e)| \in [2.01, 2.4]$, which originates from a few events with large weights and large statistical uncertainties of

[3]Nevertheless, real efficiencies for both working points have been estimated and found to be identical.

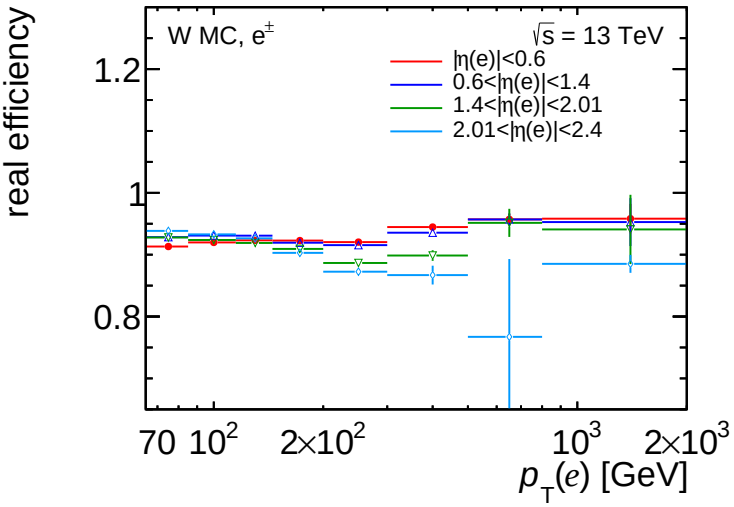

Figure 9.8: Real efficiencies depending on $p_{\text{T}}(e)$ and $|\eta(e)|$ in the electron channel.

the inclusive W MC samples. Further details can be found in Appendix B. Furthermore, the real efficiencies decrease (increase) slightly for large transverse momenta and large (small) pseudorapidities. Lastly, a minimum in the real efficiency at $p_{\mathrm{T}}(e) \approx 200 - 300$ GeV is visible, which originates from the electron isolation requirement demanded on the tight level. As described in Chapter 8.1, the isolation requirement consists of two requirements where the transition area is at $p_{\mathrm{T}}(e) \approx 233\,\mathrm{GeV}$.
An additional dependency on the angular difference between the electron and missing transverse momentum, $\Delta\phi(e, E_{\mathrm{T}}^{\mathrm{miss}})$, has been studied, where no significant impact on the real efficiency has been found. The real efficiency binned in three variables can be found in Figure C.1 in Appendix C.
Finally, another study has been performed in order to estimate potential differences due to the electron charge. The real efficiency, separated into e^+ and e^- channel, is displayed in Figure C.2 in Appendix C. Only small differences between the e^+ and e^- channel are found, where statistical fluctuations induced by the inclusive W MC sample are expected in the region of high m_{T}^W. As a result, no additional separation in the electron's charge is used.

9.4 Measurement of the fake efficiencies

Besides the real efficiencies, the fake efficiencies need to be estimated for the evaluation of the multijet background. A fake enriched region is defined, where only changes with respect to the signal region event selection defined in Chapter 8.1 are mentioned here:

- The $E_{\mathrm{T}}^{\mathrm{miss}}$ requirement is inverted to $E_{\mathrm{T}}^{\mathrm{miss}} < 65\,\mathrm{GeV}$.
- The m_{T}^W requirement is dropped.

This region will be called QCD enriched region because multijet events that contribute e.g. due to a jet which is misidentified as a fake electron are characterised by a small missing transverse momentum $E_{\mathrm{T}}^{\mathrm{miss}}$. The dominant source for such jets are dijet events, where usually no neutrinos are found in the final state. As a consequence, the inversion of the $E_{\mathrm{T}}^{\mathrm{miss}}$ requirement ensures a fake electron enriched region and, in addition, provides orthogonality of the region where the fake efficiencies are estimated and the region where the fake efficiencies are applied.
Another consequence of the inversion of the $E_{\mathrm{T}}^{\mathrm{miss}}$ requirement is a substantial difference in the estimated fake efficiencies between the `loose` and the `tight` $E_{\mathrm{T}}^{\mathrm{miss}}$ working point, because a different amount of events fulfil the inverted $E_{\mathrm{T}}^{\mathrm{miss}}$ requirement, due to the shift of the $E_{\mathrm{T}}^{\mathrm{miss}}$ distribution, as discussed in the previous section. Although the `loose` $E_{\mathrm{T}}^{\mathrm{miss}}$ working point is nominally used, the fake efficiencies for both working points have to be determined in order to calculate the `mixed` $E_{\mathrm{T}}^{\mathrm{miss}}$ based multijet estimate as discussed in Chapter 9.2. In the following, the fake efficiencies for the `loose` $E_{\mathrm{T}}^{\mathrm{miss}}$ working point will be discussed, while the fake efficiencies for the `tight` $E_{\mathrm{T}}^{\mathrm{miss}}$ working point are only briefly described. Nevertheless, all releveant distributions for the `tight` $E_{\mathrm{T}}^{\mathrm{miss}}$ are added in Appendix C.
The estimation of the fake efficiency relies on a data-driven approach, where the fake efficiencies are obtained from MC-Data comparisons instead of MC samples directly. Therefore, data is compared to the summed contribution from all MC samples, representing the real

electron contributions. The mismatch of the data and the MC sum is identified as fake electrons. For this reason, the contributions from all MC processes are subtracted from the data events in order to obtain the electron fakes. The subtraction is demanded on the loose and on the tight level separately. The amount of fake electrons fulfilling the tight level are divided by the amount of fake electrons fulfilling the loose level, resulting into the fake efficiency. A visualisation of this estimation of the fake efficiency is shown exemplarily for the tight level $E_{\mathrm{T}}^{\mathrm{miss}}$ distribution, where the nominal MC-Data comparison and fake electrons from the subtraction are shown in Figure 9.9.
In order to cover all dependencies, the fake efficiencies as a function of the transverse momentum $p_{\mathrm{T}}(e)$, the pseudorapidity $\eta(e)$ and the absolute value of the angle between the electron and the missing transverse momentum $|\Delta\phi(e, E_{\mathrm{T}}^{\mathrm{miss}})|$ is investigated. The estimated fake efficiencies in each of the variables are presented in Figure 9.10. Each fake efficiency is presented for two regions in the transverse momentum of the electron. The red distribution displays the lower $p_{\mathrm{T}}(e)$ fake efficiency in the range of $65\,\mathrm{GeV} < p_{\mathrm{T}}(e) < 145\,\mathrm{GeV}$ and the blue distribution focuses on the high $p_{\mathrm{T}}(e)$ fake efficiency with $p_{\mathrm{T}}(e) > 145\,\mathrm{GeV}$. The main motivation for the separation is given by the trigger threshold at a transverse momentum of $p_{\mathrm{T}}(e) = 140\,\mathrm{GeV}$. As introduced in Chapter 7.1, the trigger requires an identification requirement, which is lowered from *mediumLH* to *looseLH* at that threshold. Since the identification criteria from the trigger is stricter than the loose level of the Matrix Method for $p_{\mathrm{T}}(e) < 140\,\mathrm{GeV}$, the loose level is effectively raised to the *mediumLH* working point of trigger criteria. For this reason, it is more likely that fake objects are able to fulfil the tight level of the Matrix Method, because they already fulfil the identification requirement from the trigger. For $p_{\mathrm{T}}(e) > 140\,\mathrm{GeV}$ the *looseLH* working point of the trigger is close to the loose level of the Matrix Method. For this reason, the difference between the loose level and the tight level of the Matrix Method is larger and therefore less of the loose events are expected to fulfil the tight level requirement. As a consequence, a substantially smaller fake efficiency is expected for $p_{\mathrm{T}}(e) > 140\,\mathrm{GeV}$.
The explained discontinuity in the fake efficiency as a function of the transverse momentum

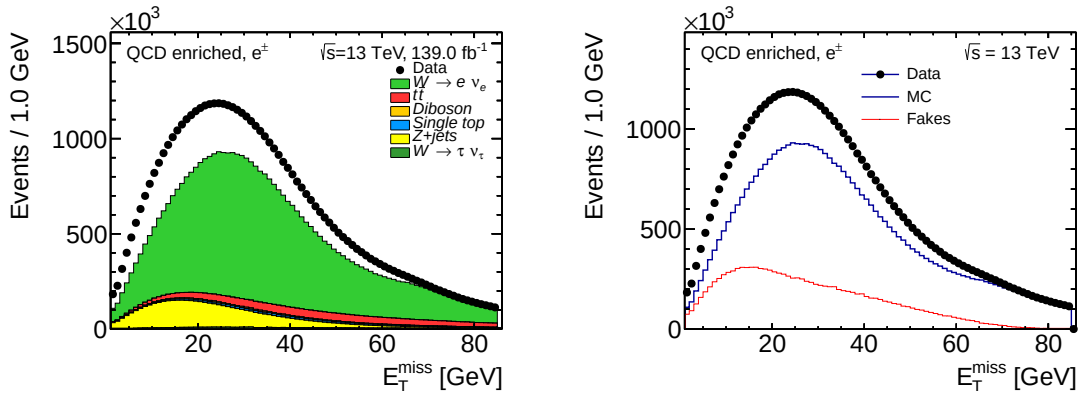

Figure 9.9: Visualisation of the determination of fake efficiencies, exemplarily for the tight level comparison of data and MC for the `loose` $E_{\mathrm{T}}^{\mathtt{miss}}$ working point. In a), the comparison of data and MC events and in b) additionally, the number of fakes from the subtraction of data and MC is shown explicitly.

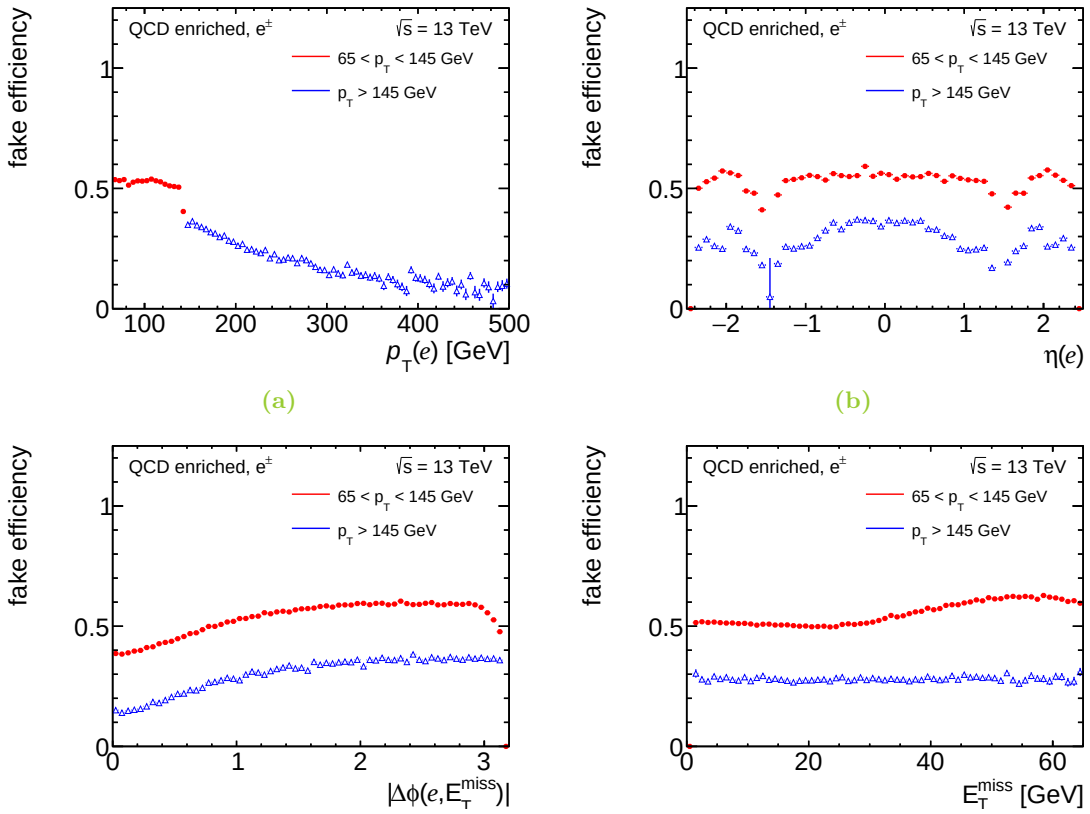

Figure 9.10: Fake electron efficiency for $|\Delta\phi(e, E_{\mathrm{T}}^{\mathrm{miss}})|$, $\eta(e)$, $p_{\mathrm{T}}(e)$ and $E_{\mathrm{T}}^{\mathrm{miss}}$ separated based on the transverse momentum of 65 GeV $< p_{\mathrm{T}}(e) <$ 145 GeV (red) and $p_{\mathrm{T}}(e) >$ 145 GeV (blue) for the `loose` $E_{\mathrm{T}}^{\mathtt{miss}}$ working point.

can be indeed observed in Figure 9.10a. In addition, the same effect is visible for $\eta(e)$, $E_{\mathrm{T}}^{\mathrm{miss}}$ and $|\Delta\phi(e, E_{\mathrm{T}}^{\mathrm{miss}})|$, where the high $p_{\mathrm{T}}(e)$ fake efficiency is smaller compared to the low $^{p}_{\mathrm{T}}(e)$ fake efficiency. Besides the dependency observed in the transverse momentum, further dependencies in $\eta(e)$ are displayed in Figure 9.10b where a discontinuity in the fake efficiency close to the transition region from the central to the forward region at $|\eta(e)| \in [1.37, 1.52]$ is visible. Other than that, the fake efficiency differs as a function of the transverse momentum in the forward region, i.e. comparing the red and blue line in the region $|\eta(e)| > 1.52$. Lastly, the fake efficiency as a function of $|\Delta\phi(e, E_{\mathrm{T}}^{\mathrm{miss}})|$ is given in Figure 9.10c. A fake efficiency of 40 %(15 %) for small angles and $p_{\mathrm{T}}(e) <$ 145 GeV ($p_{\mathrm{T}}(e) >$ 145 GeV) and an increase for larger angles can be observed. For $p_{\mathrm{T}}(e) <$ 140 GeV and $|\Delta\phi(e, E_{\mathrm{T}}^{\mathrm{miss}})| \approxeq \pi$ the fake efficiency decreases. The fake efficiency as a function of $E_{\mathrm{T}}^{\mathrm{miss}}$ is shown in Figure 9.10d. The dependency on the $E_{\mathrm{T}}^{\mathrm{miss}}$ requirement can not be used for a parametrisation because it is inverted to ensure the orthogonality. Since a parametrisation is not possible a rather flat dependence is important, which can only be observed for $p_{\mathrm{T}}(e) >$ 145 GeV.
The same dependencies of the fake efficiency are investigated for the `tight` $E_{\mathrm{T}}^{\mathtt{miss}}$ working point, as shown in Figure 9.11. The fake efficiency as a function of the transverse momentum

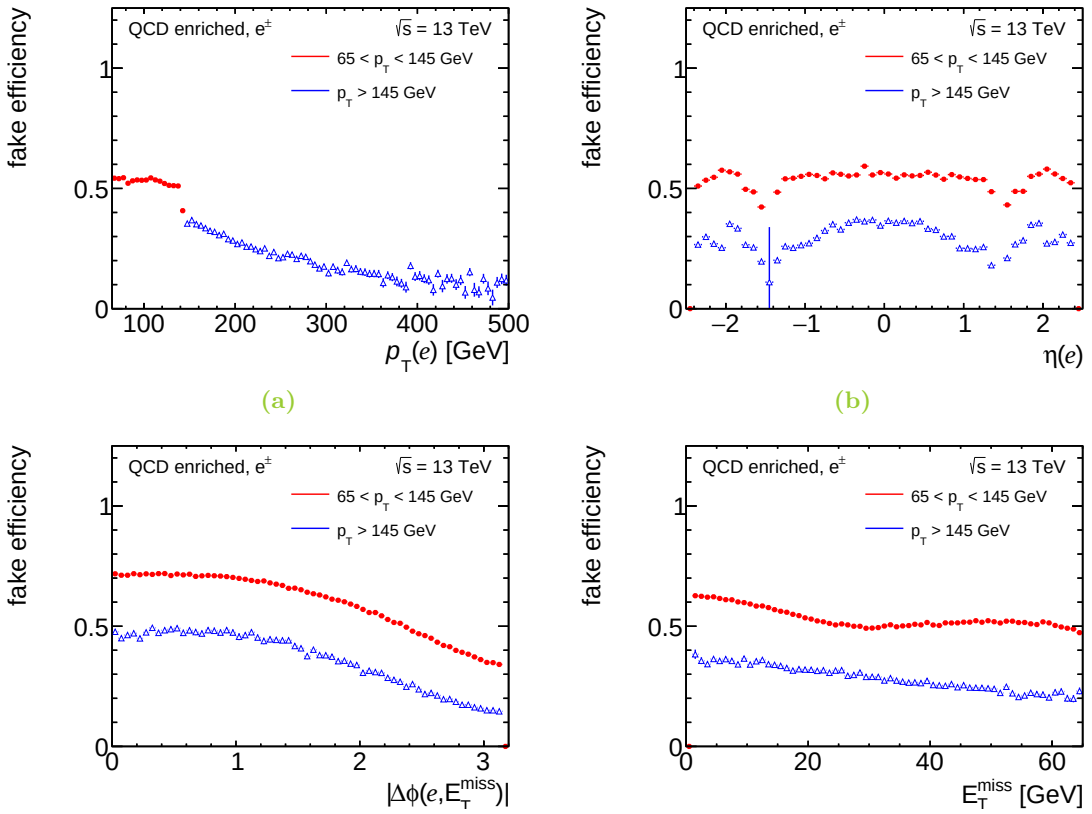

Figure 9.11: Fake electron efficiency for $|\Delta\phi(e, E_{\mathrm{T}}^{\mathrm{miss}})|$, $\eta(e)$, $p_{\mathrm{T}}(e)$ and $E_{\mathrm{T}}^{\mathrm{miss}}$ separated based on the transverse momentum of 65 GeV $< p_{\mathrm{T}}(e) <$ 145 GeV (red) and $p_{\mathrm{T}}(e) >$ 145 GeV (blue) for the `tight` $E_{\mathrm{T}}^{\mathtt{miss}}$ working point.

$p_{\mathrm{T}}(e)$ and the pseudorapitiy $\eta(e)$, in Figure 9.11a and Figure 9.11b respectively, are quite similar to what has been observed for the `loose` $E_{\mathrm{T}}^{\mathtt{miss}}$ working point. In contrast, the fake efficiency as a function of $|\Delta\phi(e, E_{\mathrm{T}}^{\mathrm{miss}})|$ behaves very differently. Large fake efficiencies are visible at small angles monotonously decreasing until $|\Delta\phi(e, E_{\mathrm{T}}^{\mathrm{miss}})| = \pi$. The different trend can be traced back to the differences visible for the $E_{\mathrm{T}}^{\mathrm{miss}}$ distribution. Importantly, a flat $E_{\mathrm{T}}^{\mathrm{miss}}$ dependence can not be observed in Figure 9.11.
For the final calculation of the multijet estimate, twelve bins in the angle between the electron and the missing transverse momentum, four bins in the absolute value of the pseudorapidity and eleven bins in the transverse momentum of the electron are used in order to cover the dependencies of the fake efficiency. These fake efficiencies for the `loose MET` working point are shown in Figure 9.12 and Figure 9.13, where in each six $|\Delta\phi(e, E_{\mathrm{T}}^{\mathrm{miss}})|$ bins are shown. For each of the plots, the $|\eta(e)|$ binning is indicated by differently coloured distributions of the transverse momentum $p_{\mathrm{T}}(e)$.
The same trends that have been discussed for Figure 9.10 can be observed in the three-dimensionally binned fake efficiencies, which will be used, together with the two-dimensionally binned real efficiencies described in Chapter 9.3, in order to estimate the nominal multijet

background via the Matrix Method.
The three-dimensionally binned fake efficiencies for the `tight` $E_{\mathrm{T}}^{\mathtt{miss}}$ working point are shown in Figure C.3 and Figure C.4 in Appendix C.

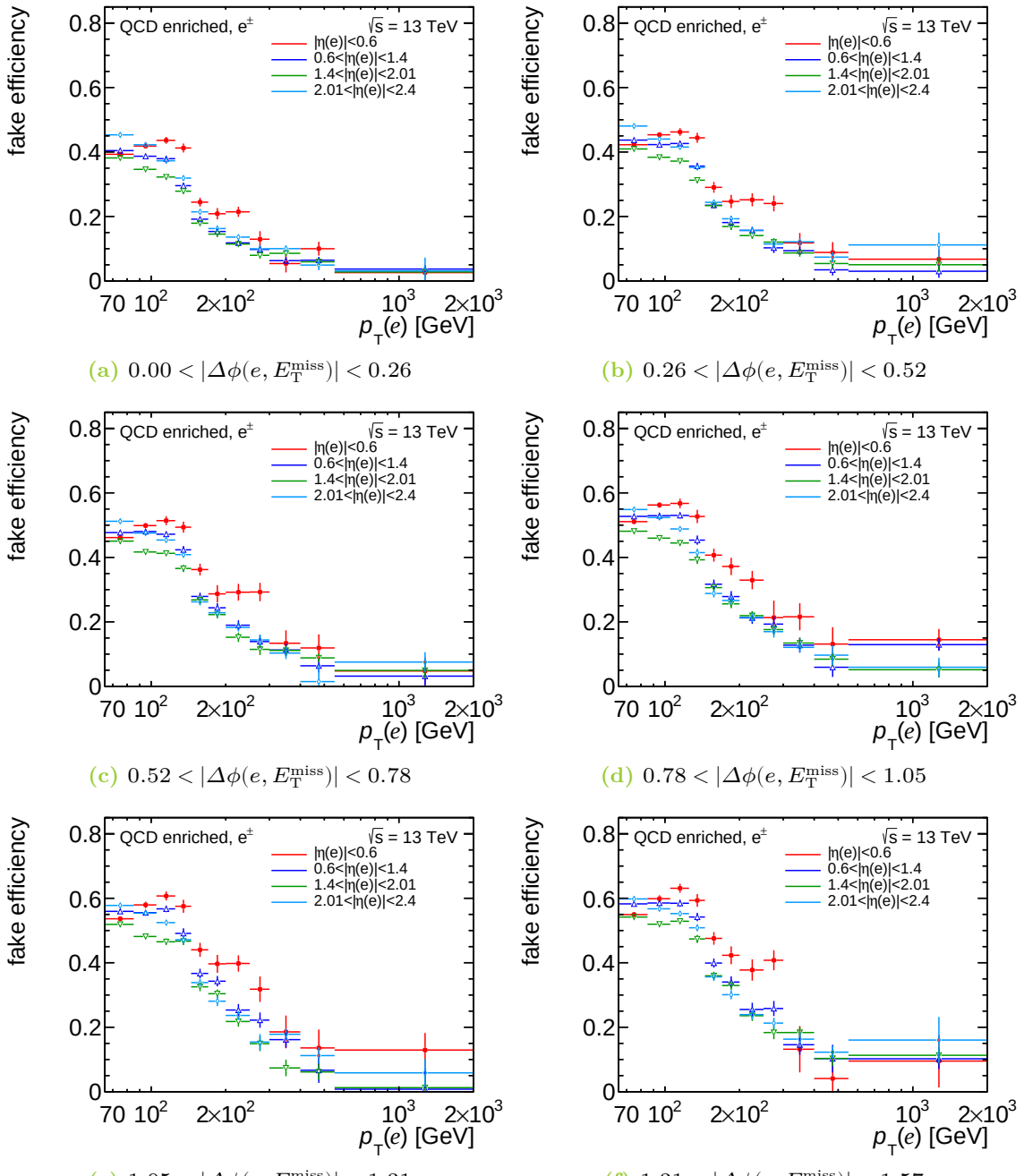

(a) $0.00 < |\Delta\phi(e, E_{\mathrm{T}}^{\mathrm{miss}})| < 0.26$

(b) $0.26 < |\Delta\phi(e, E_{\mathrm{T}}^{\mathrm{miss}})| < 0.52$

(c) $0.52 < |\Delta\phi(e, E_{\mathrm{T}}^{\mathrm{miss}})| < 0.78$

(d) $0.78 < |\Delta\phi(e, E_{\mathrm{T}}^{\mathrm{miss}})| < 1.05$

(e) $1.05 < |\Delta\phi(e, E_{\mathrm{T}}^{\mathrm{miss}})| < 1.31$

(f) $1.31 < |\Delta\phi(e, E_{\mathrm{T}}^{\mathrm{miss}})| < 1.57$

Figure 9.12: Three-dimensional fake efficiency binned in the transverse momentum $p_{\mathrm{T}}(e)$, the absolute value of the pseudorapidity $|\eta(e)|$ and the first six bins of the absolute value of the angle between the electron and missing transverse momentum $|\Delta\phi(e, E_{\mathrm{T}}^{\mathrm{miss}})|$ for the `loose` $E_{\mathrm{T}}^{\mathtt{miss}}$ working point.

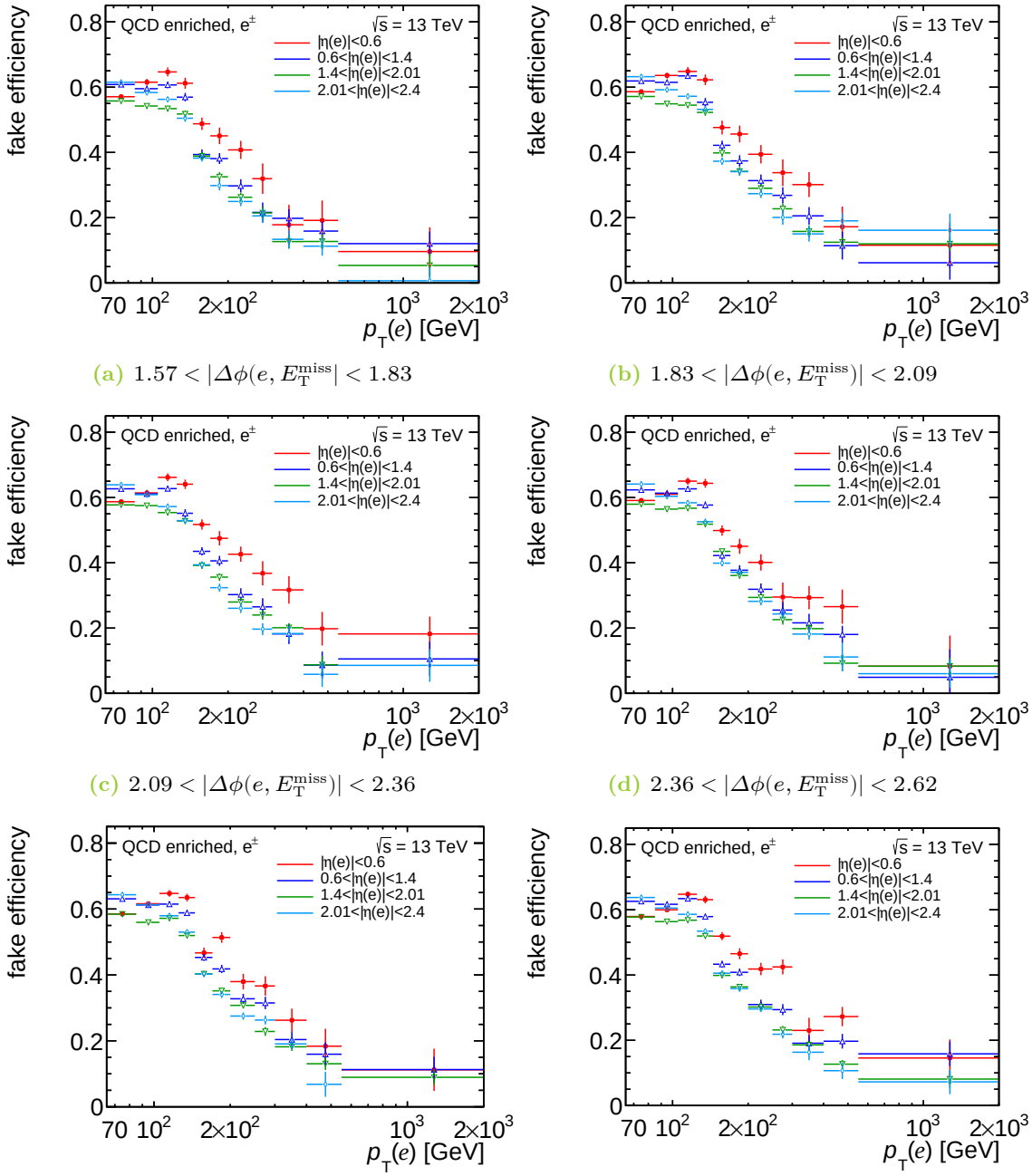

(a) $1.57 < |\Delta\phi(e, E_{\mathrm{T}}^{\mathrm{miss}}| < 1.83$

(b) $1.83 < |\Delta\phi(e, E_{\mathrm{T}}^{\mathrm{miss}})| < 2.09$

(c) $2.09 < |\Delta\phi(e, E_{\mathrm{T}}^{\mathrm{miss}})| < 2.36$

(d) $2.36 < |\Delta\phi(e, E_{\mathrm{T}}^{\mathrm{miss}})| < 2.62$

(e) $2.62 < |\Delta\phi(e, E_{\mathrm{T}}^{\mathrm{miss}})| < 2.88$

(f) $2.88 < |\Delta\phi(e, E_{\mathrm{T}}^{\mathrm{miss}})| < 3.14$

Figure 9.13: Three-dimensional fake efficiency binned in the transverse momentum $p_{\mathrm{T}}(e)$, the absolute value of the pseudorapidity $|\eta(e)|$ and the last six bins of the absolute value of the angle between the electron and missing transverse momentum $|\Delta\phi(e, E_{\mathrm{T}}^{\mathrm{miss}})|$ for the `loose` $E_{\mathrm{T}}^{\mathtt{miss}}$ working point.

9.5 Systematic uncertainties on the multijet background

Since the requirements in the estimation of the real- and fake efficiencies such as the definition of the phase space, where the fake efficiencies are estimated, is arbitrary to a certain extend, a set of systematic uncertainties is defined. The set of the systematic uncertainties accounts for the uncertainties that are inherent to the Matrix Method. A detailed introduction to systematic uncertainties is given in Chapter 11. The following criteria are separately varied in the estimation of the fake efficiency, where each variation corresponds to a systematic uncertainty:

1. Restrict the missing transverse momentum to $E_{\mathrm{T}}^{\mathrm{miss}} \in [0, 30]$ GeV.
2. Restrict the missing transverse momentum to $E_{\mathrm{T}}^{\mathrm{miss}} \in [30, 65]$ GeV.
3. Scale the cross-section of all MC samples in the background subtraction by $\pm 6\,\%$.
4. Require at least 1 jet, with $p_T(jet) > 30\,\mathrm{GeV}$ and $\Delta R(jet, e) > 0.2$.
5. Calculate $E_{\mathrm{T}}^{\mathrm{miss}}$ according to the `mixed` $E_{\mathrm{T}}^{\mathtt{miss}}$ WP.

The first and second variation of the event selection is combined as one asymmetric two-sided systematic uncertainty, i.e. consisting of an up- and down-variation. The threshold of the $E_{\mathrm{T}}^{\mathrm{miss}}$ variations is determined based on the fake efficiency in Figure 9.10d, where a constant efficiency is observed until $E_{\mathrm{T}}^{\mathrm{miss}} = 30\,\mathrm{GeV}$ and a slight increase between $E_{\mathrm{T}}^{\mathrm{miss}} = 30\,\mathrm{GeV}$ and 65 GeV. The systematic uncertainty is denoted as `MJ EL MET`. Another two-sided systematic uncertainty is obtained from the variation of the MC cross-sections by $\pm 6\,\%$, labelled as `MJ EL MC scaling`. The fourth variation, denoted as `MJ EL 1 jet`, yields a one-sided systematic uncertainty where the event selection is modified by an additional jet requirement, enhancing the similarity to dijet events. And finally, a one-sided systematic uncertainty is defined in order to cover differences observed in the definition of the $E_{\mathrm{T}}^{\mathrm{miss}}$ estimation, referred to as `MJ EL mix MET`, as discussed in Chapter 9.2.
Each variation of the event selection is used to calculate individual fake efficiencies and the corresponding multijet estimate, which is compared to the nominal multijet estimate in order to determine the size of each systematic uncertainty and is presented after the signal region selection in Figure 9.14. The measurement binning, as introduced in Chapter 8.3, is used where the double-differential measurement binning displays the six bins, where the $|\eta(e)|$ distribution for each m_{T}^{W} bin is shown side-by-side. The first m_{T}^{W} bin, which is not part of the cross-section measurement, is highlighted in grey colour.
The systematic uncertainty is estimated for the combination of the e^+ and e^- channel. In Figure 9.14a and Figure 9.14c, the systematic uncertainty with respect to the nominal multijet is shown. The systematic uncertainty on the measured cross-section is approximated by the scaling of the uncertainty to the difference of data and background events per bin. The obtained expected impact of the systematic uncertainty on the cross-section is displayed in Figure 9.14b and Figure 9.14d.
Each systematic uncertainty is smoothed, by averaging over neighbouring bins, in order to reduce statistical fluctuations. The smoothing procedure from the ROOT framework is applied with respect to the nominal multijet, as shown in Figure 9.14a and Figure 9.14c. Importantly, the smoothing procedure does not work for the $m_{\mathrm{T}}^{W} \otimes |\eta(e)|$ distribution. As a

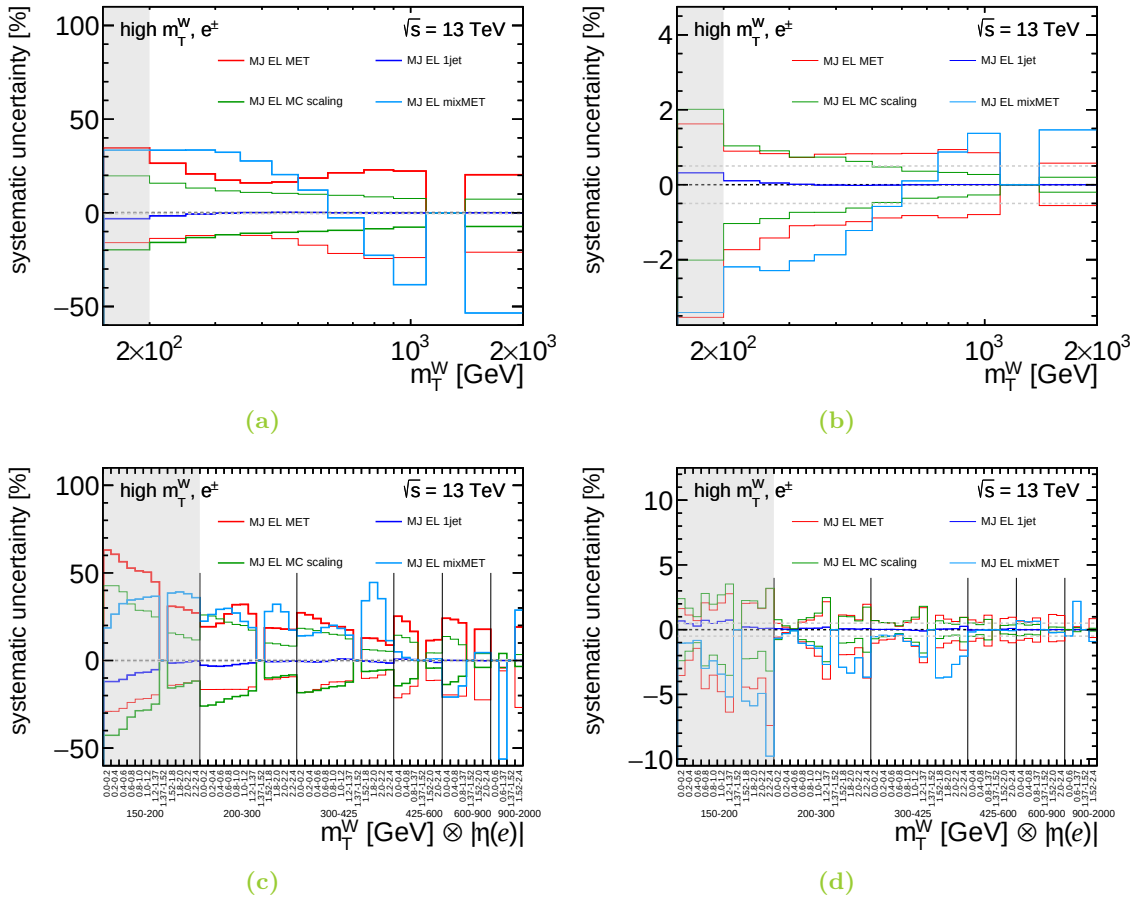

Figure 9.14: Relative systematic uncertainties of the multijet estimate after the signal region selection as a function of the transverse mass of the W boson m_{T}^{W} and the transverse mass of the W boson and the absolute value of the pseudorapidity of the electron $m_{\mathrm{T}}^{W} \otimes |\eta(e)|$ in the measurement binning. The systematic uncertainty is shown with respect to the nominal multijet estimate in a) and c), while the expected systematic uncertainty on cross-section, i.e. normalised to data subtracted by the background processes, is given in b) and d).

consequence, only fluctuations as a function of $|\eta(e)|$ are reduced. The `MJ EL MC scaling` systematic uncertainty is symmetrised additionally.
The largest impact is observed for the one-sided `mixed` $E_{\mathrm{T}}^{\mathtt{miss}}$ variation with an uncertainty of $-53\,\%$ at high m_{T}^{W}, as shown in Figure 9.14a. The remaining systematic uncertainty on the nominal multijet estimate extend up to approximately $^{+35\,\%}_{-22\,\%}$ for the full range of m_{T}^{W}, where especially the `MJ EL 1 jet` systematic uncertainty is much smaller. As a side note, an uncertainty of $0\,\%$ is displayed in the range of $m_{\mathrm{T}}^{W} \in [1100, 1400]\,\mathrm{GeV}$. Since negative estimates of the multijet background are artificially set to zero, the corresponding systematic uncertainties are zero as well. The approximated systematic uncertainty on the cross-section in the measurement range, i.e. $m_{\mathrm{T}}^{W} > 200\,\mathrm{GeV}$, is within $\pm 2.2\,\%$ as displayed in Figure 9.14b. It should be noted, that these systematic uncertainties are assumed to be largely uncorrelated and, for this reason, the quadrature sum is needed.

In Figure 9.14c, the systematic uncertainties are presented for the double-differential cross-section measurement binning. The systematic uncertainties are the largest in the range of $m_{\mathrm{T}}^{W} \in [150, 200]\,\mathrm{GeV}$ and decrease for increasing transverse masses. Furthermore, it can be seen that most systematic uncertainties with respect to the nominal multijet decrease for increasing $|\eta(e)|$ in all m_{T}^{W} bins. The opposite trend is observed for the approximated systematic uncertainty on the cross-section. In this case, the uncertainty increases as a function of $|\eta(e)|$ and in particular large uncertainties are present for $|\eta(e)| \in [1.2, 1.4]$ and $|\eta(e)| \in [2.2, 2.4]$. In the range, where the measurement is performed an up-variation of 41 % and a down variation of $-25\,\%$ at most can be observed in Figure 9.14c, which corresponds to an uncertainty of up to $^{+3.0\,\%}_{-4.5\,\%}$ on the cross-section as shown in Figure 9.14d.
Importantly, it should be highlighted that an increase in the multijet estimate results in a decrease of the cross-section.

9.6 Background estimate of the multijet in two different regions

In the following, the Data-prediction agreement including the estimated fake electron background, denoted as multijet, is studied. The summed contributions from MC processes and the estimated multijet is compared to data in two regions different to the signal region. A reasonable agreement, in order to show whether the multijet is well-modelled, is targeted for the application of the real and fake efficiencies in the signal region.

9.6.1 Multijet closure region

The first region, the so-called multijet closure region (CR), is defined to be as close as possible to the region, where the fake efficiencies have been estimated as outlined in Chapter 9.4. The CR is defined with respect to the event selection described in Chapter 8.1 by the following requirements:

- The $E_{\mathrm{T}}^{\mathrm{miss}}$ requirement is inverted to $E_{\mathrm{T}}^{\mathrm{miss}} < 65\,\mathrm{GeV}$.
- The m_{T}^{W} requirement is dropped.

The phase space corresponding to the CR consists dominantly of electron fakes, which mostly originate from jet events, where the `loose` $E_{\mathrm{T}}^{\mathtt{miss}}$ working point is expected to provide a non-optimal energy estimate, as discussed in Chapter 9.2. Data events are compared to MC and multijet contributions in the CR. The systematic uncertainties for the multijet are evaluated in order to investigate the modelling of the multijet estimate.
Since the evaluation of the `mixed` $E_{\mathrm{T}}^{\mathtt{miss}}$ related systematic uncertainty depends on the phase space, it is necessary to estimate the `loose` $E_{\mathrm{T}}^{\mathtt{miss}}$ fractions for the CR first. These are estimated following the same procedure as described in Chapter 9.2.2.
The same binning as for the determination of the fake efficiencies in the transverse momentum of the electron $p_{\mathrm{T}}(e)$, the absolute value of the electron's pseudorapidity $|\eta(e)|$ and the absolute value of the angle between the electron and missing transverse momentum $|\Delta\phi(e, E_{\mathrm{T}}^{\mathrm{miss}})|$ is used, where the first six bins and the following six bins in $|\Delta\phi(e, E_{\mathrm{T}}^{\mathrm{miss}})|$ are shown in Figure 9.15 and Figure 9.16, respectively.

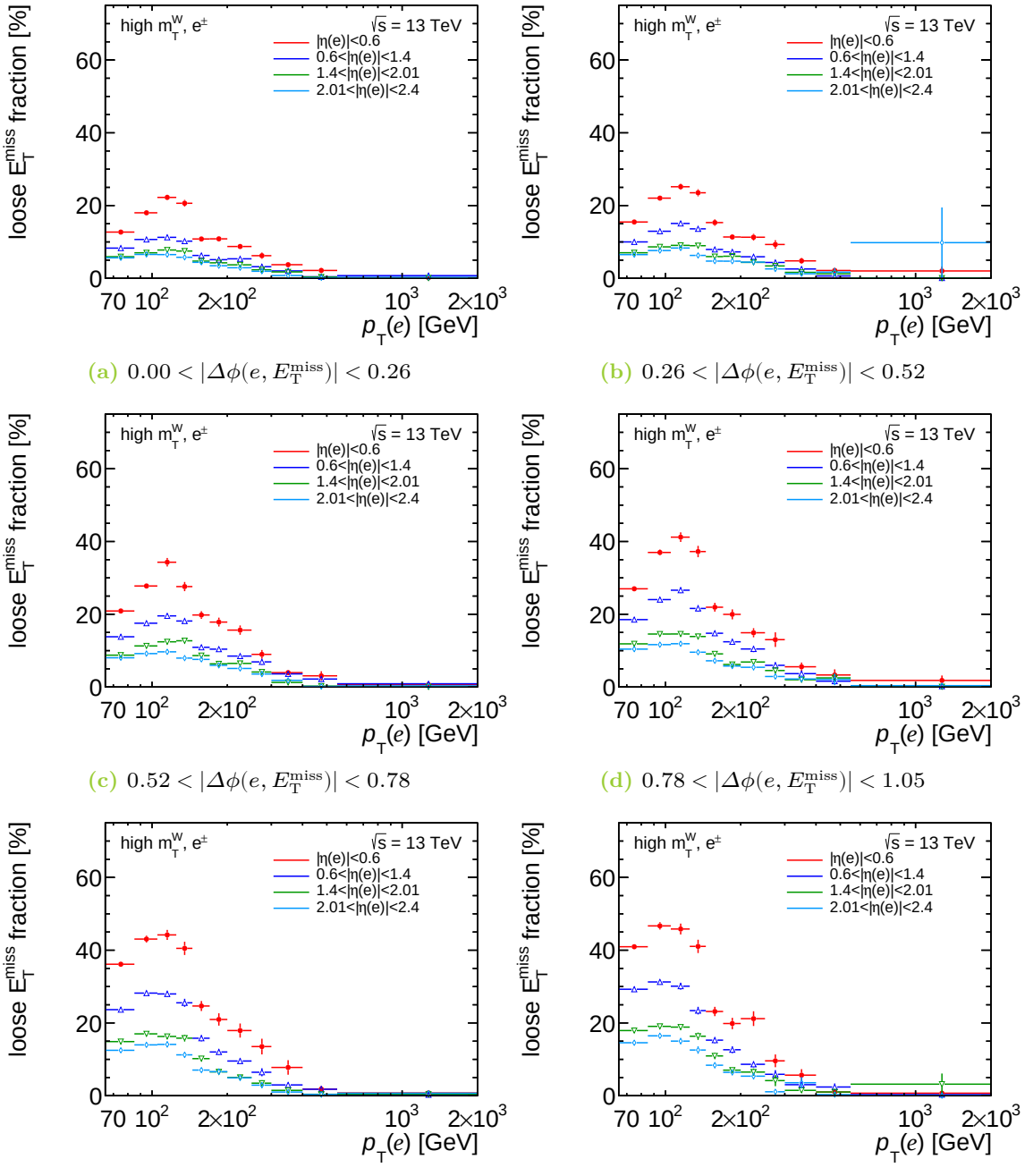

(a) $0.00 < |\Delta\phi(e, E_{\mathrm{T}}^{\mathrm{miss}})| < 0.26$

(b) $0.26 < |\Delta\phi(e, E_{\mathrm{T}}^{\mathrm{miss}})| < 0.52$

(c) $0.52 < |\Delta\phi(e, E_{\mathrm{T}}^{\mathrm{miss}})| < 0.78$

(d) $0.78 < |\Delta\phi(e, E_{\mathrm{T}}^{\mathrm{miss}})| < 1.05$

(e) $1.05 < |\Delta\phi(e, E_{\mathrm{T}}^{\mathrm{miss}})| < 1.31$

(f) $1.31 < |\Delta\phi(e, E_{\mathrm{T}}^{\mathrm{miss}})| < 1.57$

Figure 9.15: `Loose` $E_{\mathrm{T}}^{\mathrm{miss}}$, i.e. real electron, fractions in the control region binned three-dimensionally in the transverse momentum of the electron $p_{\mathrm{T}}(e)$, the absolute value of the electron's pseudorapidity $|\eta(e)|$ and the first six bins in $|\Delta\phi(e, E_{\mathrm{T}}^{\mathrm{miss}})|$ obtained from MC-Data comparisons, where the electron fulfils the loose identification criteria only.

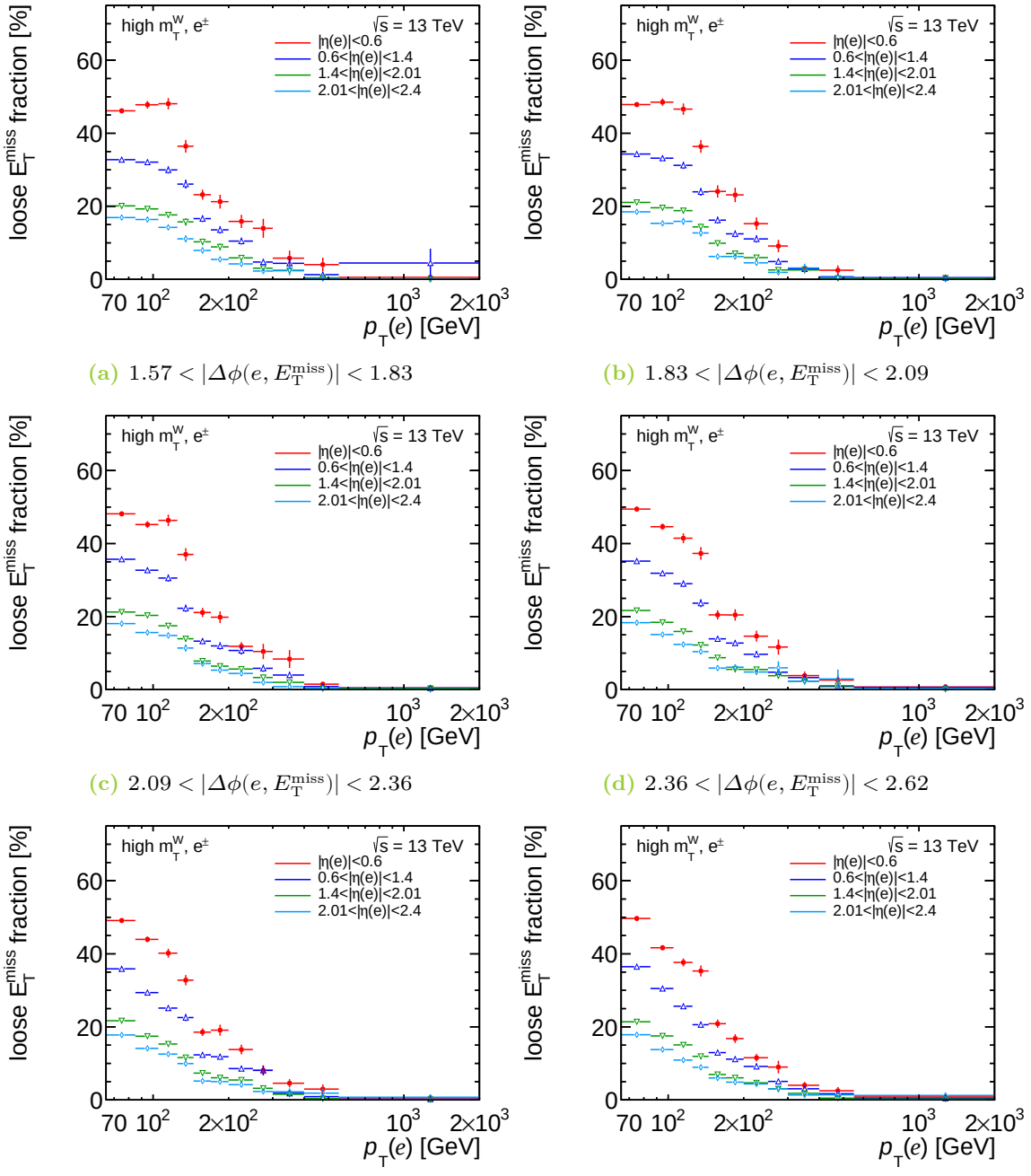

(a) $1.57 < |\Delta\phi(e, E_{\mathrm{T}}^{\mathrm{miss}})| < 1.83$

(b) $1.83 < |\Delta\phi(e, E_{\mathrm{T}}^{\mathrm{miss}})| < 2.09$

(c) $2.09 < |\Delta\phi(e, E_{\mathrm{T}}^{\mathrm{miss}})| < 2.36$

(d) $2.36 < |\Delta\phi(e, E_{\mathrm{T}}^{\mathrm{miss}})| < 2.62$

(e) $2.62 < |\Delta\phi(e, E_{\mathrm{T}}^{\mathrm{miss}})| < 2.88$

(f) $2.88 < |\Delta\phi(e, E_{\mathrm{T}}^{\mathrm{miss}})| < 3.14$

Figure 9.16: `Loose` $E_{\mathrm{T}}^{\mathrm{miss}}$, i.e. real electron, fractions in the control region binned three-dimensionally in the transverse momentum of the electron $p_{\mathrm{T}}(e)$, the absolute value of the electron's pseudorapidity $|\eta(e)|$ and the last six bins in $|\Delta\phi(e, E_{\mathrm{T}}^{\mathrm{miss}})|$ obtained from MC-Data comparisons, where the electron fulfils the loose identification criteria only.

Overall, it can be observed that the `loose` $E_{\mathrm{T}}^{\mathtt{miss}}$ fractions, i.e. the percentage of real electrons in the data, is 50% or less in all bins. The percentage of real electron is the highest for low $|\eta(e)|$ and low $p_{\mathrm{T}}(e)$, decreasing continuously in the forward region and for higher $p_{\mathrm{T}}(e)$ bins. While the maximal fraction of real electrons is found for $p_{\mathrm{T}}(e) \approx 110\,\mathrm{GeV}$ in the first seven $|\Delta\phi(e, E_{\mathrm{T}}^{\mathrm{miss}})|$ bins, the maximum shifts towards lower $p_{\mathrm{T}}(e)$ for later $|\Delta\phi(e, E_{\mathrm{T}}^{\mathrm{miss}})|$ bins.
It can be concluded that the amount of electron fakes originating from jets is much higher in the CR if comparing to the `loose` $E_{\mathrm{T}}^{\mathtt{miss}}$ fractions estimated for the signal region. In the CR, most of the electron fakes originate from jet events, which is expected based on the results discussed in Chapter 9.2.1. Due to the large `tight` $E_{\mathrm{T}}^{\mathtt{miss}}$ fractions, the `mixed` $E_{\mathrm{T}}^{\mathtt{miss}}$ working point is expected to provide a sizeable systematic uncertainty in the CR. As a result, the multijet estimate corresponding to the `tight` $E_{\mathrm{T}}^{\mathtt{miss}}$ working point would lead to a more reasonable modelling.

MC-Data comparisons for $p_{\mathrm{T}}(e)$, $E_{\mathrm{T}}^{\mathrm{miss}}$, $|\Delta\phi(e, E_{\mathrm{T}}^{\mathrm{miss}})|$, m_{T}^{W}, $\eta(e)$ and $\phi(e)$ for the e^+ and e^- channel in the CR are shown in Figure 9.17 and Figure 9.18. The statistical uncertainty and the systematic uncertainties from the multijet estimate are added in quadrature and then represented by the uncertainty band. The systematic uncertainties corresponding to the multijet estimate are estimated following the procedure described for the signal region in Chapter 9.5.
In the ratio, data and prediction agree approximately within the estimated uncertainty band, represented by the grey coloured area, for the e^+ and e^- channel. Several trends can be observed in the ratios of the kinematic distributions, where the data points are at the edge of the uncertainty band and some even beyond: A linear shape is observed in the ratio over the full range of the $E_{\mathrm{T}}^{\mathrm{miss}}$ distribution and in the range of $m_{\mathrm{T}}^{W} \in [30, 130]$ in the m_{T}^{W} distribution. In addition, a decrease for absolute values of the angles below $\pi/2$ is found in the ratio of the $|\Delta\phi(e, E_{\mathrm{T}}^{\mathrm{miss}})|$ distribution. Lastly, data points are not covered by the uncertainty band for $|\eta(e)| \in [1.2, 1.4]$ and $|\eta(e)| \in [2.2, 2.4]$.
First of all, it has to be considered, that the nominal ratio belongs to the `loose` $E_{\mathrm{T}}^{\mathtt{miss}}$ working point, where the energy calibration has been shown to be suboptimal and, for this reason, differences are expected to occur. Exactly this flaw of the estimated MJ should be covered by the developed `mixed MET` systematic uncertainty. The `mixed MET` systematic uncertainty provides indeed the largest contribution of the total MJ systematic uncertainty and covers to a large fraction the observed differences between data and the nominal prediction. The MC-Data comaprisons, where only the `mixed MET` systematic uncertainty is added as an uncertainty band, are shown exemplarily for the e^+ channel in Figure C.5 in Appendix C.
Furthermore, there are two potential sources for differences between the two regions in $|\Delta\phi(e, E_{\mathrm{T}}^{\mathrm{miss}})|$: First, the event topologies differ for the two regions, where large $|\Delta\phi(e, E_{\mathrm{T}}^{\mathrm{miss}})|$ correspond to a back-to-back topology of the electron and $E_{\mathrm{T}}^{\mathrm{miss}}$ and, in contrast, small $|\Delta\phi(e, E_{\mathrm{T}}^{\mathrm{miss}})|$ refer to a boosted topology of the electron and $E_{\mathrm{T}}^{\mathrm{miss}}$. The former is expected to be produced from a decay of a particle, where the decaying particle has a small transverse momentum. In contrast, the later topology is expected to originate from a decay of a particle, where the decaying particle has a large transverse momentum. The largest contribution at small $|\Delta\phi(e, E_{\mathrm{T}}^{\mathrm{miss}})|$ is the multijet production, where dominantly dijet events contribute. In this case, one of the jets with a large transverse momentum is misidentified as an electron,

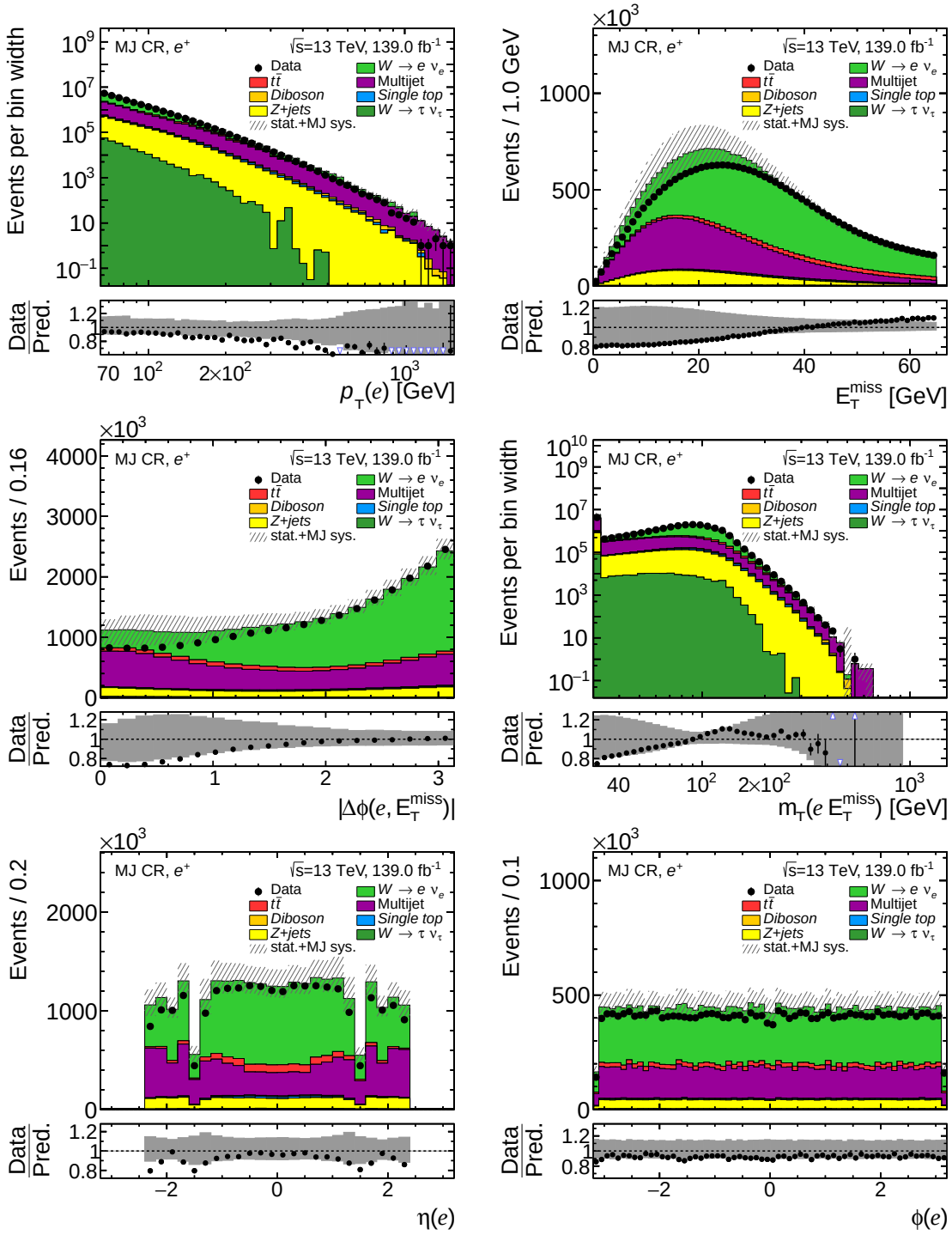

Figure 9.17: Comparison of summed MC, the estimated multijet and data in the closure region for the e^+ channel. The uncertainty band is composed of to the statistical uncertainty and the systematic uncertainties corresponding to the multijet estimate, which have been added in quadrature.

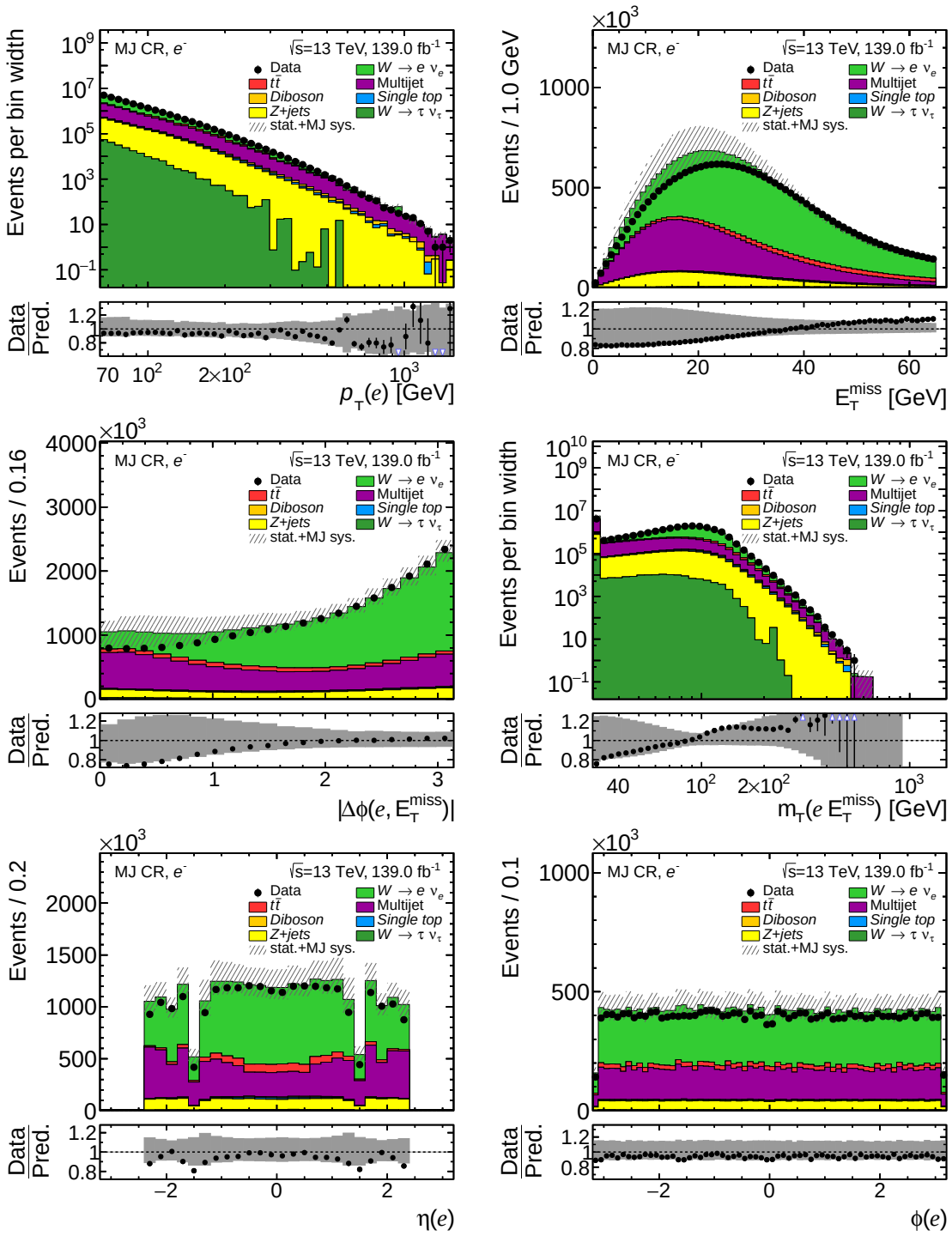

Figure 9.18: Comparison of summed MC, the estimated multijet and data in the closure region for the e^- channel. The uncertainty band is composed of to the statistical uncertainty and the systematic uncertainties corresponding to the multijet estimate, which have been added in quadrature.

while the other jet has a very small transverse momentum. A suboptimal energy estimate of the fake electron, that is truly a jet, could lead to the reconstruction of fake $E_{\mathrm{T}}^{\mathrm{miss}}$. In that way, the different ratio at small $|\Delta\phi(e, E_{\mathrm{T}}^{\mathrm{miss}})|$ might be related to the difference of the `loose` $E_{\mathrm{T}}^{\mathtt{miss}}$ and `tight` $E_{\mathrm{T}}^{\mathtt{miss}}$ working points. Second, the phase space of small $|\Delta\phi(e, E_{\mathrm{T}}^{\mathrm{miss}})|$ is affected by mismeasurements.
Then, it has to be taken into account that the investigated variables are partly highly correlated, where e.g. a difference between data and prediction in $E_{\mathrm{T}}^{\mathrm{miss}}$ is visible in m_{T}^{W} as well. Similarly, the difference in the ratio at $|\Delta\phi(e, E_{\mathrm{T}}^{\mathrm{miss}})| < 1.5$ is correlated to the difference in the ratio of the missing transverse momentum $E_{\mathrm{T}}^{\mathrm{miss}}$.
Lastly, it should be highlighted that the disagreement in such phase spaces were investigated in the search for a W' boson [94], where the trends in the ratio as a function of $E_{\mathrm{T}}^{\mathrm{miss}}$ and in the range of $m_{\mathrm{T}}^{W} \in [110, 200]\,\mathrm{GeV}$ were seen as well.

In addition, a difference in the agreement of data and prediction as a function of the transverse momentum $p_{\mathrm{T}}(e)$ is observed for the e^+ and e^- channel. For the multijet estimate, the combined $e^{\pm}$ fake efficiencies are used, because from a physics point of view no motivation for a non-negligible charge-dependence of the fake efficiencies has been found. Since the observed charge-dependent difference in the agreement is covered by the systematic uncertainty of estimated multijet, it has not been studied further throughout this thesis.

9.6.2 Multijet validation region

Although the agreement of data and predicted events in the CR is important to show that the Matrix Method is able to provide a reasonable estimate, the validity in a phase space which differs from the region, where the fake efficiencies are estimated, has to be studied. The multijet validation region (VR) is defined with respect to the event selection defined in Chapter 8.1, where the following requirements are modified:

- The $E_{\mathrm{T}}^{\mathrm{miss}}$ requirement is removed.
- The m_{T}^{W} requirement is removed.

In comparison to the CR, the $E_{\mathrm{T}}^{\mathrm{miss}} < 65\,\mathrm{GeV}$ requirement is removed, which enhances the similarity to the event topology of the signal region.
The MC-Data comparisons for $p_{\mathrm{T}}(e)$, $E_{\mathrm{T}}^{\mathrm{miss}}$, $|\Delta\phi(e, E_{\mathrm{T}}^{\mathrm{miss}})|$, m_{T}^{W}, $\eta(e)$ and $\phi(e)$ in the validation region for the e^+ and e^- channel are shown in Figure 9.19 and 9.20. The uncertainty band represents the statistical uncertainty and the systematic uncertainties from the MJ estimate as explained in more detail in Chapter 9.5. The `loose` $E_{\mathrm{T}}^{\mathtt{miss}}$ fractions, i.e. percentages of real electrons, for the VR have been estimated in order to determine the `mixed` $E_{\mathrm{T}}^{\mathtt{miss}}$ systematic uncertainty and are shown for completeness in Figure C.6 and Figure C.7 in Appendix C.

The phase space covered by the CR and VR are not orthogonal to each other, i.e. the CR is a subset of the VR. Since the predicted number of events decrease as a function of $E_{\mathrm{T}}^{\mathrm{miss}}$, the behaviour in the VR is characterised by the events in the CR. As a consequnce, a similar behaviour can be observed for the absolute value of the pseudorapidity $|\eta(e)|$, the azimuthal angle $\phi(e)$, the absolute value of the angle between the electron and the missing transverse momentum $|\Delta\phi(e, E_{\mathrm{T}}^{\mathrm{miss}})|$ and the transverse momentum of the electron $p_{\mathrm{T}}(e)$,

where in both regions the amount of data events agree with the predicted events from MC and multijet within the uncertainty band. In contrast to the CR, high missing transverse momenta $E_{\mathrm{T}}^{\mathrm{miss}} > 65\,\mathrm{GeV}$ are included in the VR and the modelling up to $E_{\mathrm{T}}^{\mathrm{miss}} \approx 1\,\mathrm{TeV}$ is shown. Subsequently, the transverse mass of the W boson extends up to several TeV, i.e. covers the phase space of the signal region, as well.
In general, a reasonable agreement of the selected data events and the prediction within the systematic uncertainties is observed in most variables. Nevertheless, similar trends for low $E_{\mathrm{T}}^{\mathrm{miss}}$, where in the ratio a linear increase in the range $E_{\mathrm{T}}^{\mathrm{miss}} \in [10, 70]$, and at small $|\Delta\phi(e, E_{\mathrm{T}}^{\mathrm{miss}})|$, where the ratio differs substantially from unity, are visible. Furthermore, deviations of data and prediction can be found at $E_{\mathrm{T}}^{\mathrm{miss}} \in [70, 200]\mathrm{GeV}$, which are not covered by the estimated systematic uncertainty of the multijet. Differences in this range of $E_{\mathrm{T}}^{\mathrm{miss}}$ are known from other analyses, such as the search for a W' boson [94], where the differences are not expected to be related to the estimation via the Matrix Method, but potentially arise from further issues in the $E_{\mathrm{T}}^{\mathrm{miss}}$ modelling.
As already discussed for the CR, a small difference in the agreement of data and prediction as a function of the transverse momentum $p_{\mathrm{T}}(e)$ between the e^+ and e^- channel are found in the VR as well. In addition, deviations between the e^- and e^+ channel are visible for $E_{\mathrm{T}}^{\mathrm{miss}} > 200\,\mathrm{GeV}$, where it should be considered that the transverse momentum and missing transverse momentum are strongly correlated in a final state with a single electron and single electron neutrino.
Finally, a reasonable agreement between data and prediction within the uncertainty band is achieved for the key variables, m_{T}^W and $|\eta(e)|$, in the CR and the VR. The approximately linear increase in the ratio of data and prediction for $m_{\mathrm{T}}^W \in [40, 200]\,\mathrm{GeV}$ was investigated in detail and is covered by the systematic uncertainty, where the largest fraction of the uncertainty is provided by the `mixed` $E_{\mathrm{T}}^{\mathtt{miss}}$ systematic uncertainty. Since the final cross-section measurement is performed for $m_{\mathrm{T}}^W > 200\,\mathrm{GeV}$, where the agreement of data and prediction is found to be reasonable, it can be concluded that the multijet background is well-modelled by the Matrix Method.

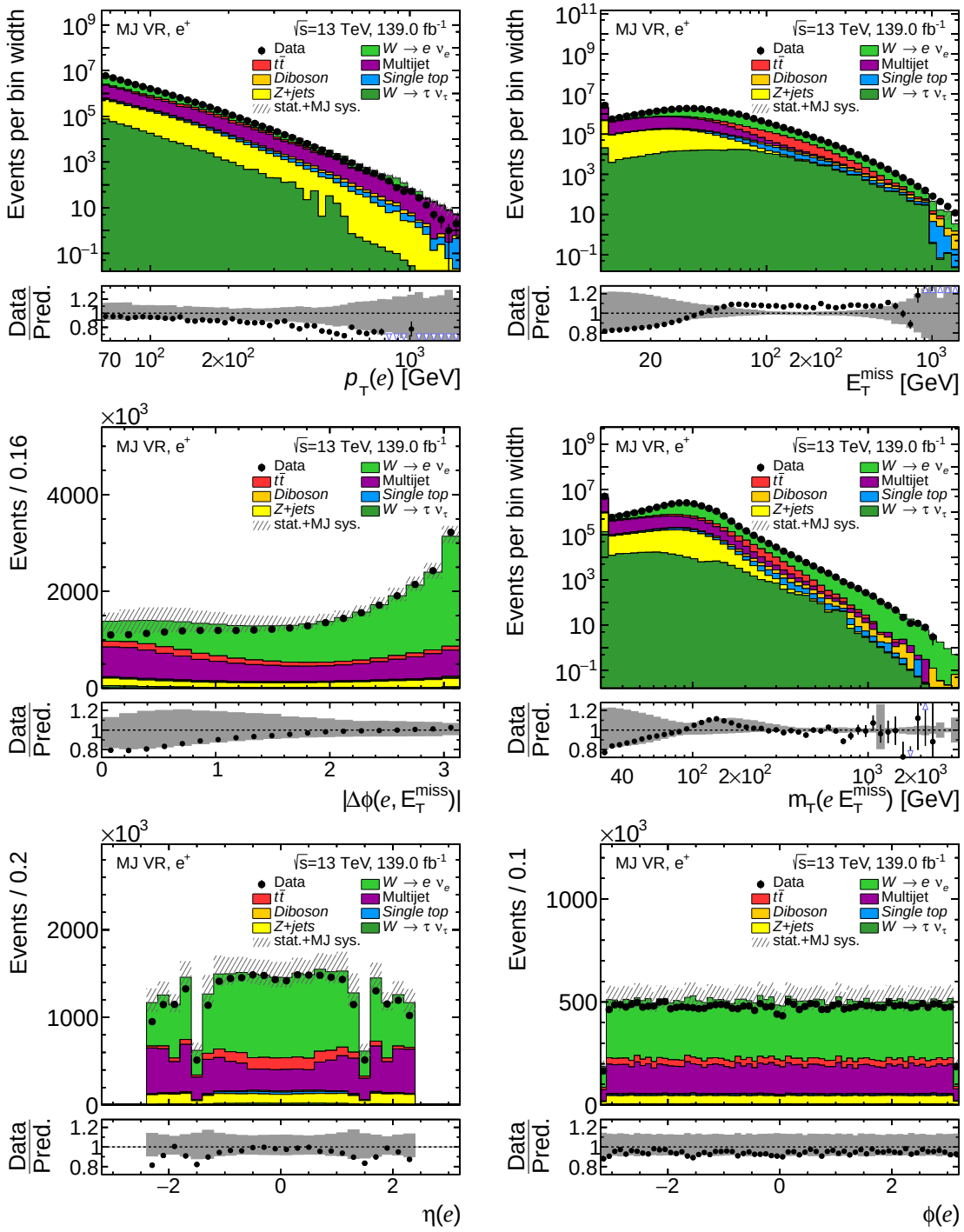

Figure 9.19: Comparison of the summed MC and the estimated multijet with data in the validation region in the e^+ channel. The uncertainty band is composed of the statistical uncertainty and the systematic uncertainties of the multijet estimate, which have been added in quadrature.

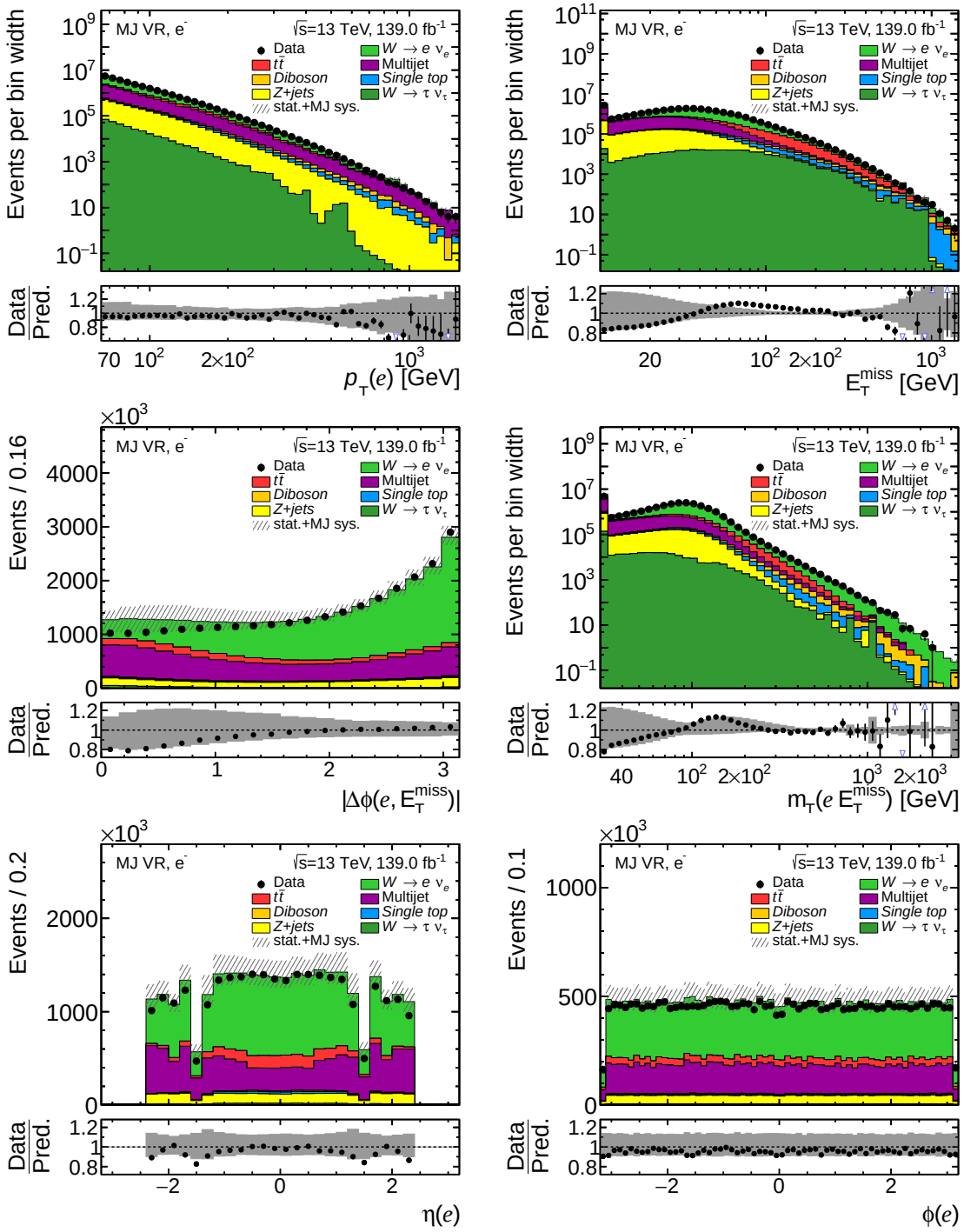

Figure 9.20: Comparison of summed MC and the estimated multijet with data in the validation region for the e^- channel. The uncertainty band is composed of the statistical uncertainty and the systematic uncertainties of the multijet estimate, which have been added in quadrature.

10 Comparison of data and prediction

In the following, the sum of the expected signal and background events, denoted as prediction, are compared to the number of measured data after the signal region selection. A good agreement of the prediction with the number of data events is not a pre-requisite for a measurement of the cross-section, but provides an important insight how well the phase space and the contribution from each process are understood.
The statistical and systematic uncertainties are presented as an uncertainty band in the following, where the more general introduction and a detailed breakdown of single systematic uncertainties can be found in Chapter 11. The sources for systematic uncertainties covered in this section refer to the calibrated objects such as the electron, potential jets and the missing transverse momentum, the multijet estimation via the Matrix Method and theoretical systematic uncertainties of the $t\bar{t}$ process. Only systematic uncertainties with an impact of at least 0.5% on the cross-section in at least one bin are considered.
First, an overview of the contributions of the signal and background processes is given. Then, the comparisons of data and prediction in several different control variables and finally in the measurement binning of the single and double-differential cross-section are shown.

An overview of the fractions of each process with respect to the prediction for the e^+ and e^- channels is shown in Figure 10.1, where the signal process contributes with 67.5 % and 56.9 % in the e^+ and e^- channel, respectively. In this case, different fractions in the e^+ and e^- channel are expected due to the W boson charge asymmetry. Consequently, the signal process provides the highest fraction of events, whereas the background with the largest fraction is the $t\bar{t}$ process, which yields a fraction of about $20.6 - 28.0$ %, depending on the

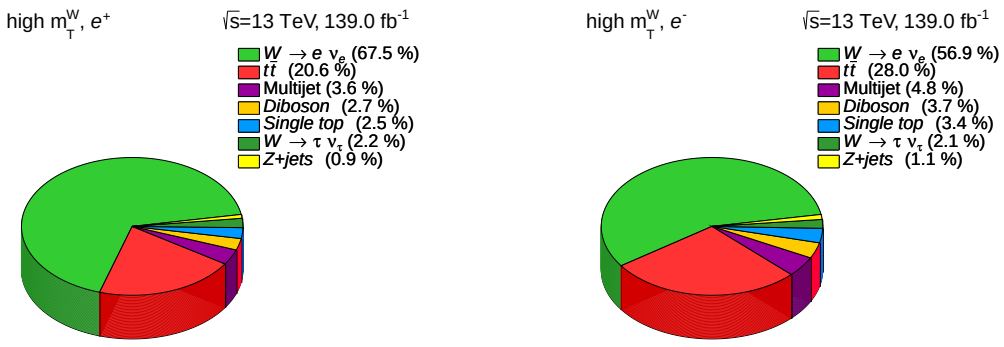

(a) (b)

Figure 10.1: Relative contribution of the different processes in the signal region for (a) the e^+ and (b) the e^- channel.

channel. The second largest background contribution is provided by the multijet process. The MC modelling of the $t\bar{t}$ contribution has been studied in several dedicated validation regions throughout the parallel analysis of the muon channel, which is described in detail in Reference [45] and Reference [46], where it has been concluded that the $t\bar{t}$ process is well-modelled by the MC.

Distributions of the transverse momentum of the electron, $p_{\mathrm{T}}(e)$, the missing transverse momentum, $E_{\mathrm{T}}^{\mathrm{miss}}$, the transverse mass of the W boson, m_{T}^{W}, the pseudorapidity, $\eta(e)$, the azimuthal angle, $\phi(e)$ and the absolute value of the angle between the electron and the missing transverse momentum, $|\Delta\phi(e, E_{\mathrm{T}}^{\mathrm{miss}})|$ are shown for the e^+ and e^- channels in Figure 10.2 and Figure 10.3. In order to illustrate the peculiarities of the signal region, the $m_{\mathrm{T}}^{W} \in [150, 200]$ GeV bin below the phase space that is actually measured is removed in Figure 10.2 and Figure 10.3. In each of the distributions, a comparison of the prediction and data events and the ratio of data events over prediction per bin are presented. The uncertainty band, illustrating the statistical and the systematic uncertainties, is highlighted with grey colour in the ratio. Overall, a good agreement between data and prediction for the e^+ and e^- channel can be observed, where almost all data points agree within the uncertainty band.
The event topology of the signal process is characterised by W bosons that are mostly produced with high masses and low transverse momenta, where the decay products, i.e. the electron and electron neutrino, fulfil a back-to-back topology. Consequently, the transverse momentum of the electron and the missing transverse momentum are expected to fulfil $p_{\mathrm{T}}(e) \approx E_{\mathrm{T}}^{\mathrm{miss}} \approx \frac{m_{\mathrm{T}}^{W}}{2}$ in the majority of the considered events.
In Figure 10.2 and Figure 10.3, an absolute value of the angle $|\Delta\phi(e, E_{\mathrm{T}}^{\mathrm{miss}})| \approx \pi$ illustrates the aforementioned back-to-back topology of the signal process. As a result, also the relation between the transverse momenta and the transverse mass of the W boson holds approximately, where the maximum of the transverse momentum $p_{\mathrm{T}}(e)$ and of the missing transverse momentum $E_{\mathrm{T}}^{\mathrm{miss}}$ is visible slightly above 100 GeV, which is a consequence of the $m_{\mathrm{T}}^{W} \geq 200$ GeV requirement of the signal selection.
The distribution of the azimuthal angle of the electron is expected to be flat, because no flight direction of the decay product from the W boson is preferred. Similarly, the positive and negative pseudorapidities, accounting for half of the detector each, are symmetric.
Finally, the m_{T}^{W} distribution is shown in a fine binning. The distribution is monotonously decreasing over the whole range, which is expected since the on-shell W boson mass at $m_{\mathrm{T}}^{W} \approx 80$ GeV is far below the requirement of the signal selection.

Finally, the transverse mass of the W boson in the binning of the single-differential cross-section measurement, as defined in Chapter 8.3, for the e^+ and e^- channel is shown in Figure 10.4. The additional low m_{T}^{W} bin, indicated by the grey coloured area, is re-included here. The statistical uncertainties at high m_{T}^{W} are reduced by increased bin sizes with respect to the finer binned distribution in Figure 10.2 and Figure 10.3. A very good agreement between the measured data and prediction in the full range of m_{T}^{W} can be observed, where all data points agree within the statistical and systematic uncertainties.

In addition, the distributions of the absolute value of the pseudorapidity in bins of the transverse masses $m_{\mathrm{T}}^{W} \otimes |\eta(e)|$ in the binning of the double-differential cross-section measurement for the e^+ and e^- channel are shown in Figure 10.5 and Figure 10.6.

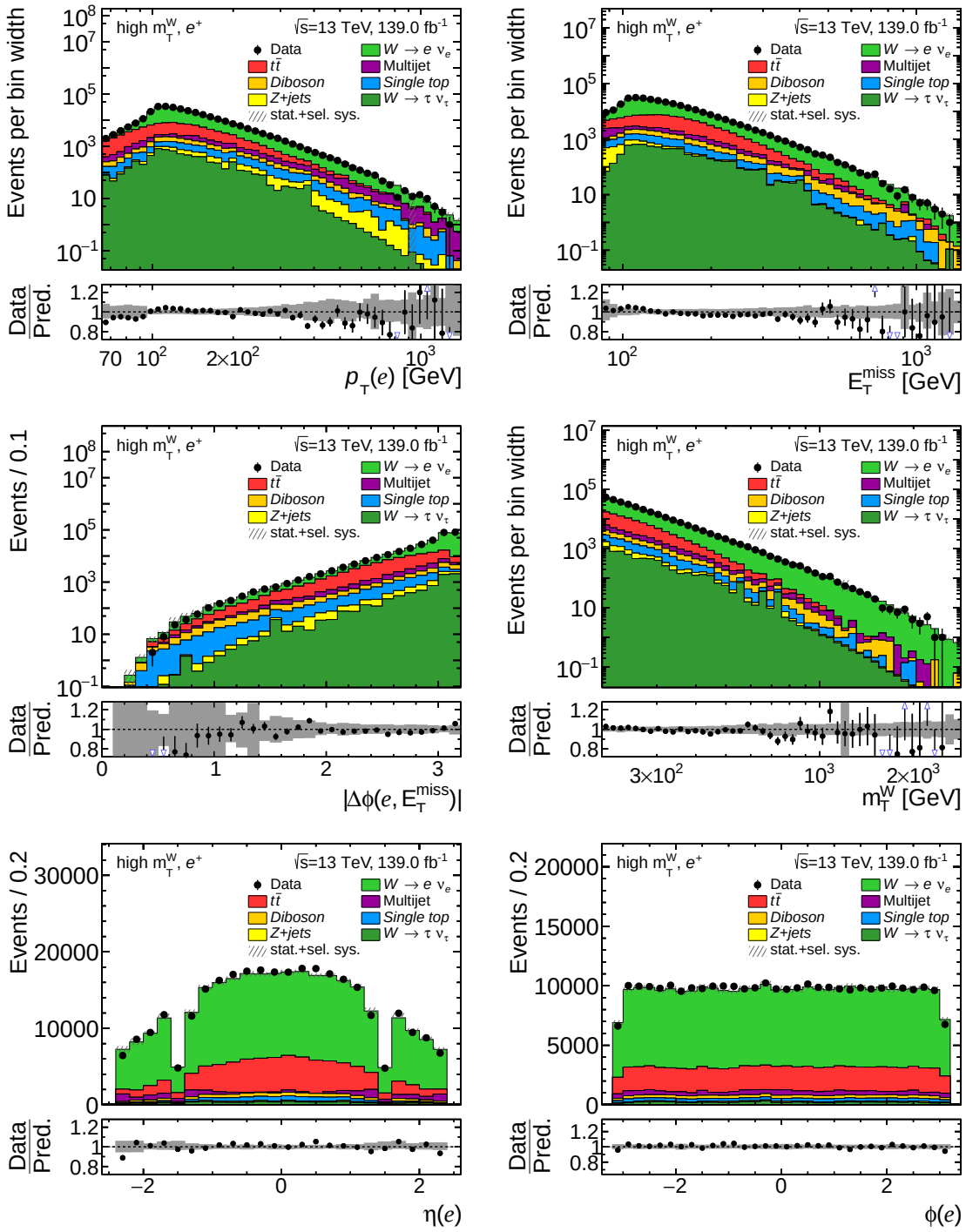

Figure 10.2: Comparison of data and prediction in the signal region, labelled high m_T^W, for the e^+ channel. The uncertainty band consists of the combined statistical uncertainty and of the systematic uncertainty, with an impact of more than 0.5% on the cross-section. The statistical uncertainty of data events is represented by the uncertainty bars.

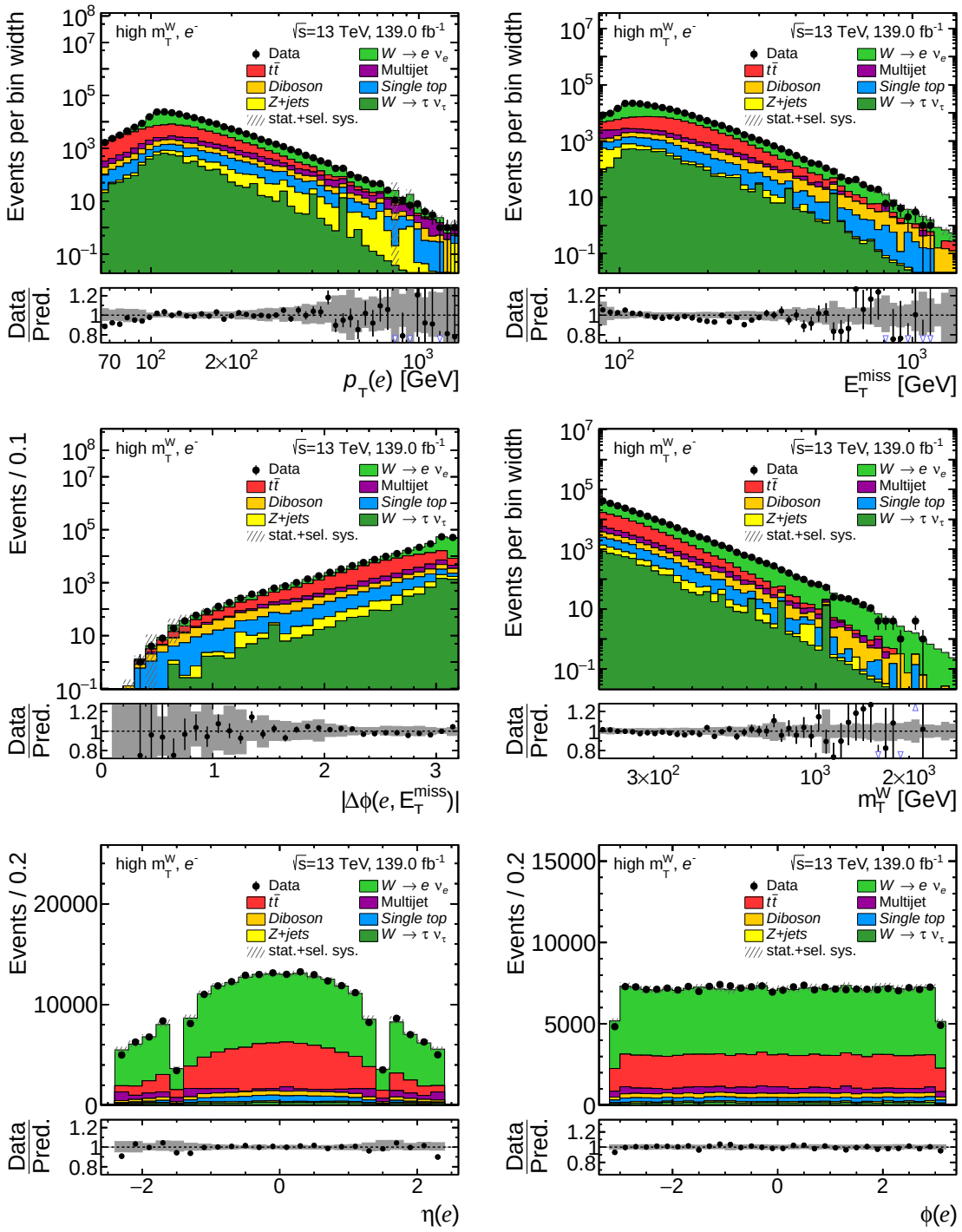

Figure 10.3: Comparison of data and prediction in the signal region, labelled high m_T^W, for the e^- channel. The uncertainty band consists of the combined statistical uncertainty and of the systematic uncertainty, with an impact of more than 0.5% on the cross-section. The statistical uncertainty of data events is represented by the uncertainty bars.

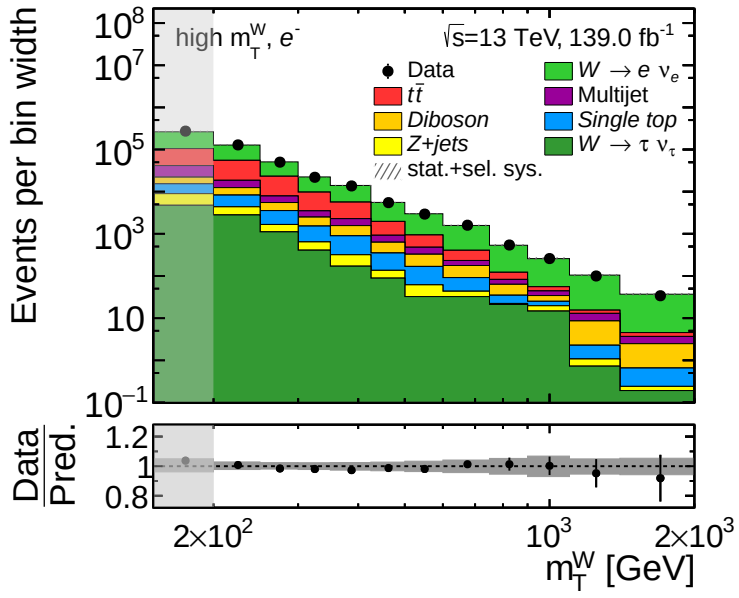

(a)

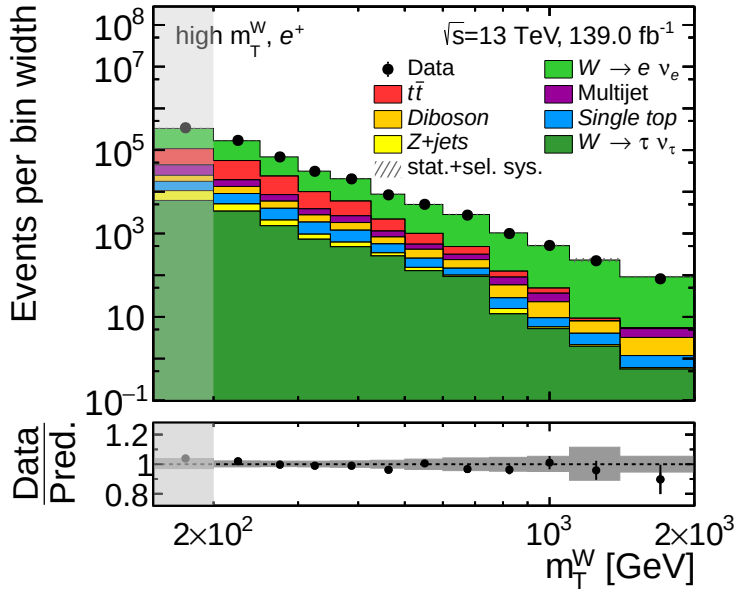

(b)

Figure 10.4: Comparison of data and prediction in the measurement binning of the single-differential cross-section for a) the e^- and b) the e^+ channel in the signal region. The uncertainty band consists of the combined statistical uncertainty and of the systematic uncertainty with an impact of more than 0.5% on the cross-section. The statistical uncertainty of data events is represented by the uncertainty bars.

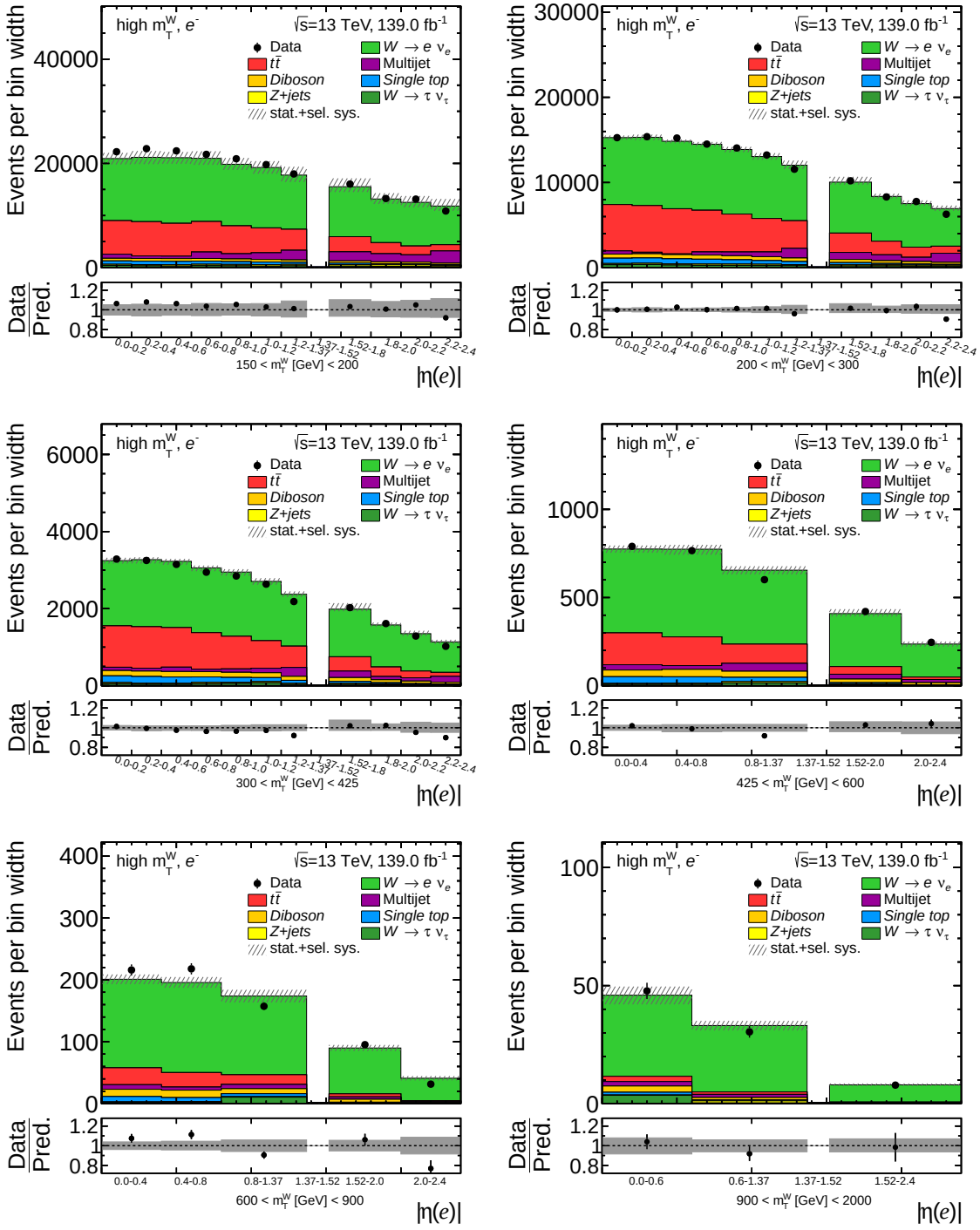

Figure 10.5: Comparison of data and prediction in the measurement binning of the double-differential cross-section for the e^- channel in the signal region. The two-dimensional binning is divided into six $|\eta(e)|$ distributions, where one $|\eta(e)|$ distribution corresponds to one m_{T}^W bin. The uncertainty band consists of the combined statistical uncertainty and of the systematic uncertainty, with an impact of more than 0.5% on the cross-section. The statistical uncertainty of data events is represented by the uncertainty bars.

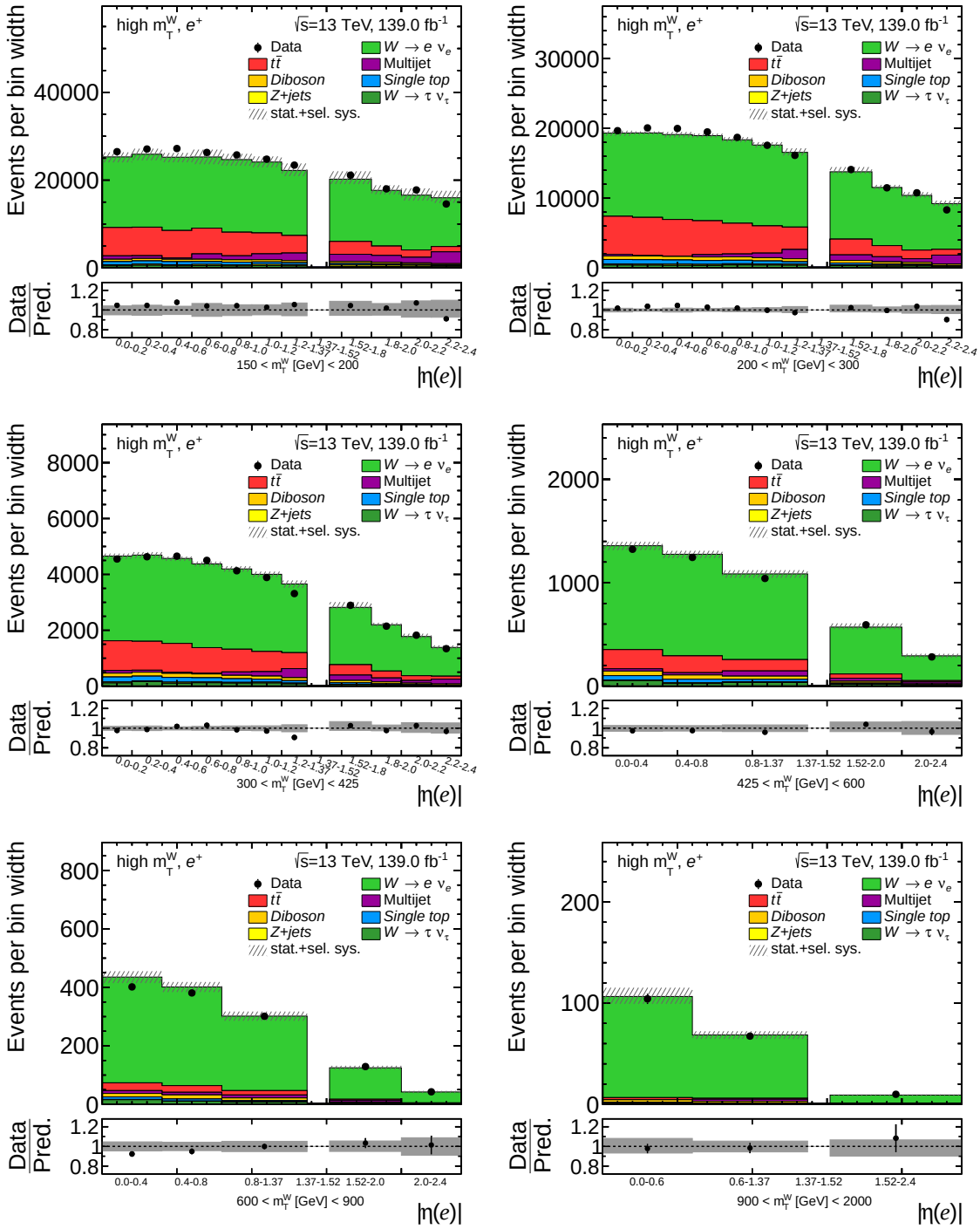

Figure 10.6: Comparison of data and prediction in the measurement binning of the double-differential cross-section for the e^+ channel in the signal region. The two-dimensional binning is divided into six $|\eta(e)|$ distributions, where one $|\eta(e)|$ distribution corresponds to one m_{T}^W bin. The uncertainty band consists of the combined statistical uncertainty and of the systematic uncertainty, with an impact of more than 0.5% on the cross-section. The statistical uncertainty of data events is represented by the uncertainty bars.

In Figure 10.5 and Figure 10.6, the double-differential measurement binning is represented by six separated $|\eta(e)|$ distributions, where one $|\eta(e)|$ distribution corresponds to one m_{T}^{W} bin. The correspondence to a certain m_{T}^{W} bin is given by a label below the labelling of the x-axis. Additionally, the low transverse mass bin $m_{\mathrm{T}}^{W} \in [150, 200]$ GeV is shown.
As previously noted, a symmetric distribution of events as a function of the pseudorapidity η is expected, due to the symmetry of the ATLAS detector, and the absolute value of the pseudorapidity is therefore used in the double-differential cross-section measurement. The absolute value of the pseudorapidity provides roughly twice as many events and a reduced statistical uncertainty, while the η dependence is still well-described. Furthermore, additional bins could be added in the binning of $|\eta(e)|$, which would not be possible for η, while keeping the statistical uncertainty. Nevertheless, differences according to positive and negative pseudorapidities have been studied and are presented in Figure D.2 and Figure D.3 in Appendix D. It can be concluded that the differences for $\pm\eta$ are negligible within the statistical uncertainty and the assumption of the η symmetry is justified.
A good agreement between the prediction and the data events within the uncertainties can be observed in all distributions for the double-differential cross-section measurement, where several peculiarities are discussed in the following:
In all distributions a mostly equidistant binning is used. One exception is made in the transition region of the barrel and end-cap of the LAr calorimeter at $1.37 < |\eta(e)| < 1.52$, where the events are explicitly vetoed, because the energy measurement of electrons is less precise in this region. In the neighbouring bins of the empty bin at $1.37 < |\eta(e)| < 1.52$, an increase of the uncertainty band, which is driven by the systematic uncertainties, indicates the worse energy measurement.
A disagreement of data and prediction, exceeding the uncertainty band, is observed for $|\eta(e)| > 2.2$ in several m_{T}^{W} bins, where especially the lower m_{T}^{W} bins are affected. Two sources for the disagreement have to be considered: First, the area has sizeable contributions from the multijet background, because the energy measurement is less precise. Second, the lepton scale factor is a binned quantity that depends on the transverse momentum and pseudorapidity of the lepton. The lepton scale factor binning as a function of the absolute value of the pseudorapidity

$$|\eta(e)| = [0, 0.1, 0.6, 0.8, 1.15, 1.37, 1.52, 1.81, 2.01, 2.37, 2.47] \,, \tag{10.1}$$

taken from Reference [95], is broader than the binning used for the measurement in this thesis. A potentially too large scale factor for $|\eta(e)| \in [2.2, 2.4]$ could arise from the broad bin of the current lepton scale factor, because this does not sufficiently describe the dependency. A detailed study concerning a finer η binning of the lepton scale factor is investigated by a dedicated performance group at ATLAS indicating an improvement at high $|\eta(e)|$ and close to the transition region of the barrel and end-cap of the LAr calorimeter, but the final impact on this measurement could not be estimated at the given timeline. Lastly, small differences in the agreement of data and prediction for the e^{+} and e^{-} channel, especially in the higher m_{T}^{W} bins, are visible. A potential source for these deviations are statistical fluctuations in the signal or background processes. However, the overall agreement within the uncertainty is reasonable and, for this reason, no further studies are performed.
At the end, another representation of the double-differential cross-section binning, the $m_{\mathrm{T}}^{W} \otimes |\eta(e)|$ distribution, is illustrated in Figure 10.7, where the same distributions shown in Figure 10.5 and Figure 10.6 are combined side-by-side. Consequently, the same conclusions

can be drawn as for the separated, individual distributions. The combined representation allows a more compact visualisation and is technically needed for the unfolding as discussed in detail in Chapter 12.

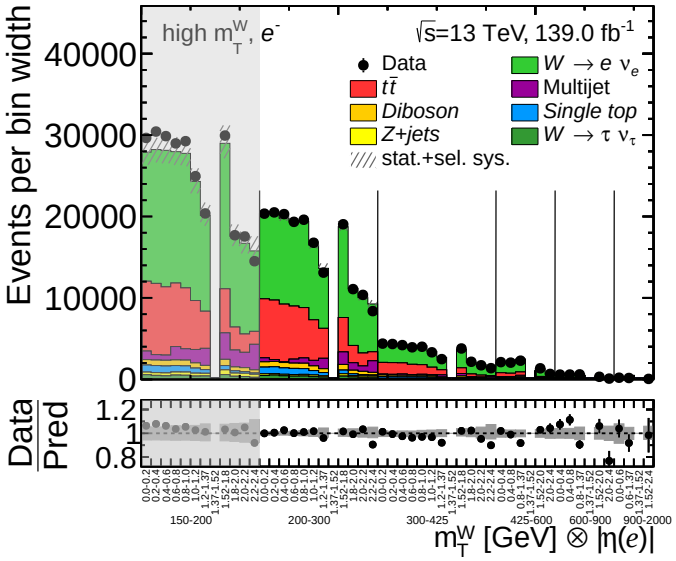

(a)

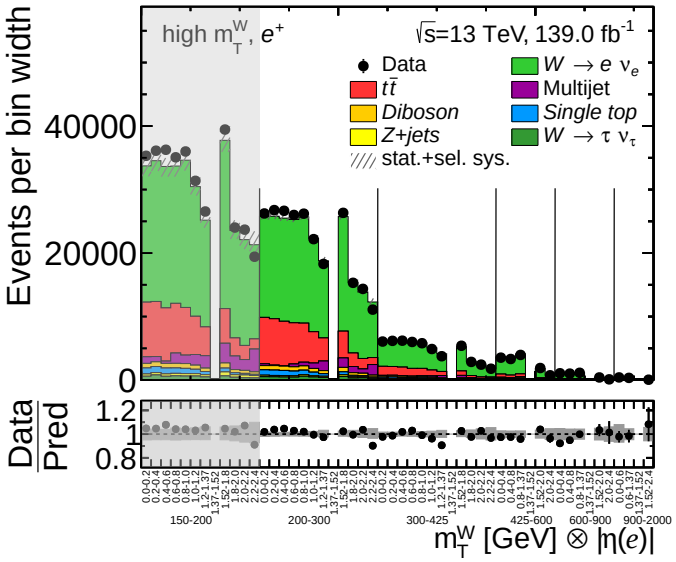

(b)

Figure 10.7: Comparison of data and prediction in the measurement binning of the double-differential cross-section for a) the e^- and b) the e^+ channel after the signal region selection. The two-dimensional binning is transformed into a one–dimensional distribution. The uncertainty band consists of the combined statistical uncertainty and of the systematic uncertainty, with an impact of more than 0.5% on the cross-section. The statistical uncertainty of data events is represented by the uncertainty bars.

11 Systematic uncertainties

This chapter is dedicated to the different sources of systematic uncertainties that are considered in the cross-section measurement. Systematic uncertainties are categorised into a set of four sources: theoretical, experimental, fake electron background and unfolding systematic uncertainties. The systematic uncertainties referring to the multijet background estimation have already been introduced in Chapter 9.5. Another set of uncertainties is related to the unfolding procedure, as explained in Chapter 12.7.
A systematic uncertainty can be defined as a two-sided systematic, where the systematically varied parameter is evaluated at two additional points besides the nominal value, and a one-sided systematic, where a single systematic variation is used. In case of two-sided systematic uncertainties, the two-point variations are referred to as an up and a down variation. In addition, a two-sided systematic uncertainty is defined as *symmetric*, if the absolute size of the up and down variations is identical and differs only by its sign, and is asymmetric otherwise. All one-sided systematic uncertainties are asymmetric by definition.
The impact of the theoretical and experimental systematic uncertainties on the measured variables m_{T}^{W} and $m_{\mathrm{T}}^{W} \otimes |\eta(e)|$ is discussed, where each systematic uncertainty is smoothed, in order to reduce statistical fluctuations, and two-sided systematic uncertainties are symmetrised unless stated otherwise. A standard smoothing procedure from the ROOT framework is applied, where statistical fluctuations are reduced by averaging over neighbouring bins. Importantly, the standard smoothing does not work for the $m_{\mathrm{T}}^{W} \otimes |\eta(e)|$ distribution. As a consequence, only fluctuations as a function of $|\eta(e)|$ are reduced for $m_{\mathrm{T}}^{W} \otimes |\eta(e)|$ and result into different sizes of the systematic uncertainties as a function of m_{T}^{W} and $m_{\mathrm{T}}^{W} \otimes |\eta(e)|$, especially in the $m_{\mathrm{T}}^{W} \in [150, 200]\,\mathrm{GeV}$ bin.
Since more than a hundred two-sided systematic uncertainties are considered and a substantial fraction of them is very small or negligible, only systematic uncertainties that induce a difference of more than 0.5% on the measured cross-section in at least one bin are discussed and presented in the following.

11.1 Theoretical systematic uncertainties

Theoretical systematic uncertainties are described in the following, where parameters required in the calculation of the SM prediction are varied. Different parameters are separately discussed, where the

1. ISR and FSR uncertainties,
2. factorisation and renormalisation scale uncertainties,
3. PDF uncertainties,

4. hard scattering uncertainties,
5. hadronisation uncertainties,
6. HDAMP uncertainties

are considered. Parameters are varied to estimate the systematic uncertainties either based on alternative MC samples, where a single parameter is varied, or based on the on-the-fly weights, where additional multiplicative weights are applied to the nominal sample. Whether a variation is obtained by the former or latter approach depends on the uncertainty.
The ISR and FSR accounts for additional radiations, where exemplarily a gluon is radiated by one of the two incoming quarks that produce the W boson in the ccDY process. A two-point systematic is provided as on-the-fly weights for each source of additional radiation.
The factorisation and renormalisation scale uncertainties are stored as on-the-fly weights for the nominal MC samples. An up and down variation of the factorisation and the renormalisation scale is obtained by recalculating the SM predictions, where each scale is varied by a factor of two. In total, seven combinations of $\mu_F \in [0.5, 1.0, 2.0]$ and $\mu_R \in [0.5, 1.0, 2.0]$ are taken into account, where the combinations $\mu_F = 0.5(2.0)$ and $\mu_R = 2.0(0.5)$ are not considered. The envelope of all combinations determines the final systematic uncertainty.
The nominal PDFs are associated with a corresponding error set providing the PDF uncertainties. In this thesis, the PDF uncertainty is obtained based on a hundred variations contained in the PDF error set. Every individual variation is evaluated and compared to the central value of the PDF. Evaluating the RMS of all variations allows to assign a single systematic uncertainty in the end.
The hard scattering and hadronisation uncertainty rely on alternative MC samples. The former is obtained by the replacement of the MC generator, where the difference of the distribution of the nominal and the alternative MC sample is taken as an uncertainty. Similarly, the replacement of the MC showering allows to determine a hadronisation uncertainty.
The HDAMP uncertainty relies on a variation of the POWHEG-specific HDAMP parameter, which determines the damping of radiation with high transverse momenta. Commonly, alternative MC samples are used for the estimation of the corresponding HDAMP uncertainty.

11.1.1 Signal process

The nominal signal MC, as outlined in Chapter 6.3, does not contain the variations required for the estimation of theoretical systematic uncertainties. For this reason, an alternative MC sample, referred to as POWHEG+HERWIG 7, has been generated. Its validation has been performed throughout this thesis as briefly discussed in Section 6.4. During the MC generation, the required on-the-fly weights for the variation of the renormalisation and factorisation scale as well as several modern PDFs were included. In addition, the alternative sample allows to define a hadronisation uncertainty. However, the systematic uncertainties corresponding to ISR and FSR and the HDAMP uncertainty are not covered.
Furthermore, two issues remain unsolved: First, the calculated cross-section obtained from the generation of the alternative MC sample is $10 - 11\%$ larger compared to the nominal signal MC sample. Subsequently, a $10 - 11\%$ difference at the truth and reconstructed distributions between the nominal and the alternative signal sample are observed. Second, unphysically large event weights were found, where too large weights per event and in the

weight normalisation result in non-continuous distributions.
Nevertheless, a first estimate of the theoretical systematic uncertainties corresponding to the factorisation and renormalisation scales as well as the hadronisation uncertainty are evaluated. A partial dataset, corresponding to the data recorded during the years 2015 and 2016, is considered.

In general, theoretical systematic uncertainties affect the fiducial level distribution and, as a consequence, the reconstructed level distribution changes as well. While usually only systematic variations at reconstructed level have to be considered, both levels of the signal MC are used as inputs to the unfolding, as described in Chapter 5. For this reason, the relative difference[1] at both levels has to be evaluated. While their relative differences are discussed in the following, a final systematic uncertainty for the theoretical uncertainties can only be assigned after the unfolding.

[1]The relative difference of two variables, x_1 and x_2, is calculated as $\frac{x_1 - x_2}{x_2}$.

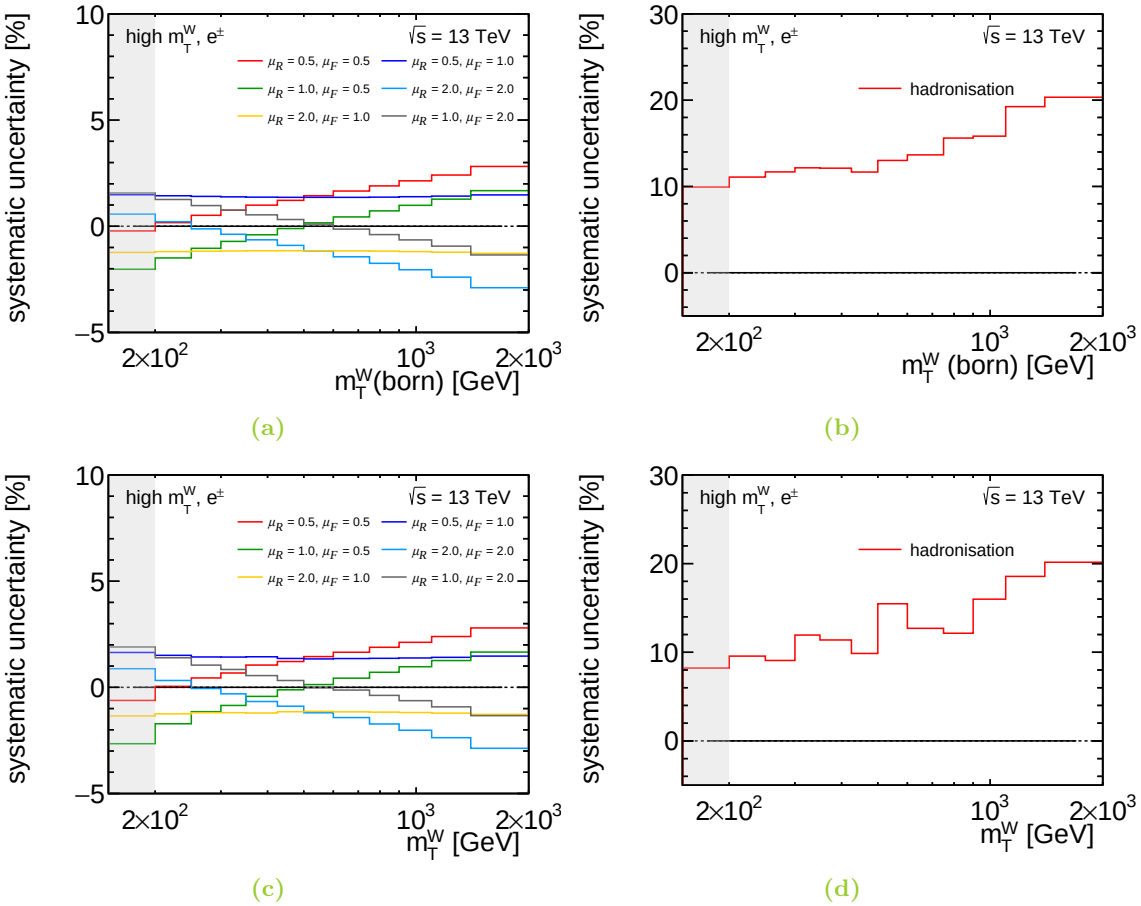

Figure 11.1: Distributions at fiducial level are shown in a) and b),while the distributions at reconstructed level are presented in c) and d). Relative difference of the systematic variation corresponding to the factorisation and renormalisation as well as hadronisation of the signal process as a function of m_{T}^W for the combination of the e^+ and e^- channel.

The relative differences as a function of m_{T}^{W} at fiducial and reconstructed level are shown in Figure 11.1. The relative differences corresponding to the factorisation and renormalisation scales are presented at fiducial level and at reconstructed level in Figure 11.1a and in Figure 11.1c, respectively. Since the relative difference between the nominal distribution and the systematically varied distribution of the POWHEG+HERWIG 7 is calculated, no offset due to the different cross-section is expected.
Overall, a very similar behaviour of these distributions is found: On one hand, an approximately flat offset is observed for the $\mu_R = 2.0, \mu_F = 1.0$ and $\mu_R = 0.5, \mu_F = 1.0$ variation. On the other hand, linear shape differences are found in case of the additional scale variations, where variations with $\mu_F = 0.5$ increase and variations with $\mu_F = 2.0$ decrease in $m_{\mathrm{T}}^{W} \in [150, 2000]\,\mathrm{GeV}$.
In Figure 11.1b and Figure 11.1d, the relative difference between the distribution of the nominal signal MC and the alternative MC, corresponding to the hadronisation systematic uncertainty are shown at fiducial and reconstructed level. Due to the cross-section difference, an expected $10-11\%$ offset is visible at both levels. Neglecting the offset, an approximately linear shape difference as a function of m_{T}^{W} is observed at both levels. Deviations from the approximately linear shape can be found, which are substantial for $m_{\mathrm{T}}^{W} \in [250, 900]$ GeV at reconstructed level. In contrast to the relative differences corresponding to the factorisation and renormalisation scales, the fiducial and reconstructed distributions for the hadronisation are less similar.
The relative differences as a function of $m_{\mathrm{T}}^{W} \otimes |\eta(e)|$ are shown for completeness in Appendix E, where a flat $|\eta(e)|$ distribution in $m_{\mathrm{T}}^{W} \in [150, 425]\,\mathrm{GeV}$ and an increasing difference for increasing $|\eta(e)|$ in $m_{\mathrm{T}}^{W} \in [425, 2000]\,\mathrm{GeV}$ can be found. In addition, even larger fluctuations are observed.
As mentioned above, the fiducial and reconstructed distributions of the signal process enter the unfolding procedure and, for this reason, the impact on the cross-section can only be obtained after the unfolding as described in Chapter 12.6.

11.1.2 $t\bar{t}$ process

In contrast to the signal MC, all required variations of the theoretical systematic uncertainties are available for the $t\bar{t}$ process and are discussed in the following.
First of all, the estimation of the uncertainties corresponding to the PDF as well as the ISR and FSR require an additional step before their final evaluation. For this reason, these uncertainties are discussed first. The nominal PDF of the $t\bar{t}$ MC is `NNPDF3.0NLO`, where additionally a set of 100 variations is available. Each single PDF variation as a function of the measured variables is represented by one of the red distributions in Figure 11.2a and Figure 11.2b. The deviations of the varied PDFs from the nominal PDF extend up to 20% as a function of m_{T}^{W} and to more than 40% in one bin of the $m_{\mathrm{T}}^{W} \otimes |\eta(e)|$ distribution. In both cases, the RMS of each set of PDF variations is calculated and, in addition, shown as the dark blue distribution. This final PDF uncertainty will be discussed further in the following.
Then, the systematic uncertainty corresponding to the factorisation and renormalisation scale is prepared by evaluating all combinations, as shown in Figure 11.2c and Figure 11.2d, for the measured variables. It can be observed that all combinations are small for low m_{T}^{W}. Variations with $\mu_R = 2.0$ increase until their maximum of about 8% at high m_{T}^{W}, whereas the

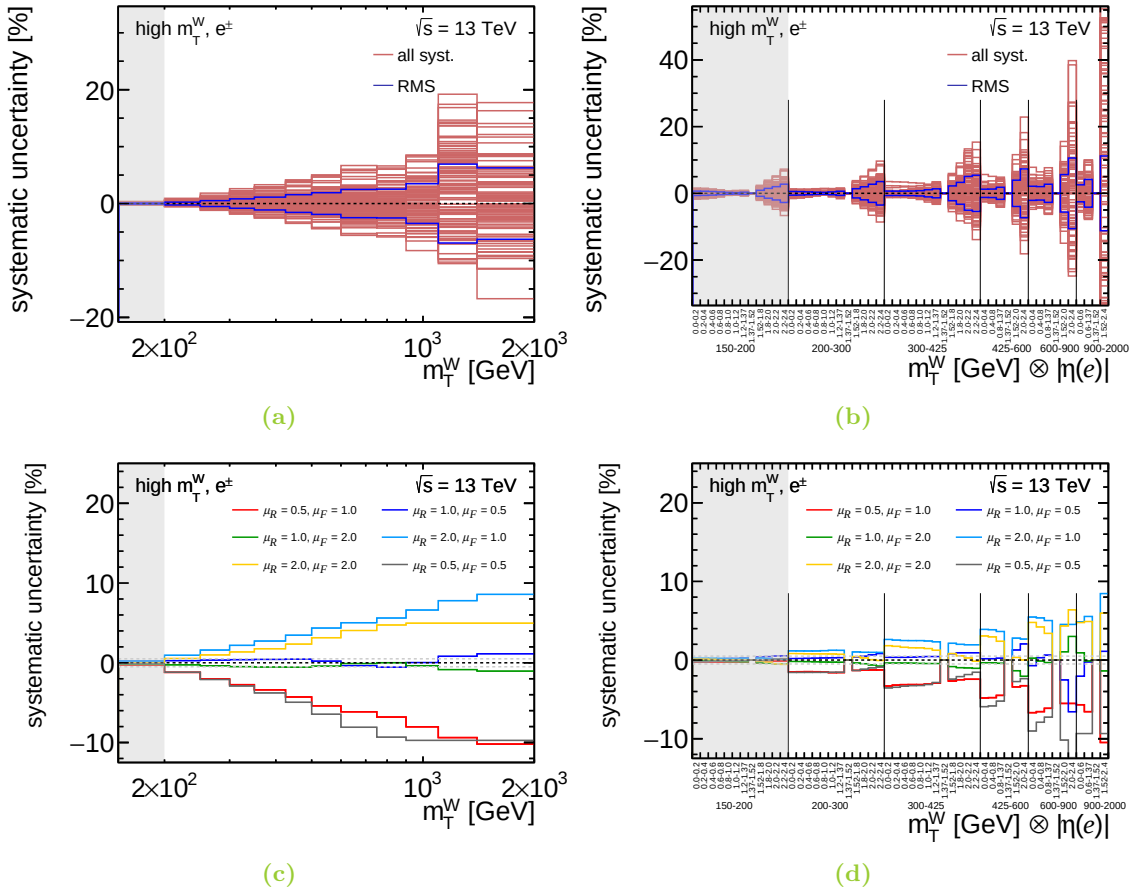

Figure 11.2: Preparation of the PDF as well as factorisation and renormalisation systematic uncertainties corresponding to the $t\bar{t}$ background as a function of the measured variables for the combination of the e^+ and e^- channel. All PDF variations and their RMS are visualised in a) and b), while all combinations of the μ_R, μ_F scales are shown in c) and d).

$\mu_R = 0.5$ variations decrease until their largest difference of about -8%. Since the envelope is reasonably defined by the $\mu_R = 0.5, \mu_F = 0.5$ and the $\mu_R = 2.0, \mu_F = 1.0$ variation, these are added as a single two-sided systematic uncertainty with an up and a down variation instead of using the envelope in the following.

As mentioned before, the HDAMP, hard scattering and hadronisation systematic uncertainties are based on alternative MC samples. While the POWHEG specific parameter is varied from HDAMP $= 1.5m_t$ to HDAMP $= 3.0m_t$, the POWHEG generator is exchanged with Madgraph and the PYTHIA 8 showering is replaced with HERWIG 7. Three additional sets of MC samples are used. As a side note, these alternative MC samples are generated using the AF2 detector simulation. In order to obtain the systematic uncertainty on the nominal $t\bar{t}$ sample with FS, the systematically varied alternative MC samples are compared to the nominal $t\bar{t}$ sample with AF2 and the resulting relative difference is transferred to the nominal $t\bar{t}$ sample with FS.

All theoretical systematic uncertainties corresponding to the $t\bar{t}$ MC as a function of the measured variables are presented in Figure 11.3. Two representations of the uncertainties

are provided: First, the uncertainties with respect to the nominal distribution of the $t\bar{t}$ MC, shown in Figure 11.3a and Figure 11.3c. Second, the uncertainties are normalised to the difference of data and the predicted background contributions, which provides a measure that is proportional to the systematic uncertainty on the measured cross-section. This is visualised in Figure 11.3b and Figure 11.3d.
An increasing uncertainty as a function of m_{T}^{W} is observed in Figure 11.3a and Figure 11.3c. Most variations can be found within $\pm 15\,\%$, where only the HDAMP uncertainty extends up to $43\,\%$. A relative impact on the cross-section of $2\,\%$ at the largest is estimated from the representation in Figure 11.3b and Figure 11.3d. In addition, the shape and the sign of the systematic uncertainties change, as a consequence of the normalisation. The change of the sign enters due to the subtraction, whereas the different shape is characterised by the size of the nominal $t\bar{t}$ contribution relative to the amount of data.

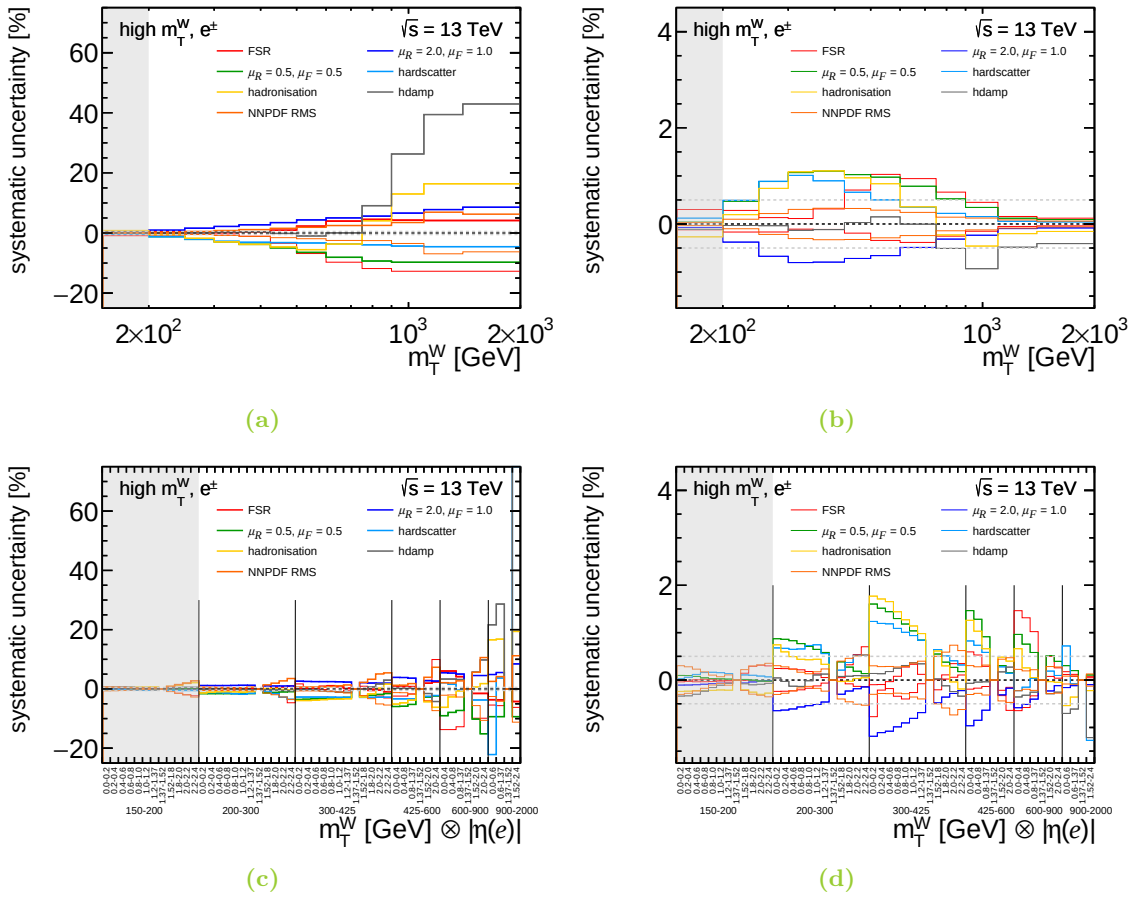

Figure 11.3: Theoretical systematic uncertainties corresponding to the $t\bar{t}$ background as a function of the measured variables, m_{T}^{W} and $m_{\mathrm{T}}^{W} \otimes |\eta(e)|$ for the combination of the e^+ and e^- channel. While the systematic uncertainties corresponding to the $t\bar{t}$ MC are shown in a) and c), the systematic uncertainty is normalised to the difference of data and the predicted background contributions in b) and d). The dashed grey line represents the 0.5% threshold.

11.2 Experimental systematic uncertainties

Another source of uncertainties accounts for the experimental setup, where the detector architecture itself, but also the measurement of quantities such as the energy of particles within the detector are considered. These uncertainties are summarised as experimental systematic uncertainties.
The systematic uncertainties related to the missing transverse momentum, the electron, the jets as well as the pile up and luminosity uncertainty at reconstructed level are briefly discussed.

11.2.1 Soft track term of the missing transverse momentum

The missing transverse momentum, as introduced in Chapter 7.5, depends on the calibrated momenta of considered particles and the additional soft term. While systematic uncertainties related to the former are covered by the systematic uncertainties associated to each different particle, for example the energy of the electron for the electron $E_{\mathrm{T}}^{\mathrm{miss}}$ term, and reflected by a change of the $E_{\mathrm{T}}^{\mathrm{miss}}$ distribution with respect to the nominal distribution, systematic uncertainties related to the soft term have to be considered additionally and are described in the following.
Three systematic uncertainties are associated to the $E_{\mathrm{T}}^{\mathrm{miss}}$ soft term, where one two-sided scaling systematic uncertainty, *SoftTrk Scale*, and two one-sided resolution systematics, *SoftTrk Reso Para* and *SoftTrk Reso Perp*, are provided. The systematic uncertainties are obtained by the application of either a scaling or a smearing in the MC sample. The *SoftTrk Scale* systematic uncertainty relies on a scaling of the transverse momenta of the considered tracks. In contrast, the two resolution systematic uncertainties consist of a smearing of the soft term magnitude in parallel, denoted *Para*, or perpendicularly, denoted *Perp*, to the transverse momenta of the considered tracks.
The systematic uncertainties corresponding to the soft term of the $E_{\mathrm{T}}^{\mathrm{miss}}$ as a function of the measured variables are shown in Figure 11.4. Deviations between each systematic

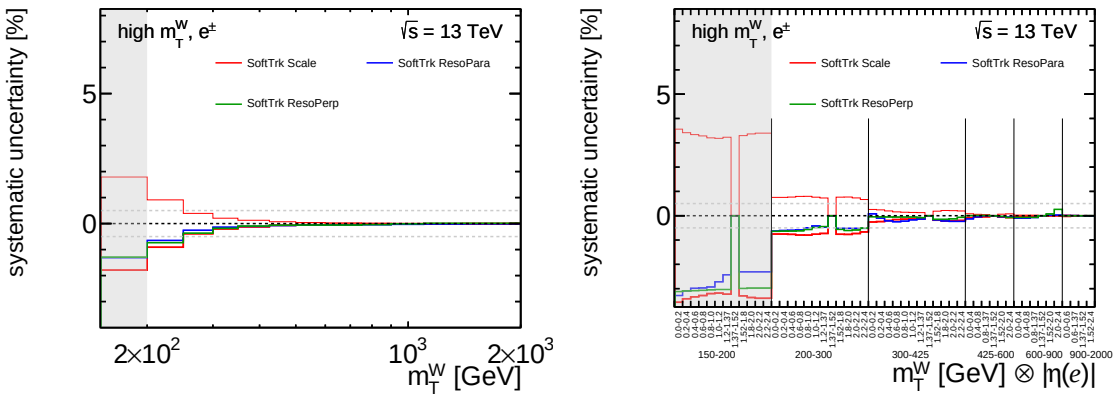

Figure 11.4: Systematic uncertainty of the missing transverse momentum $E_{\mathrm{T}}^{\mathrm{miss}}$ as a function of the measured variables, m_{T}^{W} and $m_{\mathrm{T}}^{W} \otimes |\eta(e)|$ for the combination of the e^{+} and e^{-} channel. The dashed grey line represents the 0.5% threshold.

uncertainty and the nominal distribution are displayed, where the largest uncertainty of approximately 3.5% is found in the lowest m_{T}^{W} bin of the $m_{\mathrm{T}}^{W} \otimes |\eta(e)|$ distribution and decreases in bins referring to larger m_{T}^{W}. Consequently, the largest uncertainty in the measurement range above $m_{\mathrm{T}}^{W} = 200\,\mathrm{GeV}$ is smaller, where the largest deviation is up to 1% in the $m_{\mathrm{T}}^{W} \otimes |\eta(e)|$ distribution. Overall, an approximately flat deviation as a function of $|\eta(e)|$ can be observed.

11.2.2 Electron energy scale

The systematic uncertainties of the energy calibration are subdivided into the variation of the scale and the resolution. The former will be discussed in this paragraph, while the next paragraph is dedicated to the latter. Both sources of uncertainties as a function of the transverse energy and pseudorapidity of the electron are provided in the same uncertainty model, named `FULL_ETACORRELATED_v1`, which is centrally provided by the e/γ (EG) performance group of the ATLAS collaboration.
The `FULL_ETACORRELATED_v1` uncertainty model covers variations in all steps of the electron energy calibration and contains 21 two-sided systematic uncertainties associated to the energy scale of the electron, where four uncertainties contribute with more than 0.5% in at least one bin of the measured variables. These four systematic uncertainties as a function of the measured variables are shown in Figure 11.5. The largest systematic uncertainty associated to the energy scale is the `L2GAIN` uncertainty corresponding to the non-linearity in the cell energy measurement at the second layer of the electromagnetic calorimeter. An increasing uncertainty as a function of the transverse mass with up to $\pm 2.5\%$ in the last m_{T}^{W} bin is found. In the $m_{\mathrm{T}}^{W} \otimes |\eta(e)|$ distribution an additional dependency is observed, where the uncertainty as a function of $|\eta(e)|$ increases in the range of $|\eta(e)| \in [0.60, 1.37]$. The other presented systematic uncertainties are as well increasing as a function of m_{T}^{W} up to 1% over the whole range. In contrast to the `L2GAIN` uncertainty, their size increases as a function of $|\eta(e)|$ in $|\eta(e)| \in [1.52, 2.4]$. For $m_{\mathrm{T}}^{W} \otimes |\eta(e)| = [300, 425]\mathrm{GeV} \otimes [2.2, 2.4]$, the largest uncertainty is the `L1GAIN` uncertainty, which corresponds to same source of systematic uncertainty as the

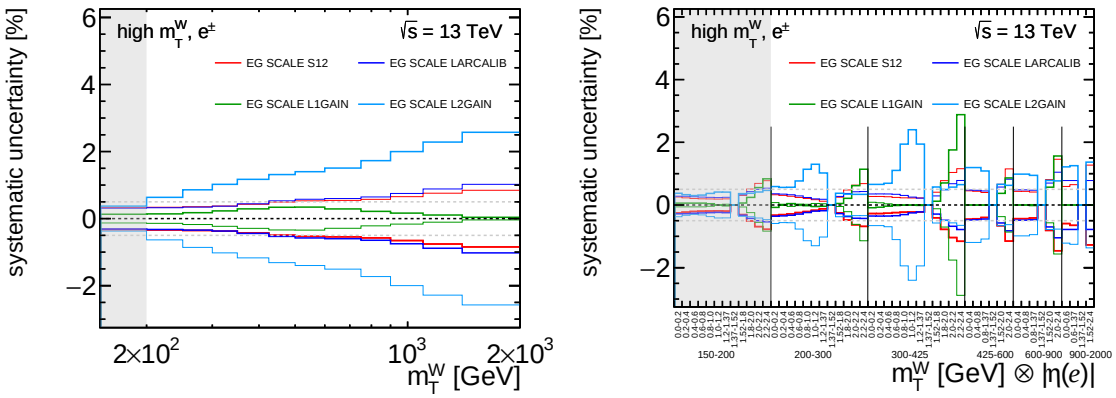

Figure 11.5: Systematic uncertainty associated to the energy scale of electrons as a function of the measured variables, m_{T}^{W} and $m_{\mathrm{T}}^{W} \otimes |\eta(e)|$ for the combination of the e^{+} and e^{-} channel. The dashed grey line represents the 0.5% threshold.

L2GAIN uncertainty, but in the first layer of the electromagnetic calorimeter. Further details of every single systematic uncertainty and its estimation can be found in Reference [96].

11.2.3 Electron energy resolution and photon energy scale

The systematic uncertainties corresponding to the energy resolution and photon scale are provided by the EG performance group as well. In total, five two-sided systematic uncertainties for the photon energy scale and seven two-sided systematic uncertainties for the electron energy resolution can be found in the FULL_ETACORRELATED_v1 uncertainty model. Their impact on the cross-section has been studied and is found to be smaller than 0.5%.

11.2.4 Electron scale factor

The efficiency corrections, as introduced in Chapter 7.2.4, for the electrons are estimated based on the tag-and-probe method applied to $Z \to \ell\ell$ decays. Systematic uncertainties of the electron SF are obtained by the variation of the tag-and-probe method, where for example the event selection required throughout the method is varied. For this thesis, the so-called TOTAL uncertainty model is chosen, which is centrally provided in ATLAS. The model consists of one two-sided systematic uncertainty for each electron SF, corresponding to the trigger, isolation, identification and reconstruction efficiency. For the additional charge misidentification SF, two two-sided systematic uncertainties are provided, where the statistical and systematic uncertainties are separated. The considered systematic uncertainties corresponding to the electron SF are presented in Figure 11.6. The systematic uncertainty associated to the electron isolation SF reaches its largest value of up to about 3% for $m_{\mathrm{T}}^{W} \in [600, 900]$GeV and $|\eta(e)| \in [2.0, 2.4]$. For the electron identification SF, a systematic uncertainty of 1% is observed in the lowest m_{T}^{W} bin that increases to 4.5% for increasing m_{T}^{W}. In addition, both uncertainties increase as a function of $|\eta(e)|$. For this reason, the uncertainty reaches 5% in single $|\eta(e)|$ bins.

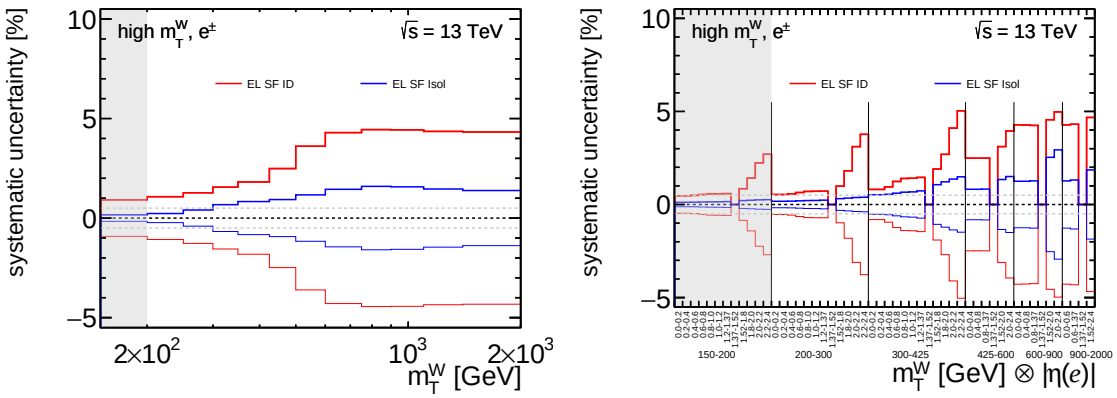

Figure 11.6: Systematic uncertainty associated to the electron scale factor as a function of the measured variables, m_{T}^{W} and $m_{\mathrm{T}}^{W} \otimes |\eta(e)|$ for the combination of the e^+ and e^- channel. The dashed grey line represents the 0.5% threshold.

It will be shown, that the largest systematic uncertainty in the region of $m_{\mathrm{T}}^{W} > 500\,\mathrm{GeV}$ is associated to the electron identification SF. As a consequence, a more complex uncertainty model is recommended, since the systematic uncertainties in the `TOTAL` uncertainty model are expected to be overestimated with respect to more complex uncertainty models. This study is not part of this thesis, where the presented systematic uncertainty for the electron identification SF should be considered as the upper limit.

11.2.5 Jet energy resolution

The systematic uncertainties associated to the jet energy are grouped into scale and resolution uncertainties as well, which are provided by the Jet/$E_{\mathrm{T}}^{\mathrm{miss}}$ group of the ATLAS collaboration. The `SimpleJER` uncertainty model providing eight variations is chosen in this thesis. Although no jet requirements are explicitly demanded in the event selection, the evaluation of the JER systematic uncertainty is required, because jets are used in the calculation of the missing transverse momentum. In addition, jets are considered in the overlap removal.
In Figure 11.7, the considered systematic uncertainties corresponding to the JER are presented. In the m_{T}^{W} and $m_{\mathrm{T}}^{W} \otimes |\eta(e)|$ distribution, the largest relative impact of up to 5.5% is observed for $m_{\mathrm{T}}^{W} \in [150 - 200]\mathrm{GeV}$ and $|\eta(e)| \in [2.2, 2.4]$. The JER systematic uncertainties decrease as a function of m_{T}^{W} and are smaller than 0.5% for $m_{\mathrm{T}}^{W} > 300\,\mathrm{GeV}$. As a result, these uncertainties are only substantial in the additional low m_{T}^{W} bin and already below 1% in the first bin of the actual measurement.

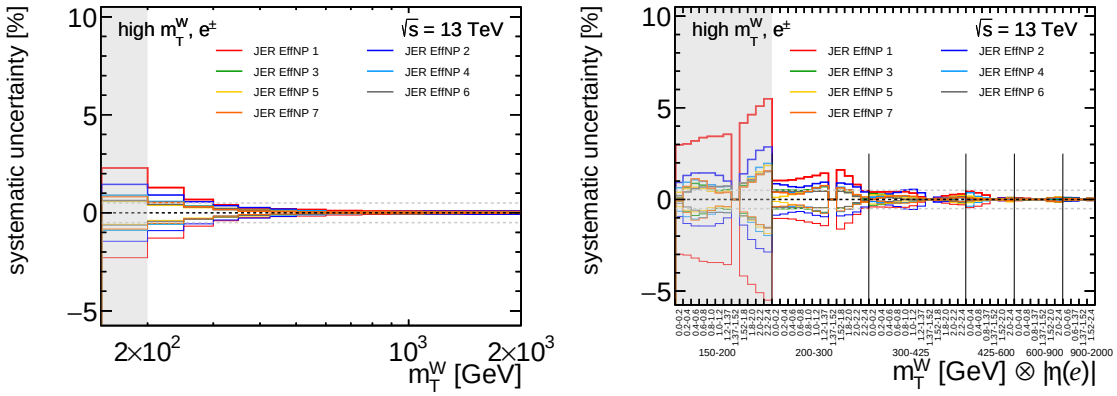

Figure 11.7: Systematic uncertainty of the jet energy resolution as a function of the measured variables, m_{T}^{W} and $m_{\mathrm{T}}^{W} \otimes |\eta(e)|$ for the combination of the e^{+} and e^{-} channel. The dashed grey line represents the 0.5% threshold.

11.2.6 Jet energy scale

For the jet energy scale, the so-called `Category Reduction` uncertainty model provided by the Jet/$E_{\mathrm{T}}^{\mathrm{miss}}$ group offers a set of 28 uncertainties. The systematic uncertainties associated to the jet energy scale, fulfilling the 0.5% threshold, are presented in Figure 11.8, where the relative impact of the uncertainties is largest as a function of $|\eta(e)|$ in the low m_{T}^{W} bin. A relative impact of the systematic uncertainty as a function of m_{T}^{W} on the cross-section of less

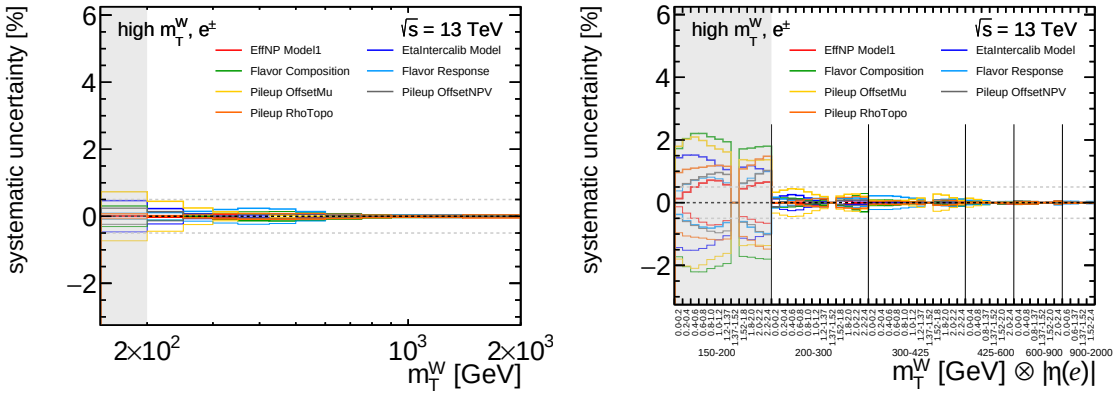

Figure 11.8: Systematic uncertainty of the jet energy scale as a function of the measured variables, m_{T}^{W} and $m_{\mathrm{T}}^{W} \otimes |\eta(e)|$ for the combination of the e^+ and e^- channel. The dashed grey line represents the 0.5% threshold.

than 0.5% for most bins is observed. In contrast, systematic uncertainties of up to 2.2% are found as a function of $m_{\mathrm{T}}^{W} \otimes |\eta(e)|$. It can be concluded that the jet energy scale systematic uncertainties are small in the region of the measurement $m_{\mathrm{T}}^{W} > 200\,\mathrm{GeV}$, whereas a relative impact of several percent as a function of $m_{\mathrm{T}}^{W} \otimes |\eta(e)|$ can be observed below.

11.2.7 Pile-up

The pile-up distribution at reconstructed level is achieved by the application of a pile-up reweighting SF, which adjusts the pile-up distribution of the MC sample to the pile-up distribution observed in data events. The pile-up reweighting tool, centrally provided by the ATLAS collaboration, can be used to obtain the nominal weight and the associated systematic uncertainty. In Figure 11.9, the systematic uncertainty for the pile-up reweighting SF as a function of the measured variables is shown. While the largest uncertainty of up

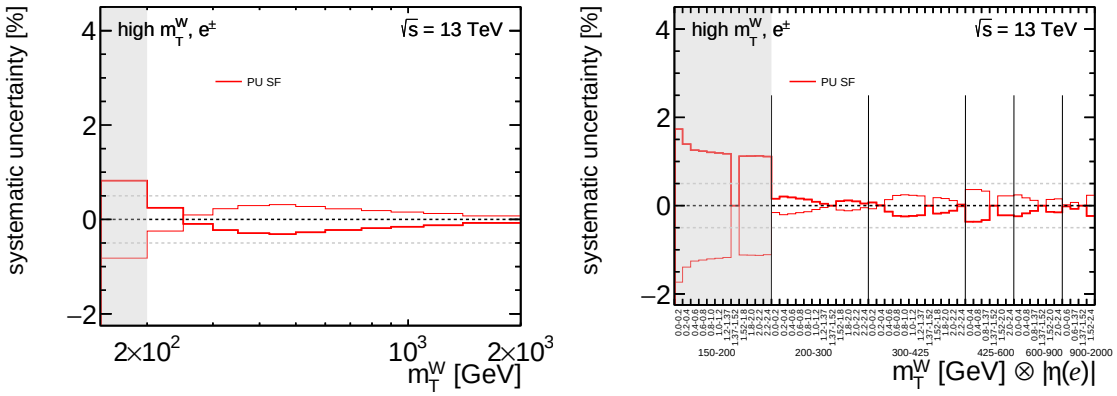

Figure 11.9: Systematic uncertainty associated to the pile up reweighting as a function of the measured variables, m_{T}^{W} and $m_{\mathrm{T}}^{W} \otimes |\eta(e)|$ for the combination of the e^+ and e^- channel. The dashed grey line represents the 0.5% threshold.

to 1.75% can be observed for $m_{\mathrm{T}}^{W} \otimes |\eta(e)| \in [150, 200]\mathrm{GeV} \otimes [0.0, 0.2]$, no relative impact of more than 0.5% is found in the region of $m_{\mathrm{T}}^{W} > 200\,\mathrm{GeV}$. As a result, the relative impact of the pile-up reweighting systematic on the measurement is almost negligible.

11.2.8 Luminosity

As outlined in Chapter 6.1, the integrated luminosity that corresponds to the analysed dataset is $\mathcal{L} = 139.0 \pm 2.4\ \mathrm{fb}^{-1}$, which can be transformed into an uncertainty of 1.7% as reported in Reference [52]. The integrated luminosity has to be considered in addition to the reported systematic uncertainties, as presented in Chapter 13.

11.2.9 Experimental systematic uncertainties of the background processes

Besides the signal process, each real electron background is affected by the experimental systematic uncertainties as well. Since the amount of background events is smaller compared to signal events, a reduced relative impact of the experimental systematic uncertainties from the background processes is expected.
Nevertheless, the relative impact of the experimental systematic uncertainties from the $t\bar{t}$ background, which provides the dominant background contribution as described in Section 10, was evaluated at an earlier stage of the measurement. At this stage, only the measurement of the single-differential cross-section as a function of m_{T}^{W} has been studied. It was shown, that the relative impact of the systematic uncertainties is at or below 0.5%. Consequently, it has been decided that these uncertainties are not part of the cross-section measurement. Nevertheless, a reinvestigation of the experimental uncertainties for the $t\bar{t}$ background remains important, because the uncertainties per bin are expected to be larger in case of the double-differential cross-section measurement as a function of $m_{\mathrm{T}}^{W} \otimes \eta$, which are not evaluated on the timescale of this thesis.

12 Unfolding

In the following, it is explained how the single- and double-differential cross-sections at the fiducial level, i.e. after the removal of detector effects that refer to the reconstruction, are obtained by unfolding the measured data. While the theoretical details of the unfolding procedure, which is IBU, have been discussed in Chapter 5, this chapter focuses on the application of the theoretical unfolding concepts on this measurement. In addition, the estimation of the statistical and systematic uncertainties on the unfolded cross-section are presented and an unfolding systematic uncertainty is discussed.

12.1 Iterative Bayesian Unfolding

Technically, the IBU is implemented via `RooUnfold` [97]. In this thesis, a custom interface to the `RooUnfold` package is used, where the reconstructed and truth level distribution of the measured variable as well as the response matrix have to be provided as inputs. Furthermore, the correction factors are implicitly defined as an input, since they are calculable from the three former input distributions.
While the reconstructed distribution of the measured variable is taken from the comparisons of data and background prediction after the signal region selection, the truth level distribution of the measured variables is obtained from the W MC after the fiducial selection. The following subsections are dedicated to the description of the response matrix, the efficiency ϵ_j and the in-smearing f_{in}^i, required for the unfolding according to Equation 5.8 in Chapter 5. In the end, the advantages of an unfolding with an additional bin, a so-called *shadow bin*, are discussed.

12.1.1 Response matrix

The iterative procedure in the unfolding is based on the response matrix R, where the migration of events at fiducial level and at reconstructed level is displayed. For this reason, only events fulfilling both selections enter the response matrix. Importantly, the migration of events e.g. generated below $m_T^W < 150\,\text{GeV}$ and reconstructed after the signal region selection are not part of the response matrix. The same holds true for events generated within the fiducial level but not reconstructed after the signal region selection. Two correction factors are used in order to account for each source of events that are not covered in the response matrix, which will be explained in the following subsections.
The response matrix is calculated based on the W MC only, where the x-axis corresponds to the distribution at reconstructed level and the y-axis to the distribution at fiducial level. After the events are filled, a normalisation and scaling into percent for each truth level bin is performed. The response matrix as a function of the transverse mass of the W boson m_{T}^W

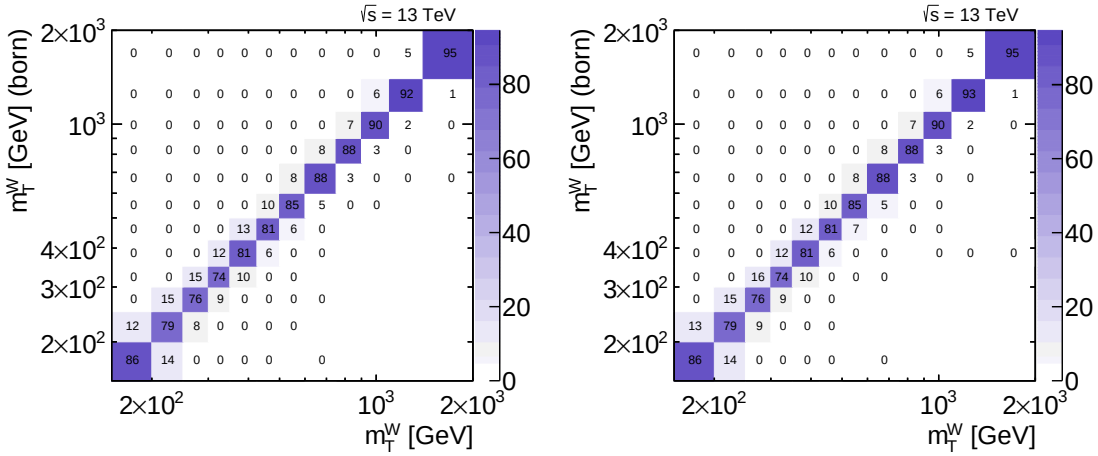

Figure 12.1: Response matrix R for the measured variable m_{T}^{W} in the measurement binning for the a) e^- and b) e^+ channel. The normalisation is performed for each truth level bin, where under- and overflow bin are not taken into account. Afterwards, the normalised values are scaled to percent.

in the e^+ and e^- channels are presented in Figure 12.1.
In comparison to the migration matrix, as discussed in Chapter 8.3.2, the values on the diagonal increase especially for low m_{T}^{W}. The difference to the migration matrix is expected, due to the application of the fiducial selection for the response matrix, where all events from below $m_{\mathrm{T}}^{W} = 150\,\mathrm{GeV}$ are not considered. At the diagonal, the smallest value of 74% is visible in the third measurement bin, $m_{\mathrm{T}}^{W} \in [300, 350]\,\mathrm{GeV}$, while the largest value of 95% can be found in the last m_{T}^{W} bin. Furthermore, the only substantial migration occur with respect to the neighbouring bin in m_{T}^{W} and are below a percent in all other bins. A probability, displayed as a zero in the matrix corresponds to a number which is rounded to zero, whereas no entry refers to a probability of exactly zero percent.
Differences for the response matrix in the e^+ and e^- channel are very small, where deviations of 1% at most are observed. Importantly, the rounding induces an effect of 1% as well even if the difference might be much smaller.
In Figure 12.2, the response matrix as a function of $m_{\mathrm{T}}^{W} \otimes |\eta(e)|$ in the e^- channel is shown. The response matrix for the e^+ channel is very similar and for this reason, it is shown in Figure F.3 in Appendix F. The visualisation for the double-differential cross-section measurement, as discussed for Figure 10.7, is technically required. Since a single response matrix has to be provided to the `RooUnfold` package, only this representation allows to display the migrations across m_{T}^{W} and $|\eta(e)|$ in the same distribution. As a side note, although the response matrix is shown by a two-dimensional distribution, in fact a four-dimensional representation of the migrations is reflected. The measurement binning, as introduced in Chapter 8 is used. In Figure 12.2, the $m_{\mathrm{T}}^{W} \otimes |\eta(e)|$ distribution corresponding to the reconstructed level at the x-axis and corresponding to the born level after the fiducial selection at the y-axis is shown. The labelling of the $|\eta(e)|$ bin is displayed on the respective axis and subsequently the labelling of the m_{T}^{W} bins. Each m_{T}^{W} bin is separated from each other by vertical and perpendicular lines.

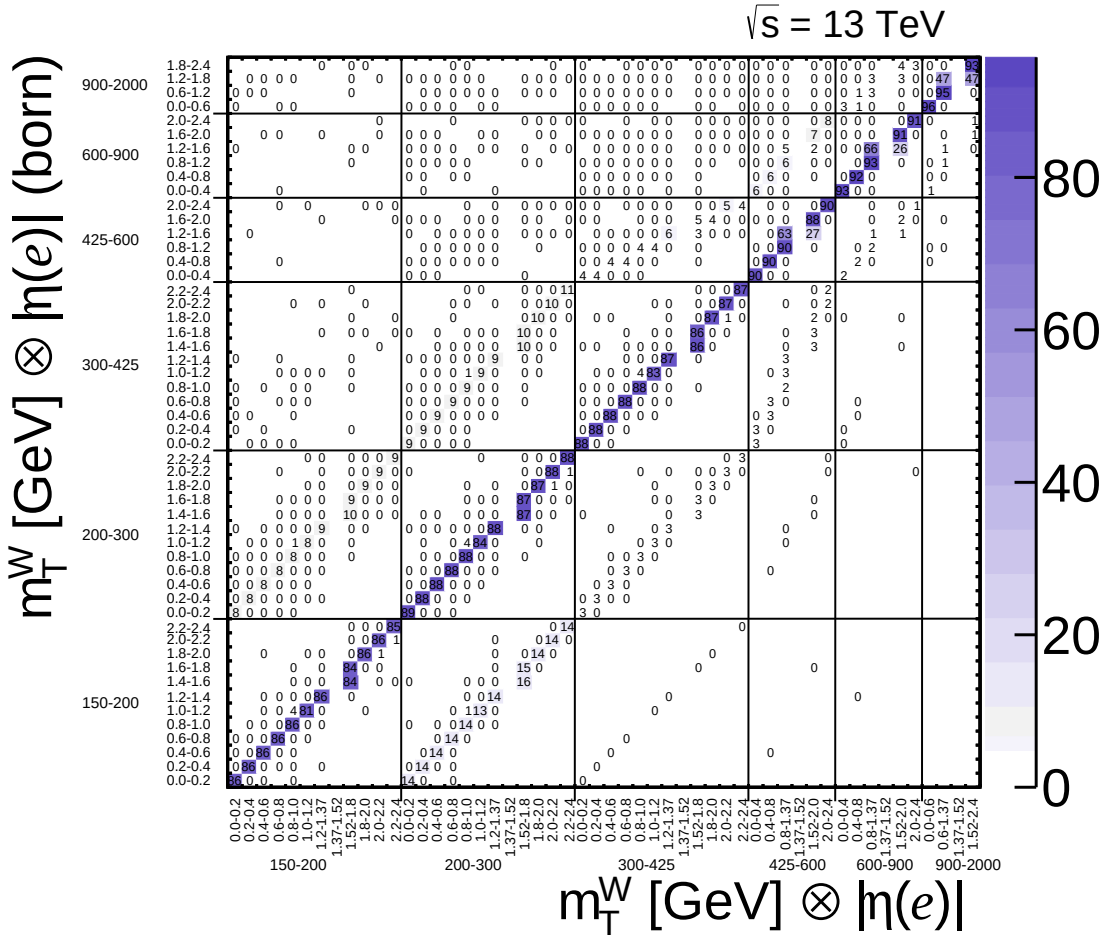

Figure 12.2: Response matrix R for the measured variable $m_{\mathrm{T}}^{W} \otimes |\eta(e)|$ in the measurement binning for the e^- channel. The normalisation for each truth level bin is scaled to percent, where the under- and overflow bins are not taken into account in the normalisation.

In this representation, events migrating in $|\eta(e)|$ can be found in the *squares* that arise from the combination of vertical and perpendicular lines corresponding boundaries of the m_{T}^{W} bins. For example, an event generated at born level in $m_{\mathrm{T}}^{W} \in [200, 300]$ in $|\eta(e)| \in [1.0 - 1.2]$ is reconstructed with a probability of 4% in the lower $|\eta(e)|$ bin and 88% in the same $|\eta(e)|$ bin. Overall, the migrations across $|\eta(e)|$ are very small.
Furthermore, the migrations of events across m_{T}^{W} are found for the comparison of certain $|\eta(e)|$ bins in one specific *square* and e.g. a neighbouring *square*. For example, an event generated at born level in $m_{\mathrm{T}}^{W} \in [200, 300]$ GeV and in $|\eta(e)| \in [0.0 - 0.2]$ is reconstructed with a probability of 8% in the lower m_{T}^{W} bin, 89% in the same m_{T}^{W} bin and 3% in a higher m_{T}^{W} bin. As a result, the observed off-diagonals in each of the neighbouring *squares* correspond to the migration across m_{T}^{W}, where a similar behaviour as in Figure 12.1 is found. Finally, a deviation from the otherwise mostly diagonal response matrix is observed, which originates from the different binning at reconstructed level, where the transition region between the barrel and endcap is vetoed, and the fiducial level. While events generated in

the transition region are reconstructed in the neighbouring bin at higher pseudorapidities for the first three m_{T}^{W} bins, a split into bins with a lower and higher absolute value of the pseudorapidity for the later three m_{T}^{W} bins is observed. The different behaviour originates from the interplay of the $|\eta(e)|$ bin size and the relative location of the transition region, i.e. can be explained by the chosen binning at reconstructed and fiducial level only.

12.1.2 Correction factors: efficiency and acceptance

Two binned correction factors are applied once in the method of IBU, i.e. they are not entering the iterative procedure. Both correction factors are estimated using the W MC only. The first factor, f_{in}^{i}, referred to as *in-smearing correction* is used in order to correct the reconstruction level distribution. Since only events that pass the fiducial and signal region selection enter the response matrix, the in-smearing corrects for the amount of events that *smear* into the measurement range, i.e. in particular on-shell W bosons with a true mass of approximately 80 GeV that are reconstructed with $m_{\mathrm{T}}^{W} > 150\,\mathrm{GeV}$. The correction factor is defined as

$$f_{in}^{i} = \frac{N_{reco \wedge fiducial}^{i}}{N_{reco}^{i}}\,, \tag{12.1}$$

where the number of all events per bin i which fulfil the fiducial and signal region selection, $N_{reco \wedge fiducial}^{i}$, is divided by the number of all events at reconstructed level in each bin i, N_{reco}^{i}.
The in-smearing correction in the binning for the single- and double-differential cross-sections, including the additional low $m_{\mathrm{T}}^{W} \in [150, 200]$ GeV bin, are presented in Figure 12.3. The highest correction is visible in the additional low m_{T}^{W} bin across all distributions and charges. The fraction of events that smears from outside into the measurement range is described by $1 - f_{in}^{i}$. Roughly 60% of events smear into the low m_{T}^{W} bin, whereas the fraction decreases to approximately 15% in the first measured m_{T}^{W} bin and approaches zero as a function of m_{T}^{W}. This is expected, because the low m_{T}^{W} region is affected by events smearing from below $m_{\mathrm{T}}^{W} = 150\,\mathrm{GeV}$ in the measurement range. The effect has a similar size for the e^{+} and e^{-} channel.
Another effect is visible for $m_{\mathrm{T}}^{W} > 700\,\mathrm{GeV}$, where a slight decrease (increase) of the correction factor is visible for the e^{-} (e^{+}) channel. This trend originates from the irreducible charge-misidentification in the reconstruction process, where the opposite charge at reconstructed level with respect to the charge at generated level of the electron is measured. This effect increases for electrons with very high transverse momentum $p_{\mathrm{T}}(e)$, because the tracks are less bend in the magnetic field and are misidentified more easily. In a way, the charge-misidentification can be understood as another source of in-smearing events, where events are not smeared across m_{T}^{W} but across the electrons charge.
The in-smearing correction as a function of $m_{\mathrm{T}}^{W} \otimes |\eta(e)|$ in the measurement binning at reconstructed level shows the same trend discussed for m_{T}^{W}, where the additional corrections as a function of $|\eta(e)|$ can be investigated. As a result, the correction factor as a function of $|\eta(e)|$ is flat, i.e. no strong dependency is observed.
Finally, it should be noted that the in-smearing corrections of zero at $|\eta(e)| \in [1.37, 1.52]$ are artificially introduced, because these bins are empty in the denominator and numerator.

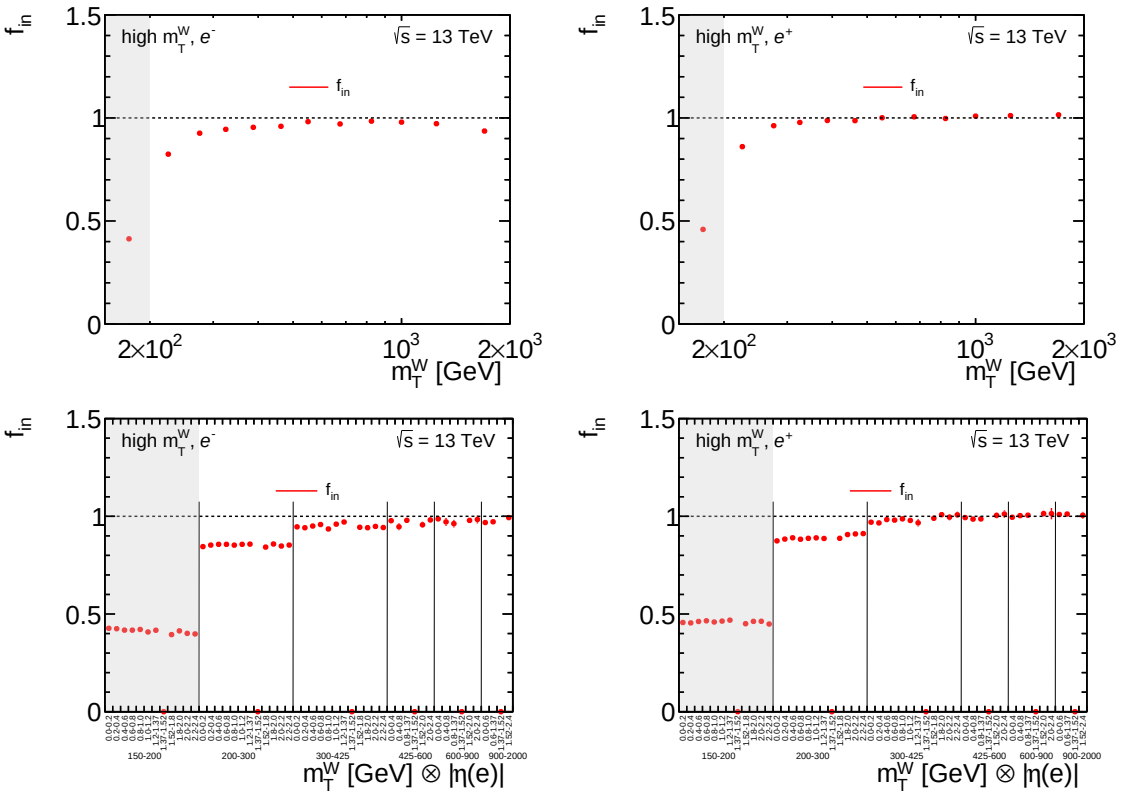

Figure 12.3: The in-smearing correction, f_{in}^i, per bin i of the reconstructed level distribution as a function of the transverse mass of the W boson m_{T}^W and the absolute value of the pseudorapidity and transverse mass $m_{\mathrm{T}}^W \otimes |\eta(e)|$ separated into the e^+ and e^- channel in the measurement binning.

The second factor is the efficiency ϵ_j, which is applied to the truth level distribution. The correction targets events that are available on truth level, i.e. have been generated in the MC sample, but not on the reconstructed level, e.g. due to inefficiencies in the reconstruction process. The efficiency is defined as

$$\epsilon_j = \frac{N^j_{reco \wedge fiducial}}{N^j_{fiducial}}\,, \tag{12.2}$$

where in each bin j of the truth level distribution, the number of all events passing the fiducial and signal region selection, $N^j_{reco \wedge fiducial}$, is divided by the number of events passing the fiducial selection $N^j_{fiducial}$.
In Figure 12.4, the efficiency ϵ_i as a function of the transverse mass m_{T}^W and the transverse mass and the absolute value of the pseudorapidity $m_{\mathrm{T}}^W \otimes |\eta(e)|$ is shown. Here, the fiducial level binning is used, which is different from the reconstructed level binning as explained in Chapter 8.3.
In all four distributions an efficiency mostly in the range of $\epsilon \in [0.7, 0.9]$ is observed in the measurement region, while a smaller efficiency of $\epsilon \approxeq 0.5$ is visible in the additional low m_{T}^W bin. The correction factor slighty increases as a function of m_{T}^W, while a drop close to the

transition region between $|\eta(e)| \in [1.37, 1.52]$ in each m_{T}^{W} bin and a decrease for forward electrons in the last three m_{T}^{W} bins is observed.
In the measurement range, a fraction of $20 - 30\%$ of the events are generated but not reconstructed. This inefficiency originates mostly from the requirements on $|\eta(e)|$, $p_{\mathrm{T}}(e)$ and $E_{\mathrm{T}}^{\mathrm{miss}}$ in the event selection at reconstructed level, as described in Chapter 8.1. In addition, the chosen identification and isolation criteria of the electron as well as the single electron trigger requirements reduce the amount of reconstructed events.
A charge dependence of the efficiency correction in the e^- and e^+ channel is not observed.

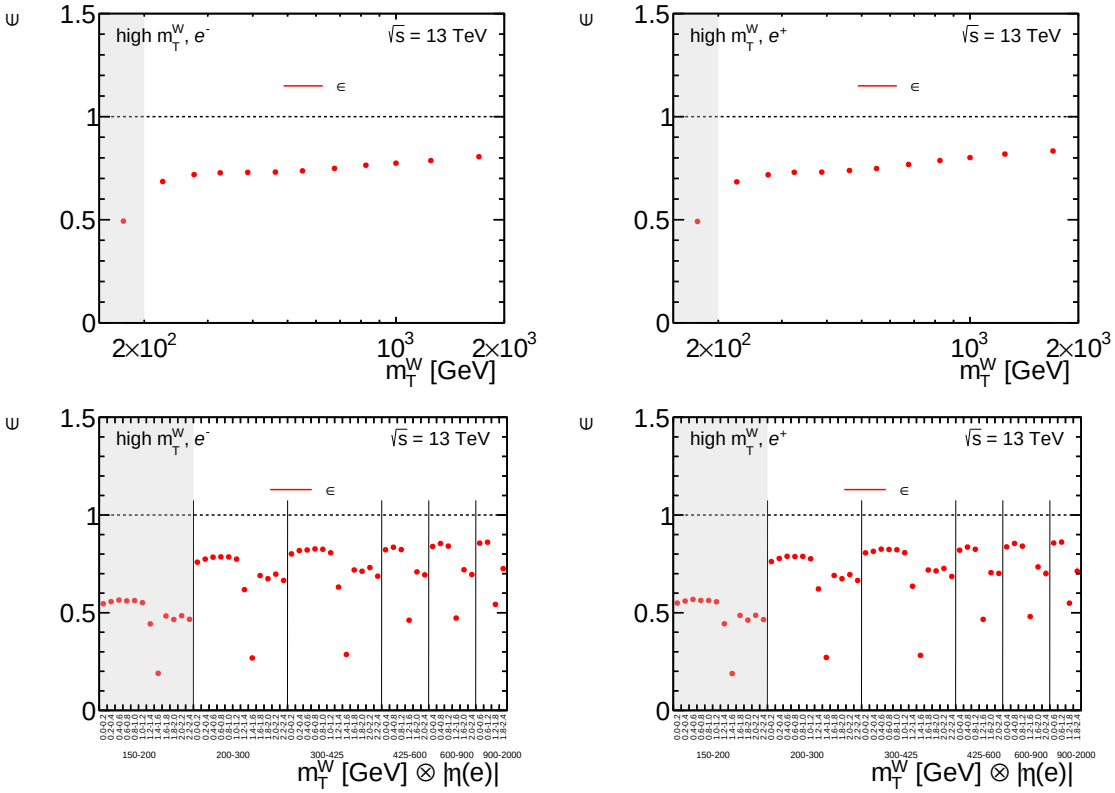

Figure 12.4: The efficiency ϵ_j per bin j of the MC truth level distribution as a function of the transverse mass of the W boson m_{T}^{W} and the absolute value of the pseudorapidity and transverse mass $m_{\mathrm{T}}^{W} \otimes |\eta(e)|$ separated into the e^+ and e^- channel in the measurement binning.

12.1.3 Unfolding using a shadow bin

A common strategy for the unfolding of phase spaces affected by large migration effects, in particular at the lower or upper boundaries of the measurement region, is based on an additional bin, a so-called *shadow bin*. This is included in the unfolding procedure, but the measured result is not published. In this thesis, large migrations occur across m_{T}^{W}, where especially on-shell W bosons migrate into the measurement region. For this reason, the

low $m_{\mathrm{T}}^{W} \in [150, 200]$ GeV bin is used as a shadow bin in the single- and double-differential cross-section measurement.

The investigations to assess the usefulness of a shadow bin described in this paragraph have been performed throughout the parallel measurement in the muon channel [46]. It has been shown in the muon channel that the in-smearing in the first measurement bin, i.e. in $m_{\mathrm{T}}^{W} \in [200, 250]$ GeV, is reduced from 30% to approximately 15%, due to the usage of a shadow bin. As a result, the fraction of migrating events is clearly reduced, which is expected to stabilise the unfolding procedure. Since the migrations do not substantially differ in the electron and muon final state, the shadow bin is used in the electron channel as well.

For this thesis, an additional study was performed, where a larger shadow bin is considered. The advantage of a large shadow bin, which includes the resonant mass peak of the W boson, would be that nearly all migrations participate in the iterative procedure of the IBU und no additional in-smearing corrections for migrations would be necessary.
It should be highlighted that the transverse momentum and missing transverse momentum requirement in the signal region selection are chosen such that the sum adds up to the lower edge of the transverse mass, 150 GeV, in order to explicitly allow events to populate the shadow bin. Otherwise, only very few events would enter the shadow bin, making it essentially useless, due to low statistics and the fact that events would still smear into the first m_{T}^{W} bin due to e.g. the higher $p_{\mathrm{T}}(e)$ requirement. In order to enlarge the shadow bin, not only the m_{T}^{W} requirement needs to be lowered, but also the $p_{\mathrm{T}}(e)$ and $E_{\mathrm{T}}^{\mathrm{miss}}$ requirements. Due to stricter requirements in the single electron trigger below $p_{\mathrm{T}}(e) < 60$ GeV and since the multijet estimation via the Matrix Method relies on the estimation of fake efficiencies in the region of $E_{\mathrm{T}}^{\mathrm{miss}} < 65$ GeV, a larger shadow bin is not considered beyond this point.

12.2 Technical closure test

A standard test is the *technical closure test*, which is used to ensure that the unfolding based on the custom interface to the `RooUnfold` implementation is technically set up correctly. Most important for that are the consistent definition of selection requirements on fiducial and reconstructed level, including the consideration of under- and overflow bins of the distributions.
The technical closure test is performed using the signal MC only, where the reconstructed distribution of the measurement variables from the W MC replaces the distribution of data events. Since the response matrix, including the estimated correction factors, and the fiducial distribution are based on the W MC as well, the unfolded distribution of the reconstructed W MC distribution and the fiducial distribution are expected to be identical. Consequently, a ratio yields a perfect agreement in all bins.
Distributions for the two measured variables at reconstructed level, at fiducial level and the unfolded distribution of the signal MC in the e^{+} and e^{-} channel are shown in Figure 12.5. In addition, a ratio of the unfolded distribution and the distribution at fiducial level, labelled truth, is presented. The variables in the measurement binning are displayed, where in case of $m_{\mathrm{T}}^{W} \otimes |\eta(e)|$ the equidistant $|\eta(e)|$ binning corresponding to the fiducial level is used. The

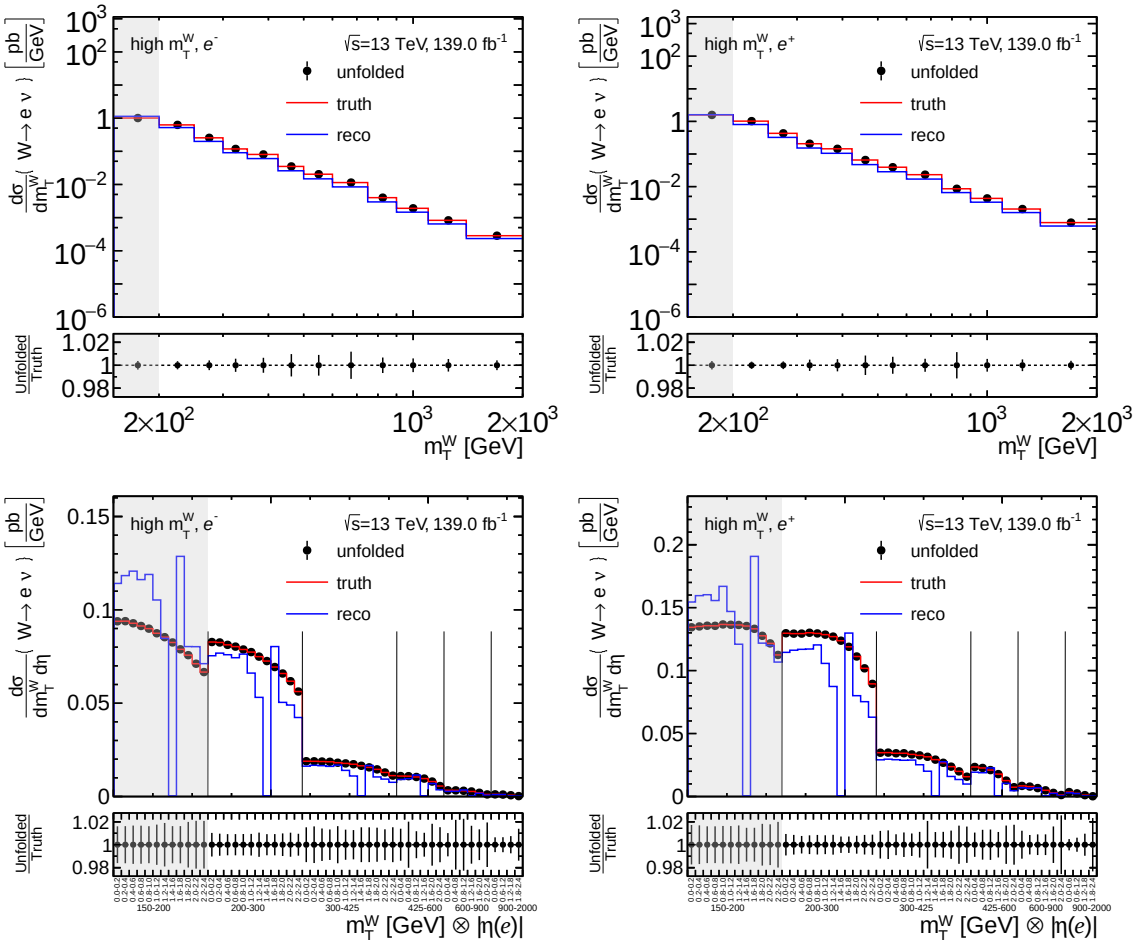

Figure 12.5: Technical closure test of the unfolding procedure, where the signal MC is taken as the input of the unfolding. The distribution of the reconstructed and fiducial level of the W MC and the unfolded distribution are shown. In addition, the latter two are compared in a ratio. For $m_{\mathrm{T}}^{W} \otimes |\eta(e)|$, the presentation of the fiducial level binning is chosen, although the reconstructed distribution is still binned in the measurement binning corresponding to the reconstructed level.

binning for the distribution of the reconstructed level, which differs with respect to the fiducial level, is not shown here.
The expected perfect agreement between the unfolded distribution and the fiducial level distribution as a function of the measured variables for the e^+ and e^- channel can be observed. As a consequence, the technical setup is assumed to work correctly.

12.3 Stress test

The so-called stress test allows to check the robustness of the unfolding setup, where shape differences with respect to the modelling in the MC are induced and the difference in the

unfolded distribution is investigated. Similar to the technical closure test, where perfect closure has been shown, the stress test is based on the W MC only. Here, the W MC replaces the measured data distribution, but the difference to the closure test is that a linear reweighting is applied before the unfolding.
Three different linear reweighting functions are defined, where each provides a multiplicative weight applied per event. The weights induce a difference of $\pm 20\%$ and $+50\%$ at the lower and upper bound of the invariant mass of the W boson m_{inv} distribution via

$$w_{\pm 20\%} = \mp \frac{0.4}{2000} \cdot m_{inv} + (1 \pm 0.2)\,, \tag{12.3}$$

$$w_{+50\%} = -\frac{1}{2000} \cdot m_{inv} + 1.5\,. \tag{12.4}$$

The application of these weights to the transverse mass of the W boson result into a very similar linear shape difference. The stress test is exemplarily visualised as a function of $m_{\text{T}}^{W} \otimes |\eta(e)|$ in the fiducial level binning for the e^- channel in Figure 12.6. The number of iterations in the unfolding is varied in the range of $N_{\text{iter}} = [1, 4]$. The nominal cross-section, labelled 0%, and the three reweighted distributions, labelled according to the percentage used in the reweighting, are compared. The visualisation of the stress test is identical for each different number of iterations, where the nominal and the three reweighted cross-sections are shown in the upper panel. Each cross-section is presented for the fiducial level represented by solid lines and the unfolded level, where the reweighted, reconstructed distributions of the W MC were unfolded, represented by filled dots. The different colours correspond to differently reweighted distributions.
In addition, a ratio of each stressed, i.e. reweighted, distribution and the nominal distribution at the fiducial level before the unfolding can be observed in the middle panel. The stressed distributions differ to the nominal distribution and the linear reweighting can be seen as a function of m_{T}^{W}, where a flat distribution as a function of $|\eta(e)|$ per m_{T}^{W} bin is expected.
Lastly, a ratio of the unfolded distributions and their corresponding fiducial level distributions, labelled truth, is added. In Figure 12.6b, it can be observed that all unfolded distributions agree within 2% with their fiducial level distribution, where the agreement is mostly below 1%, if the shadow bin is neglected. Since the shadow bin is used to stabilise the unfolding only, its disagreement should not impact the conclusions on the stress test.
The comparison of the lower panel in Figure 12.6a, Figure 12.6b, Figure 12.6c and Figure 12.6d, respectively, allows to see the evolution of the agreement, where the largest differences are observed for $N_{\text{iter}} = 1$. After two iterations a reasonable agreement, i.e. the smallest differences between the unfolded and fiducial level distributions, is found already. Especially in Figure 12.6d, it can be seen that the agreement becomes worse for $N_{\text{iter}} = 4$ compared to $N_{\text{iter}} = 3$ in Figure 12.6c.
Since the statistical uncertainty increases as a function of an increasing number of iterations, as explained in Chapter 12.5.1, it is concluded that the unfolding is able to handle linear shape differences reasonably within two iterations $N_{\text{iter}} = 2$.
Finally, the visualisations of the stress test as a function of $m_{\text{T}}^{W} \otimes |\eta(e)|$ in the e^+ channel, and as a function of m_{T}^{W} in both channels are shown in Appendix F in Figure F.7, which lead to the same conclusions.

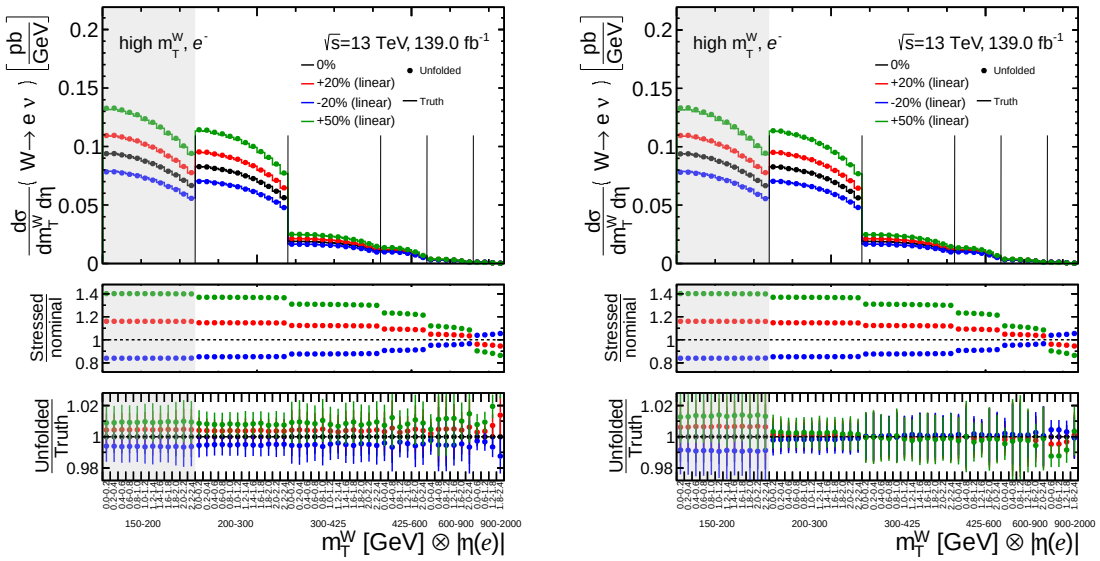

(a) $N_{\text{iter}} = 1$

(b) $N_{\text{iter}} = 2$

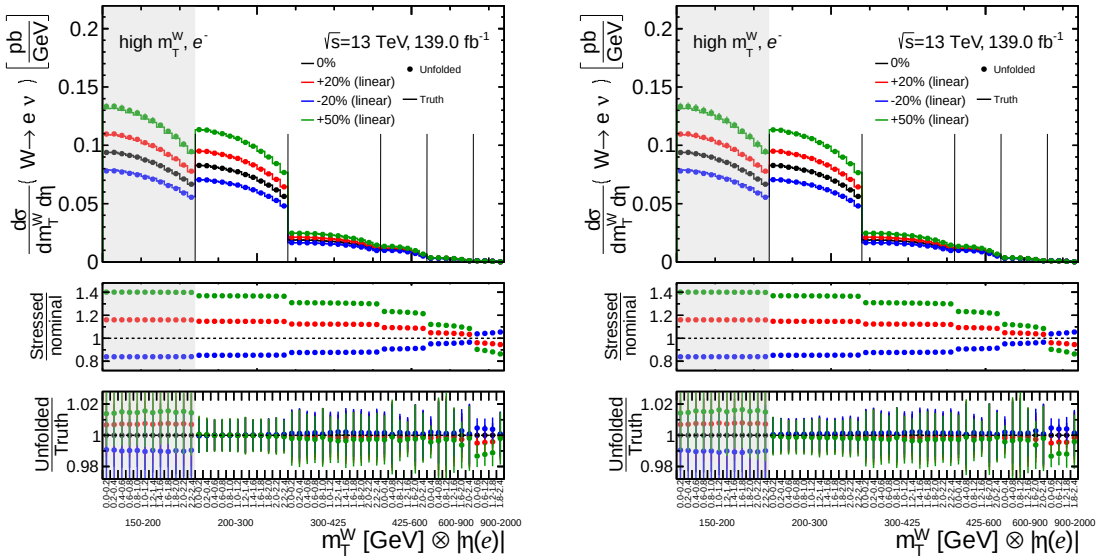

(c) $N_{\text{iter}} = 3$

(d) $N_{\text{iter}} = 4$

Figure 12.6: Visualisation of the stress test for the measured variable $m_{\mathrm{T}}^W \otimes |\eta(e)|$ after three and four iterations in the unfolding for the e^- channel.

12.4 Calculation of the covariance matrix

In the following, the determination of the covariance matrix, which is a symmetric square matrix, is described. Its estimation is required for the calculation of the statistical uncertainty on the cross-section after the unfolding and for the regularisation of the IBU, as described

in Chapter 12.5. The covariance matrix consists of variances and covariances, where the variances are found on the diagonal. Subsequently, the correlation matrix can be obtained from the covariance matrix.
Commonly, the calculation of the covariance matrix is based on toy data, which can be generated either by multiple replicas fluctuating *each bin* of the measured distribution or by multiple variations for *each event*. In this thesis, the generation of toy datasets relies on the former approach. The following steps are performed in order to calculate the covariance matrix:

1. The generation of a toy dataset,
2. the background subtraction and unfolding for the generated toy dataset,
3. the calculation of the covariance matrix.

The first and second step are repeated multiple times, before the covariance matrix is caluclated in the third step. First, a toy dataset is generated based on the prediction and the measured data. A replica, i.e. one toy dataset, is created by the variation of the amount of events in each bin i of the measured distribution by the statistical uncertainty. For data, a Poisson distribution

$$\mathcal{P}(N_i^{\text{data}}) \tag{12.5}$$

is used, where the event yield N_i^{data} in each bin is used as the mean value, resulting into a statistically varied amount of data events. For the prediction, the variation is based on a Gaussian distribution with a mean $\mu = 0$ and standard deviation $\sigma = 1$. A random number ξ_i^{toy} of the Gaussian distribution is drawn and multiplied to the statistical uncertainty of the MC distribution $\delta_{i,\text{mcstat}}$. As a result, the variation of the event yield is defined as

$$\Delta_{i,\text{mcstat}}^{toy} = \xi_i^{toy} \cdot \delta_{i,\text{mcstat}} \,. \tag{12.6}$$

The event yield in the toy dataset per bin i is calculated based on the formula

$$N_i^{toy} = \mathcal{P}(N_i^{data}) \cdot \left(1 + \frac{\Delta_{i,\text{mcstat}}^{toy}}{N_i^{nominal}}\right) , \tag{12.7}$$

where the fluctuated amount of events for data and the prediction and the number of events before the variations $N_i^{nominal}$ is used.
In the second step, the same unfolding as for the nominal data distribution via the IBU, including the correction factors and the background subtraction, for each generated toy dataset is performed.
Finally, the covariance matrix $Cov_{i,j}$, which is based on all generated toy datasets, is defined as

$$Cov_{i,j} = \frac{1}{N_{toy}} \sum_{0}^{N_{toy}} (h_i^{nominal} - h_i^{toy})(h_j^{nominal} - h_j^{toy}) \,, \tag{12.8}$$

where the sum of all differences between the nominal unfolded result $h_k^{nominal}$ and the unfolded result of each toy dataset h_k^{toy} in the k-th bin an the total number of generated toy

datasets N_{toy} are used. The number of generated toy datasets N_{toy} has to be chosen such that the covariance matrix is independent of statistical fluctuations and still reasonable in terms of computing resources.
The correlation matrix $Corr_{i,j}$, where the bin-to-bin correlations of the measured distributions are calculated, can be derived from the covariance matrix by evaluating

$$Corr_{i,j} = \frac{Cov_{i,j}}{\sigma_i \sigma_j}\,, \tag{12.9}$$

where the uncertainty σ_m for $m = i, j$ is defined as $\sigma_m = \sqrt{Cov_{m,m}}$.
Exemplarily, the covariance and correlation matrix after two iterations in the IBU based on 5000 toy datasets, including variations of the statistical uncertainty of data and MC based events, as a function of m_{T}^W, in the e^+ channel is shown in Figure 12.7 and Figure 12.8. The covariance and correlation matrix as a function of m_{T}^W in the e^- channel can be found in Appendix F in Figure F.4 and the covariance matrix as a function of $m_{\mathrm{T}}^W \otimes |\eta(e)|$ in Figure F.5.
In Figure 12.7 and Figure 12.8, the bins of the m_{T}^W distribution are displayed on x- and y-axis and covariance or correlation is represented on the z-axis. In Figure 12.7, the variance is visible at the diagonal of the covariance matrix and is used as the statistical uncertainty of the unfolded cross-section for the measurement as presented in Chapter 13. It can be observed that the variance is always larger than the covariance in each m_{T}^W bin, where e.g in the fifth bin a variance of $3.3 \cdot 10^{-6}$ is found and the covariance decreases for increasing distance to the variance. In Figure 12.8, the correlation matrix is displayed, where the diagonal is correlated with itself by reconstruction. The highest correlations are observed in the first four off-diagonal m_{T}^W bins.
The calculated covariance matrices can be compared to the covariance matrix calculated by the `RooUnfold` implementation. It has been checked, that the covariances agree, where

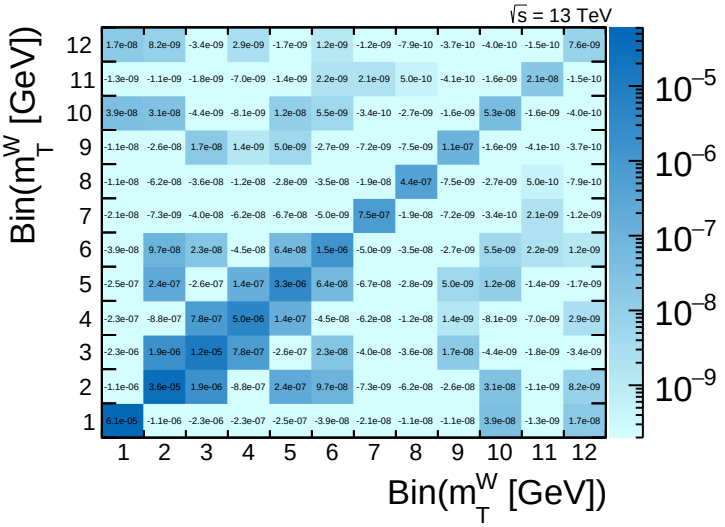

Figure 12.7: Covariance matrix after two iterations in the IBU based on the statistical uncertainty of data and MC based events, generated with 5000 toy datasets, as a function of m_{T}^W for the e^+ channel.

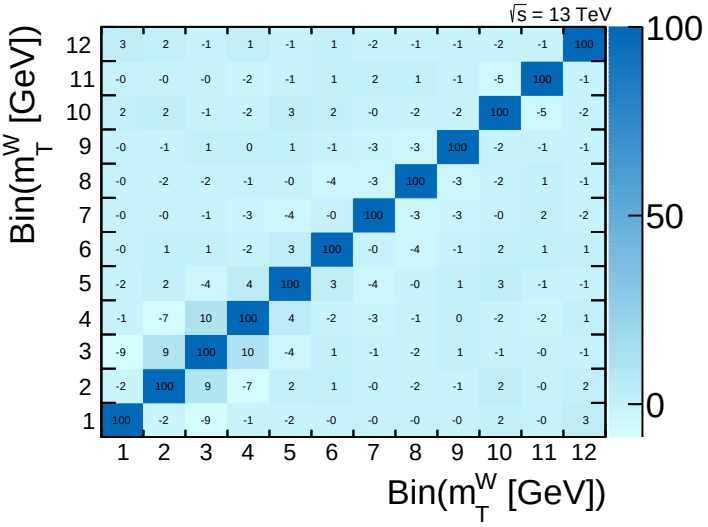

Figure 12.8: Correlation matrix after two iterations in the IBU based on the statistical uncertainty of data and MC based events, generated with 5000 toy datasets, as a function of m_{T}^{W} for the e^{+} channel.

it has to be pointed out, that the statistical uncertainty of data events only is used in `RooUnfold` and, for this reason, in the cross-check. As a result, in order to correctly consider the statistical uncertainty of the MC samples in the full measurement, the covariance matrix consisting of statistical variations in data and MC based processes is used.

12.5 Regularisation

The process of unfolding, which commonly approximates the inversion of a matrix, belongs to the category of ill-posed problems. The so-called regularisation allows to add information in order to solve an ill-posed problem. In IBU, the regularisation parameter is the number of iterations. The truth distribution after the fiducial selection is used as the 0-th prior in the bayesian approach. As a result, a strong regularisation, i.e. smaller number of iterations, enhances the similarity to the induced truth level of the MC. In contrast, a decreasing regularisation strength, i.e. increasing number of iterations, enhances the similarity to the measured distribution of data events. The information provided in this paragraph and further details can be found in Ref. [50, 97].
This section focuses on the regularisation in the IBU. In order to find the optimal value for the number of iterations, the residuals and the statistical uncertainty, χ^2 tests and the so-called average global correlation coefficient test are discussed.

12.5.1 Residuals and statistical uncertainty w.r.t. the previous iteration

First, two basic quantities, the residuals and the statistical uncertainty, as a function of the number of iterations are investigated. Both studies are based on a fraction of the Run 2 statistics, corresponding to the integrated luminosity of 36.2 fb^{-1}, obtained

during 2015 and 2016. An alternative signal MC sample is used, which is generated with POWHEG-BOX v2 and the parton shower is simulated with HERWIG 7, as described in Chapter 6.3. In the following, this sample is denoted as `Powheg+Herwig7`. As discussed in Chapter 11, a couple of issues related to the `Powheg+Herwig7` MC sample remain unresolved. Nevertheless, the quantities studied here are independent of these open issues. Importantly, the `Powheg+Herwig7` sample is statistically independent of the nominal signal MC.

Residuals are defined as the difference between the unfolded distribution after $N+1$ and N iterations in the IBU. Technically, another modified closure test is performed, where the `Powheg+Herwig7` sample provides the distribution of the reconstructed level and is unfolded using the nominal signal MC. The procedure is performed for different numbers of iterations, $N_{\text{iter}} \in [1, 7]$. The residuals as a function of the number of iterations for the measured variables are presented in Figure 12.9. In Figure 12.9a, each of the twelve bins of the unfolded distribution of m_{T}^{W} is represented by a different colour. Although the residuals differ in size depending on the bin, an overall trend of decreasing residuals as a function of increasing number of iterations N_{iter} is observed. A very similar behaviour can be observed for the unfolded distribution of $m_{\text{T}}^{W} \otimes |\eta(e)|$ in Figure 12.9b.

The statistical uncertainty for the two measured variables, m_{T}^{W} and $m_{\text{T}}^{W} \otimes |\eta(e)|$, as a function of the number of iterations N_{iter} is shown in Figure 12.10. Again, different colours represent bins of m_{T}^{W} and $m_{\text{T}}^{W} \otimes |\eta(e)|$ in Figure 12.10a and Figure 12.10b, respectively. The statistical uncertainty increases as a function of increasing number of iterations N_{iter}. As a consequence, the number of iterations in the IBU should be kept as small as possible in order to neglect high statistical uncertainties in the measurement.

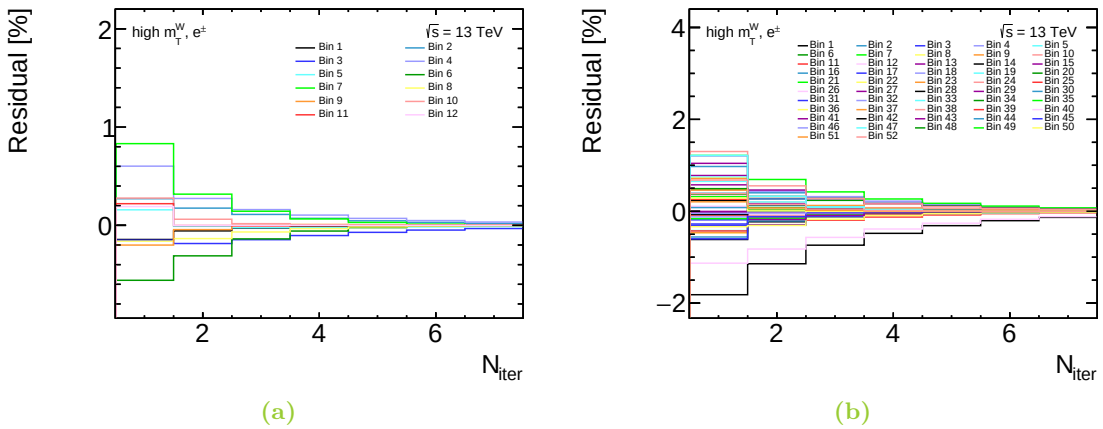

Figure 12.9: Unfolding residuals with respect to the previous iteration as a function of N_{iter} for m_{T}^{W} and $m_{\text{T}}^{W} \otimes |\eta(e)|$ for the combination of the e^+ and e^- channel.

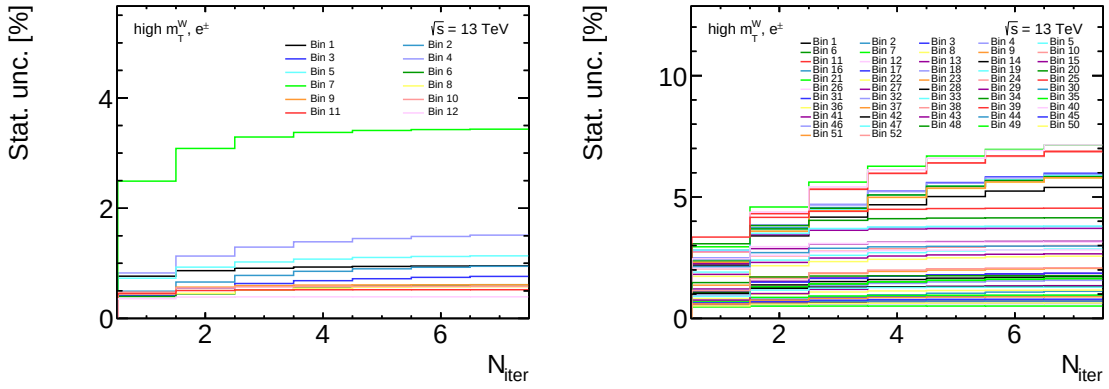

(a) (b)

Figure 12.10: Statistical uncertainties as a function of the number of iterations N_{iter} for m_{T}^W and $m_{\text{T}}^W \otimes |\eta(e)|$ for the combination of the e^+ and e^- channel.

12.5.2 χ^2 tests

A common procedure used for the optimisation of the number of iterations in the IBU is based on a χ^2 test, where the consistency of the unfolded distribution and the MC truth level distribution after the fiducial selection is investigated. Such a test is defined as

$$\chi^2 = V_{N_b}(x_{\text{unfolded}} - x_{\text{truth}})^T \cdot Cov_{N_b}^{-1} \cdot V_{N_b}(x_{\text{unfolded}} - x_{\text{truth}})\,, \tag{12.10}$$

where the vector V_{N_b} refers to the difference between the unfolded x_{unfolded} and MC truth level x_{truth} distribution for the number of bins N_b and the inverse of the covariance matrix Cov^{-1}, as described in Chapter 12.4, is used. The χ^2 is calculated as a function of the number of iterations. A minimum in the χ^2 distribution would refer to an optimal agreement between the unfolded and truth level distribution.
In this thesis, a χ^2 test based on the covariance matrix, where only the statistical uncertainty of data events is used for the generation of toy data, is performed. As a result, an approximately flat distribution is obtained, where no minimum of the χ^2 values as a function of the measured variables can be observed. This behaviour originates from the m_{T}^W distribution, which is monotonously and steeply decreasing in the measurement range. Consequently, the calculated χ^2 strongly depends on the first considered m_{T}^W bin and does not provide a reasonable consistency check. For completeness, the obtained χ^2 distribution as a function of the number of iterations as a function of m_{T}^W is shown in Figure F.8 in Appendix F.

12.5.3 Average global correlation coefficient test

The so-called average global correlation coefficient test [98] is based on the covariance matrix as well, where correlations induced by the iterative procedure of the IBU and their evolution as a function of the number of iterations in the IBU are exploited. Bin-by-bin correlations are a consequence of the iterative procedure and the corresponding regularisation. A measure

for the average global correlation ρ_{avg} is defined as

$$\rho_{avg} = \frac{1}{N_b}\sum_{j=1}^{N_b}\rho_j \quad \text{with} \quad \rho_j = \sqrt{1-\left((Cov_{N_b})_{jj}\cdot(Cov^{-1}_{N_b})_{jj}\right)^{-1}}, \tag{12.11}$$

where the covariance matrix Cov_{N_b}, the inverse of the covariance matrix $Cov^{-1}_{N_b}$ and the number of bins N_b of the unfolded distribution are used. For this test, the covariance matrix based on the statistical uncertainty of data events is obtained from 5000 toy datasets. The precise evaluation of $Cov^{-1}_{N_b}$ is crucial for the estimation of the average global correlation coefficient, because small deviations can lead to imaginary numbers in the calculation of ρ_j, if the argument of the square root is a negative number.
In general, the average global correlation evolves as a function of the number of iterations. For a small number of iterations positive correlations are expected, whereas negative correlations occur in the limit of many iterations [98]. As a consequence, a minimum in the distribution of the average global correlation is expected, due to the change of the sign of the induced correlations, offering a measure for the optimal number of iterations. The evolution of the correlation for $N_{\text{iter}} = 1, 2, 5$ in the e^+ channel is exemplarily shown in Appendix F in Figure F.6.
In Figure 12.11, the average global correlation for the single-differential cross-section measured in m_{T}^W as a function of the number of iterations N_{iter} is shown. A very similar shape of the average global correlation is visible for the e^+ and e^- channel in the range of $N_{\text{iter}} \in [1, 6]$, where the difference corresponds to a small flat offset in the two channels. The minima, i.e. the optimal number of iterations in the IBU for the m_{T}^W distribution, can be found at $N_{\text{iter}} = 2$.
Subsequently, the average global correlation for the double-differential cross-section in $m_{\text{T}}^W \otimes |\eta(e)|$ is studied. In this case, the average global correlation yields imaginary numbers in the estimated coefficients, which are found to originate from a non-optimal matrix inversion. A variation of the number of toys, using 1000 and 10000 toy datasets, or a scaling of the covariance matrix, in order to exclude problems with small numbers in the matrix inversion, have been performed, but no improvements could be obtained.

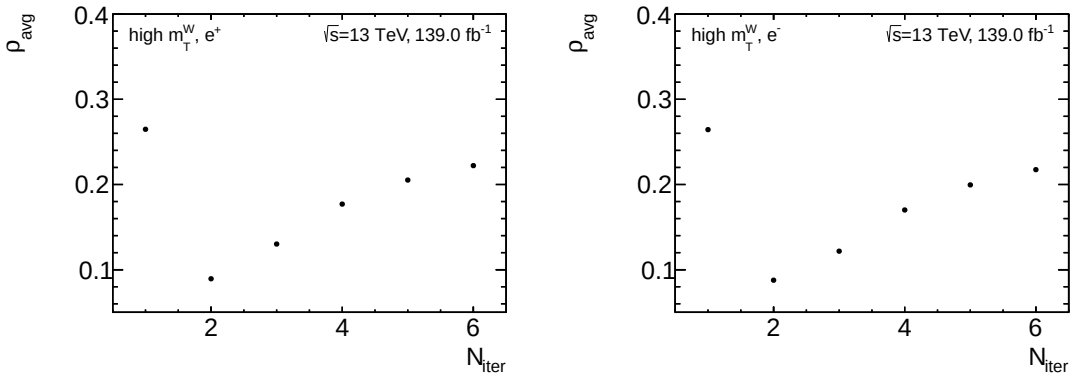

Figure 12.11: Average global correlation ρ_{avg} as a function of the number of iterations in the IBU N_{iter} for the single-differential cross-section measurement in m_{T}^W separated into the e^+ and e^- channel.

12.5.4 Conclusions on the number of iterations

An optimised number of two iterations in the unfolding procedure is chosen for the following reasons: First, differences of the residuals are expected to be small for a higher number of iterations. Second, the number of iterations should be kept as small as possible in order to avoid the increase of the statistical uncertainty. Third, the stress test shows that the unfolding is able to recover linear shape differences reasonably after two iterations already. This holds true for both measured variables. In addition, the distribution of the average global correlation shows a clear minimum for the single-differential cross-section measurement.
As a side note, the presented tests can be performed for a covariance matrix that is based on the statistical uncertainty and, in addition, the systematic uncertainties. The inclusion of systematic uncertainties induce a very high amount of additional correlations and no minima in the χ^2 distribution or the average global correlation test has been found. Furthermore, it has been seen that especially the statistical uncertainty increases as a function of N_{iter}. As a result, the covariance matrix based on the statistical and systematic uncertainties is not considered further.

12.6 Unfolding of experimental and theoretical systematic uncertainties

After the optimal number of iterations in the IBU is found, the unfolding of experimental and theoretical systematic uncertainties is discussed in the following. The unfolding of systematic uncertainties relies on the number of iterations and allows to assign a systematic uncertainty on the unfolded cross-section. In the IBU, one of the following two methods are commonly used. A single one-sided systematic uncertainty on the signal process is assumed for the description of the two methods: In the first method, the measured distribution of the W MC is replaced by the systematically varied distribution. Afterwards, the unfolding using the same response matrix as for the nominal measured distribution is performed. In the second method, the response matrix built from the W MC is replaced by the response matrix created from the systematically varied MC. Then, the nominal measured distribution of the W MC is unfolded using this varied response matrix. In both methods, the resulting unfolded distribution is compared to the nominal unfolded distribution in order to obtain the systematic uncertainty on the unfolded distribution.
Both methods have been investigated for this measurement and it has been found, that both methods provide the same size of the systematic uncertainty on the unfolded distribution. In this thesis, the first method is used because less computational resources are required.

The largest unfolded experimental systematic uncertainties of the signal process as a function of the measured variables are shown in Figure 12.12. Only systematic uncertainties with an expected impact of at least 0.5% on the cross-section are considered. While the systematic uncertainties of the electron scale factor, the electron energy scale and the jet energy resolution are presented here, the systematic uncertainties of the $E_{\text{T}}^{\text{miss}}$ soft term and the jet energy scale can be found in Appendix F in Figure F.9.

The unfolded distributions of the systematic uncertainties for two iterations in the IBU can be found in Figure 12.12. Each systematic uncertainty is represented by one colour, where the solid and the dashed line correspond to the up and down variations, respectively. The blue band represents the total uncertainty in each of the distributions, where the contributions of the single systematic uncertainties of each plot are summed up in quadrature. Overall,

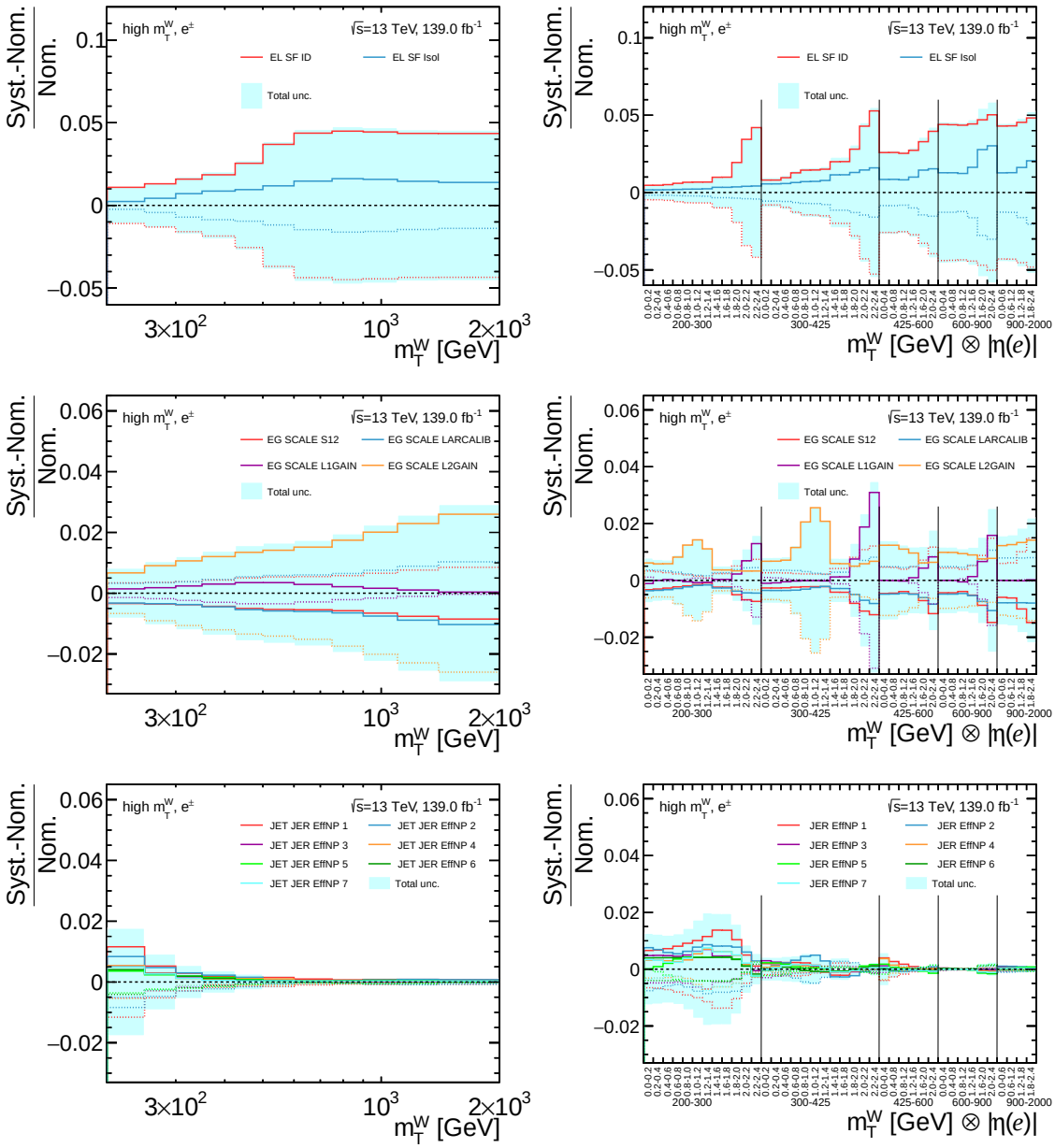

Figure 12.12: Unfolded systematic uncertainties corresponding to the electron scale factor, the electron energy scale and the jet energy resolution for the signal process as a function of the measured variables, m_{T}^{W} and $m_{\mathrm{T}}^{W} \otimes |\eta(e)|$ for the combination of the e^+ and e^- channel. Only systematic uncertainties with an impact of at least 0.5% in any bin are considered.

the shape of the systematic uncertainties is very similar to the ones at reconstructed level, as discussed in Chapter 11.2.

In addition, the theoretical systematic uncertainties of the $t\bar{t}$ background and the systematic uncertainties corresponding to the multijet estimate are unfolded. In this thesis, the systematic uncertainties are unfolded via the replacement of the measured MC distribution, as explained for systematic uncertainties corresponding to the signal process. For background processes this procedure does not rely on MC only and, therefore, is adapted in the following way: In the first step, the nominal unfolded distribution is obtained, where the background processes are subtracted from the measured distribution of data and the unfolding procedure using the signal MC is performed. In the second step, the systematically varied unfolded distribution is obtained. For this reason, the systematically varied backgrounds are subtracted from the measured data distribution. Afterwards, the unfolding procedure is applied. The difference of the nominal unfolded and the systematically varied unfolded distribution is assigned as the systematic uncertainty on the cross-section.
In Figure 12.13, the unfolded theoretical systematic uncertainties of the $t\bar{t}$ background and the systematic uncertainties corresponding to the multijet estimate as a function of the measured variables, m_{T}^{W} and $m_{\mathrm{T}}^{W} \otimes |\eta(e)|$, are presented. The presented unfolded systematic uncertainties on the cross-section can be compared to systematic uncertainties at reconstructed level shown in Chapter 9.5 and Chapter 11, where a similar size and shape is found.

Lastly, the theoretical systematic uncertainties of the signal process are unfolded and their impact on the cross-section is evaluated. As outlined in Chapter 11.1.1, the systematic uncertainties corresponding to the cross-section are obtained only after the unfolding. In the following, the unfolding procedures for the theoretical uncertainties of the signal process are described, where two different approaches are used.
The unfolding of the renormalisation and factorisation systematic uncertainty are discussed first. A partial dataset, corresponding to data taken in 2015 and 2016, is unfolded using the response matrix and correction factors obtained from the Powheg+Herwig 7 MC. Afterwards, the partial dataset is unfolded again for each of the considered systematic variations, where the response matrix and the correction factors corresponding to one of the μ_R, μ_F variation is used. In the response matrix, relative differences at fiducial and at reconstructed level are considered at the same time. In the end, each unfolded distribution corresponding to a μ_R, μ_F variation is compared to the unfolded distribution corresponding to the nominal Powheg+Herwig 7 MC in order to estimate the final systematic uncertainty on the cross-section.
Another unfolding procedure is performed in case of the hadronisation systematic uncertainties. Instead of unfolding the measured data, the estimation of the hadronisation systematic uncertainties is based on the nominal signal and the alternative signal MC sample only. The nominal signal MC distribution at reconstructed level is unfolded with the response matrix and correction factors that correspond to the alternative signal MC sample. The obtained unfolded distribution is compared to the distribution of the nominal signal MC at fiducial level. The relative difference of these distributions is defined as the final hadronisation systematic uncertainty. Since fluctuations have already been observed in Chapter 11.1.1, the statistical uncertainty of the two MC samples are added. The statistical uncertainty of the unfolded distribution corresponding to the nominal signal MC is calculated in the IBU,

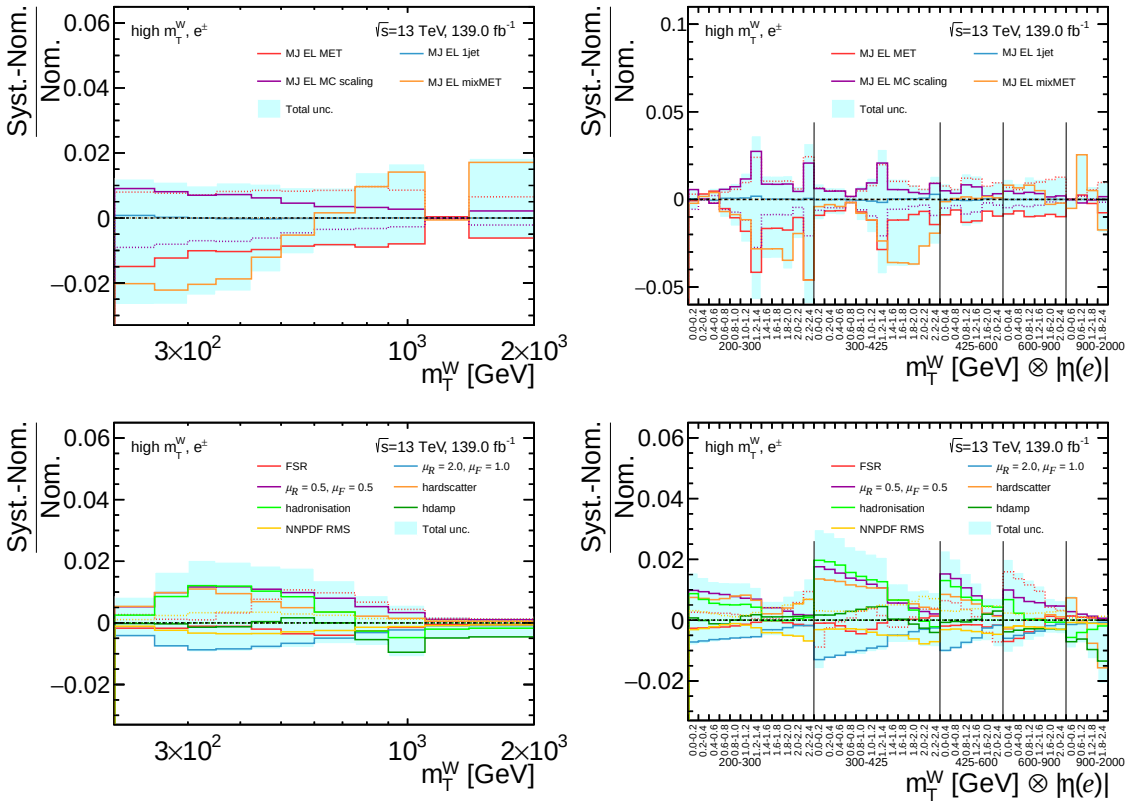

Figure 12.13: Unfolded systematic uncertainties corresponding to the multijet estimate and the theoretical systematic uncertainties for the $t\bar{t}$ background as a function of the measured variables, m_{T}^{W} and $m_{\mathrm{T}}^{W} \otimes |\eta(e)|$ for the combination of the e^+ and e^- channel. Only systematic uncertainties with an expected impact of 0.5% in any bin are considered.

while the statistical uncertainty of the POWHEG+HERWIG 7 MC has to be added manually. The covariance matrix for the alternative signal MC is calculated following the description in Chapter 12.4 and subsequently, the square root of the variance is summed in quadrature to the statistical uncertainty of the nominal signal MC. The statistical uncertainty of the fiducial level distribution is very small compared to the other statistical uncertainties and, in order to obtain uncorrelated statistical uncertainties of the nominal signal MC, artificially set to zero.

The unfolded renormalisation and factorisation systematic uncertainties and the hadronisation systematic uncertainties as a function of the measured variables are presented for the combination of the e^+ and e^- channel in Figure 12.14. The renormalisation and factorisation systematic uncertainties as a function of the measured variables are shown in Figure 12.14a and Figure 12.14b. Overall, their relative difference is very small. The threshold for systematic uncertainties of 0.5% on the cross-section is fulfilled by the $\mu_R = 2.0, \mu_F = 2.0$ variation for $m_{\mathrm{T}}^{W} \otimes |\eta(e)| \in [300, 425]\,\mathrm{GeV} \otimes [1.8, 2.0]$. Since the systematic uncertainties in the neighbouring bins are much smaller, it is assumed that the large uncertainty in this bin originates from a statistical fluctuation or artificially large event weight. Consequently, the renormalisation and factorisation systematic uncertainties are not further considered.

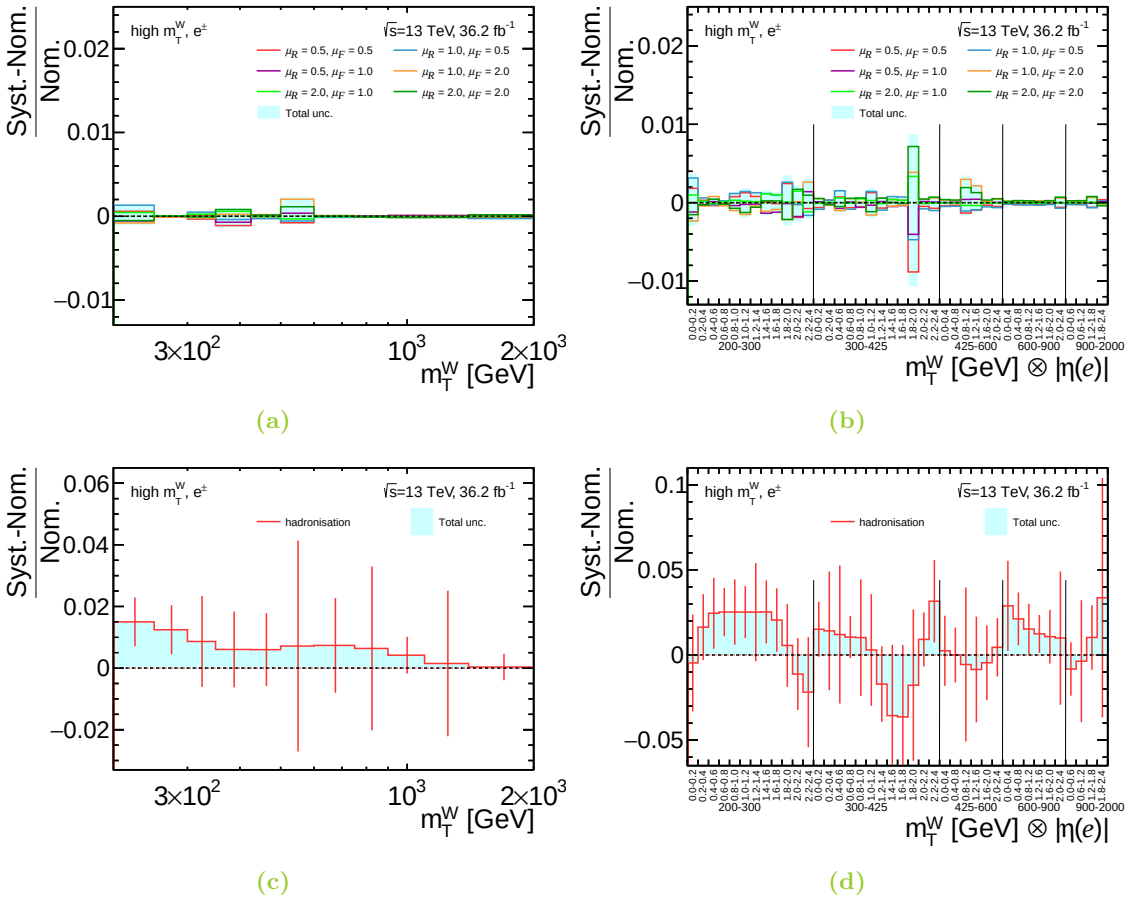

Figure 12.14: Unfolded theoretical systematic uncertainties of the signal process as a function of the measured variables for the combination of the e^+ and e^- channel. Only systematic uncertainties with an impact of 0.5% in any bin are considered. The renormalisation and factorisation systematic uncertainties are shown in a) and b), while the hadronisation systematic uncertainty is displayed in c) and d). For the hadronisation systematic uncertainty, the statistical uncertainty of the nominal signal MC sample and the alternative signal MC sample is added, which are represented by error bars. A smoothing procedure has been applied to the hadronisation systematic uncertainty only.

In Figure 12.14c and Figure 12.14d, the hadronisation systematic uncertainties as a function of the measured variables are presented. In contrast to the μ_R, μ_F variations, larger relative differences of up to 1.5% for m_{T}^W and up to 3.5% are found for $m_{\mathrm{T}}^W \otimes |\eta(e)|$. If the combined statistical uncertainties of the both MCs is taken into account, remaining relative differences of more than 0.5% are observed in one bin as a function of m_{T}^W and in three bins as a function of $m_{\mathrm{T}}^W \otimes |\eta(e)|$.
At the timescale of this thesis, it has not been possible to further study the observed fluctuations and remaining differences. Three main conclusions are drawn: First, the estimated statistical uncertainties cover almost the full relative difference of the systematic uncertainties. Second, the bins with an impact more than 0.5% on the cross-section are discontinuously distributed as a function of the measured variables and might originate

from fluctuations. Third, even if remaining differences would be taken into account, their impact is very small compared to the experimental systematic uncertainties and the multijet systematic uncertainty. As a result, both considered theoretical systematic uncertainties for the signal process are assumed to be negligible and not further considered.

12.7 Systematic uncertainty of the unfolding procedure

In the end, a systematic uncertainty corresponding to the unfolding procedure has to be determined. Although the unfolding systematic uncertainty could not be estimated at the timescale of this thesis due to the open issues with the alternative MCs, the estimation procedure is described shortly.

Three different sources are commonly considered for an unfolding systematic uncertainty: First, a so-called *basic unfolding uncertainty* is determined, where the sensitivity of the IBU to differences between the signal MC and the data in the measured variables is studied. Technically, a so-called data-driven closure test needs to be performed. The signal MC distribution at reconstructed level is used, where a truth level reweighting in the measured variables is applied in order to match the signal MC to the distribution of measured data events. Then, the procedure of the technical closure test, introduced in Chapter 12.2, is applied. In the end, the difference of the reweighted truth level distribution and the unfolded distribution of the reweighted reconstructed level distribution is defined as the *basic unfolding uncertainty*.
Second, a *hidden variables* study should be performed. This systematic uncertainty is estimated similarly as the *basic unfolding uncertainty*. A truth reweighting is applied such that the number of predicted MC events and the measured data agrees in variables, that are not unfolded in this measurement. This uncertainty should estimate the potential mismodelling that could arise from these variables.
Third, the difference of the unfolded distributions of the nominal signal MC sample and an alternative MC sample is estimated. Here, the alternative MC is reweighted such that it agrees with the nominal signal MC on truth level. Afterwards, the reweighted alternative MC is unfolded using the response matrix of the nominal signal MC. The differences of the unfolded distribution and the truth level distribution of the alternative MC is used as a systematic uncertainty.

Even though these tests could not be performed at the time scale of this thesis, it should be noted that the stress test, as described in Chapter 12.3, provides a first estimate of a systematic uncertainty corresponding to the unfolding procedure. Although the linear reweighting in the stress test is certainly not sufficient to account for differences between the MC and data events and in particular for bin-wise fluctuations entirely, it has been shown that substantial linear shape differences can be handled with a precision of less than one percent.

13 Results

In the following the single-differential cross-section as a function of the transverse mass of the W boson, m_{T}^{W}, and the double-differential cross-section as a function of the transverse mass and the absolute value of the pseudorapidity are presented. The measurement of the cross-sections consists of the optimised value for the regularisation, i.e. the number of iterations $N_{\mathrm{iter}} = 2$, the estimated statistical uncertainty obtained from the covariance matrices and the systematic uncertainties. The experimental systematic uncertainties of the signal process and theoretical systematic uncertainties of the $t\bar{t}$ background are considered. In addition, the systematic uncertainties of the multijet estimate via the Matrix Method are shown. As outlined in Chapter 11, only a subset of all systematic uncertainties is considered in the measurement, where an impact of at least 0.5% on the cross-section is required.

13.1 Unfolded single-differential cross-section in m_{T}^{W}

The final unfolded single-differential cross-section in the e^+ and e^- channel are shown in Figure 13.1. The unfolded data as a function of the transverse mass of the W boson for the e^- and the e^+ channel are presented in Figure 13.1a and Figure 13.1b. The statistical uncertainty of the unfolded data is represented by black error bars, whereas the light blue uncertainty band consists of the systematic uncertainties and the dark blue uncertainty

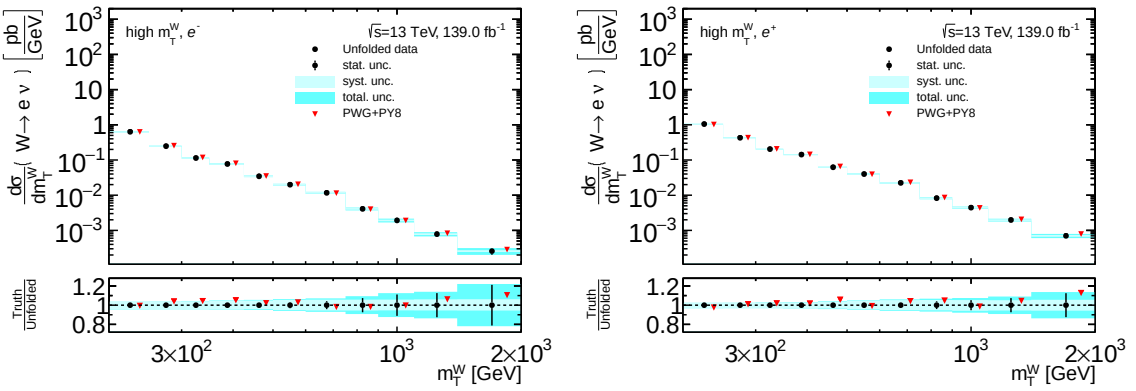

(a) (b)

Figure 13.1: Unfolded single-differential cross-section as a function of the transverse momentum of the W boson, m_{T}^{W} in the a) e^- and b) e^+ channel. The statistical uncertainty of the data represented by error bars is shown. The statistical uncertainty of the MC samples, obtained from the covariance matrix, and the systematic uncertainties with an impact of more than 0.5% are included in the uncertainty band.

band accounts for the total uncertainty, i.e. displays the squared sum of the statistical and systematic uncertainties. Furthermore, the m_{T}^{W} distribution at fiducial level obtained from the signal MC, labelled as PWG+PY8, is displayed by the red triangles.
Overall, it can be observed that the total uncertainty is characterised by the systematic uncertainties at low m_{T}^{W} and, in contrast, the statistical uncertainty at high m_{T}^{W}. All in all, a reasonable agreement within the uncertainty band between the PWG+PY8 distribution and the unfolded data distribution is found in both channels.

An alternative representation of the measured cross-sections is shown in Tab. 13.1 and Tab. 13.2, where the contribution of each single systematic uncertainty is included.

Table 13.1: Final measured single-differential cross-section as a function of the transverse mass of the W boson where the statistical and systematic uncertainties (larger than 0.5%) are shown separately for the e^{-} channel.

bin edges [GeV]	200 - 250	250 - 300	300 - 350	350 - 425	425 - 500	500 - 600	600 - 750	750 - 900	900 - 1100	1100 - 1400	1400 - 2000
σ [pb/GeV]	6.32e-01	2.46e-01	1.13e-01	7.67e-02	3.43e-02	1.98e-02	1.16e-02	4.07e-03	1.92e-03	7.80e-04	2.58e-04
Data stat. unc. [%]	0.55	0.88	1.26	1.55	2.28	2.94	3.63	5.84	8.32	12.27	20.65
MC stat. unc. [%]	0.52	0.72	0.90	0.96	1.26	1.26	2.03	4.53	7.39	2.74	4.77
tot. sys. unc. [%]	3.55 -4.74	3.55 -4.25	4.14 -4.14	4.68 -4.17	4.80 -4.17	5.34 -4.92	5.59 -5.37	5.66 -5.45	5.86 -5.48	6.10 -5.54	6.19 -5.60
SoftTrk Scale	-0.94 0.94	-0.25 0.25	-0.09 0.10	-0.04 0.04	-0.00 0.00	-0.03 0.03	-0.01 0.01	-0.04 0.04	-0.04 0.04	-0.04 0.04	-0.03 0.03
SoftTrk ResoPara	-0.58	-0.25	-0.17	-0.14	-0.10	-0.07	-0.01	-0.01	-0.01	-0.01	-0.01
SoftTrk ResoPerp	-0.72	-0.33	-0.17	-0.09	-0.05	-0.06	-0.05	-0.06	-0.04	-0.03	-0.03
EG SCALE S12	-0.36 0.36	-0.37 0.37	-0.40 0.40	-0.48 0.48	-0.56 0.56	-0.61 0.61	-0.63 0.63	-0.65 0.65	-0.73 0.73	-0.85 0.85	-0.94 0.94
EG SCALE LARCALIB	-0.34 0.34	-0.36 0.36	-0.39 0.39	-0.47 0.47	-0.58 0.58	-0.64 0.64	-0.66 0.66	-0.70 0.70	-0.82 0.82	-0.97 0.97	-1.09 1.09
EG SCALE L1GAIN	0.12 -0.12	0.19 -0.19	0.29 -0.29	0.37 -0.37	0.42 -0.42	0.44 -0.44	0.41 -0.41	0.34 -0.34	0.26 -0.26	0.17 -0.17	0.07 -0.07
EG SCALE L2GAIN	0.73 -0.73	0.97 -0.97	1.16 -1.16	1.41 -1.41	1.64 -1.64	1.68 -1.68	1.70 -1.70	1.76 -1.76	2.06 -2.06	2.52 -2.52	2.80 -2.80
JER EffNP 1	1.56 -1.55	0.66 -0.65	0.29 -0.29	-0.01 0.01	-0.12 0.12	-0.01 0.01	-0.00 0.00	0.03 -0.03	0.04 -0.04	0.04 -0.04	0.02 -0.02
JER EffNP 2	1.01 -1.01	0.60 -0.60	0.37 -0.37	0.17 -0.17	0.09 -0.09	0.10 -0.10	0.05 -0.05	0.05 -0.05	0.05 -0.05	0.02 -0.02	-0.03 0.03
JER EffNP 3	0.66 -0.66	0.42 -0.42	0.27 -0.27	0.13 -0.13	0.04 -0.04	0.02 -0.02	0.01 -0.01	0.02 -0.02	0.01 -0.01	-0.01 0.01	-0.03 0.03
JER EffNP 4	0.73 -0.73	0.33 -0.33	0.11 -0.11	0.02 -0.02	-0.00 0.00	0.01 -0.01	0.00 -0.00	0.01 -0.01	0.00 -0.00	-0.02 0.02	-0.04 0.04
JER EffNP 5	0.51 -0.51	0.30 -0.30	0.16 -0.16	0.04 -0.04	-0.00 0.00	0.02 -0.02	0.02 -0.02	0.03 -0.03	0.02 -0.02	0.00 -0.00	-0.01 0.01
JER EffNP 6	0.60 -0.60	0.39 -0.39	0.22 -0.22	0.05 -0.05	-0.02 0.02	-0.01 0.01	-0.01 0.01	0.00 -0.00	0.01 -0.01	0.01 -0.01	0.00 -0.00
JER EffNP 7	0.64 -0.64	0.33 -0.33	0.17 -0.17	0.02 -0.02	-0.04 0.04	-0.00 0.00	-0.01 0.01	0.01 -0.01	0.01 -0.01	0.01 -0.01	0.00 -0.00
JES EffNP Model1	0.00 -0.00	-0.08 0.08	-0.12 0.12	-0.14 0.14	-0.13 0.13	-0.08 0.08	-0.03 0.03	-0.01 0.01	-0.01 0.01	-0.02 0.02	-0.02 0.02
JES EtaIntercalib Model	0.27 -0.27	0.07 -0.07	-0.05 0.05	-0.12 0.12	-0.11 0.11	-0.06 0.06	-0.04 0.04	-0.02 0.02	-0.01 0.01	0.00 -0.00	0.01 -0.01
JES Flavor Composition	0.18 -0.18	-0.11 0.11	-0.27 0.27	-0.32 0.32	-0.27 0.27	-0.17 0.17	-0.09 0.09	-0.04 0.04	-0.03 0.03	-0.03 0.03	-0.02 0.02
JES Flavor Response	0.12 -0.12	0.27 -0.27	0.32 -0.32	0.34 -0.34	0.31 -0.31	0.21 -0.21	0.11 -0.11	0.07 -0.07	0.08 -0.08	0.08 -0.08	0.08 -0.08
JES Pileup OffsetMu	0.50 -0.50	0.15 -0.15	0.05 -0.05	0.06 -0.06	0.04 -0.04	0.01 -0.01	-0.02 0.02	-0.01 0.01	-0.01 0.01	-0.00 0.00	-0.01 0.01
JES Pileup OffsetNPV	0.14 -0.14	-0.05 0.05	-0.10 0.10	-0.11 0.11	-0.11 0.11	-0.08 0.08	-0.04 0.04	-0.00 0.00	0.01 -0.01	0.01 -0.01	0.01 -0.01
JES Pileup RhoTopo	0.02 -0.02	-0.10 0.10	-0.15 0.15	-0.17 0.17	-0.18 0.18	-0.13 0.13	-0.06 0.06	-0.02 0.02	-0.02 0.02	-0.02 0.02	-0.02 0.02
EL SF ID	1.11 -1.11	1.36 -1.36	1.68 -1.68	1.97 -1.97	2.68 -2.68	3.78 -3.78	4.46 -4.46	4.52 -4.52	4.49 -4.49	4.39 -4.39	4.36 -4.36
EL SF Isol	0.24 -0.24	0.45 -0.45	0.74 -0.74	0.90 -0.90	0.99 -0.99	1.23 -1.23	1.56 -1.56	1.71 -1.71	1.68 -1.68	1.54 -1.54	1.45 -1.45
PU SF	0.28 -0.28	-0.15 0.15	-0.32 0.33	-0.35 0.35	-0.28 0.28	-0.16 0.16	-0.12 0.12	-0.10 0.10	-0.06 0.06	-0.03 0.03	-0.03 0.03
MJ EL MET	-1.93 1.03	-1.56 0.98	-1.30 0.92	-1.33 1.03	-1.25 1.07	-1.39 1.28	-1.00 1.01	-1.12 1.15	-1.07 1.13	-0.84 0.80	-0.31 0.02
MJ EL 1jet	0.09	0.02	-0.00	-0.02	-0.03	-0.02	-0.00	0.00	0.00	-0.00	-0.00
MJ EL MC scaling	1.18 -1.18	1.05 -1.05	0.92 -0.92	0.93 -0.93	0.81 -0.81	0.71 -0.71	0.39 -0.39	0.39 -0.39	0.40 -0.40	0.45 -0.45	0.38 -0.38
MJ EL mixMET	-2.70	-2.87	-2.63	-2.30	-1.28	-0.54	0.29	1.15	1.93	2.47	2.32
FSR	-0.18 0.32	-0.21 0.36	-0.20 0.32	-0.20 0.42	-0.45 0.93	-0.77 1.69	-0.52 1.60	-0.09 1.11	0.13 0.65	0.10 0.33	0.10 0.35
$t\bar{t}$ $\mu_R = 2.0$, $\mu_F = 1.0$	-0.52	-0.99	-1.22	-1.21	-1.03	-0.95	-0.65	-0.45	-0.32	-0.20	-0.25
$t\bar{t}$ $\mu_R = 0.5$, $\mu_F = 0.5$	0.65	1.27	1.59	1.62	1.48	1.48	1.04	0.60	0.29	0.13	0.13
$t\bar{t}$ hardscatter	0.77	1.45	1.81	2.05	1.68	0.47	-0.74	-0.53	0.35	0.60	0.76
$t\bar{t}$ hadronisation	0.39	1.28	1.85	2.18	1.75	1.03	0.10	-0.33	-0.21	0.22	0.97
$t\bar{t}$ hdamp	-0.07	0.01	0.26	0.45	0.37	0.02	-0.33	-0.28	-0.01	0.10	0.13
$t\bar{t}$ NNPDF RMS	-0.14 0.14	-0.32 0.32	-0.46 0.46	-0.48 0.48	-0.49 0.49	-0.45 0.45	-0.35 0.35	-0.25 0.25	-0.23 0.23	-0.26 0.26	-0.18 0.18

Table 13.2: Final measured single-differential cross-section as a function of the transverse mass of the W boson where the statistical and systematic uncertainties (larger than 0.5%) are shown separately for the e^+ channel.

bin edges [GeV]	200 - 250	250 - 300	300 - 350	350 - 425	425 - 500	500 - 600	600 - 750	750 - 900	900 - 1100	1100 - 1400	1400 - 2000
σ [pb/GeV]	1.04e+00	4.27e-01	2.03e-01	1.42e-01	6.20e-02	3.97e-02	2.23e-02	8.21e-03	4.42e-03	1.97e-03	6.99e-04
Data stat. unc. [%]	0.40	0.61	0.86	1.06	1.54	1.92	2.48	3.86	5.10	7.25	12.19
MC stat. unc. [%]	0.42	0.51	0.69	0.70	1.23	1.04	1.64	1.23	1.17	1.34	2.69
tot. sys. unc. [%]	2.40 -3.20	2.42 -3.07	2.69 -3.02	2.93 -3.16	3.42 -3.48	4.36 -4.29	5.06 -4.96	5.32 -5.22	5.40 -5.90	5.22 -5.58	5.61 -5.71
SoftTrk Scale	-0.68 0.68	-0.25 0.25	-0.13 0.13	-0.08 0.08	-0.03 0.03	-0.02 0.02	-0.01 0.01	-0.00 0.00	-0.01 0.01	-0.00 0.00	0.00 -0.00
SoftTrk ResoPara	-0.52	-0.09	-0.03	-0.04	-0.04	-0.06	-0.07	-0.06	-0.05	-0.02	0.00
SoftTrk ResoPerp	-0.62	-0.25	-0.09	-0.04	-0.03	-0.04	-0.05	-0.02	0.01	0.03	0.04
EG SCALE S12	-0.33 0.33	-0.34 0.34	-0.36 0.36	-0.38 0.38	-0.44 0.44	-0.48 0.48	-0.49 0.49	-0.54 0.54	-0.63 0.63	-0.72 0.72	-0.75 0.75
EG SCALE LARCALIB	-0.31 0.31	-0.33 0.33	-0.36 0.36	-0.43 0.43	-0.50 0.50	-0.53 0.53	-0.54 0.54	-0.61 0.61	-0.74 0.74	-0.86 0.86	-0.93 0.93
EG SCALE L1GAIN	0.16 -0.16	0.18 -0.18	0.21 -0.21	0.24 -0.24	0.28 -0.28	0.28 -0.28	0.23 -0.23	0.16 -0.16	0.11 -0.11	0.07 -0.07	0.05 -0.05
EG SCALE L2GAIN	0.63 -0.63	0.86 -0.86	1.00 -1.00	1.09 -1.09	1.23 -1.23	1.36 -1.36	1.51 -1.51	1.76 -1.76	2.02 -2.02	2.25 -2.25	2.52 -2.52
JER EffNP 1	0.90 -0.90	0.44 -0.44	0.29 -0.29	0.25 -0.25	0.22 -0.22	0.17 -0.17	0.12 -0.12	0.09 -0.09	0.10 -0.10	0.10 -0.10	0.10 -0.10
JER EffNP 2	0.64 -0.64	0.42 -0.42	0.30 -0.30	0.16 -0.16	0.08 -0.08	0.05 -0.05	0.01 -0.01	0.03 -0.03	0.09 -0.09	0.11 -0.11	0.10 -0.10
JER EffNP 3	0.43 -0.43	0.22 -0.22	0.11 -0.11	0.09 -0.09	0.11 -0.11	0.10 -0.10	0.04 -0.04	-0.02 0.02	-0.01 0.01	0.02 -0.02	0.03 -0.03
JER EffNP 4	0.40 -0.40	0.26 -0.26	0.17 -0.17	0.13 -0.13	0.12 -0.12	0.10 -0.10	0.06 -0.06	0.04 -0.04	0.05 -0.05	0.05 -0.05	0.04 -0.04
JER EffNP 5	0.28 -0.28	0.22 -0.22	0.20 -0.20	0.20 -0.20	0.18 -0.18	0.12 -0.12	0.07 -0.07	0.05 -0.05	0.05 -0.05	0.04 -0.04	0.04 -0.04
JER EffNP 6	0.28 -0.28	0.19 -0.19	0.17 -0.17	0.16 -0.16	0.13 -0.13	0.09 -0.09	0.05 -0.05	0.03 -0.03	0.04 -0.04	0.04 -0.04	0.04 -0.04
JER EffNP 7	0.42 -0.42	0.27 -0.27	0.15 -0.15	0.10 -0.10	0.11 -0.11	0.09 -0.09	0.06 -0.06	0.04 -0.04	0.04 -0.04	0.04 -0.04	0.04 -0.04
JES EffNP Model1	-0.05 0.05	-0.05 0.05	-0.03 0.03	-0.02 0.02	-0.04 0.04	-0.06 0.06	-0.04 0.04	-0.01 0.01	-0.00 0.00	-0.02 0.02	-0.04 0.04
JES EtaIntercalib Model	0.16 -0.16	0.02 -0.02	-0.01 0.01	-0.02 0.02	-0.05 0.05	-0.06 0.06	-0.03 0.03	-0.01 0.01	0.01 -0.01	0.00 -0.00	0.00 -0.00
JES Flavor Composition	0.05 -0.05	-0.01 0.01	-0.05 0.05	-0.09 0.09	-0.11 0.11	-0.09 0.09	-0.07 0.07	-0.05 0.05	-0.04 0.04	-0.04 0.04	-0.04 0.04
JES Flavor Response	0.01 -0.01	0.18 -0.18	0.23 -0.23	0.19 -0.19	0.14 -0.14	0.09 -0.09	0.05 -0.05	0.03 -0.03	0.03 -0.03	0.04 -0.04	0.05 -0.05
JES Pileup OffsetMu	0.34 -0.34	0.22 -0.22	0.12 -0.12	0.07 -0.07	0.03 -0.03	0.00 -0.00	0.01 -0.01	0.00 -0.00	0.00 -0.00	-0.00 0.00	-0.01 0.01
JES Pileup OffsetNPV	0.13 -0.13	0.06 -0.06	-0.01 0.01	-0.05 0.05	-0.06 0.06	-0.05 0.05	-0.03 0.03	-0.01 0.01	0.00 -0.00	-0.00 0.00	-0.02 0.02
JES Pileup RhoTopo	0.00 -0.00	-0.04 0.04	-0.04 0.04	-0.03 0.03	-0.04 0.04	-0.06 0.06	-0.05 0.05	-0.03 0.03	-0.02 0.02	-0.02 0.02	-0.03 0.03
EL SF ID	1.07 -1.07	1.26 -1.26	1.53 -1.53	1.78 -1.78	2.47 -2.47	3.64 -3.64	4.33 -4.33	4.48 -4.48	4.43 -4.43	4.34 -4.34	4.34 -4.34
EL SF Isol	0.23 -0.23	0.42 -0.42	0.70 -0.70	0.85 -0.85	0.93 -0.93	1.15 -1.15	1.42 -1.42	1.57 -1.57	1.53 -1.53	1.42 -1.42	1.37 -1.37
PU SF	0.13 -0.13	-0.17 0.17	-0.24 0.24	-0.28 0.28	-0.36 0.36	-0.39 0.39	-0.30 0.30	-0.18 0.18	-0.14 0.14	-0.17 0.17	-0.22 0.22
MJ EL MET	-1.21 0.65	-1.04 0.63	-0.84 0.58	-0.86 0.69	-0.80 0.73	-0.61 0.60	-0.74 0.75	-0.77 0.82	-0.70 0.73	0.04 -0.04	-0.78 0.88
MJ EL 1jet	0.07	0.02	-0.00	-0.02	-0.02	-0.01	-0.00	-0.00	0.00	-0.00	-0.00
MJ EL MC scaling	0.73 -0.73	0.66 -0.66	0.57 -0.57	0.59 -0.59	0.50 -0.50	0.32 -0.32	0.33 -0.33	0.29 -0.29	0.21 -0.21	-0.01 0.01	0.17 -0.17
MJ EL mixMET	-1.75	-1.96	-1.73	-1.62	-1.21	-0.59	-0.03	0.82	1.13	-0.05	1.45
FSR	-0.15 0.17	-0.17 0.19	-0.14 0.29	-0.11 0.46	-0.07 0.53	-0.04 0.67	-0.02 0.80	0.11 0.54	-0.08 0.35	-0.28 0.07	-0.41 0.04
$t\bar{t}$ $\mu_R = 2.0$, $\mu_F = 1.0$	-0.35	-0.61	-0.68	-0.62	-0.57	-0.49	-0.41	-0.26	-0.21	-0.05	-0.03
$t\bar{t}$ $\mu_R = 0.5$, $\mu_F = 0.5$	0.45	0.80	0.90	0.91	0.88	0.76	0.64	0.43	0.42	0.14	0.10
$t\bar{t}$ hardscatter	0.41	0.67	0.72	0.63	0.44	0.20	0.07	0.12	-0.27	-0.49	-0.69
$t\bar{t}$ hadronisation	0.17	0.51	0.69	0.66	0.54	0.37	0.18	-0.02	-1.76	-1.30	-1.10
$t\bar{t}$ hdamp	0.01	0.14	0.13	-0.02	-0.11	-0.08	-0.04	-0.28	-2.02	-1.37	-1.23
$t\bar{t}$ NNPDF RMS	-0.09 0.09	-0.19 0.19	-0.26 0.26	-0.28 0.28	-0.27 0.27	-0.21 0.21	-0.20 0.20	-0.09 0.09	-0.08 0.08	-0.02 0.02	-0.03 0.03

13.2 Unfolded double-differential cross-section in $m_{\mathrm{T}}^W \otimes |\eta(e)|$

The final unfolded double-differential cross-section as a function of the transverse mass of the W boson and the absolute value of the electron's pseudorapiditiy, $m_{\mathrm{T}}^W \otimes |\eta(e)|$, for the e^- and the e^+ channel are presented in Figure 13.2 and Figure 13.3, respectively. The unfolded distribution of the absolute value of the pseudorapidity of the electron $|\eta(e)|$ is separately shown for each m_{T}^W bin. As for the single-differential cross-section, the statistical uncertainties of data are represented by black error bars, while the systematic and total

uncertainty is accounted for by the light and dark uncertainty band, respectively. In addition, the statistical uncertainty of the MC processes is included in the total uncertainty band and the fiducial distribution of the signal MC, labelled as `PWG+PY8`, is added.

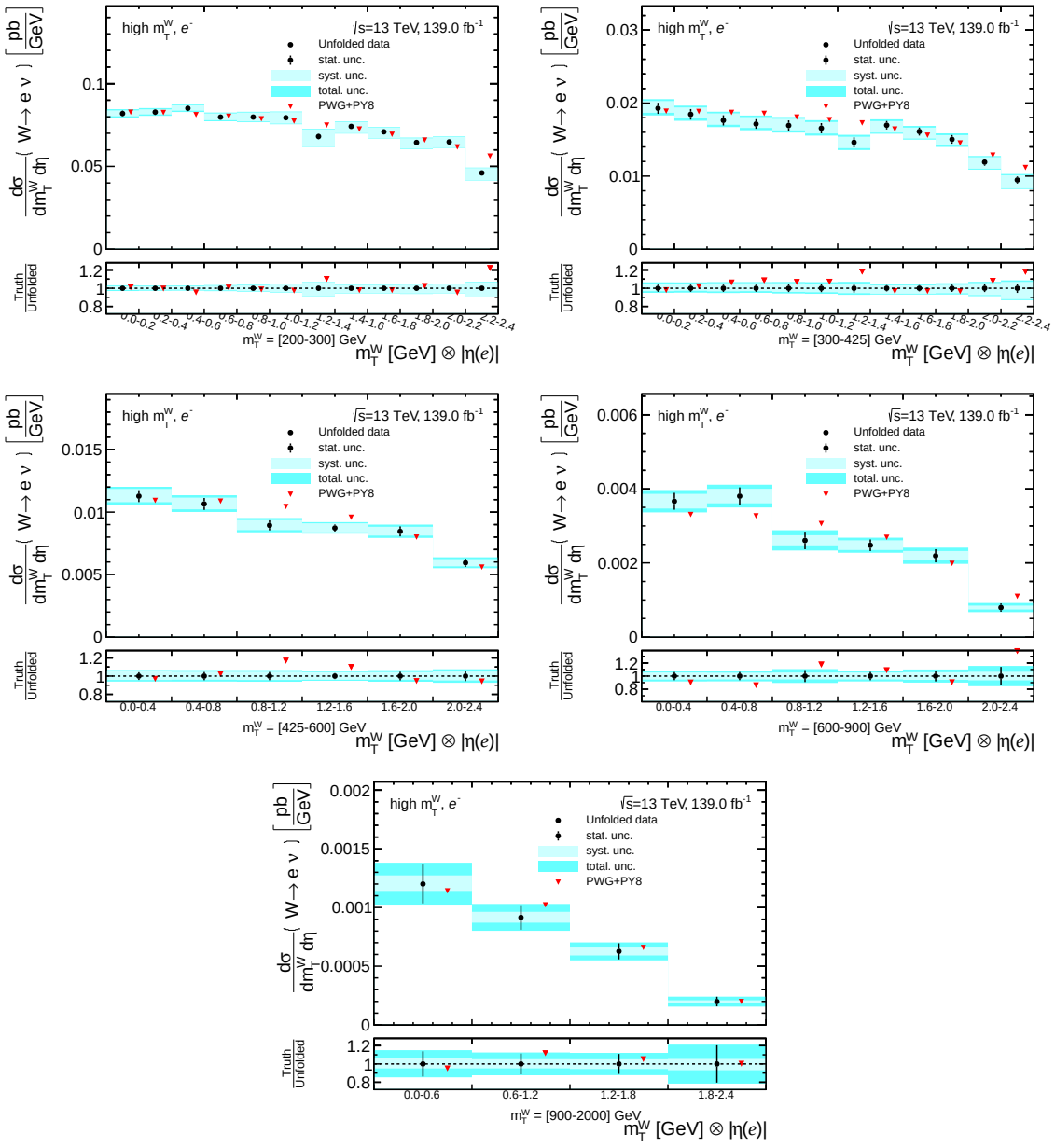

Figure 13.2: Unfolded double-differential cross-section as a function of the transverse momentum of the W boson and the absolute value of the electron's pseudorapidity, $m_{\mathrm{T}}^{W} \otimes |\eta(e)|$ in the e^- channel. The statistical uncertainty of the data is represented by uncertainty bars. The statistical uncertainty of the MC samples, obtained from the covariance matrix, and the systematic uncertainties with an impact of more than 0.5% are included in the uncertainty band.

In Figure 13.2, the double-differential cross-section in $m_T^W \otimes |\eta(e)|$ in the e^- channel is shown. From theoretical physics point of view, a smooth $|\eta(e)|$ distribution, as described by the PWG+PY8 MC, is expected. While mostly smooth $|\eta(e)|$ distributions are observed in the

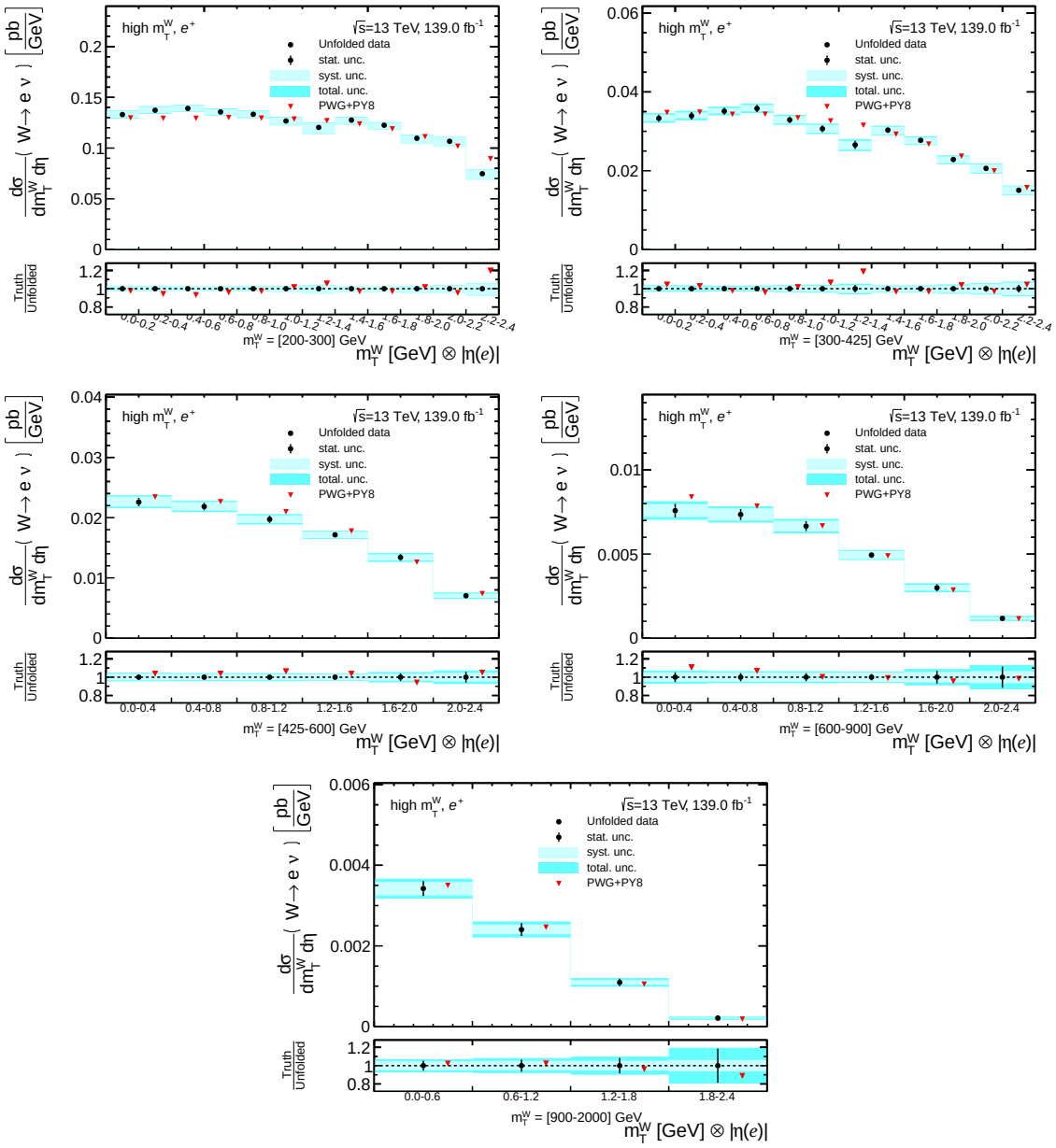

Figure 13.3: Unfolded double-differential cross-section as a function of the transverse momentum of the W boson and the absolute value of the electron's pseudorapidity, $m_T^W \otimes |\eta(e)|$ in the e^+ channel. The statistical uncertainty of the data is represented by uncertainty bars. The statistical uncertainty of the MC samples, obtained from the covariance matrix, and the systematic uncertainties with an impact of more than 0.5% are included in the uncertainty band.

third and fifth m_{T}^{W} bin, several discontinuities are found in the other m_{T}^{W} bins. Two small drops are located in the range of $1.2 < |\eta(e)| < 1.4$ and the last $|\eta(e)|$ bin of the first and second m_{T}^{W} bin, which are related to the differences observed in the agreement between data and the prediction at reconstructed level. As discussed in Chapter 10, deviations might partially originate from the too coarse binning of the electron scale factor that is used.
In Figure 13.3, the double-differential cross-section in $m_{\mathrm{T}}^{W} \otimes |\eta(e)|$ in the e^{+} channel is shown. Similar discontinuities, as discussed for the e^{-} channel, are found in the first and second m_{T}^{W} bin. In contrast, a smooth $|\eta(e)|$ distribution is obtained in the last three m_{T}^{W} bins.
The ratio between the unfolded data and the distribution at fiducial level of the `PWG+PY8` MC sample is shown for each unfolded distribution in both channels, where agreement within the total uncertainty band is found in most bins. Overall, a more precise agreement between the `PWG+PY8` MC and unfolded data is found in the e^{+} channel.
The tabular representation of the measured double-differential cross-section, including the contribution of each systematic uncertainties separately, are shown in Appendix G.

A consistency test of the single- and double-differential cross-sections is performed, where the single-differential cross-section is integrated across m_{T}^{W} bins in order to match the binning of the double-differential cross-section measurement and compared to the cross-section from the double-differential cross-section measurement, where the integration has to be done across the $|\eta(e)|$ bins. Both cross-sections, binned in m_{T}^{W}, and the relative difference obtained from the single-differential, labelled *1D*, and the double-differential, labelled *2D*, cross-section measurement are presented in Tab. 13.3.

Table 13.3: Consistency check between the single-differential cross-section as a function of m_{T}^{W} and the single-differential cross-section obtained from the integration of the $|\eta(e)|$ bins in each m_{T}^{W} bin.

bin edges [GeV]	200 - 300	300 - 425	425 - 600	600 - 900	900 - 2000
e^{+}					
$\frac{d\sigma}{dm_{\mathrm{T}}^{W}}$ from 1D [pb/GeV]	1.47e+00	3.45e-01	1.02e-01	3.05e-02	7.08e-03
$\frac{d\sigma}{dm_{\mathrm{T}}^{W}}$ from 2D [pb/GeV]	1.46e+00	3.42e-01	1.02e-01	3.06e-02	7.11e-03
rel. difference [%]	-0.47	-0.69	0.31	0.57	0.43
e^{-}					
$\frac{d\sigma}{dm_{\mathrm{T}}^{W}}$ from 1D [pb/GeV]	8.78e-01	1.90e-01	5.41e-02	1.57e-02	2.95e-03
$\frac{d\sigma}{dm_{\mathrm{T}}^{W}}$ from 2D [pb/GeV]	8.75e-01	1.89e-01	5.42e-02	1.56e-02	2.96e-03
rel. difference [%]	-0.35	-0.45	0.059	0.53	0.085

As a result, relative differences of less than a percent for the e^{+} and the e^{-} channel are observed, i.e. the differential cross-sections as a function of m_{T}^{W} from the single and double-differential measurement are consistent.

14 Conclusion and Outlook

In this thesis, the measurement of the single-differential cross-section as a function of the transverse mass of the W boson, m_{T}^{W}, produced in the charged-current Drell-Yan (ccDY) process, consisting of the production of a W boson that decays into an electron and an electron neutrino, was presented. In addition, the double-differential cross-section as a function of the transverse mass of the W boson and the absolute value of the electron's pseudorapidity, $m_{\mathrm{T}}^{W} \otimes |\eta(e)|$, was measured. The analysed dataset was recorded by the ATLAS experiment at the Large Hadron Collider, where proton proton collisions at a centre-of-mass energy of $\sqrt{s} = 13\,\mathrm{TeV}$ are recorded during Run 2, corresponding to an integrated luminosity of $\mathcal{L} = 139\ \mathrm{fb}^{-1}$.
The cross-sections were measured for transverse masses ranging from $m_{\mathrm{T}}^{W} = 200\,\mathrm{GeV}$ up to $m_{\mathrm{T}}^{W} = 2000\,\mathrm{GeV}$ and the absolute value of the electron's pseudorapidity in the range of $|\eta(e)| \in [0.0, 2.4]$. The region of high transverse masses of the W boson is expected to provide sensitivity to PDFs and parameters of effective field theories. In particular the double-differential cross-section as a function of $m_{\mathrm{T}}^{W} \otimes \eta$ is expected to allow for constraints on the partonic content of the proton.

A dedicated event selection in order to select a high fraction of ccDY events is defined, where one single electron and transverse missing momentum in the final state is required. Furthermore, each event has to fulfil a transverse mass of the W boson $m_{\mathrm{T}}^{W} > 150\,\mathrm{GeV}$, a transverse momentum of the electron $p_{\mathrm{T}}(e) > 65\,\mathrm{GeV}$, an absolute value of the electron's pseudorapiditiy $|\eta(e)| < 2.4$ and a missing transverse momentum $E_{\mathrm{T}}^{\mathrm{miss}} > 85\,\mathrm{GeV}$. The number of expected events from signal and background processes is mostly predicted by Monte Carlo (MC) simulations. Only the number of events corresponding to the so-called multijet (MJ) background relies on the data-driven Matrix Method. The MJ background consists of *fake* electrons, which are objects such as jets, that are misidentified as electrons in the detector. One of the main achievements of this thesis is a detailed investigation of occurring issues in data-driven methods that depend on the $E_{\mathrm{T}}^{\mathrm{miss}}$ modelling. A systematic uncertainty that targets differences in the $E_{\mathrm{T}}^{\mathrm{miss}}$ based on the composition of true objects in data that result in fake electrons is developed. The number of predicted events according to the Standard Model are compared to data events. Overall, a good agreement in all investigated variables is found. The ccDY process contributes with 67.5 % and 56.9 % in the e^{+} and e^{-} channel, while the largest background originates from $t\bar{t}$ production with 20.6 % and 28.0 % in the e^{+} and e^{-} channel.
A substantial amount of events produced at the peak of the W boson mass distribution migrate in particular to the first bins of the m_{T}^{W} and $m_{\mathrm{T}}^{W} \otimes |\eta(e)|$ distributions. The measured data distributions are unfolded to a fiducial volume at the born level using the technique of Iterative Bayesian Unfolding (IBU), where the iterative procedure is well-suited to correct for migrations. The fiducial volume is characterised by the following requirements at born level: A transverse mass of the W boson $m_{\mathrm{T}}^{W}(born) > 200\,\mathrm{GeV}$, a transverse momentum

of the electron $p_{\mathrm{T}}(e_{\mathrm{born}}) > 65\,\mathrm{GeV}$, an absolute value of the electron's pseudorapiditiy $|\eta(e_{\mathrm{born}})| < 2.4$ and a transverse momentum of the electron neutrino $p_{\mathrm{T}}(\nu_{\mathrm{e}}) > 85\,\mathrm{GeV}$. Further achievements are the optimisation of the unfolding, where the optimal regularisation parameter, i.e. the number of iterations, is studied and a detector-motivated binning is introduced to account for peculiarities of the detector.
Statistical and systematic uncertainties on the unfolded differential cross-sections are estimated. The experimental systematic uncertainties on the signal process, the theoretical systematic uncertainties of the $t\bar{t}$ process and the systematic uncertainties of the MJ background were studied. Only the ones with an impact with at least 0.5% on the cross-section in any bin of the measured variables are considered for the final results. After the unfolding, the largest contributions correspond to the systematic uncertainties of the MJ background and the systematic uncertainty corresponding to the electron scale factor. For this thesis, it has been concluded that the theoretical uncertainties on the ccDY process are very small and consequently were neglected. A more detailed study based on the full Run 2 dataset could offer the possibility to validate or disproof this assumption. While the systematic uncertainties yield with $2-5\%$ the largest fraction of the total uncertainty for $m_{\mathrm{T}}^{W} < 750\,\mathrm{GeV}$, the statistical uncertainty becomes dominant for $m_{\mathrm{T}}^{W} > 1000\,\mathrm{GeV}$. In between, both sources of uncertainties are approximately of the same size. The highest sensitivity with a total uncertainty of $2-3\%$ and $3-4\%$ is found for the e^{+} and e^{-} channel in the range of $m_{\mathrm{T}}^{W} \in [250, 350]\,\mathrm{GeV}$.
The unfolded differential cross-sections are compared to the fiducial level distributions obtained from the signal MC, referred to as `Powheg+Pythia8`. All in all, a reasonable agreement between the distributions of the unfolded differential cross-sections and `Powheg+Pythia8` within the given uncertainties is found. Deviations between the double-differential cross-sections and `Powheg+Pythia8` are present in the range of $1.2 < |\eta(e)| < 1.4$ and $|\eta(e)| \in [2.2, 2.4]$ in each of the low m_{T}^{W} bins. These differences are expected to partially originate from a too coarse binning of the electron scale factor. In the end, the consistency between the unfolded single-differential cross-section and the unfolded double-differential cross-section as a function of m_{T}^{W} is shown.

The reported single-differential and double-differential cross-sections of the charged-current Drell-Yan process can be improved in several ways. Especially, a finer binned electron scale factor offers the opportunity to substantially improve the agreement between unfolded results and the fiducial level distribution of `Powheg+Pythia8` in the double-differential cross-section measurement. In addition, the estimation of the systematic uncertainty associated to the unfolding procedure would allow to obtain the final size of the total systematic uncertainty. The single-differential and double-differential cross-sections represent the basis for several future studies. The combination of the cross-sections of the e^{+} and e^{-} channel with the cross-sections of the μ^{+} and μ^{-} channel, obtained in the parallel measurement as described in Reference [46], would provide a consistency check of lepton universality. Furthermore, the presented cross-sections allow constraining the parton distribution functions of the proton and parameters of effective field theories.

A MC samples and theoretical cross-sections

Table A.1: Overview of the various samples for positively charged W bosons decaying into a positron and an electron neutrino. The inclusive cross-section is given for the first sample, where the m_W^{max} requirement has to be fulfilled afterwards, reducing the given cross-section effectively. In contrast, the cross-section in the indicated m_W range is given elsewhere.

process	m_W^{min} [GeV]	m_W^{max} [GeV]	σ [pb]	DSID
$W^+ \to e\nu$	-	120	$1.13 \cdot 10^4$	361100
$W^+ \to e\nu$	120	180	32.1	301060
$W^+ \to e\nu$	180	250	5.00	301061
$W^+ \to e\nu$	250	400	1.75	301062
$W^+ \to e\nu$	400	600	$3.12 \cdot 10^{-1}$	301063
$W^+ \to e\nu$	600	800	$6.08 \cdot 10^{-2}$	301064
$W^+ \to e\nu$	800	1000	$1.77 \cdot 10^{-2}$	301065
$W^+ \to e\nu$	1000	1250	$7.29 \cdot 10^{-3}$	301066
$W^+ \to e\nu$	1250	1500	$2.51 \cdot 10^{-3}$	301067
$W^+ \to e\nu$	1500	1750	$9.86 \cdot 10^{-4}$	301068
$W^+ \to e\nu$	1750	2000	$4.25 \cdot 10^{-4}$	301069
$W^+ \to e\nu$	2000	2250	$1.95 \cdot 10^{-4}$	301070
$W^+ \to e\nu$	2250	2500	$9.33 \cdot 10^{-5}$	301071
$W^+ \to e\nu$	2500	2750	$4.63 \cdot 10^{-5}$	301072
$W^+ \to e\nu$	2750	3000	$2.35 \cdot 10^{-5}$	301073
$W^+ \to e\nu$	3000	3500	$1.84 \cdot 10^{-5}$	301074
$W^+ \to e\nu$	3500	4000	$5.10 \cdot 10^{-6}$	301075
$W^+ \to e\nu$	4000	4500	$1.43 \cdot 10^{-6}$	301076
$W^+ \to e\nu$	4500	5000	$4.01 \cdot 10^{-7}$	301077
$W^+ \to e\nu$	5000	-	$1.53 \cdot 10^{-7}$	301078

Table A.2: Overview of the various samples for negatively charged W bosons decaying into an electron and an anti-electron neutrino. The inclusive cross-section is given for the first sample, where the m_W^{max} requirement has to be fulfilled afterwards, reducing the given cross-section effectively. In contrast, the cross-section in the indicated m_W range is given elsewhere.

process	m_W^{min} [GeV]	m_W^{max} [GeV]	σ [pb]	DSID
$W^- \to e\nu$	-	120	$8.28 \cdot 10^4$	361103
$W^- \to e\nu$	120	180	22.2	301080
$W^- \to e\nu$	180	250	3.28	301081
$W^- \to e\nu$	250	400	1.08	301082
$W^- \to e\nu$	400	600	$1.75 \cdot 10^{-1}$	301083
$W^- \to e\nu$	600	800	$3.10 \cdot 10^{-2}$	301084
$W^- \to e\nu$	800	1000	$8.29 \cdot 10^{-3}$	301085
$W^- \to e\nu$	1000	1250	$3.16 \cdot 10^{-3}$	301086
$W^- \to e\nu$	1250	1500	$1.00 \cdot 10^{-3}$	301087
$W^- \to e\nu$	1500	1750	$3.68 \cdot 10^{-4}$	301088
$W^- \to e\nu$	1750	2000	$1.49 \cdot 10^{-4}$	301089
$W^- \to e\nu$	2000	2250	$6.53 \cdot 10^{-5}$	301090
$W^- \to e\nu$	2250	2500	$3.02 \cdot 10^{-5}$	301091
$W^- \to e\nu$	2500	2750	$1.45 \cdot 10^{-5}$	301092
$W^- \to e\nu$	2750	3000	$7.26 \cdot 10^{-6}$	301093
$W^- \to e\nu$	3000	3500	$5.67 \cdot 10^{-6}$	301094
$W^- \to e\nu$	3500	4000	$1.60 \cdot 10^{-6}$	301095
$W^- \to e\nu$	4000	4500	$4.72 \cdot 10^{-7}$	301096
$W^- \to e\nu$	4500	5000	$1.43 \cdot 10^{-7}$	301097
$W^- \to e\nu$	5000	-	$6.16 \cdot 10^{-8}$	301098

B Issues with large weights from the W MC sample

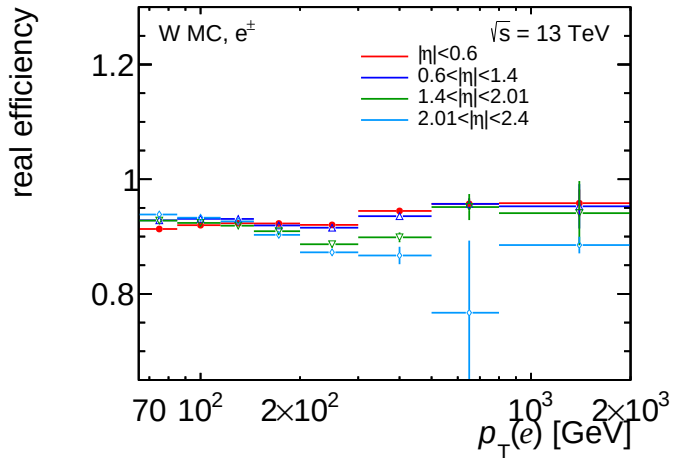

(a)

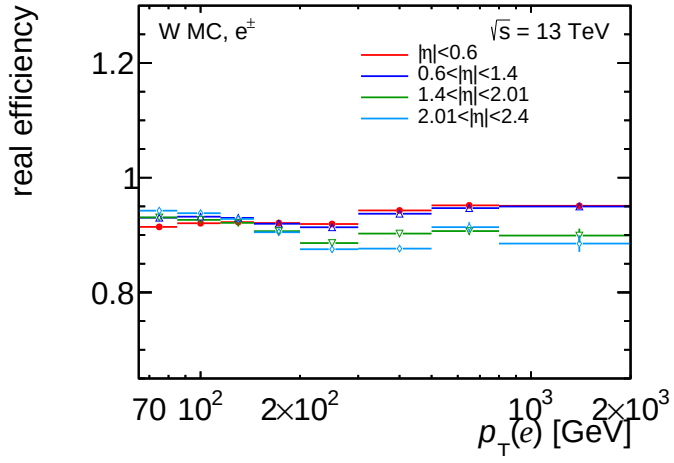

(b)

Figure B.1: Real efficiencies depending on $p_{\mathrm{T}}(e)$ and $|\eta(e)|$ in the electron channel for a) the full W MC and for b) the sliced samples of the W MC only. Single events with large weight in comparison to the weights in the slices migrate to high $p_{\mathrm{T}}(e)$ and induce fluctuations. In this thesis, the real efficiencies are evaluated based on the full W MC.

C Background estimation supplemental material

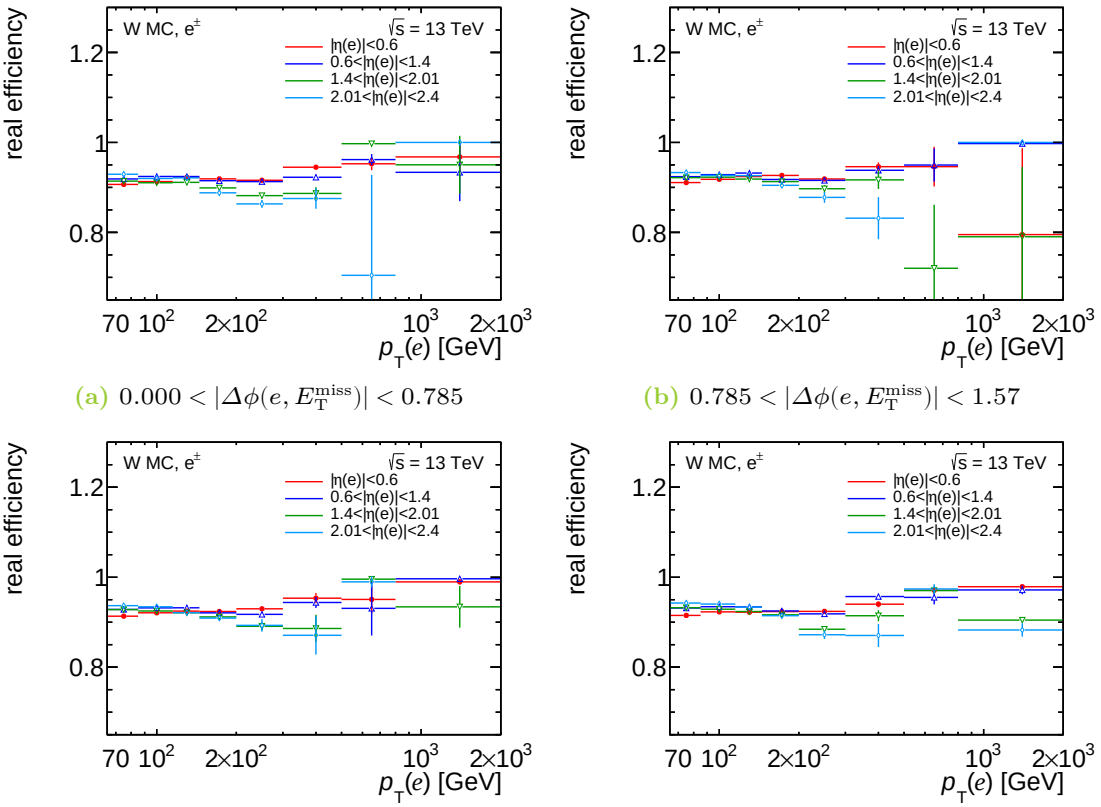

(a) $0.000 < |\Delta\phi(e, E_{\mathrm{T}}^{\mathrm{miss}})| < 0.785$

(b) $0.785 < |\Delta\phi(e, E_{\mathrm{T}}^{\mathrm{miss}})| < 1.57$

(c) $1.57 < |\Delta\phi(e, E_{\mathrm{T}}^{\mathrm{miss}})| < 2.335$

(d) $2.335 < |\Delta\phi(e, E_{\mathrm{T}}^{\mathrm{miss}})| < 3.145$

Figure C.1: Real efficiencies in eight bins of $p_{\mathrm{T}}(e)$, four bins of $|\eta(e)|$ and additionally four bins of $|\Delta\phi(e, E_{\mathrm{T}}^{\mathrm{miss}})|$ in the combined e^+ and e^- channel for the full W MC.

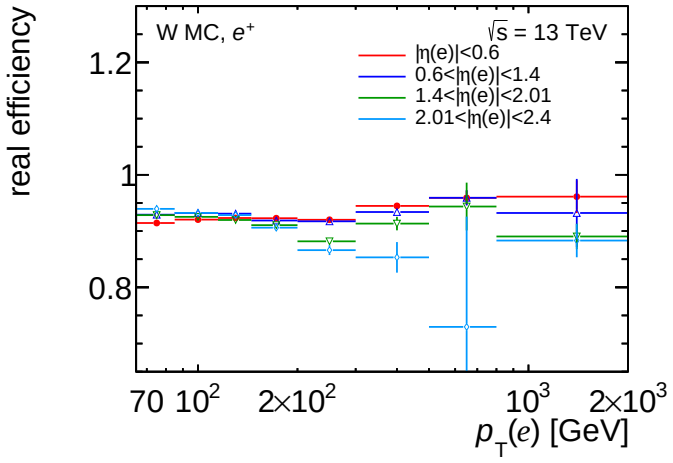

(a)

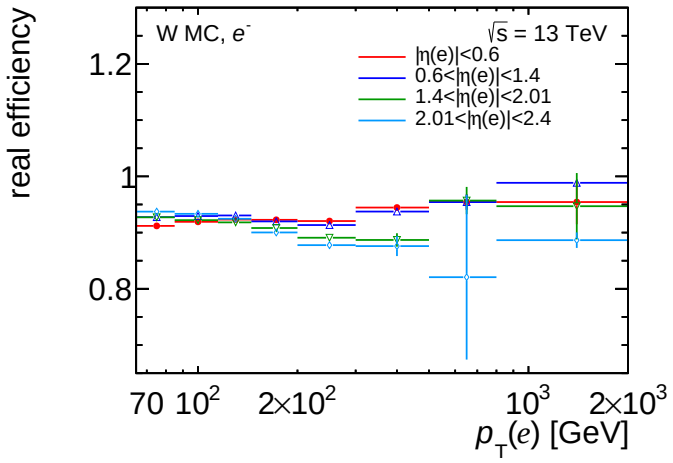

(b)

Figure C.2: Real efficiencies depending on $p_T(e)$ and $|\eta(e)|$ in (a) the e^+ and (b) the e^- channel for the full W MC.

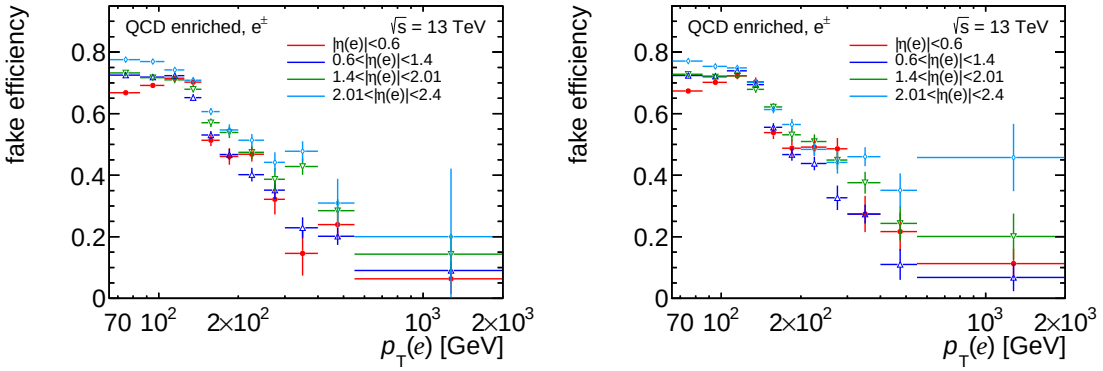

(a) $0.00 < |\Delta\phi(e, E_{\mathrm{T}}^{\mathrm{miss}})| < 0.26$

(b) $0.26 < |\Delta\phi(e, E_{\mathrm{T}}^{\mathrm{miss}})| < 0.52$

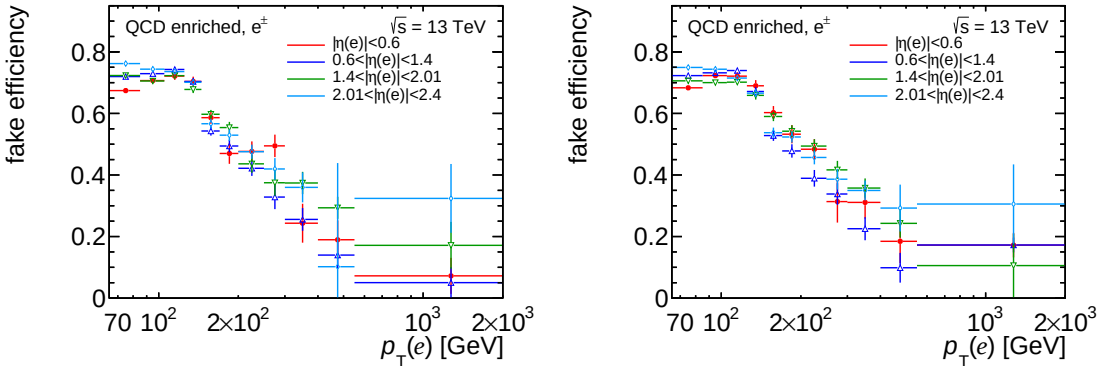

(c) $0.52 < |\Delta\phi(e, E_{\mathrm{T}}^{\mathrm{miss}})| < 0.78$

(d) $0.78 < |\Delta\phi(e, E_{\mathrm{T}}^{\mathrm{miss}})| < 1.05$

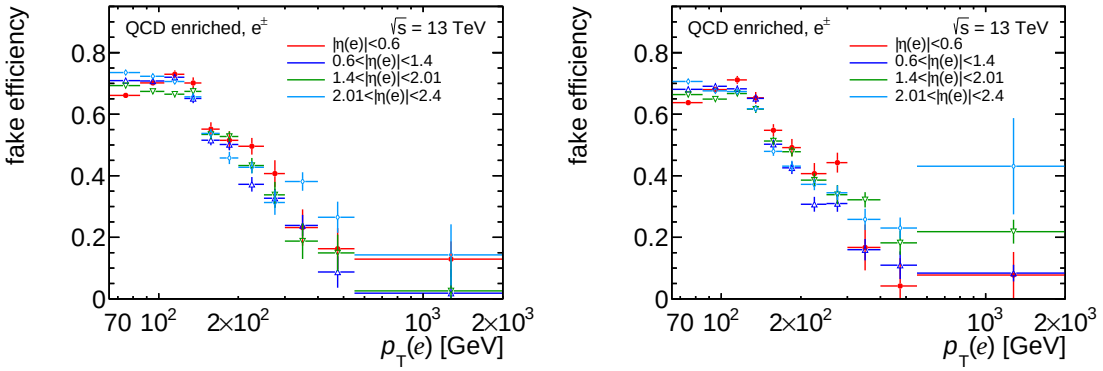

(e) $1.05 < |\Delta\phi(e, E_{\mathrm{T}}^{\mathrm{miss}})| < 1.31$

(f) $1.31 < |\Delta\phi(e, E_{\mathrm{T}}^{\mathrm{miss}})| < 1.57$

Figure C.3: Three-dimensional fake efficiency binned in the transverse momentum $p_{\mathrm{T}}(e)$, the absolute value of the pseudorapidity $\eta(e)$ and the first six bins of the absolute value of the angle between the electron and missing transverse momentum $|\Delta\phi(e, E_{\mathrm{T}}^{\mathrm{miss}})|$ for the `tight` $E_{\mathrm{T}}^{\mathtt{miss}}$ working point.

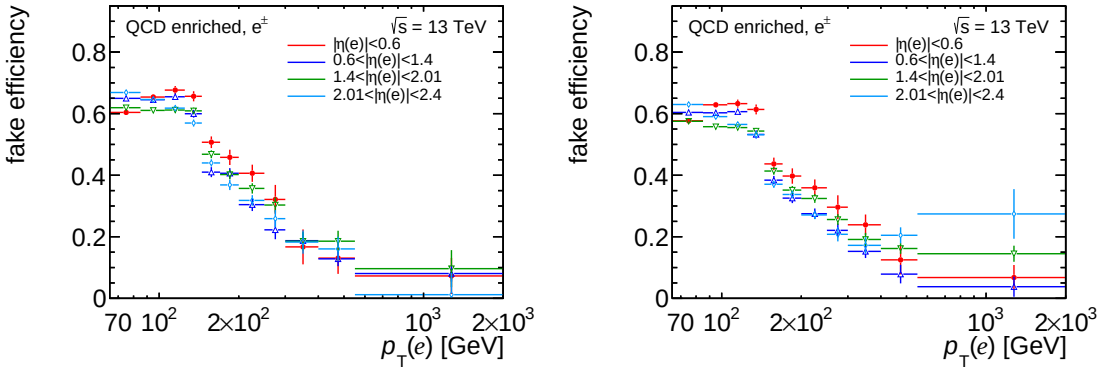

(a) $1.57 < |\Delta\phi(e, E_{\mathrm{T}}^{\mathrm{miss}})| < 1.83$

(b) $1.83 < |\Delta\phi(e, E_{\mathrm{T}}^{\mathrm{miss}})| < 2.09$

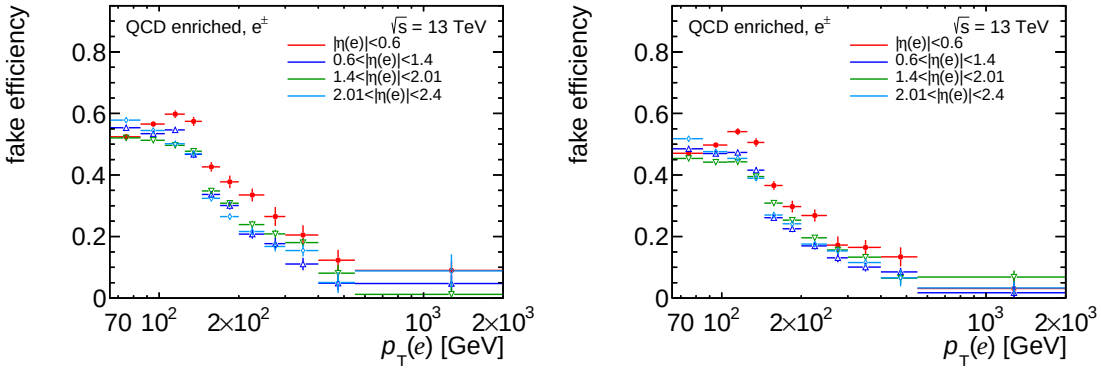

(c) $2.09 < |\Delta\phi(e, E_{\mathrm{T}}^{\mathrm{miss}})| < 2.36$

(d) $2.36 < |\Delta\phi(e, E_{\mathrm{T}}^{\mathrm{miss}})| < 2.62$

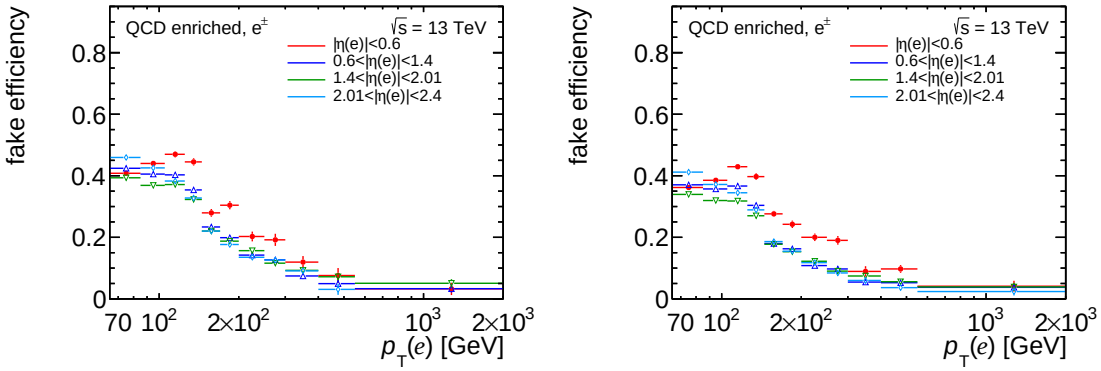

(e) $2.62 < |\Delta\phi(e, E_{\mathrm{T}}^{\mathrm{miss}})| < 2.88$

(f) $2.88 < |\Delta\phi(e, E_{\mathrm{T}}^{\mathrm{miss}})| < 3.14$

Figure C.4: Three-dimensional fake efficiency binned in the transverse momentum $p_{\mathrm{T}}(e)$, the absolute value of the pseudorapidity $\eta(e)$ and the last six bins of the absolute value of the angle between the electron and missing transverse momentum $|\Delta\phi(e, E_{\mathrm{T}}^{\mathrm{miss}})|$ for the `tight` $E_{\mathrm{T}}^{\mathrm{miss}}$ working point.

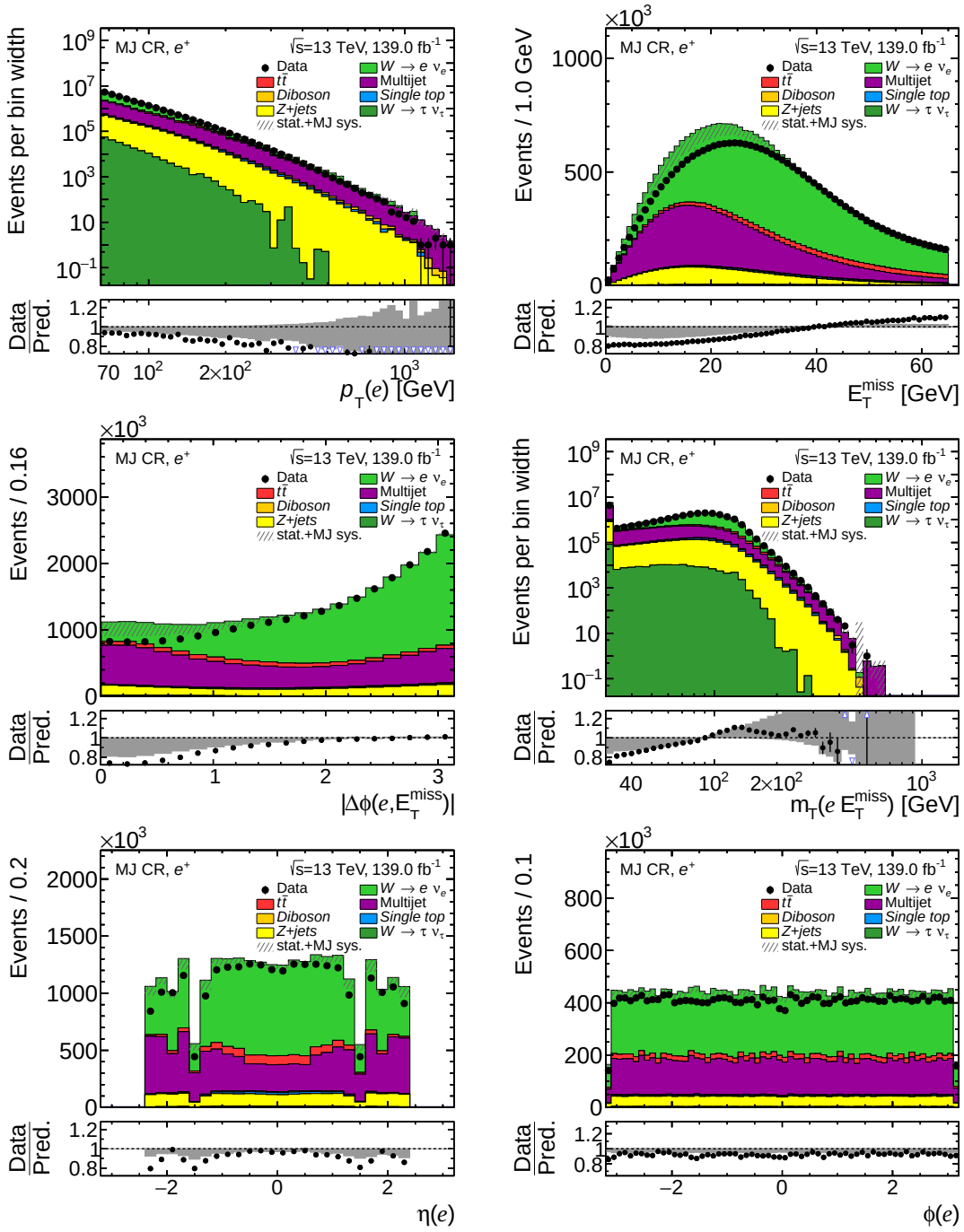

Figure C.5: Comparison of summed MC, the estimated multijet and data in the closure region (CR) for the e^+ channel. Only the `mixed` E_T^{miss} systematic uncertainty, instead of the total MJ systematic uncertainty, is shown.

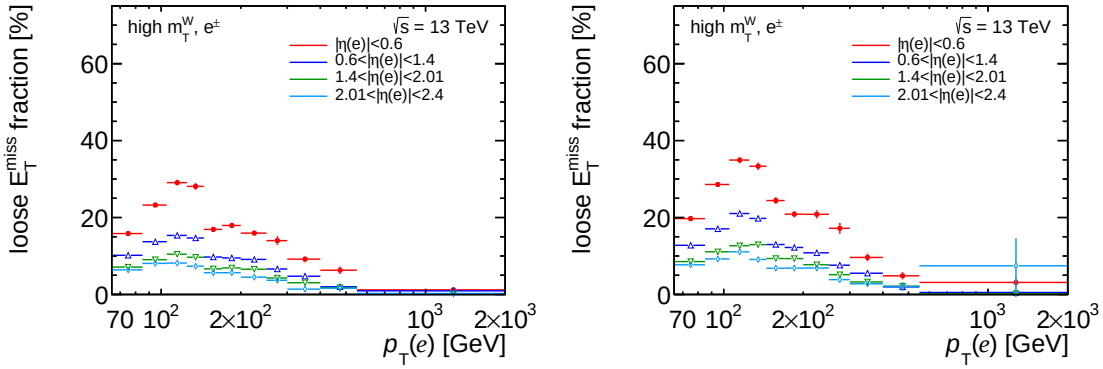

(a) $0.00 < |\Delta\phi(e, E_{\mathrm{T}}^{\mathrm{miss}})| < 0.26$ (b) $0.26 < |\Delta\phi(e, E_{\mathrm{T}}^{\mathrm{miss}})| < 0.52$

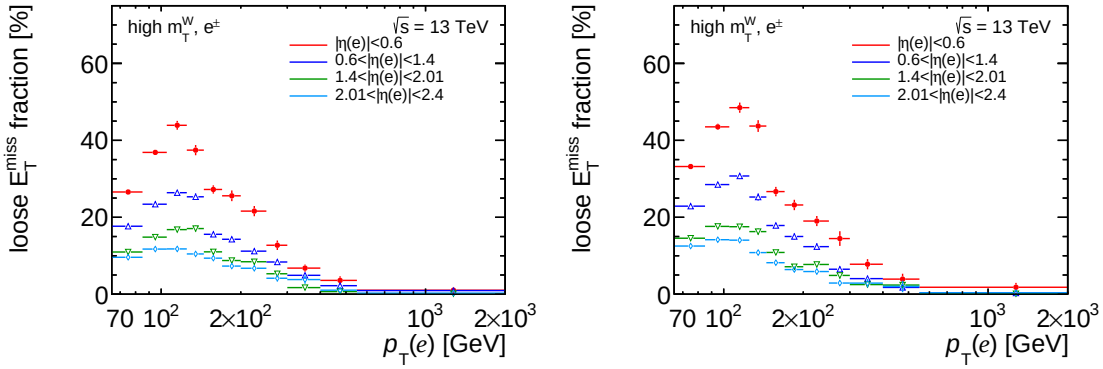

(c) $0.52 < |\Delta\phi(e, E_{\mathrm{T}}^{\mathrm{miss}})| < 0.78$ (d) $0.78 < |\Delta\phi(e, E_{\mathrm{T}}^{\mathrm{miss}})| < 1.05$

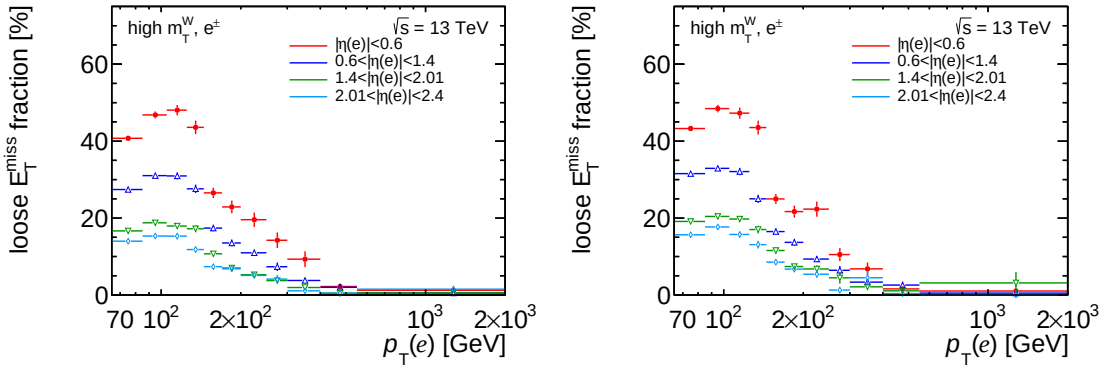

(e) $1.05 < |\Delta\phi(e, E_{\mathrm{T}}^{\mathrm{miss}})| < 1.31$ (f) $1.31 < |\Delta\phi(e, E_{\mathrm{T}}^{\mathrm{miss}})| < 1.57$

Figure C.6: `Loose` $E_{\mathrm{T}}^{\mathtt{miss}}$, i.e. real electron, fractions in the validation region (VR) binned three-dimensionally in the transverse momentum of the electron $p_{\mathrm{T}}(e)$, the absolute value of the pseudorapidity $|\eta(e)|$ and the former bins in $|\Delta\phi(e, E_{\mathrm{T}}^{\mathrm{miss}})|$ obtained from MC-Data comparisons, where the electron fulfils the loose identification criteria only.

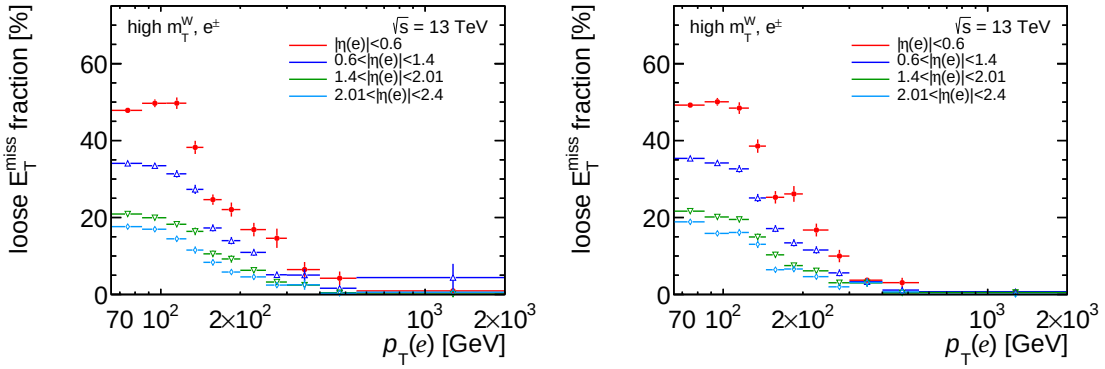

(a) $1.57 < |\Delta\phi(e, E_{\mathrm{T}}^{\mathrm{miss}})| < 1.83$

(b) $1.83 < |\Delta\phi(e, E_{\mathrm{T}}^{\mathrm{miss}})| < 2.09$

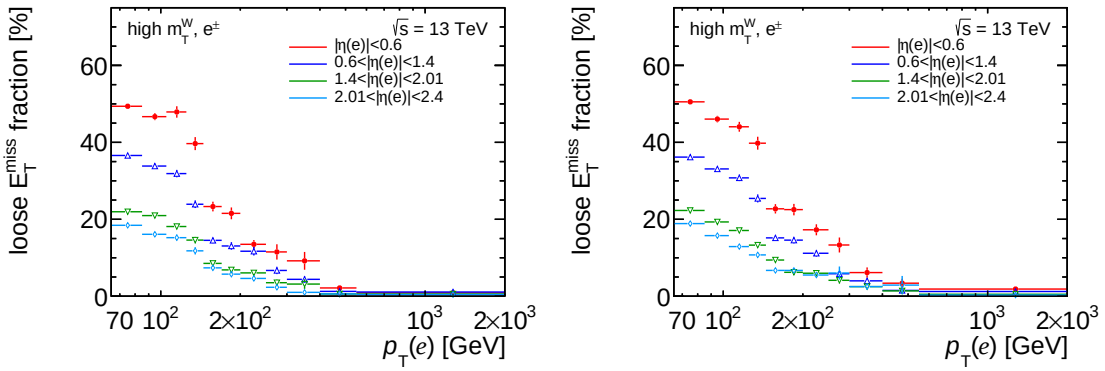

(c) $2.09 < |\Delta\phi(e, E_{\mathrm{T}}^{\mathrm{miss}})| < 2.36$

(d) $2.36 < |\Delta\phi(e, E_{\mathrm{T}}^{\mathrm{miss}})| < 2.62$

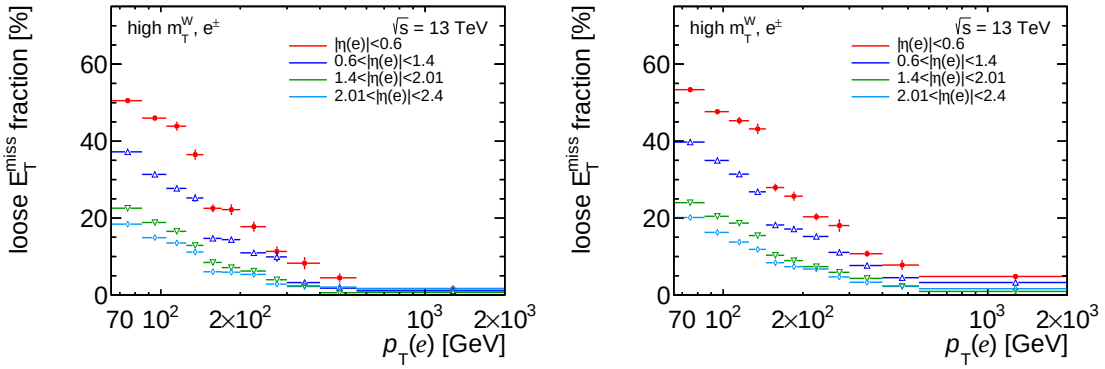

(e) $2.62 < |\Delta\phi(e, E_{\mathrm{T}}^{\mathrm{miss}})| < 2.88$

(f) $2.88 < |\Delta\phi(e, E_{\mathrm{T}}^{\mathrm{miss}}) < 3.14$

Figure C.7: `Loose` $E_{\mathrm{T}}^{\mathtt{miss}}$, i.e. real electron, fractions in the validation region (VR) binned three-dimensionally in the transverse momentum of the electron $p_{\mathrm{T}}(e)$, the absolute value of the pseudorapidity $|\eta(e)|$ and the later bins in $|\Delta\phi(e, E_{\mathrm{T}}^{\mathrm{miss}})|$ obtained from MC-Data comparisons, where the electron fulfils the loose identification criteria only.

D Comparison of data with MC samples supplemental material

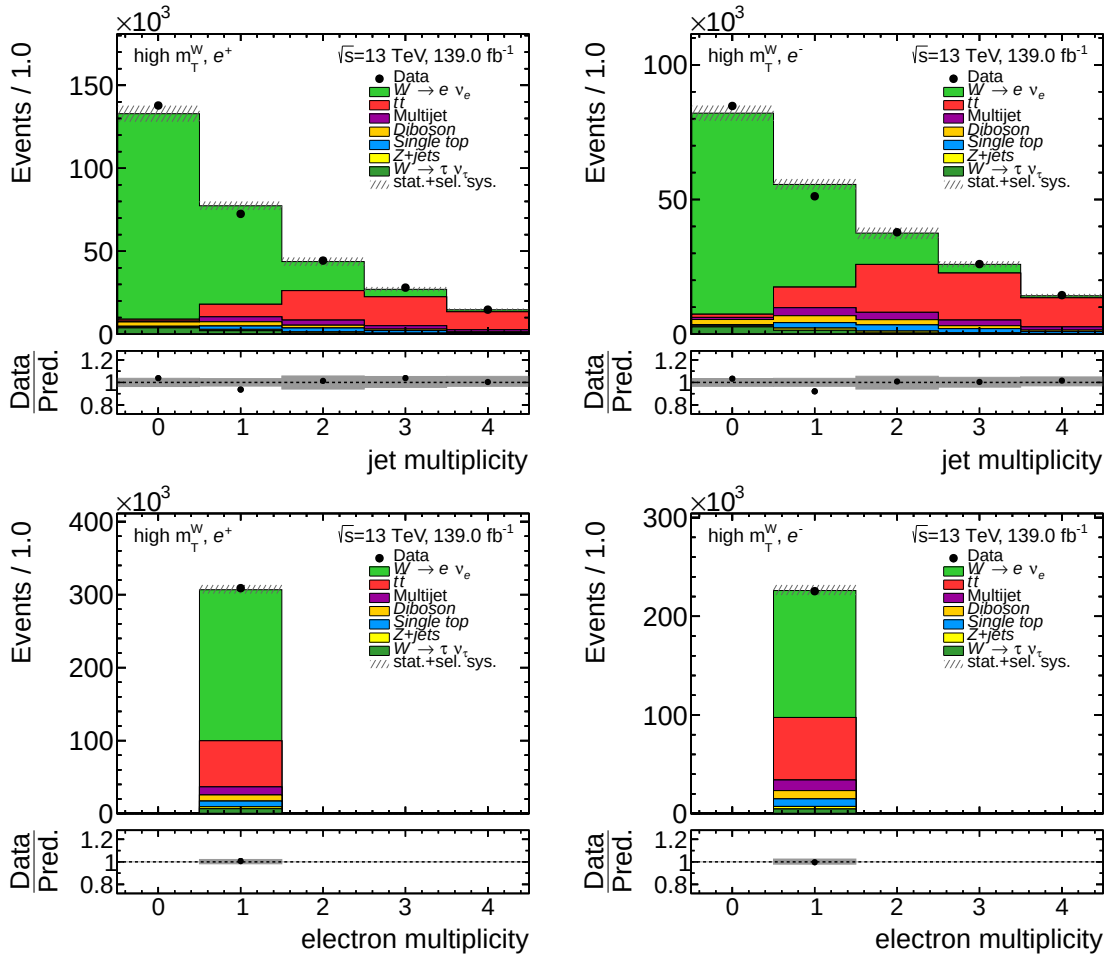

Figure D.1: Comparison of data and prediction in the signal region, labelled high m_T^W, for the e^+ and e^- channel. The uncertainty band consists of the combined statistical uncertainty from the MC and the systematic uncertainties with an impact of more than 0.5% on the measured cross-section. The statistical uncertainty of data events are represented by the uncertainty bars.

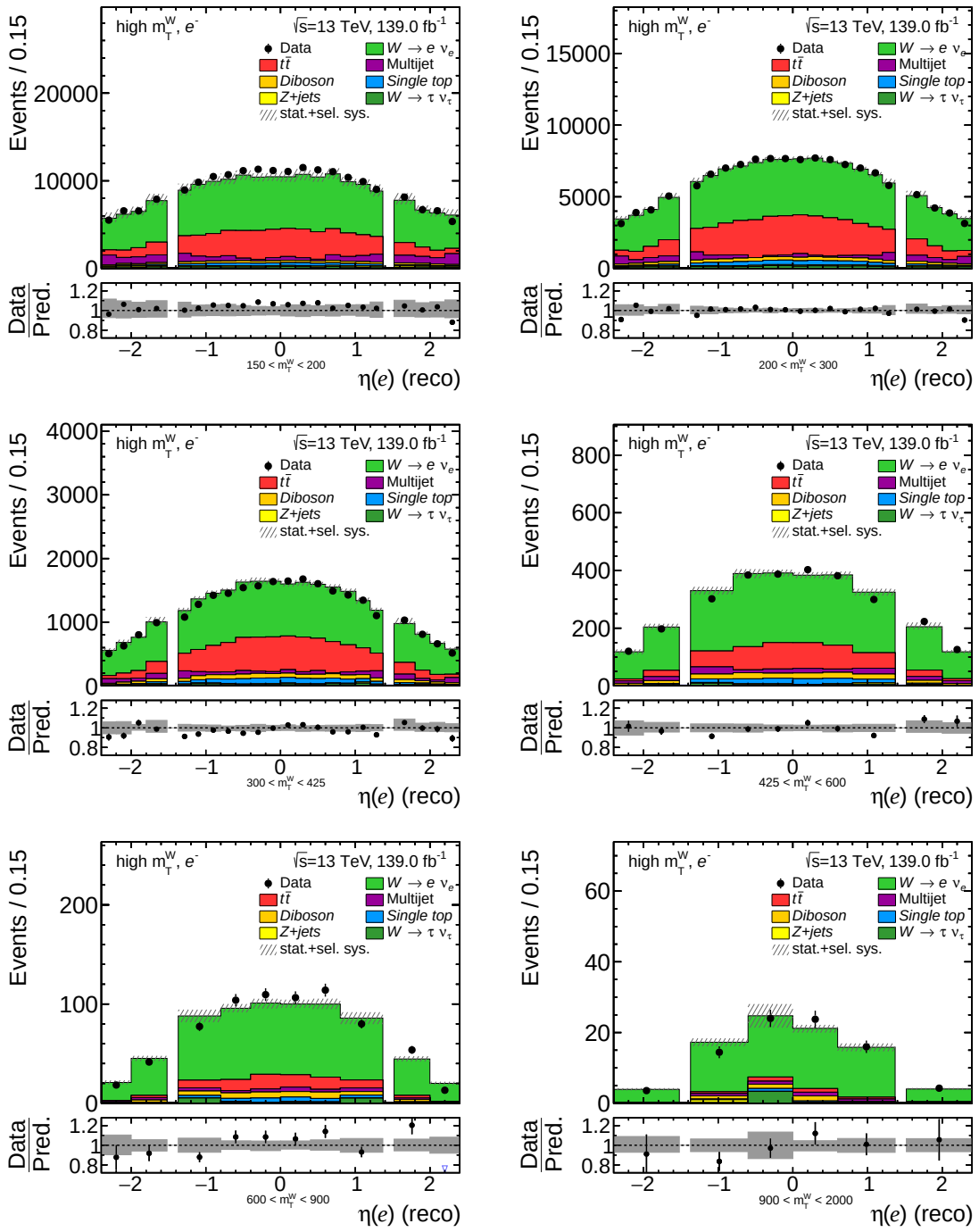

Figure D.2: Comparison of the prediction, i.e. summed MC and the estimated multijet, and data in the measurement binning of the double-differential cross-section for the e^- channel after the signal region selection. The two-dimensional binning is divided into six different distributions of η for each m_{T}^W bin. The uncertainty band consists of the statistical and systematic uncertainty of the signal MC, where only systematic uncertainties with an impact of 0.5% are considered. The statistical uncertainty of data events are represented by the uncertainty bars.

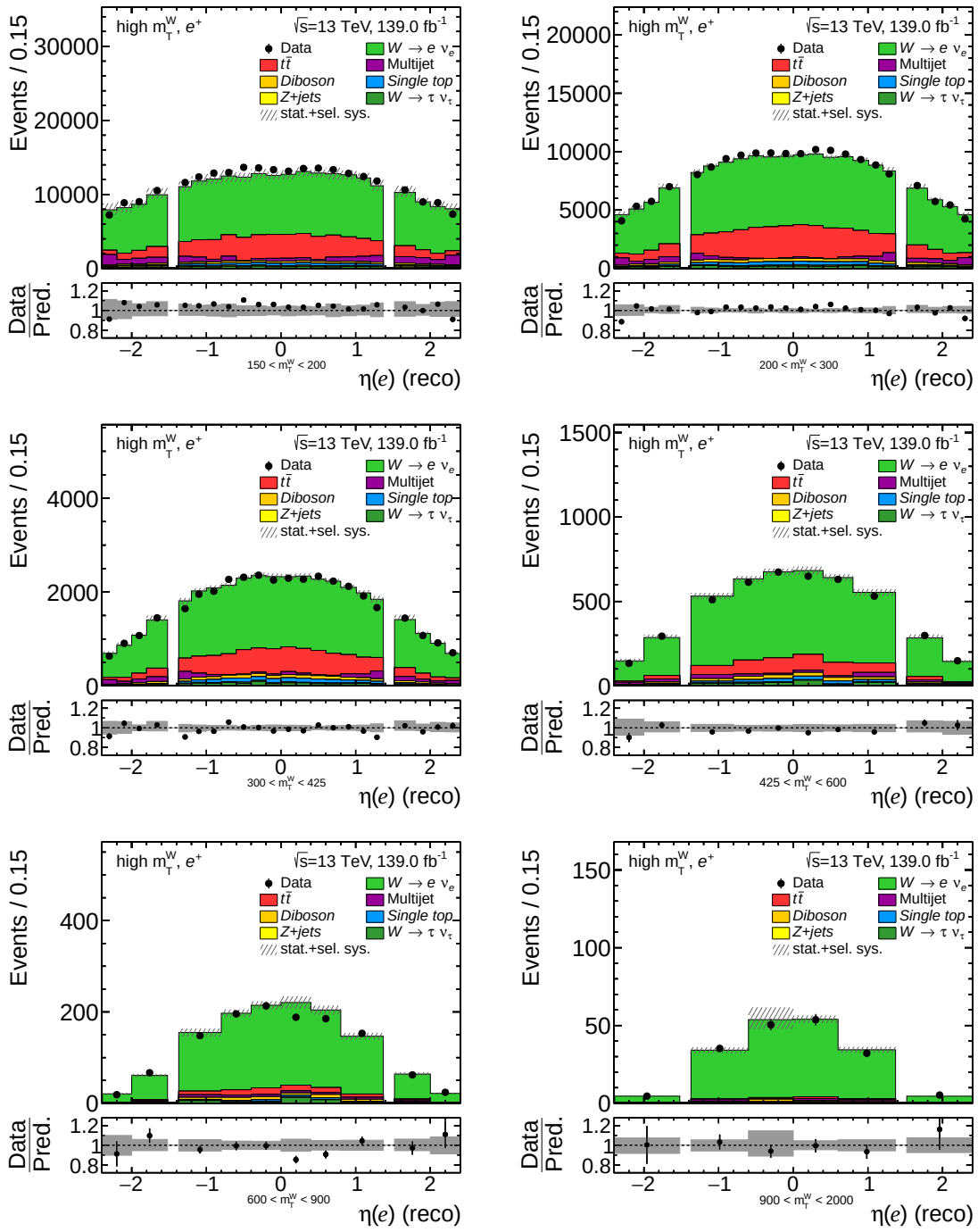

Figure D.3: Comparison of the prediction, i.e. summed MC and the estimated multijet, and data in the measurement binning of the double-differential cross-section for the e^+ channel after the signal region selection. The two-dimensional binning is divided into six different distributions of η for each m_{T}^W bin. The uncertainty band consists of the statistical and systematic uncertainty of the signal MC, where only systematic uncertainties with an impact of 0.5% are considered. The statistical uncertainty of data events are represented by the uncertainty bars.

E Systematic uncertainties supplemental material

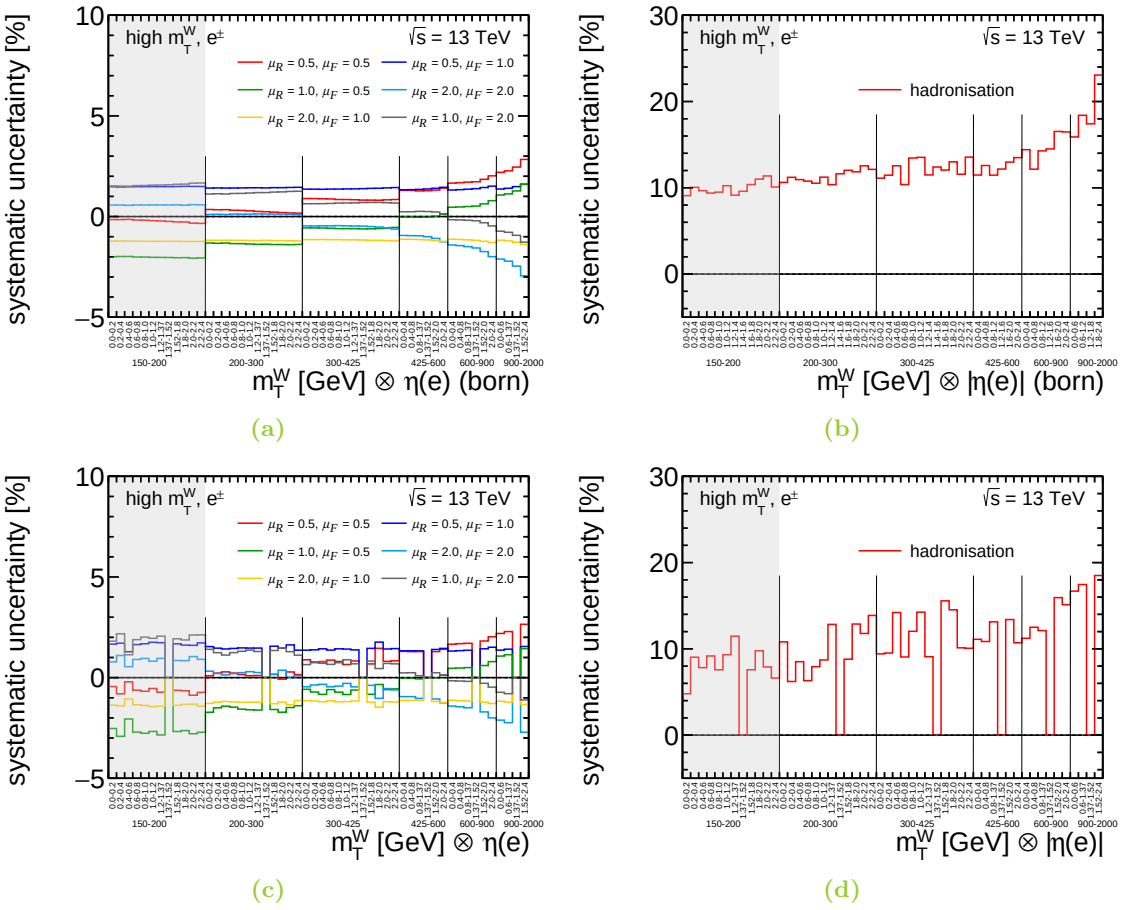

Figure E.1: Relative difference of the systematic variation corresponding to the hadronisation as well as factorisation and renormalisation of the signal process as a function of $m_{\mathrm{T}}^{W} \otimes |\eta(e)|$ for the combination of the e^+ and e^- channel. While the relative difference at fiducial level is presented in a) and b), the relative difference at reconstructed level can be found in c) and d).

F Unfolding supplemental material

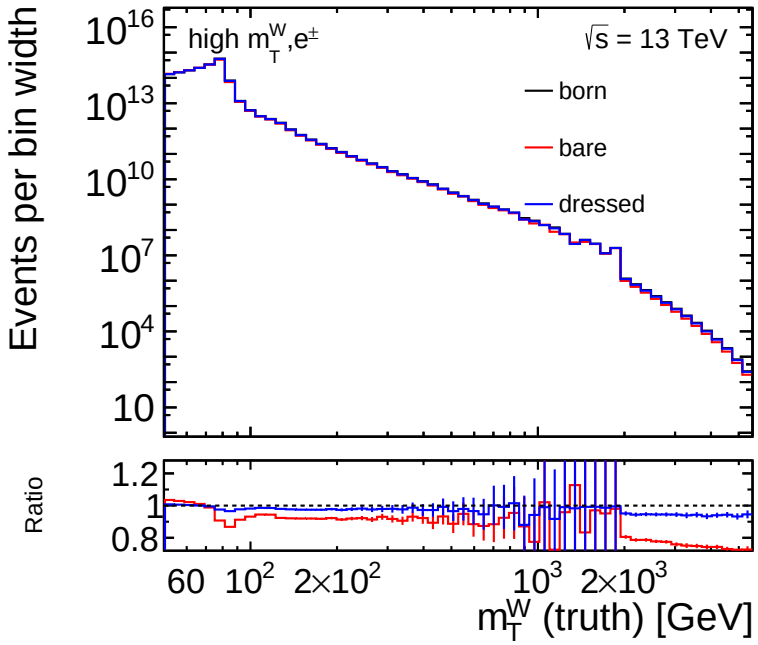

Figure F.1: Comparison of the bare, born and dressed level as a function of the transverse mass of the W boson without requiring any selection.

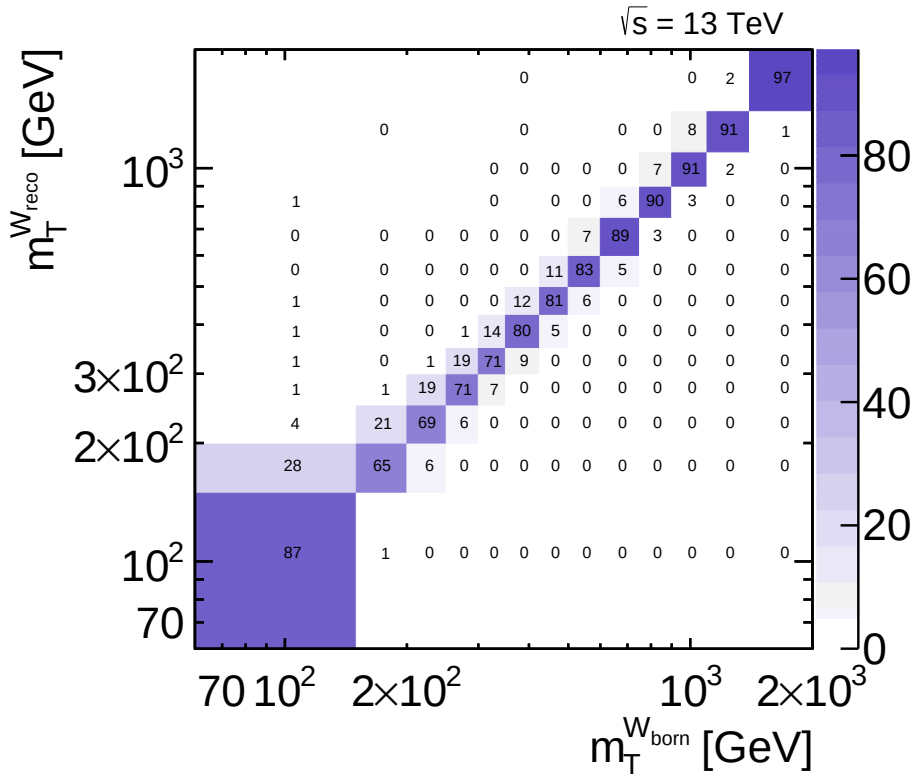

Figure F.2: Migration matrix $M_{reco,truth}$ for the $W^+ \to e^+\nu$ signal process. The given numbers are in percent, while under- and overflow bin are considered in the normalisation.

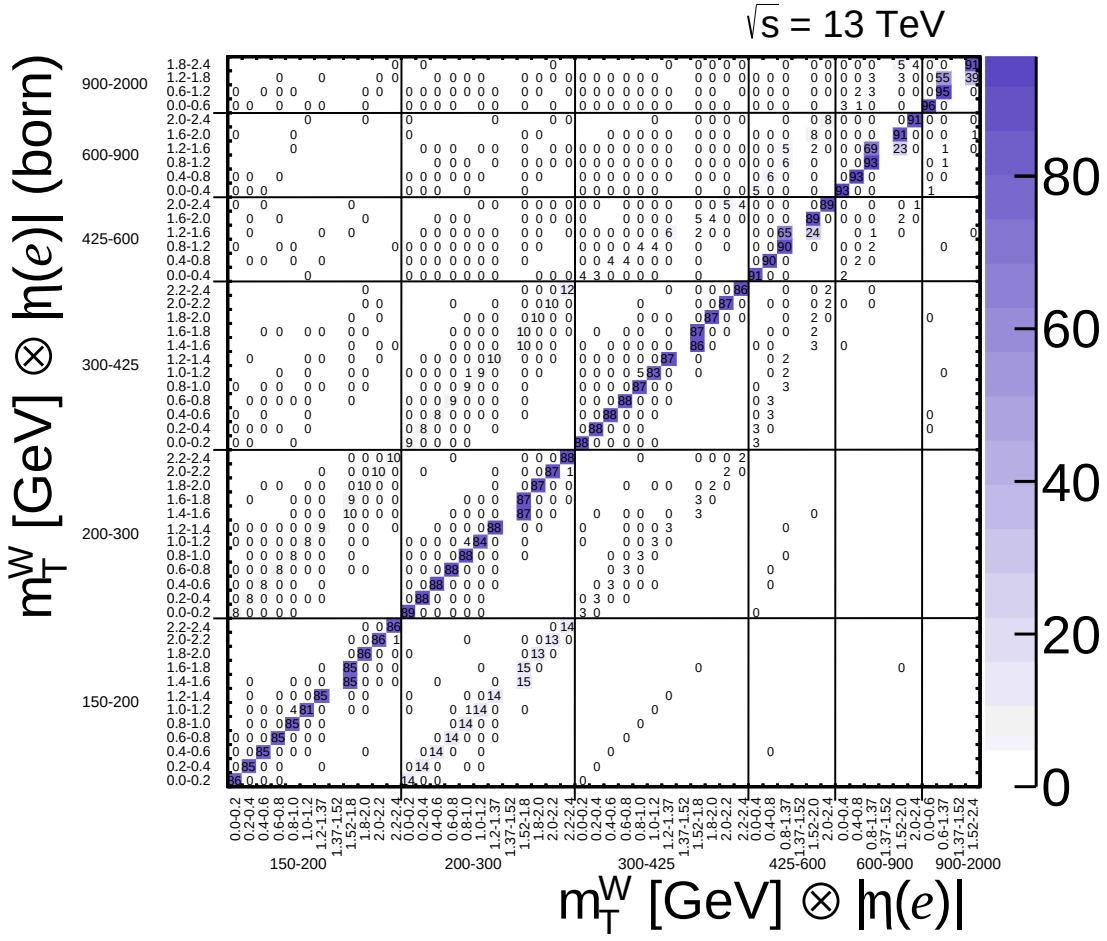

Figure F.3: Response matrix R for the measured variable $m_{\mathrm{T}}^{W} \otimes |\eta(e)|$ in the measurement binning for the e^+ channel. The normalisation for each truth level bin, where under- and overflow bin are not taken into account, are performed. Afterwards, the normalised values are scaled to percent.

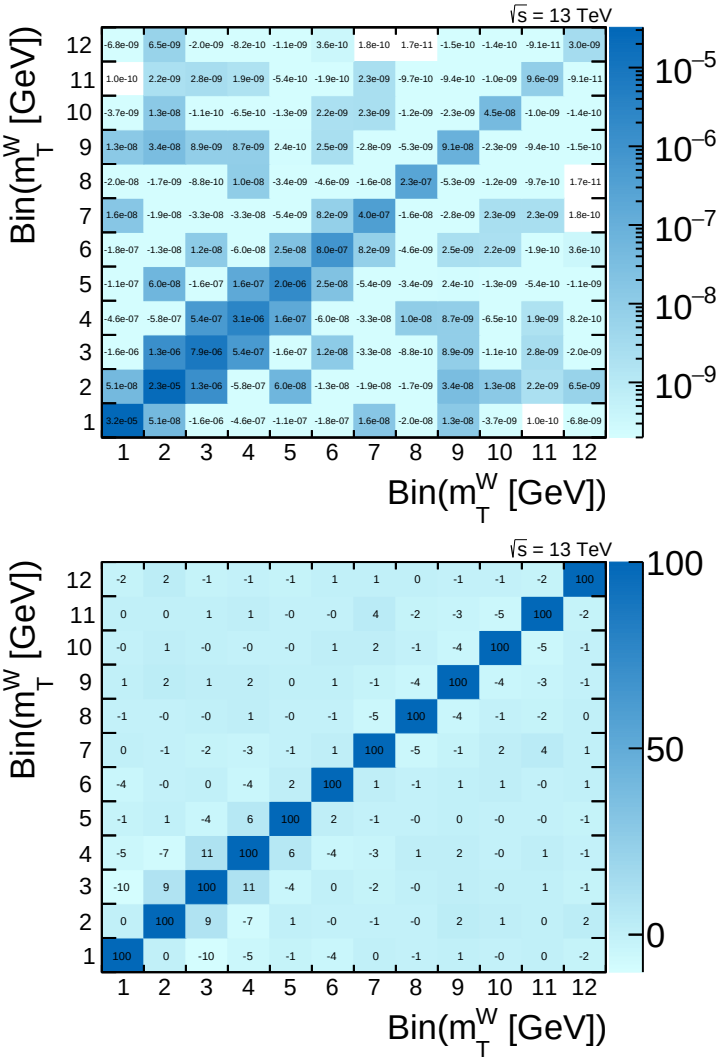

Figure F.4: Covariance matrix and correlation matrix after two iterations in the IBU based on the statistical uncertainty of data and MC based events, generated with 5000 toy data sets, as a function of m_{T}^{W} for the e^{-} channel.

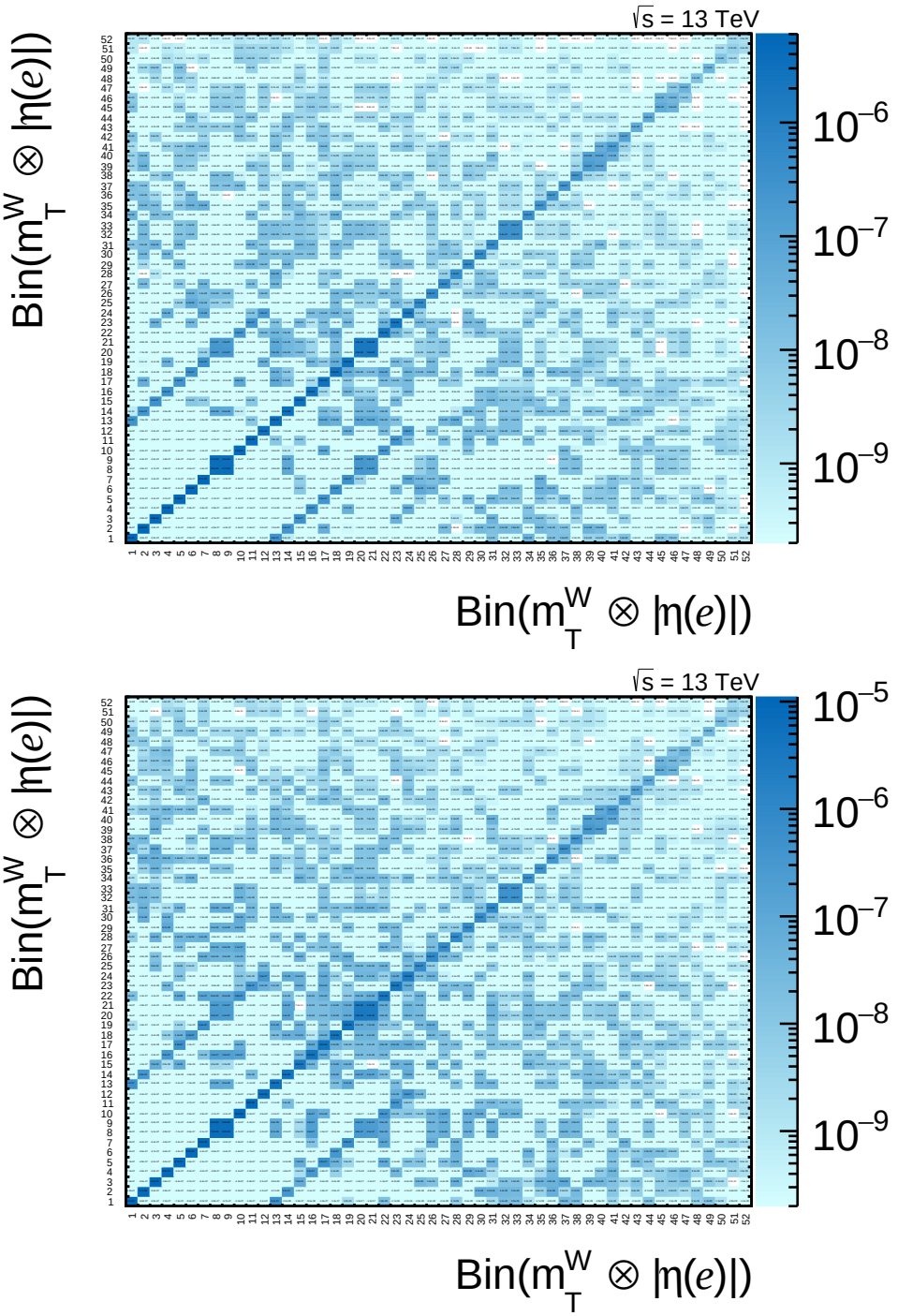

Figure F.5: Covariance matrix after two iterations based on the statistical uncertainty of data and MC based events, generated with 5000 toy data sets, as a function of $m_{\mathrm{T}}^{W} \otimes |\eta(e)|$ for the e^+ and e^- channel.

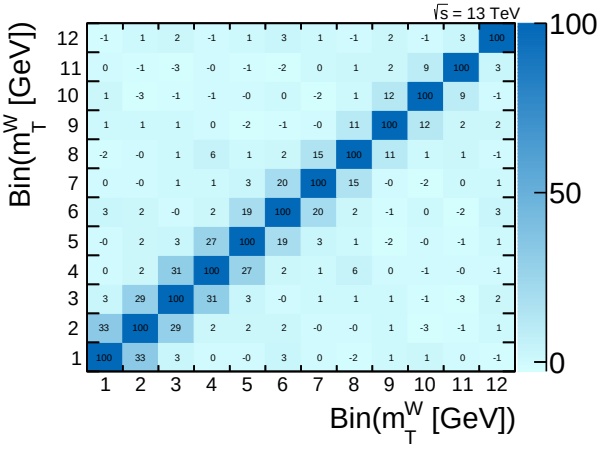

(a)

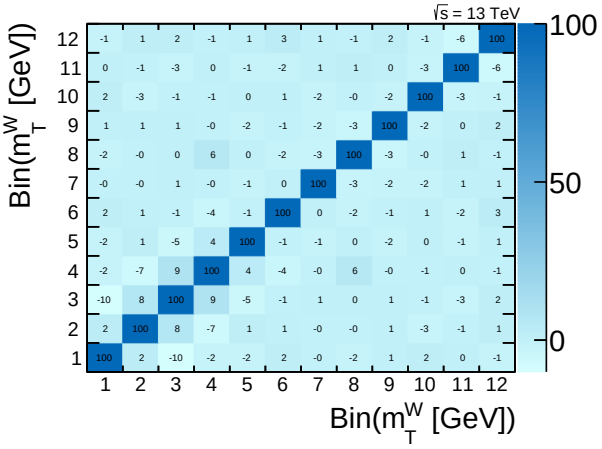

(b)

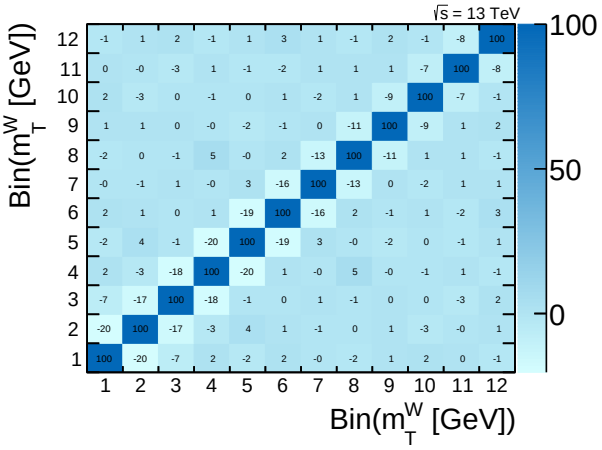

(c)

Figure F.6: Correlation matrix after a) one, b) two and c) five iterations based on the statistical uncertainty of data events, generated with 5000 toy data sets, as a function of m_{T}^{W} for the e^{+} channel.

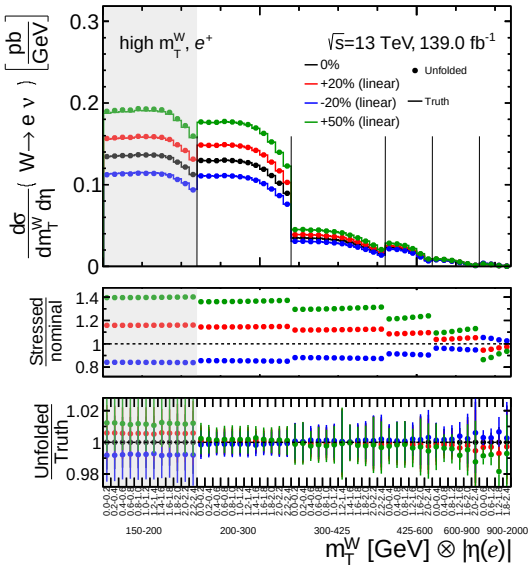

(a) $N_{\text{iter}} = 2$

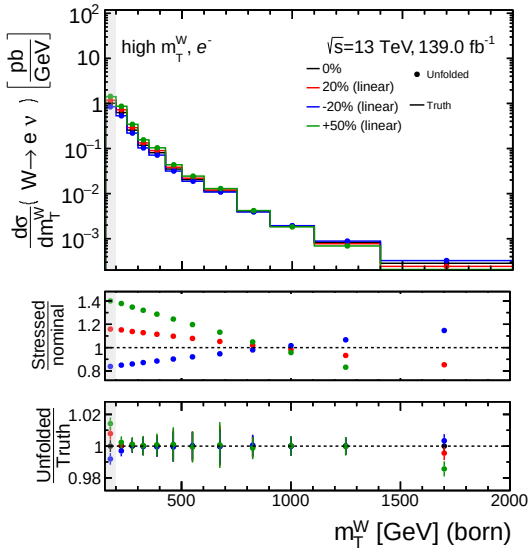

(b) $N_{\text{iter}} = 2$

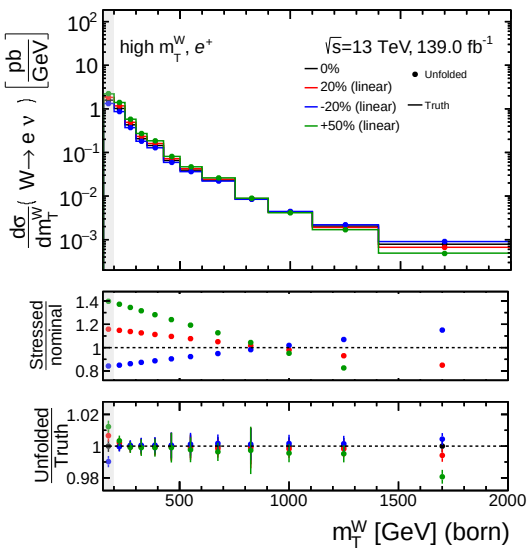

(c) $N_{\text{iter}} = 2$

Figure F.7: Visualisation of the stress test for the measured variable $m_{\mathrm{T}}^{W} \otimes |\eta(e)|$ after two iterations in the unfolding for the e^+ channel. In addition, the stress test for the measured variable m_{T}^{W} after two iterations in the unfolding for the e^- and e^+ channel.

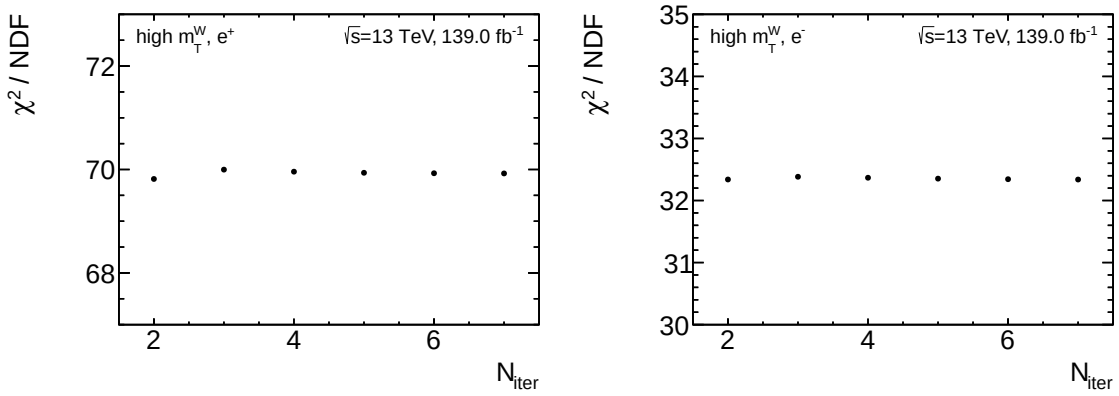

(a) (b)

Figure F.8: χ^2/NDF w.r.t the MC truth distribution as a function of the number of iterations N_{iter} for m_{T}^W in the e^+ and e^- channel.

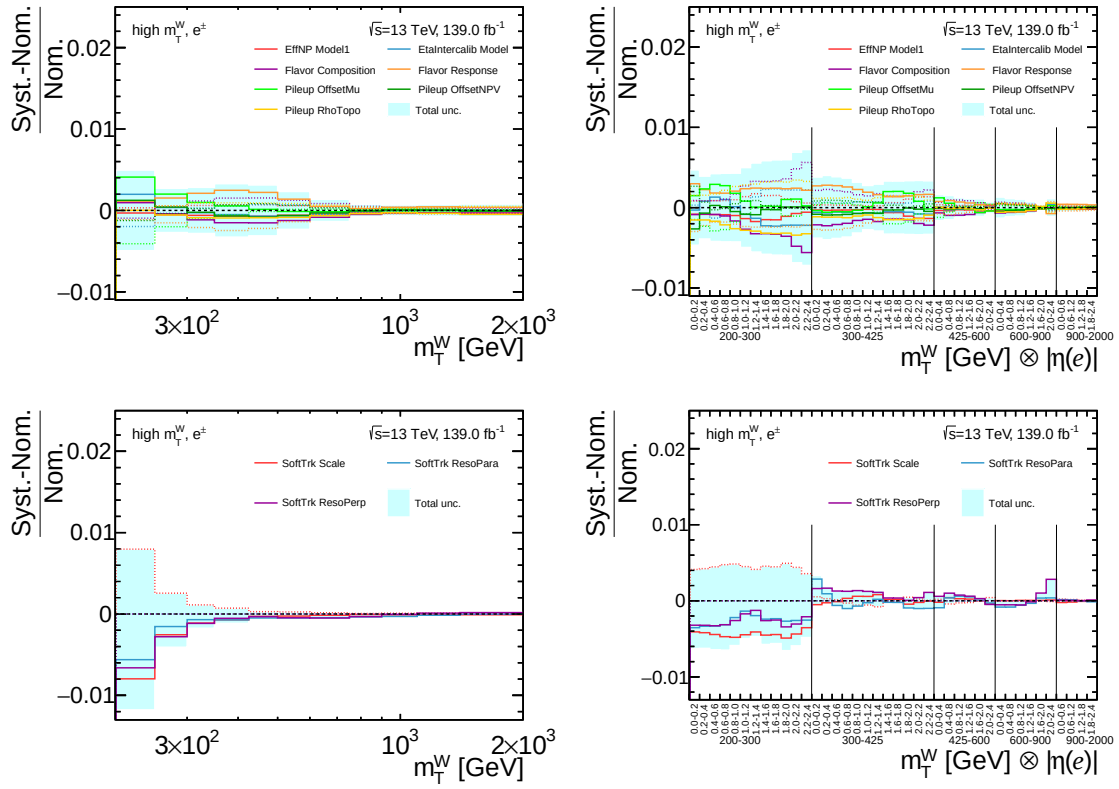

Figure F.9: Unfolded systematic uncertainties of the signal process as a function of the measured variables, m_{T}^W and $m_{\text{T}}^W \otimes |\eta(e)|$ for the combination of the e^+ and e^- channel.

G Tabular presentation of the measured cross sections

Table G.1: Final measured double-differential cross-section as a function of the transverse momentum of the W boson and the absolute value of the electron's pseudorapidity for $m_{\mathrm{T}}^{W} = [200 - 300]\,\mathrm{GeV}$ in the e^{+} channel. The statistical uncertainty of the data and of the MC samples, obtained from the covariance matrix, and the systematic uncertainties with an impact of more than 0.5% are presented separately.

$\eta(l)$ bin edges	0.0 - 0.2	0.2 - 0.4	0.4 - 0.6	0.6 - 0.8	0.8 - 1.0	1.0 - 1.2	1.2 - 1.4	1.4 - 1.6	1.6 - 1.8	1.8 - 2.0	2.0 - 2.2	2.2 - 2.4
σ [pb/GeV]	1.33e-01	1.37e-01	1.39e-01	1.36e-01	1.33e-01	1.27e-01	1.20e-01	1.28e-01	1.23e-01	1.10e-01	1.07e-01	7.47e-02
Data stat. unc. [%]	1.13	1.08	1.06	1.09	1.11	1.15	1.33	0.99	0.99	1.28	1.24	1.62
MC stat. unc. [%]	1.23	1.13	0.83	1.05	1.15	1.11	1.26	0.91	0.91	1.11	1.25	1.36
tot. sys. unc. [%]	2.86 -2.47	2.43 -2.13	2.13 -1.90	2.06 -2.12	2.26 -2.39	2.60 -3.02	3.66 -5.10	2.08 -3.23	2.08 -3.23	2.67 -4.25	3.76 -4.18	5.50 -7.54
SoftTrk Scale	-0.30 0.31	-0.33 0.33	-0.39 0.40	-0.43 0.44	-0.40 0.41	-0.30 0.30	-0.24 0.24	-0.29 0.29	-0.28 0.29	-0.29 0.30	-0.25 0.25	-0.15 0.16
SoftTrk ResoPara	-0.34	-0.34	-0.31	-0.18	-0.03	0.07	0.06	-0.17	-0.16	-0.23	-0.22	-0.21
SoftTrk ResoPerp	-0.42	-0.40	-0.40	-0.32	-0.19	-0.08	-0.11	-0.26	-0.26	-0.25	-0.19	-0.14
EG SCALE S12	-0.25 0.25	-0.25 0.25	-0.23 0.23	-0.20 0.20	-0.18 0.18	-0.14 0.14	-0.09 0.09	-0.24 0.24	-0.24 0.24	-0.48 0.48	-0.64 0.64	-0.71 0.71
EG SCALE LARCALIB	-0.33 0.33	-0.33 0.33	-0.32 0.32	-0.28 0.28	-0.22 0.22	-0.19 0.19	-0.19 0.19	-0.24 0.24	-0.24 0.24	-0.35 0.35	-0.41 0.41	-0.42 0.42
EG SCALE L1GAIN	-0.17 0.17	0.00 -0.00	0.06 -0.06	0.01 -0.01	-0.06 0.06	-0.12 0.12	-0.10 0.10	0.05 -0.05	0.05 -0.05	0.23 -0.23	0.66 -0.66	1.18 -1.18
EG SCALE L2GAIN	0.61 -0.61	0.60 -0.60	0.61 -0.61	0.81 -0.81	1.17 -1.17	1.31 -1.31	1.02 -1.02	0.35 -0.35	0.35 -0.35	0.32 -0.32	0.32 -0.32	0.32 -0.32
JER EffNP 1	0.66 -0.66	0.67 -0.67	0.67 -0.67	0.60 -0.60	0.57 -0.57	0.60 -0.60	0.73 -0.73	0.98 -0.98	0.98 -0.98	0.69 -0.69	0.19 -0.19	-0.20 0.20
JER EffNP 2	1.29 -1.29	0.98 -0.98	0.60 -0.60	0.43 -0.43	0.43 -0.43	0.44 -0.43	0.42 -0.42	0.38 -0.38	0.38 -0.38	0.39 -0.39	0.31 -0.31	0.16 -0.16
JER EffNP 3	0.74 -0.74	0.70 -0.70	0.62 -0.62	0.57 -0.57	0.58 -0.58	0.51 -0.51	0.38 -0.38	0.10 -0.10	0.10 -0.10	0.04 -0.04	0.02 -0.02	-0.09 0.09
JER EffNP 4	0.58 -0.58	0.57 -0.57	0.55 -0.55	0.54 -0.54	0.54 -0.54	0.50 -0.50	0.43 -0.43	0.40 -0.40	0.40 -0.40	0.38 -0.38	0.06 -0.06	-0.63 0.63
JER EffNP 5	-0.15 0.15	-0.09 0.09	0.09 -0.09	0.29 -0.29	0.38 -0.38	0.30 -0.30	0.11 -0.11	0.08 -0.08	0.08 -0.08	0.18 -0.18	0.15 -0.15	0.00 -0.00
JER EffNP 6	0.03 -0.03	0.04 -0.04	0.13 -0.13	0.27 -0.27	0.37 -0.37	0.35 -0.35	0.28 -0.28	0.12 -0.12	0.12 -0.12	0.10 -0.10	-0.05 0.05	-0.47 0.47
JER EffNP 7	0.66 -0.66	0.59 -0.59	0.49 -0.49	0.45 -0.45	0.44 -0.44	0.41 -0.41	0.36 -0.36	0.30 -0.30	0.30 -0.30	0.29 -0.29	0.11 -0.11	-0.39 0.39
JES EffNP Model1	0.03 -0.03	-0.03 0.03	-0.08 0.08	-0.12 0.12	-0.11 0.11	-0.08 0.08	-0.05 0.05	-0.07 0.07	-0.07 0.07	-0.06 0.06	-0.05 0.05	-0.03 0.03
JES EtaIntercalib Model	0.20 -0.20	0.13 -0.13	0.17 -0.17	0.21 -0.21	0.13 -0.13	-0.02 0.02	-0.12 0.12	-0.18 0.18	-0.18 0.18	-0.20 0.20	-0.27 0.27	-0.34 0.34
JES Flavor Composition	-0.43 0.43	-0.31 0.31	-0.21 0.21	-0.15 0.15	-0.13 0.13	-0.15 0.15	-0.16 0.17	-0.26 0.26	-0.26 0.26	-0.30 0.30	-0.39 0.39	-0.50 0.50
JES Flavor Response	0.62 -0.62	0.40 -0.40	0.22 -0.22	0.14 -0.14	0.12 -0.12	0.09 -0.09	0.05 -0.05	0.18 -0.18	0.18 -0.18	0.25 -0.25	0.26 -0.26	0.18 -0.18
JES Pileup OffsetMu	0.10 -0.10	0.08 -0.08	0.09 -0.09	0.11 -0.11	0.15 -0.15	0.13 -0.13	0.08 -0.08	0.03 -0.03	0.03 -0.02	0.09 -0.09	0.16 -0.16	0.18 -0.18
JES Pileup OffsetNPV	0.19 -0.19	0.06 -0.06	0.01 -0.01	-0.02 0.02	-0.06 0.06	-0.11 0.11	-0.11 0.11	0.02 -0.02	0.02 -0.02	0.05 -0.05	0.02 -0.02	-0.01 0.01
JES Pileup RhoTopo	-0.41 0.41	-0.19 0.19	-0.08 0.08	-0.11 0.11	-0.20 0.20	-0.24 0.24	-0.21 0.21	-0.17 0.17	-0.17 0.17	-0.19 0.19	-0.27 0.27	-0.39 0.39
EL SF ID	0.47 -0.47	0.47 -0.47	0.51 -0.51	0.59 -0.59	0.65 -0.65	0.66 -0.66	0.67 -0.67	0.98 -0.98	0.98 -0.98	1.92 -1.92	3.40 -3.40	4.18 -4.18
EL SF Isol	0.17 -0.17	0.17 -0.17	0.18 -0.18	0.20 -0.20	0.21 -0.21	0.22 -0.22	0.24 -0.24	0.33 -0.33	0.33 -0.33	0.35 -0.35	0.39 -0.39	0.41 -0.41
PU SF	-0.05 0.05	-0.07 0.07	-0.00 0.00	0.04 -0.04	-0.01 0.02	-0.12 0.12	-0.17 0.17	-0.03 0.03	-0.03 0.03	0.05 -0.05	0.02 -0.02	-0.08 0.08
MJ EL MET	-0.28 0.20	0.24 -0.09	0.42 -0.19	-0.65 0.33	-0.83 0.44	-1.66 0.89	-3.71 2.03	-1.31 0.83	-1.30 0.82	-1.48 0.89	-0.87 0.50	-4.14 2.19
MJ EL 1jet	0.05	-0.02	-0.04	0.05	0.06	0.10	0.20	0.02	0.02	0.03	-0.00	0.05
MJ EL MC scaling	0.32 -0.32	-0.09 0.09	-0.23 0.23	0.43 -0.43	0.58 -0.58	1.14 -1.14	2.38 -2.38	0.69 -0.69	0.69 -0.69	0.75 -0.75	0.39 -0.39	1.89 -1.89
MJ EL mixMET	0.12	0.31	0.40	-0.66	-0.75	-0.94	-1.82	-2.24	-2.24	-3.07	-1.68	-3.79
FSR	-0.19 0.28	-0.19 0.24	-0.19 0.18	-0.18 0.15	-0.17 0.10	-0.12 0.02	-0.03 -0.02	0.01 0.03	0.01 0.03	-0.01 0.13	-0.08 0.22	-0.21 0.38
$t\bar{t}$ $\mu_R = 2.0$, $\mu_F = 1.0$	-0.61	-0.58	-0.55	-0.52	-0.49	-0.46	-0.42	-0.24	-0.24	-0.18	-0.14	-0.13
$t\bar{t}$ $\mu_R = 0.5$, $\mu_F = 0.5$	0.83	0.78	0.73	0.68	0.65	0.63	0.58	0.35	0.35	0.25	0.15	0.12
$t\bar{t}$ hardscatter	0.86	0.82	0.73	0.61	0.53	0.49	0.31	-0.18	-0.19	-0.10	0.07	0.25
$t\bar{t}$ hadronisation	1.06	0.71	0.38	0.25	0.23	0.22	0.15	-0.10	-0.10	-0.13	-0.14	-0.16
$t\bar{t}$ hdamp	0.37	0.20	-0.00	-0.08	-0.04	0.03	0.07	-0.02	-0.02	-0.04	0.01	0.07
$t\bar{t}$ NNPDF RMS	-0.25 0.25	-0.23 0.23	-0.17 0.17	-0.12 0.12	-0.09 0.09	-0.14 0.14	-0.20 0.20	-0.33 0.33	-0.33 0.33	-0.41 0.41	-0.44 0.44	-0.56 0.56

Table G.2: Final measured double-differential cross-section as a function of the transverse momentum of the W boson and the absolute value of the electron's pseudorapidity for $m_{\mathrm{T}}^{W} = [300 - 425]\,\mathrm{GeV}$ in the e^{+} channel. The statistical uncertainty of the data and of the MC samples, obtained from the covariance matrix, and the systematic uncertainties with an impact of more than 0.5% are presented separately.

$\eta(l)$ bin edges	0.0 - 0.2	0.2 - 0.4	0.4 - 0.6	0.6 - 0.8	0.8 - 1.0	1.0 - 1.2	1.2 - 1.4	1.4 - 1.6	1.6 - 1.8	1.8 - 2.0	2.0 - 2.2	2.2 - 2.4
σ [pb/GeV]	3.33e-02	3.39e-02	3.51e-02	3.58e-02	3.29e-02	3.06e-02	2.66e-02	3.03e-02	2.77e-02	2.28e-02	2.06e-02	1.51e-02
Data stat. unc. [%]	2.17	2.16	2.08	2.03	2.11	2.25	2.88	2.04	2.06	2.70	2.80	3.48
MC stat. unc. [%]	1.73	1.86	1.37	1.58	1.48	1.75	2.58	1.32	1.33	1.55	1.76	2.19
tot. sys. unc. [%]	2.78 -2.10	2.47 -1.84	2.22 -1.77	2.34 -2.03	2.91 -2.83	3.32 -3.34	3.97 -4.64	2.72 -3.59	2.73 -3.61	3.47 -4.51	5.10 -5.40	6.75 -7.31
SoftTrk Scale	-0.11 0.11	-0.08 0.09	-0.05 0.05	0.01 -0.01	0.01 -0.01	0.04 -0.04	0.06 -0.06	0.01 -0.01	0.01 -0.01	0.01 -0.01	0.07 -0.07	0.08 -0.08
SoftTrk ResoPara	0.57	0.19	-0.08	-0.14	-0.15	-0.13	-0.08	0.07	0.07	0.09	0.13	0.14
SoftTrk ResoPerp	0.14	0.12	0.07	0.08	0.08	0.11	0.14	0.16	0.17	0.17	0.21	0.20
EG SCALE S12	-0.28 0.28	-0.29 0.29	-0.29 0.29	-0.28 0.28	-0.28 0.28	-0.25 0.25	-0.21 0.21	-0.35 0.35	-0.35 0.35	-0.70 0.70	-1.07 1.07	-1.36 1.36
EG SCALE LARCALIB	-0.36 0.36	-0.36 0.36	-0.35 0.35	-0.35 0.35	-0.34 0.34	-0.30 0.30	-0.22 0.22	-0.30 0.30	-0.30 0.30	-0.52 0.52	-0.74 0.74	-0.96 0.96
EG SCALE L1GAIN	-0.15 0.15	-0.13 0.13	-0.07 0.07	-0.04 0.04	-0.01 0.01	-0.01 0.01	-0.03 0.03	0.02 -0.02	0.03 -0.03	0.51 -0.51	1.56 -1.56	2.99 -2.99
EG SCALE L2GAIN	0.61 -0.61	0.62 -0.62	0.65 -0.65	1.01 -1.01	1.71 -1.71	2.13 -2.13	1.79 -1.79	0.47 -0.47	0.46 -0.46	0.39 -0.39	0.51 -0.51	0.61 -0.61
JER EffNP 1	0.02 -0.02	0.01 -0.01	0.02 -0.02	-0.04 0.04	-0.06 0.07	-0.10 0.10	-0.14 0.14	-0.10 0.11	-0.11 0.11	-0.01 0.02	0.07 -0.07	0.19 -0.19
JER EffNP 2	0.22 -0.22	0.22 -0.22	0.24 -0.24	0.24 -0.24	0.21 -0.21	0.13 -0.13	0.02 -0.02	-0.16 0.17	-0.17 0.17	-0.08 0.08	0.06 -0.06	0.18 -0.18
JER EffNP 3	0.27 -0.27	0.23 -0.23	0.15 -0.15	0.05 -0.05	-0.00 0.00	-0.03 0.03	-0.04 0.04	-0.09 0.09	-0.10 0.10	-0.11 0.11	-0.07 0.07	0.04 -0.04
JER EffNP 4	0.26 -0.26	0.22 -0.22	0.13 -0.13	0.04 -0.04	-0.02 0.02	-0.06 0.06	-0.08 0.08	-0.06 0.06	-0.07 0.07	-0.04 0.04	0.04 -0.04	0.19 -0.19
JER EffNP 5	0.26 -0.26	0.23 -0.23	0.18 -0.18	0.08 -0.08	-0.03 0.03	-0.09 0.09	-0.07 0.07	0.02 -0.02	0.02 -0.02	0.05 -0.05	0.12 -0.12	0.25 -0.25
JER EffNP 6	0.13 -0.13	0.19 -0.19	0.21 -0.21	0.14 -0.14	0.03 -0.03	-0.03 0.03	-0.03 0.03	-0.01 0.01	-0.01 0.01	0.02 -0.02	0.10 -0.10	0.22 -0.22
JER EffNP 7	0.20 -0.20	0.18 -0.18	0.16 -0.16	0.09 -0.09	0.01 -0.01	-0.04 0.04	-0.06 0.06	-0.05 0.05	-0.05 0.05	-0.00 0.00	0.07 -0.07	0.17 -0.17
JES EffNP Model1	-0.02 0.02	-0.02 0.02	-0.02 0.02	-0.02 0.02	-0.02 0.02	-0.02 0.02	-0.02 0.02	-0.04 0.04	-0.04 0.04	-0.05 0.05	-0.06 0.06	-0.07 0.07
JES EtaIntercalib Model	-0.09 0.09	-0.09 0.09	-0.08 0.08	-0.08 0.08	-0.06 0.06	-0.05 0.05	-0.04 0.04	-0.04 0.04	-0.04 0.04	-0.06 0.06	-0.09 0.09	-0.09 0.09
JES Flavor Composition	-0.17 0.18	-0.18 0.18	-0.14 0.14	-0.13 0.13	-0.11 0.11	-0.10 0.10	-0.11 0.11	-0.02 0.02	-0.02 0.02	0.08 -0.08	0.11 -0.11	0.11 -0.11
JES Flavor Response	0.28 -0.28	0.29 -0.29	0.29 -0.29	0.26 -0.26	0.18 -0.18	0.14 -0.14	0.14 -0.14	0.06 -0.06	0.06 -0.06	0.02 -0.02	0.02 -0.02	0.02 -0.02
JES Pileup OffsetMu	-0.10 0.10	-0.02 0.02	0.02 -0.02	0.01 -0.01	0.02 -0.02	0.03 -0.03	0.03 -0.03	0.09 -0.09	0.09 -0.09	0.16 -0.16	0.18 -0.18	0.19 -0.19
JES Pileup OffsetNPV	-0.13 0.13	-0.10 0.10	-0.03 0.03	-0.02 0.02	-0.06 0.06	-0.04 0.04	0.02 -0.02	0.01 -0.01	0.01 -0.01	-0.02 0.02	-0.03 0.03	-0.03 0.03
JES Pileup RhoTopo	-0.13 0.13	-0.14 0.14	-0.12 0.12	-0.11 0.11	-0.06 0.07	-0.04 0.04	-0.04 0.04	-0.03 0.03	-0.03 0.03	-0.01 0.01	0.01 -0.01	0.05 -0.05
EL SF ID	0.79 -0.79	0.79 -0.79	0.93 -0.93	1.24 -1.24	1.41 -1.41	1.44 -1.44	1.50 -1.50	1.98 -1.98	1.98 -1.98	2.77 -2.77	4.26 -4.25	5.25 -5.25
EL SF Isol	0.55 -0.55	0.55 -0.55	0.57 -0.57	0.64 -0.64	0.69 -0.69	0.71 -0.71	0.78 -0.78	1.12 -1.12	1.13 -1.13	1.28 -1.28	1.45 -1.45	1.60 -1.60
PU SF	0.22 -0.22	0.06 -0.06	-0.14 0.14	-0.25 0.25	-0.24 0.24	-0.26 0.26	-0.29 0.30	-0.19 0.20	-0.19 0.19	-0.13 0.13	-0.08 0.08	0.06 -0.06
MJ EL MET	-0.76 0.56	-0.40 0.38	-0.13 0.14	0.01 0.04	-0.70 0.46	-1.19 0.74	-2.78 1.83	-0.99 0.87	-0.99 0.87	-0.96 0.83	-0.66 0.54	-1.91 1.21
MJ EL 1jet	-0.01	-0.01	-0.01	-0.02	-0.03	-0.06	-0.11	0.02	0.02	0.04	0.05	0.25
MJ EL MC scaling	0.45 -0.45	0.31 -0.31	0.13 -0.13	0.04 -0.04	0.57 -0.57	0.91 -0.91	1.96 -1.96	0.48 -0.48	0.48 -0.48	0.45 -0.45	0.28 -0.28	0.82 -0.82
MJ EL mixMET	-0.34	-0.31	-0.18	-0.08	-0.87	-0.92	-1.75	-2.38	-2.40	-2.88	-1.76	-2.41
FSR	-0.30 -0.61	-0.28 -0.35	-0.27 0.12	-0.24 0.30	-0.23 0.31	-0.18 0.22	-0.08 0.06	0.04 -0.05	0.04 -0.05	0.09 -0.06	0.21 -0.09	0.44 -0.15
$t\bar{t}$ $\mu_R = 2.0$, $\mu_F = 1.0$	-0.96	-0.90	-0.86	-0.76	-0.74	-0.70	-0.65	-0.36	-0.36	-0.30	-0.23	-0.21
$t\bar{t}$ $\mu_R = 0.5$, $\mu_F = 0.5$	1.18	1.17	1.19	1.14	1.13	0.95	0.78	0.41	0.40	0.31	0.23	0.20
$t\bar{t}$ hardscatter	0.85	0.77	0.69	0.58	0.56	0.54	0.59	0.50	0.50	0.46	0.35	0.32
$t\bar{t}$ hadronisation	1.61	1.34	0.87	0.49	0.61	0.93	1.07	0.33	0.33	0.22	0.17	0.16
$t\bar{t}$ hdamp	0.02	0.02	0.05	0.08	0.10	0.10	0.08	-0.06	-0.06	-0.18	-0.36	-0.57
$t\bar{t}$ NNPDF RMS	-0.25 0.25	-0.22 0.22	-0.23 0.23	-0.20 0.20	-0.25 0.25	-0.31 0.31	-0.38 0.38	-0.39 0.39	-0.40 0.40	-0.48 0.48	-0.79 0.79	-0.63 0.63

Table G.3: Final measured double-differential cross-section as a function of the transverse momentum of the W boson and the absolute value of the electron's pseudorapidity for $m_{\mathrm{T}}^{W} = [425 - 600]\,\mathrm{GeV}$ in the e^{+} channel. The statistical uncertainty of the data and of the MC samples, obtained from the covariance matrix, and the systematic uncertainties with an impact of more than 0.5% are presented separately.

$\eta(l)$ bin edges	0.0 - 0.4	0.4 - 0.8	0.8 - 1.2	1.2 - 1.6	1.6 - 2.0	2.0 - 2.4
σ [pb/GeV]	2.26e-02	2.18e-02	1.97e-02	1.72e-02	1.34e-02	7.03e-03
Data stat. unc. [%]	2.45	2.48	2.39	1.86	3.33	4.78
MC stat. unc. [%]	1.85	1.45	1.82	1.43	2.58	3.32
tot. sys. unc. [%]	4.08 -3.41	3.55 -3.16	3.27 -3.17	3.37 -3.32	3.87 -3.85	4.76 -4.76
SoftTrk Scale	-0.02 0.02	0.00 -0.00	0.02 -0.02	0.02 -0.02	0.02 -0.02	-0.01 0.01
SoftTrk ResoPara	-0.14	-0.02	0.03	0.02	-0.01	-0.08
SoftTrk ResoPerp	0.01	0.05	0.06	0.03	-0.06	-0.14
EG SCALE S12	-0.40 0.40	-0.29 0.29	-0.22 0.22	-0.36 0.36	-0.76 0.76	-1.29 1.29
EG SCALE LARCALIB	-0.47 0.47	-0.46 0.46	-0.42 0.42	-0.48 0.48	-0.66 0.66	-0.97 0.97
EG SCALE L1GAIN	0.00 -0.00	-0.00 0.00	-0.01 0.01	0.10 -0.10	0.41 -0.41	0.76 -0.76
EG SCALE L2GAIN	1.02 -1.02	1.01 -1.01	0.95 -0.95	0.87 -0.87	0.63 -0.63	0.62 -0.62
JER EffNP 1	0.59 -0.59	0.40 -0.40	0.20 -0.20	0.10 -0.10	-0.13 0.13	-0.18 0.18
JER EffNP 2	-0.16 0.16	-0.16 0.16	-0.12 0.12	-0.09 0.09	0.02 -0.02	0.01 -0.01
JER EffNP 3	0.40 -0.40	0.18 -0.18	0.08 -0.08	0.05 -0.05	-0.05 0.05	-0.12 0.12
JER EffNP 4	0.52 -0.52	0.26 -0.26	0.14 -0.14	0.08 -0.08	-0.05 0.05	-0.08 0.08
JER EffNP 5	0.62 -0.62	0.29 -0.29	0.14 -0.14	0.07 -0.07	-0.10 0.10	-0.27 0.27
JER EffNP 6	0.46 -0.46	0.20 -0.20	0.10 -0.10	0.05 -0.05	-0.08 0.08	-0.21 0.21
JER EffNP 7	0.53 -0.53	0.25 -0.25	0.12 -0.12	0.06 -0.06	-0.07 0.07	-0.17 0.17
JES EffNP Model1	0.00 -0.00	-0.00 0.00	-0.00 0.00	-0.02 0.02	-0.06 0.06	-0.06 0.06
JES EtaIntercalib Model	0.04 -0.04	0.03 -0.03	0.02 -0.02	0.02 -0.02	0.03 -0.03	0.08 -0.08
JES Flavor Composition	0.09 -0.09	0.05 -0.05	-0.02 0.02	-0.03 0.03	-0.04 0.04	0.04 -0.04
JES Flavor Response	0.01 -0.01	0.02 -0.02	0.01 -0.01	0.02 -0.02	0.03 -0.03	0.06 -0.06
JES Pileup OffsetMu	0.18 -0.18	0.11 -0.11	0.01 -0.01	-0.00 0.00	-0.04 0.04	-0.01 0.01
JES Pileup OffsetNPV	0.02 -0.02	0.01 -0.01	-0.00 0.00	0.00 -0.00	-0.01 0.01	-0.00 0.00
JES Pileup RhoTopo	0.06 -0.06	0.05 -0.05	0.02 -0.02	0.02 -0.02	0.02 -0.02	0.03 -0.03
EL SF ID	2.58 -2.58	2.56 -2.56	2.52 -2.52	2.70 -2.70	3.25 -3.25	3.91 -3.91
EL SF Isol	0.83 -0.83	0.84 -0.84	0.82 -0.82	0.98 -0.98	1.43 -1.43	1.52 -1.52
PU SF	-0.27 0.27	-0.24 0.24	-0.14 0.14	-0.14 0.14	-0.11 0.11	-0.26 0.27
MJ EL MET	-0.57 0.52	-0.51 0.48	-1.02 0.97	-1.00 0.95	-0.61 0.67	-0.91 0.92
MJ EL 1jet	-0.03	-0.03	-0.06	-0.04	0.03	0.09
MJ EL MC scaling	0.30 -0.30	0.29 -0.29	0.63 -0.63	0.57 -0.57	0.18 -0.18	0.32 -0.32
MJ EL mixMET	-0.06	0.02	0.13	0.08	0.16	0.15
FSR	-0.17 0.72	-0.11 0.61	-0.03 0.37	-0.01 0.20	0.01 -0.17	-0.01 -0.19
$t\bar{t}$ $\mu_R = 2.0$, $\mu_F = 1.0$	-0.74	-0.65	-0.52	-0.44	-0.25	-0.19
$t\bar{t}$ $\mu_R = 0.5$, $\mu_F = 0.5$	1.18	0.97	0.74	0.60	0.32	0.25
$t\bar{t}$ hardscatter	1.13	0.82	0.34	0.28	0.10	0.17
$t\bar{t}$ hadronisation	1.55	1.03	0.44	0.32	-0.08	-0.02
$t\bar{t}$ hdamp	0.30	0.22	0.08	0.04	-0.07	-0.11
$t\bar{t}$ NNPDF RMS	-0.24 0.24	-0.22 0.22	-0.25 0.25	-0.28 0.28	-0.34 0.34	-0.39 0.39

Table G.4: Final measured double-differential cross-section as a function of the transverse momentum of the W boson and the absolute value of the electron's pseudorapidity for $m_{\mathrm{T}}^{W} = [600 - 900]\,\mathrm{GeV}$ in the e^{+} channel. The statistical uncertainty of the data and of the MC samples, obtained from the covariance matrix, and the systematic uncertainties with an impact of more than 0.5% are presented separately.

$\eta(l)$ bin edges	0.0 - 0.4	0.4 - 0.8	0.8 - 1.2	1.2 - 1.6	1.6 - 2.0	2.0 - 2.4
σ [pb/GeV]	7.58e-03	7.35e-03	6.66e-03	4.94e-03	2.99e-03	1.17e-03
Data stat. unc. [%]	3.96	3.95	3.87	3.11	6.72	10.99
MC stat. unc. [%]	3.53	2.01	2.10	1.58	1.68	3.76
tot. sys. unc. [%]	5.13 -4.94	4.97 -4.85	4.84 -4.77	4.99 -4.94	5.80 -5.79	6.51 -6.47
SoftTrk Scale	0.03 -0.03	0.00 -0.00	-0.01 0.01	0.00 -0.00	0.03 -0.03	0.07 -0.07
SoftTrk ResoPara	-0.10	-0.12	-0.09	-0.05	0.07	0.13
SoftTrk ResoPerp	-0.03	-0.05	-0.05	-0.02	0.08	0.23
EG SCALE S12	-0.42 0.42	-0.42 0.42	-0.39 0.39	-0.52 0.51	-0.88 0.88	-1.40 1.40
EG SCALE LARCALIB	-0.51 0.51	-0.51 0.51	-0.49 0.49	-0.55 0.55	-0.71 0.71	-0.98 0.98
EG SCALE L1GAIN	-0.00 0.00	0.00 -0.00	-0.05 0.05	0.13 -0.13	0.65 -0.65	1.55 -1.55
EG SCALE L2GAIN	0.90 -0.90	0.90 -0.90	0.87 -0.87	0.85 -0.85	0.77 -0.77	0.78 -0.78
JER EffNP 1	0.02 -0.02	0.03 -0.03	0.01 -0.01	0.00 -0.00	-0.01 0.01	-0.01 0.01
JER EffNP 2	0.03 -0.03	0.03 -0.03	0.01 -0.01	0.00 -0.00	-0.00 0.00	-0.01 0.01
JER EffNP 3	0.04 -0.04	0.04 -0.04	0.02 -0.02	-0.01 0.01	-0.07 0.07	-0.08 0.08
JER EffNP 4	-0.01 0.01	-0.00 0.00	0.00 -0.00	-0.01 0.01	-0.04 0.04	-0.05 0.05
JER EffNP 5	0.01 -0.01	0.02 -0.02	0.01 -0.01	-0.01 0.01	-0.04 0.04	-0.04 0.04
JER EffNP 6	0.03 -0.03	0.02 -0.02	0.01 -0.01	-0.00 0.00	-0.05 0.05	-0.05 0.05
JER EffNP 7	-0.00 0.00	0.00 -0.00	0.00 -0.00	-0.01 0.01	-0.05 0.05	-0.05 0.05
JES EffNP Model1	-0.06 0.06	-0.05 0.05	-0.05 0.05	-0.04 0.04	-0.01 0.01	0.00 -0.00
JES EtaIntercalib Model	-0.05 0.05	-0.02 0.02	-0.01 0.01	-0.01 0.01	-0.00 0.00	-0.00 0.00
JES Flavor Composition	-0.11 0.11	-0.09 0.09	-0.07 0.07	-0.05 0.05	-0.01 0.01	-0.01 0.01
JES Flavor Response	0.05 -0.05	0.04 -0.04	0.04 -0.04	0.03 -0.03	0.02 -0.02	0.01 -0.01
JES Pileup OffsetMu	-0.02 0.02	-0.02 0.02	-0.01 0.01	-0.01 0.01	0.02 -0.02	0.03 -0.03
JES Pileup OffsetNPV	-0.04 0.04	-0.03 0.03	-0.03 0.03	-0.03 0.03	-0.05 0.05	-0.06 0.06
JES Pileup RhoTopo	-0.09 0.09	-0.06 0.06	-0.05 0.05	-0.05 0.05	-0.04 0.04	-0.04 0.04
EL SF ID	4.40 -4.40	4.36 -4.36	4.33 -4.33	4.41 -4.41	4.70 -4.69	5.02 -5.02
EL SF Isol	1.28 -1.28	1.27 -1.27	1.23 -1.23	1.61 -1.61	2.77 -2.77	3.01 -3.01
PU SF	-0.34 0.34	-0.28 0.28	-0.18 0.18	-0.17 0.17	-0.13 0.13	-0.14 0.14
MJ EL MET	-0.63 0.54	-0.63 0.53	-0.83 0.76	-0.85 0.87	-0.89 1.17	-1.04 1.32
MJ EL 1jet	-0.00	-0.00	-0.00	-0.00	0.00	-0.00
MJ EL MC scaling	0.41 -0.41	0.36 -0.36	0.36 -0.36	0.31 -0.31	0.15 -0.15	0.21 -0.21
MJ EL mixMET	0.59	0.53	0.56	0.33	-0.28	-0.22
FSR	-0.93 1.37	-0.82 1.20	-0.59 0.85	-0.38 0.66	0.22 0.14	0.30 0.16
$t\bar{t}$ $\mu_R = 2.0$, $\mu_F = 1.0$	-0.54	-0.46	-0.32	-0.26	-0.08	-0.07
$t\bar{t}$ $\mu_R = 0.5$, $\mu_F = 0.5$	1.00	0.72	0.48	0.40	0.16	0.14
$t\bar{t}$ hardscatter	-0.42	-0.28	-0.09	-0.06	-0.01	-0.01
$t\bar{t}$ hadronisation	0.32	0.27	0.20	0.01	-0.55	-0.44
$t\bar{t}$ hdamp	0.24	0.10	-0.01	-0.12	-0.46	-0.35
$t\bar{t}$ NNPDF RMS	-0.18 0.18	-0.14 0.14	-0.16 0.16	-0.18 0.18	-0.23 0.23	-0.30 0.30

Table G.5: Final measured double-differential cross-section as a function of the transverse momentum of the W boson and the absolute value of the electron's pseudorapidity for $m_{\mathrm{T}}^{W} = [900 - 2000]\,\mathrm{GeV}$ in the e^{+} channel. The statistical uncertainty of the data and of the MC samples, obtained from the covariance matrix, and the systematic uncertainties with an impact of more than 0.5% are presented separately.

$\eta(l)$ bin edges	0.0 - 0.6	0.6 - 1.2	1.2 - 1.8	1.8 - 2.4
σ [pb/GeV]	3.42e-03	2.41e-03	1.09e-03	2.07e-04
Data stat. unc. [%]	5.37	6.50	8.48	18.61
MC stat. unc. [%]	0.46	1.10	0.00	1.33
tot. sys. unc. [%]	4.74 -5.05	5.19 -4.85	5.29 -5.24	6.16 -6.21
SoftTrk Scale	-0.03 0.03	-0.02 0.02	0.01 -0.01	0.04 -0.04
SoftTrk ResoPara	0.01	0.01	0.00	0.00
SoftTrk ResoPerp	0.03	0.03	0.03	0.04
EG SCALE S12	-0.57 0.57	-0.61 0.61	-1.12 1.12	-1.82 1.82
EG SCALE LARCALIB	-0.78 0.78	-0.79 0.79	-0.87 0.87	-1.00 1.00
EG SCALE L1GAIN	-0.00 0.00	-0.00 0.00	-0.01 0.01	0.03 -0.03
EG SCALE L2GAIN	1.17 -1.17	1.27 -1.27	1.46 -1.46	1.69 -1.69
JER EffNP 1	0.12 -0.12	0.09 -0.09	0.06 -0.06	0.02 -0.02
JER EffNP 2	0.12 -0.12	0.10 -0.10	0.04 -0.04	-0.03 0.03
JER EffNP 3	0.09 -0.09	0.07 -0.07	0.04 -0.04	0.00 -0.00
JER EffNP 4	0.05 -0.05	0.05 -0.05	0.05 -0.05	0.05 -0.05
JER EffNP 5	0.07 -0.07	0.07 -0.07	0.05 -0.05	0.04 -0.04
JER EffNP 6	0.06 -0.06	0.06 -0.06	0.06 -0.06	0.06 -0.06
JER EffNP 7	0.06 -0.06	0.05 -0.05	0.05 -0.05	0.04 -0.04
JES EffNP Model1	-0.01 0.01	-0.01 0.01	-0.00 0.00	0.01 -0.01
JES EtaIntercalib Model	-0.00 0.00	-0.00 0.00	0.01 -0.01	0.02 -0.02
JES Flavor Composition	-0.03 0.03	-0.01 0.01	0.00 -0.00	0.02 -0.02
JES Flavor Response	0.03 -0.03	0.03 -0.03	0.03 -0.03	0.03 -0.03
JES Pileup OffsetMu	-0.00 0.00	-0.00 0.00	-0.00 0.00	0.00 -0.00
JES Pileup OffsetNPV	-0.00 0.00	0.01 -0.01	0.03 -0.03	0.06 -0.06
JES Pileup RhoTopo	-0.01 0.01	-0.01 0.01	-0.00 0.00	0.00 -0.00
EL SF ID	4.30 -4.30	4.31 -4.31	4.52 -4.52	4.82 -4.81
EL SF Isol	1.27 -1.27	1.29 -1.29	1.61 -1.61	2.07 -2.07
PU SF	0.03 -0.03	-0.02 0.02	-0.24 0.24	-0.52 0.52
MJ EL MET	0.02 -0.02	-0.07 0.32	-0.49 0.79	-1.02 1.38
MJ EL 1jet	-0.00	0.00	-0.00	-0.00
MJ EL MC scaling	-0.01 0.01	-0.04 0.04	0.05 -0.05	0.16 -0.16
MJ EL mixMET	-1.03	1.98	0.37	-1.59
FSR	0.02 -0.12	0.01 0.01	0.01 0.05	0.03 0.10
$t\bar{t}$ $\mu_R = 2.0$, $\mu_F = 1.0$	-0.08	-0.06	-0.07	-0.09
$t\bar{t}$ $\mu_R = 0.5$, $\mu_F = 0.5$	0.15	0.10	0.07	0.03
$t\bar{t}$ hardscatter	-0.03	-0.02	-0.02	-0.01
$t\bar{t}$ hadronisation	-0.76	-0.35	0.02	0.45
$t\bar{t}$ hdamp	-1.20	-0.70	0.02	0.90
$t\bar{t}$ NNPDF RMS	-0.07 0.07	-0.04 0.04	-0.04 0.04	-0.05 0.05

Table G.6: Final measured double-differential cross-section as a function of the transverse momentum of the W boson and the absolute value of the electron's pseudorapidity for $m_{\mathrm{T}}^{W} = [200-300]\,\mathrm{GeV}$ in the e^{-} channel. The statistical uncertainty of the data and of the MC samples, obtained from the covariance matrix, and the systematic uncertainties with an impact of more than 0.5% are presented separately.

$\eta(l)$ bin edges	0.0 - 0.2	0.2 - 0.4	0.4 - 0.6	0.6 - 0.8	0.8 - 1.0	1.0 - 1.2	1.2 - 1.4	1.4 - 1.6	1.6 - 1.8	1.8 - 2.0	2.0 - 2.2	2.2 - 2.4
σ [pb/GeV]	8.20e-02	8.28e-02	8.51e-02	7.98e-02	7.98e-02	7.94e-02	6.81e-02	7.42e-02	7.09e-02	6.44e-02	6.48e-02	4.61e-02
Data stat. unc. [%]	1.60	1.54	1.50	1.55	1.56	1.55	1.97	1.43	1.44	1.77	1.67	2.15
MC stat. unc. [%]	1.58	1.46	1.33	1.40	1.30	1.34	1.72	1.20	1.21	1.48	1.54	1.87
tot. sys. unc. [%]	2.28 -2.02	2.03 -1.70	2.21 -1.69	2.78 -2.33	3.46 -3.31	4.25 -4.52	6.26 -8.83	3.74 -5.52	3.73 -5.49	3.95 -5.80	4.56 -5.04	6.36 -9.60
SoftTrk Scale	-0.60 0.61	-0.60 0.60	-0.58 0.59	-0.57 0.57	-0.53 0.54	-0.50 0.50	-0.48 0.49	-0.54 0.54	-0.52 0.52	-0.60 0.60	-0.61 0.61	-0.62 0.62
SoftTrk ResoPara	-0.37	-0.38	-0.38	-0.31	-0.16	-0.10	-0.08	0.00	0.02	-0.13	-0.25	-0.31
SoftTrk ResoPerp	-0.25	-0.27	-0.27	-0.28	-0.24	-0.18	-0.14	-0.27	-0.25	-0.36	-0.37	-0.37
EG SCALE S12	-0.28 0.28	-0.27 0.27	-0.26 0.26	-0.26 0.26	-0.25 0.25	-0.21 0.21	-0.16 0.16	-0.29 0.29	-0.29 0.29	-0.53 0.53	-0.71 0.71	-0.80 0.80
EG SCALE LARCALIB	-0.33 0.33	-0.33 0.33	-0.33 0.33	-0.31 0.31	-0.27 0.27	-0.23 0.23	-0.20 0.20	-0.26 0.26	-0.26 0.26	-0.38 0.38	-0.47 0.47	-0.49 0.49
EG SCALE L1GAIN	-0.02 0.02	-0.02 0.02	-0.02 0.02	-0.02 0.02	-0.02 0.02	-0.02 0.02	-0.02 0.02	-0.01 0.01	-0.01 0.01	0.20 -0.20	0.75 -0.75	1.49 -1.49
EG SCALE L2GAIN	0.60 -0.60	0.58 -0.58	0.61 -0.61	0.86 -0.86	1.32 -1.32	1.51 -1.51	1.18 -1.18	0.40 -0.40	0.39 -0.39	0.35 -0.35	0.33 -0.33	0.28 -0.28
JER EffNP 1	0.30 -0.29	0.32 -0.31	0.33 -0.32	0.53 -0.52	0.99 -0.98	1.46 -1.46	1.70 -1.69	1.41 -1.41	1.39 -1.39	1.22 -1.22	0.88 -0.88	0.58 -0.57
JER EffNP 2	0.07 -0.07	0.09 -0.09	0.10 -0.10	0.21 -0.21	0.65 -0.65	1.37 -1.37	1.82 -1.82	1.28 -1.28	1.28 -1.28	1.11 -1.11	1.02 -1.02	0.85 -0.85
JER EffNP 3	0.14 -0.14	0.15 -0.15	0.15 -0.15	0.16 -0.16	0.37 -0.37	0.93 -0.93	1.34 -1.34	0.87 -0.87	0.86 -0.86	0.64 -0.64	0.39 -0.39	0.01 -0.01
JER EffNP 4	-0.12 0.12	0.08 -0.08	0.23 -0.22	0.39 -0.39	0.62 -0.62	1.00 -1.00	1.32 -1.32	1.13 -1.13	1.13 -1.13	0.87 -0.87	0.57 -0.57	0.43 -0.43
JER EffNP 5	-0.24 0.24	-0.05 0.05	0.05 -0.05	0.16 -0.16	0.51 -0.51	1.03 -1.03	1.29 -1.29	0.53 -0.53	0.53 -0.53	0.28 -0.28	0.15 -0.15	0.09 -0.09
JER EffNP 6	0.16 -0.16	0.17 -0.17	0.17 -0.17	0.17 -0.16	0.35 -0.35	0.82 -0.82	1.16 -1.16	0.70 -0.70	0.70 -0.70	0.50 -0.50	0.36 -0.36	0.27 -0.27
JER EffNP 7	-0.20 0.20	0.00 -0.00	0.19 -0.19	0.43 -0.43	0.64 -0.64	0.90 -0.90	1.08 -1.08	0.85 -0.85	0.86 -0.86	0.68 -0.68	0.41 -0.41	0.29 -0.29
JES EffNP Model1	0.00 -0.00	-0.03 0.03	-0.07 0.07	-0.14 0.14	-0.17 0.17	-0.16 0.16	-0.15 0.15	-0.10 0.10	-0.10 0.10	-0.06 0.06	-0.04 0.04	-0.00 0.00
JES EtaIntercalib Model	0.04 -0.04	0.04 -0.04	0.02 -0.02	0.02 -0.02	-0.03 0.03	-0.14 0.14	-0.21 0.21	-0.14 0.14	-0.15 0.15	-0.07 0.07	-0.07 0.07	-0.06 0.06
JES Flavor Composition	-0.24 0.25	-0.21 0.21	-0.19 0.19	-0.19 0.19	-0.22 0.22	-0.23 0.23	-0.21 0.21	-0.19 0.20	-0.21 0.21	-0.29 0.30	-0.47 0.48	-0.54 0.54
JES Flavor Response	0.02 -0.02	0.11 -0.11	0.19 -0.19	0.26 -0.25	0.29 -0.29	0.27 -0.27	0.24 -0.24	0.25 -0.24	0.25 -0.25	0.26 -0.26	0.27 -0.27	0.26 -0.26
JES Pileup OffsetMu	0.29 -0.29	0.36 -0.36	0.37 -0.37	0.27 -0.27	0.07 -0.07	-0.05 0.06	-0.11 0.11	-0.12 0.13	-0.14 0.14	-0.04 0.04	0.01 -0.01	0.01 -0.01
JES Pileup OffsetNPV	-0.17 0.17	-0.01 0.01	0.07 -0.07	0.06 -0.06	-0.03 0.03	-0.10 0.10	-0.12 0.13	-0.10 0.10	-0.11 0.11	-0.09 0.09	-0.08 0.08	-0.07 0.07
JES Pileup RhoTopo	-0.29 0.29	-0.28 0.28	-0.26 0.26	-0.21 0.22	-0.21 0.21	-0.23 0.23	-0.21 0.21	-0.12 0.12	-0.13 0.14	-0.17 0.17	-0.24 0.24	-0.21 0.21
EL SF ID	0.46 -0.46	0.46 -0.46	0.51 -0.51	0.60 -0.60	0.67 -0.67	0.69 -0.69	0.69 -0.69	1.00 -1.00	1.01 -1.01	1.98 -1.98	3.49 -3.49	4.22 -4.21
EL SF Isol	0.17 -0.17	0.17 -0.17	0.18 -0.18	0.20 -0.20	0.22 -0.22	0.23 -0.23	0.25 -0.25	0.35 -0.35	0.35 -0.35	0.38 -0.38	0.42 -0.42	0.44 -0.44
PU SF	-0.10 0.10	0.07 -0.07	0.17 -0.17	0.15 -0.15	0.04 -0.04	-0.09 0.09	-0.20 0.20	-0.19 0.20	-0.20 0.21	-0.13 0.13	-0.09 0.09	-0.07 0.07
MJ EL MET	-0.26 0.48	0.30 0.03	0.50 -0.16	-0.77 0.53	-1.53 0.82	-2.08 1.08	-5.43 2.86	-2.24 1.40	-2.21 1.39	-2.18 1.32	-1.28 0.75	-5.27 2.82
MJ EL 1jet	-0.02	-0.05	-0.06	0.02	0.06	0.08	0.21	-0.00	-0.00	0.00	-0.02	0.09
MJ EL MC scaling	0.94 -0.94	0.17 -0.17	-0.15 0.15	0.82 -0.81	1.04 -1.04	1.30 -1.30	3.46 -3.46	1.17 -1.17	1.15 -1.15	1.09 -1.09	0.56 -0.56	2.36 -2.36
MJ EL mixMET	0.21	0.27	0.39	-0.75	-1.12	-1.44	-4.41	-3.80	-3.78	-4.13	-2.36	-5.86
FSR	-0.37 -0.13	-0.33 -0.09	-0.26 0.23	-0.24 0.84	-0.16 1.13	0.00 0.74	0.09 0.08	-0.12 0.39	-0.12 0.40	-0.22 0.88	-0.19 0.83	-0.19 0.86
$t\bar{t}$ $\mu_R = 2.0$, $\mu_F = 1.0$	-0.89	-0.86	-0.82	-0.83	-0.77	-0.69	-0.68	-0.44	-0.44	-0.35	-0.24	-0.23
$t\bar{t}$ $\mu_R = 0.5$, $\mu_F = 0.5$	1.22	1.18	1.11	1.11	1.01	0.90	0.88	0.52	0.53	0.39	0.25	0.23
$t\bar{t}$ hardscatter	0.60	0.66	0.87	1.14	1.16	1.07	1.04	0.83	0.83	1.12	1.16	1.31
$t\bar{t}$ hadronisation	0.58	0.63	0.76	0.95	0.98	0.90	0.76	0.27	0.28	0.35	0.39	0.45
$t\bar{t}$ hdamp	-0.40	-0.33	-0.20	-0.08	0.06	0.15	0.23	0.34	0.35	0.31	0.24	0.24
$t\bar{t}$ NNPDF RMS	-0.41 0.41	-0.36 0.36	-0.28 0.28	-0.20 0.20	-0.14 0.14	-0.20 0.20	-0.34 0.34	-0.55 0.55	-0.55 0.55	-0.64 0.64	-0.67 0.67	-0.88 0.88

Table G.7: Final measured double-differential cross-section as a function of the transverse momentum of the W boson and the absolute value of the electron's pseudorapidity for $m_{\mathrm{T}}^{W} = [300 - 425]\,\mathrm{GeV}$ in the e^{-} channel. The statistical uncertainty of the data and of the MC samples, obtained from the covariance matrix, and the systematic uncertainties with an impact of more than 0.5% are presented separately.

$\eta(l)$ bin edges	0.0 - 0.2	0.2 - 0.4	0.4 - 0.6	0.6 - 0.8	0.8 - 1.0	1.0 - 1.2	1.2 - 1.4	1.4 - 1.6	1.6 - 1.8	1.8 - 2.0	2.0 - 2.2	2.2 - 2.4
σ [pb/GeV]	1.93e-02	1.85e-02	1.76e-02	1.71e-02	1.69e-02	1.66e-02	1.46e-02	1.70e-02	1.61e-02	1.50e-02	1.19e-02	9.47e-03
Data stat. unc. [%]	3.27	3.27	3.35	3.34	3.31	3.33	4.18	2.88	2.86	3.39	3.75	4.47
MC stat. unc. [%]	2.17	2.13	2.09	1.93	2.49	2.64	2.17	1.86	1.85	2.03	1.74	2.46
tot. sys. unc. [%]	5.17 -3.19	5.12 -2.79	5.44 -3.42	5.53 -3.19	5.46 -3.98	5.15 -4.37	5.21 -5.42	3.33 -5.98	3.33 -5.98	3.84 -5.58	5.65 -7.60	6.96 -11.99
SoftTrk Scale	-0.03 0.03	-0.02 0.02	0.00 -0.00	0.06 -0.06	0.15 -0.15	0.10 -0.10	0.10 -0.10	0.05 -0.05	0.05 -0.05	-0.11 0.11	-0.15 0.15	-0.13 0.13
SoftTrk ResoPara	-0.21	-0.05	0.03	0.03	0.13	0.19	0.16	-0.07	-0.07	-0.29	-0.38	-0.37
SoftTrk ResoPerp	0.18	0.16	0.10	0.05	0.10	0.05	0.03	-0.09	-0.09	-0.26	-0.31	-0.30
EG SCALE S12	-0.23 0.23	-0.24 0.24	-0.24 0.24	-0.24 0.24	-0.25 0.25	-0.26 0.26	-0.27 0.27	-0.49 0.49	-0.49 0.49	-0.92 0.92	-1.16 1.16	-1.22 1.22
EG SCALE LARCALIB	-0.31 0.31	-0.36 0.36	-0.40 0.40	-0.39 0.39	-0.33 0.33	-0.25 0.25	-0.23 0.23	-0.34 0.34	-0.34 0.34	-0.52 0.52	-0.62 0.62	-0.63 0.63
EG SCALE L1GAIN	-0.01 0.01	-0.01 0.01	-0.01 0.01	-0.01 0.01	-0.01 0.01	-0.01 0.01	-0.01 0.01	0.15 -0.15	0.16 -0.16	0.95 -0.95	2.20 -2.20	3.14 -3.14
EG SCALE L2GAIN	0.80 -0.80	0.80 -0.80	0.87 -0.87	1.43 -1.43	2.46 -2.46	2.90 -2.90	2.23 -2.22	0.31 -0.31	0.31 -0.31	0.26 -0.26	0.43 -0.43	0.50 -0.50
JER EffNP 1	0.00 0.00	-0.01 0.02	0.07 -0.07	0.25 -0.24	0.28 -0.28	0.31 -0.30	0.12 -0.11	-0.26 0.27	-0.26 0.27	-0.16 0.16	-0.13 0.14	-0.15 0.15
JER EffNP 2	-0.10 0.10	0.01 -0.01	0.24 -0.24	0.60 -0.60	0.81 -0.81	0.82 -0.82	0.49 -0.49	-0.19 0.19	-0.19 0.20	-0.20 0.20	-0.24 0.25	-0.30 0.31
JER EffNP 3	0.33 -0.33	0.31 -0.31	0.31 -0.31	0.34 -0.34	0.36 -0.36	0.27 -0.27	0.01 -0.01	-0.21 0.21	-0.21 0.21	-0.13 0.13	-0.04 0.04	0.01 -0.01
JER EffNP 4	-0.33 0.33	0.04 -0.03	0.16 -0.16	0.17 -0.17	0.15 -0.15	0.09 -0.09	-0.07 0.08	-0.21 0.21	-0.21 0.21	-0.18 0.18	-0.17 0.17	-0.18 0.18
JER EffNP 5	-0.07 0.07	-0.08 0.08	-0.08 0.08	-0.07 0.07	-0.10 0.10	-0.09 0.09	-0.11 0.11	-0.11 0.11	-0.11 0.11	-0.08 0.08	-0.06 0.06	-0.05 0.05
JER EffNP 6	-0.12 0.12	-0.12 0.12	-0.11 0.11	-0.10 0.10	-0.10 0.10	-0.07 0.07	-0.09 0.09	-0.12 0.12	-0.12 0.12	-0.09 0.09	-0.07 0.07	-0.07 0.07
JER EffNP 7	0.04 -0.04	0.08 -0.08	0.24 -0.24	0.44 -0.44	0.49 -0.49	0.31 -0.31	0.00 -0.00	-0.21 0.21	-0.21 0.21	-0.17 0.18	-0.14 0.14	-0.14 0.14
JES EffNP Model1	-0.22 0.22	-0.22 0.22	-0.19 0.19	-0.13 0.13	-0.12 0.12	-0.09 0.09	-0.06 0.06	-0.04 0.04	-0.04 0.04	-0.06 0.06	-0.08 0.08	-0.10 0.10
JES EtaIntercalib Model	-0.35 0.35	-0.25 0.25	-0.22 0.22	-0.24 0.24	-0.30 0.30	-0.24 0.24	-0.14 0.14	-0.10 0.10	-0.10 0.10	-0.08 0.08	-0.08 0.08	-0.08 0.08
JES Flavor Composition	-0.46 0.46	-0.47 0.47	-0.46 0.46	-0.45 0.45	-0.50 0.50	-0.44 0.44	-0.34 0.34	-0.33 0.33	-0.33 0.33	-0.40 0.40	-0.48 0.48	-0.51 0.51
JES Flavor Response	0.54 -0.54	0.44 -0.44	0.30 -0.30	0.26 -0.26	0.29 -0.29	0.23 -0.23	0.16 -0.16	0.23 -0.23	0.23 -0.23	0.34 -0.34	0.40 -0.40	0.42 -0.42
JES Pileup OffsetMu	-0.18 0.18	-0.19 0.19	-0.17 0.17	-0.11 0.11	-0.11 0.11	-0.08 0.08	-0.07 0.07	-0.08 0.08	-0.08 0.08	-0.04 0.04	-0.06 0.06	-0.12 0.12
JES Pileup OffsetNPV	-0.06 0.06	-0.07 0.07	-0.09 0.09	-0.14 0.14	-0.20 0.20	-0.15 0.15	-0.05 0.05	-0.05 0.05	-0.05 0.05	-0.04 0.04	-0.05 0.05	-0.06 0.06
JES Pileup RhoTopo	-0.26 0.26	-0.27 0.27	-0.26 0.26	-0.26 0.26	-0.29 0.29	-0.25 0.25	-0.22 0.22	-0.20 0.20	-0.20 0.20	-0.16 0.17	-0.13 0.13	-0.07 0.07
EL SF ID	0.84 -0.84	0.84 -0.84	1.00 -1.00	1.32 -1.32	1.50 -1.50	1.49 -1.49	1.52 -1.52	2.02 -2.02	2.03 -2.03	2.86 -2.86	4.33 -4.33	5.31 -5.31
EL SF Isol	0.57 -0.57	0.57 -0.57	0.60 -0.60	0.66 -0.66	0.72 -0.72	0.73 -0.73	0.78 -0.78	1.17 -1.17	1.17 -1.17	1.32 -1.32	1.46 -1.46	1.58 -1.58
PU SF	-0.42 0.42	-0.43 0.43	-0.39 0.39	-0.27 0.27	-0.19 0.19	-0.12 0.12	-0.07 0.07	-0.24 0.24	-0.24 0.24	-0.25 0.25	-0.18 0.18	-0.07 0.07
MJ EL MET	-1.11 0.85	-0.99 0.76	-1.65 1.18	-0.52 0.41	-0.69 0.53	-1.18 0.86	-3.05 2.23	-1.48 1.31	-1.47 1.30	-0.68 0.63	-0.72 0.62	-1.11 0.88
MJ EL 1jet	0.01	0.01	0.02	-0.06	-0.11	-0.15	-0.22	0.02	0.02	0.03	0.10	0.34
MJ EL MC scaling	0.78 -0.78	0.70 -0.70	1.17 -1.17	0.43 -0.43	0.63 -0.63	1.02 -1.01	2.32 -2.32	0.69 -0.69	0.69 -0.69	0.32 -0.32	0.41 -0.41	1.05 -1.05
MJ EL mixMET	-0.44	-0.36	-0.99	-0.65	-1.15	-1.33	-2.05	-5.04	-5.04	-4.12	-5.24	-9.82
FSR	-0.22 -1.34	-0.28 -0.31	-0.51 1.17	-0.77 2.12	-0.73 1.91	-0.42 1.27	-0.10 0.43	0.01 -0.53	0.01 -0.52	0.08 0.38	0.26 1.18	0.40 1.18
$t\bar{t}$ $\mu_R = 2.0$, $\mu_F = 1.0$	-1.74	-1.74	-1.72	-1.65	-1.48	-1.31	-1.21	-0.70	-0.69	-0.49	-0.42	-0.33
$t\bar{t}$ $\mu_R = 0.5$, $\mu_F = 0.5$	2.66	2.42	2.31	2.22	2.00	1.79	1.61	0.79	0.78	0.50	0.38	0.20
$t\bar{t}$ hardscatter	1.99	2.21	2.32	2.26	2.02	1.78	1.63	0.95	0.94	0.76	0.84	0.85
$t\bar{t}$ hadronisation	3.28	3.33	3.32	3.07	2.49	1.90	1.55	0.66	0.65	0.24	-0.30	-0.81
$t\bar{t}$ hdamp	0.60	0.61	0.63	0.62	0.51	0.32	0.10	-0.00	-0.00	-0.08	-0.17	-0.17
$t\bar{t}$ NNPDF RMS	-0.42 0.42	-0.42 0.42	-0.42 0.42	-0.45 0.45	-0.42 0.42	-0.55 0.55	-0.70 0.70	-0.69 0.69	-0.69 0.69	-0.82 0.82	-0.90 0.90	-0.82 0.82

Table G.8: Final measured double-differential cross-section as a function of the transverse momentum of the W boson and the absolute value of the electron's pseudorapidity for $m_{\mathrm{T}}^{W} = [425 - 600]\,\mathrm{GeV}$ in the e^- channel. The statistical uncertainty of the data and of the MC samples, obtained from the covariance matrix, and the systematic uncertainties with an impact of more than 0.5% are presented separately.

$\eta(l)$ bin edges	0.0 - 0.4	0.4 - 0.8	0.8 - 1.2	1.2 - 1.6	1.6 - 2.0	2.0 - 2.4
σ [pb/GeV]	1.13e-02	1.07e-02	8.94e-03	8.73e-03	8.46e-03	5.94e-03
Data stat. unc. [%]	3.80	3.89	3.94	2.89	4.31	5.21
MC stat. unc. [%]	1.81	2.21	2.18	1.46	1.91	1.81
tot. sys. unc. [%]	5.12 -4.28	4.77 -4.02	4.74 -4.26	4.33 -3.99	4.37 -3.98	4.99 -4.78
SoftTrk Scale	-0.01 0.01	0.11 -0.11	0.03 -0.03	0.04 -0.04	0.07 -0.07	0.00 -0.00
SoftTrk ResoPara	-0.14	0.05	0.01	0.03	0.08	0.04
SoftTrk ResoPerp	0.00	0.12	0.06	0.06	0.09	0.05
EG SCALE S12	-0.65 0.65	-0.65 0.65	-0.59 0.59	-0.59 0.59	-0.63 0.63	-0.80 0.80
EG SCALE LARCALIB	-0.71 0.71	-0.71 0.71	-0.63 0.63	-0.59 0.59	-0.52 0.52	-0.68 0.68
EG SCALE L1GAIN	-0.00 0.00	-0.00 0.00	-0.04 0.04	0.10 -0.10	0.46 -0.46	1.05 -1.05
EG SCALE L2GAIN	1.67 -1.67	1.69 -1.69	1.43 -1.43	1.14 -1.14	0.55 -0.55	0.61 -0.61
JER EffNP 1	0.04 -0.04	-0.07 0.08	0.07 -0.07	0.06 -0.06	0.11 -0.11	0.19 -0.19
JER EffNP 2	0.71 -0.71	0.30 -0.30	0.16 -0.16	0.12 -0.12	0.11 -0.11	0.16 -0.16
JER EffNP 3	0.15 -0.15	0.00 -0.00	-0.03 0.03	-0.06 0.06	-0.04 0.04	-0.00 0.00
JER EffNP 4	0.21 -0.21	0.03 -0.03	0.00 -0.00	0.00 -0.00	0.07 -0.07	0.13 -0.13
JER EffNP 5	-0.02 0.02	-0.05 0.05	-0.04 0.04	-0.03 0.04	-0.02 0.02	0.01 -0.01
JER EffNP 6	0.08 -0.08	0.01 -0.01	-0.01 0.01	-0.03 0.03	-0.05 0.05	-0.02 0.02
JER EffNP 7	0.12 -0.12	-0.02 0.02	-0.03 0.03	-0.06 0.06	-0.05 0.05	-0.02 0.02
JES EffNP Model1	-0.11 0.11	-0.12 0.12	-0.10 0.10	-0.07 0.07	-0.03 0.03	-0.01 0.01
JES EtaIntercalib Model	-0.16 0.16	-0.19 0.19	-0.13 0.13	-0.09 0.09	-0.06 0.06	-0.03 0.03
JES Flavor Composition	-0.13 0.13	-0.17 0.17	-0.07 0.07	-0.07 0.07	-0.10 0.10	-0.05 0.05
JES Flavor Response	0.34 -0.34	0.36 -0.36	0.31 -0.31	0.22 -0.22	0.04 -0.04	0.00 -0.00
JES Pileup OffsetMu	0.00 -0.00	-0.06 0.06	-0.01 0.01	-0.02 0.02	-0.07 0.07	-0.08 0.08
JES Pileup OffsetNPV	-0.08 0.08	-0.09 0.09	-0.03 0.03	-0.02 0.02	-0.02 0.02	-0.02 0.02
JES Pileup RhoTopo	-0.11 0.11	-0.13 0.13	-0.06 0.06	-0.06 0.06	-0.08 0.08	-0.06 0.06
EL SF ID	2.63 -2.63	2.66 -2.66	2.57 -2.57	2.79 -2.79	3.34 -3.34	4.01 -4.01
EL SF Isol	0.86 -0.86	0.88 -0.88	0.83 -0.83	1.02 -1.02	1.47 -1.47	1.55 -1.55
PU SF	-0.38 0.38	-0.37 0.37	-0.23 0.23	-0.22 0.22	-0.21 0.21	-0.20 0.20
MJ EL MET	-1.50 1.25	-0.73 0.69	-1.92 1.71	-1.65 1.53	-0.75 0.87	-0.99 0.97
MJ EL 1jet	-0.05	-0.05	-0.07	-0.04	0.04	0.09
MJ EL MC scaling	0.87 -0.87	0.49 -0.49	1.30 -1.30	1.02 -1.02	0.21 -0.21	0.33 -0.33
MJ EL mixMET	-0.08	0.16	0.05	-0.03	-0.04	-0.09
FSR	-0.25 -0.49	-0.22 -1.04	-0.19 -0.88	-0.27 -0.29	-0.55 1.19	-0.51 0.65
$t\bar{t}$ $\mu_R = 2.0$, $\mu_F = 1.0$	-1.48	-1.35	-1.16	-0.84	-0.23	-0.12
$t\bar{t}$ $\mu_R = 0.5$, $\mu_F = 0.5$	2.21	2.06	1.72	1.12	-0.05	-0.06
$t\bar{t}$ hardscatter	2.02	1.85	1.70	1.19	0.21	0.06
$t\bar{t}$ hadronisation	1.54	1.44	1.19	1.16	1.23	1.17
$t\bar{t}$ hdamp	-0.51	-0.25	-0.20	0.04	0.59	0.73
$t\bar{t}$ NNPDF RMS	-0.45 0.45	-0.45 0.45	-0.55 0.55	-0.57 0.57	-0.57 0.57	-0.54 0.54

Table G.9: Final measured double-differential cross-section as a function of the transverse momentum of the W boson and the absolute value of the electron's pseudorapidity for $m_{\mathrm{T}}^{W} = [600 - 900]\,\mathrm{GeV}$ in the e^{-} channel. The statistical uncertainty of the data and of the MC samples, obtained from the covariance matrix, and the systematic uncertainties with an impact of more than 0.5% are presented separately.

$\eta(l)$ bin edges	0.0 - 0.4	0.4 - 0.8	0.8 - 1.2	1.2 - 1.6	1.6 - 2.0	2.0 - 2.4
σ [pb/GeV]	3.66e-03	3.80e-03	2.61e-03	2.48e-03	2.19e-03	7.95e-04
Data stat. unc. [%]	6.01	5.71	6.64	4.77	7.98	13.60
MC stat. unc. [%]	1.52	2.47	6.22	4.13	1.43	3.24
tot. sys. unc. [%]	5.45 -5.35	5.22 -5.10	5.45 -5.09	5.44 -5.16	5.90 -5.74	6.60 -6.52
SoftTrk Scale	-0.05 0.05	-0.00 0.00	0.02 -0.02	-0.00 0.00	-0.04 0.04	-0.04 0.04
SoftTrk ResoPara	-0.04	-0.00	0.01	0.01	-0.00	-0.01
SoftTrk ResoPerp	-0.08	-0.04	-0.01	0.01	0.06	0.09
EG SCALE S12	-0.50 0.50	-0.48 0.48	-0.39 0.39	-0.53 0.53	-0.88 0.88	-1.56 1.56
EG SCALE LARCALIB	-0.54 0.54	-0.53 0.53	-0.49 0.49	-0.57 0.57	-0.77 0.77	-1.11 1.11
EG SCALE L1GAIN	-0.00 0.00	-0.00 0.00	-0.06 0.06	0.15 -0.15	0.68 -0.68	1.63 -1.63
EG SCALE L2GAIN	1.17 -1.17	1.18 -1.18	1.11 -1.11	1.00 -1.00	0.70 -0.70	0.73 -0.73
JER EffNP 1	0.09 -0.09	-0.00 0.00	-0.07 0.07	-0.07 0.07	-0.08 0.08	-0.18 0.18
JER EffNP 2	0.02 -0.02	-0.00 0.00	-0.02 0.02	-0.03 0.03	-0.06 0.06	-0.12 0.12
JER EffNP 3	0.07 -0.07	0.06 -0.06	0.04 -0.04	0.03 -0.03	0.01 -0.01	0.02 -0.02
JER EffNP 4	-0.02 0.02	-0.04 0.04	-0.02 0.02	-0.03 0.03	-0.05 0.05	-0.11 0.11
JER EffNP 5	0.07 -0.07	0.05 -0.05	0.05 -0.05	0.01 -0.01	-0.07 0.07	-0.21 0.21
JER EffNP 6	0.01 -0.01	-0.01 0.01	-0.01 0.01	-0.02 0.02	-0.06 0.06	-0.18 0.18
JER EffNP 7	-0.00 0.00	-0.03 0.03	-0.03 0.03	-0.03 0.03	-0.01 0.01	-0.02 0.02
JES EffNP Model1	0.02 -0.02	0.00 -0.00	-0.01 0.01	-0.00 0.00	0.01 -0.01	0.02 -0.02
JES EtaIntercalib Model	-0.00 0.00	-0.04 0.04	-0.06 0.06	-0.03 0.03	0.05 -0.05	0.13 -0.13
JES Flavor Composition	-0.05 0.05	-0.07 0.07	-0.07 0.07	-0.06 0.06	-0.04 0.04	-0.03 0.03
JES Flavor Response	0.03 -0.03	0.04 -0.04	0.04 -0.04	0.01 -0.01	-0.06 0.06	-0.16 0.16
JES Pileup OffsetMu	-0.00 0.00	-0.04 0.04	-0.05 0.05	-0.04 0.04	0.00 -0.00	0.05 -0.05
JES Pileup OffsetNPV	-0.06 0.06	-0.05 0.05	-0.04 0.04	-0.02 0.02	0.04 -0.04	0.13 -0.13
JES Pileup RhoTopo	-0.09 0.09	-0.07 0.07	-0.05 0.05	-0.02 0.02	0.04 -0.04	0.11 -0.11
EL SF ID	4.39 -4.39	4.43 -4.43	4.41 -4.40	4.48 -4.48	4.71 -4.71	5.03 -5.03
EL SF Isol	1.28 -1.28	1.29 -1.29	1.24 -1.24	1.67 -1.67	2.77 -2.77	3.03 -3.03
PU SF	0.26 -0.26	0.23 -0.23	0.15 -0.15	0.08 -0.08	-0.09 0.09	-0.07 0.07
MJ EL MET	-1.24 1.02	-0.65 0.63	-1.29 1.37	-1.13 1.28	-0.79 1.08	-0.90 1.18
MJ EL 1jet	0.00	-0.01	-0.01	-0.01	0.00	0.00
MJ EL MC scaling	0.56 -0.56	0.27 -0.27	0.46 -0.46	0.36 -0.36	0.13 -0.13	0.19 -0.19
MJ EL mixMET	0.88	0.64	1.03	0.64	-0.18	-0.04
FSR	-1.11 1.88	-0.70 1.53	-0.28 1.75	-0.17 1.45	0.05 0.84	0.02 0.45
$t\bar{t}$ $\mu_R = 2.0$, $\mu_F = 1.0$	-0.72	-0.58	-0.61	-0.48	-0.18	-0.12
$t\bar{t}$ $\mu_R = 0.5$, $\mu_F = 0.5$	0.97	0.79	0.84	0.81	0.76	0.54
$t\bar{t}$ hardscatter	-1.01	-0.82	-0.63	-0.41	0.07	0.02
$t\bar{t}$ hadronisation	-0.22	-0.18	-0.14	-0.10	-0.02	-0.02
$t\bar{t}$ hdamp	-0.95	-0.78	-0.60	-0.37	0.13	0.02
$t\bar{t}$ NNPDF RMS	-0.36 0.36	-0.29 0.29	-0.38 0.38	-0.36 0.36	-0.33 0.33	-0.27 0.27

Table G.10: Final measured double-differential cross-section as a function of the transverse momentum of the W boson and the absolute value of the electron's pseudorapidity for $m_{\mathrm{T}}^{W} = [900 - 2000]\,\mathrm{GeV}$ in the e^{-} channel. The statistical uncertainty of the data and of the MC samples, obtained from the covariance matrix, and the systematic uncertainties with an impact of more than 0.5% are presented separately.

$\eta(l)$ bin edges	0.0 - 0.6	0.6 - 1.2	1.2 - 1.8	1.8 - 2.4
σ [pb/GeV]	1.20e-03	9.15e-04	6.27e-04	1.99e-04
Data stat. unc. [%]	9.83	10.71	10.84	20.40
MC stat. unc. [%]	9.69	3.93	1.46	1.06
tot. sys. unc. [%]	6.10 -4.93	5.22 -4.89	5.15 -5.59	5.50 -6.89
SoftTrk Scale	-0.02 0.02	-0.01 0.01	-0.01 0.01	-0.01 0.01
SoftTrk ResoPara	0.01	0.01	0.00	-0.01
SoftTrk ResoPerp	-0.06	-0.04	-0.02	0.01
EG SCALE S12	-0.67 0.67	-0.67 0.67	-0.68 0.68	-0.72 0.72
EG SCALE LARCALIB	-0.74 0.74	-0.74 0.74	-0.73 0.73	-0.74 0.74
EG SCALE L1GAIN	-0.00 0.00	-0.01 0.01	-0.02 0.02	0.01 -0.01
EG SCALE L2GAIN	1.37 -1.37	1.33 -1.33	1.21 -1.21	1.09 -1.09
JER EffNP 1	-0.01 0.01	-0.01 0.01	-0.01 0.01	-0.01 0.01
JER EffNP 2	0.05 -0.05	0.05 -0.05	0.12 -0.12	0.18 -0.18
JER EffNP 3	-0.00 0.00	0.00 -0.00	0.04 -0.04	0.07 -0.07
JER EffNP 4	-0.00 0.00	-0.00 0.00	-0.00 0.00	-0.00 0.00
JER EffNP 5	-0.02 0.02	-0.01 0.01	0.00 -0.00	0.01 -0.01
JER EffNP 6	-0.01 0.01	-0.01 0.01	0.01 -0.01	0.02 -0.02
JER EffNP 7	-0.00 0.00	-0.00 0.00	-0.00 0.00	0.00 -0.00
JES EffNP Model1	-0.04 0.04	-0.04 0.04	-0.03 0.03	-0.03 0.03
JES EtaIntercalib Model	-0.01 0.01	-0.01 0.01	-0.02 0.02	-0.02 0.02
JES Flavor Composition	-0.05 0.05	-0.04 0.04	-0.01 0.01	0.03 -0.03
JES Flavor Response	0.08 -0.08	0.07 -0.07	0.04 -0.04	0.00 -0.00
JES Pileup OffsetMu	-0.01 0.01	-0.01 0.01	-0.02 0.02	-0.02 0.02
JES Pileup OffsetNPV	-0.02 0.02	-0.02 0.02	-0.02 0.02	-0.01 0.01
JES Pileup RhoTopo	-0.03 0.03	-0.03 0.03	-0.03 0.03	-0.02 0.02
EL SF ID	4.30 -4.30	4.30 -4.30	4.57 -4.57	4.85 -4.85
EL SF Isol	1.27 -1.27	1.27 -1.27	1.65 -1.65	2.04 -2.04
PU SF	-0.06 0.06	-0.06 0.06	-0.07 0.07	-0.08 0.08
MJ EL MET	-0.64 0.43	-0.67 0.56	-0.40 0.45	-0.15 0.34
MJ EL 1jet	-0.00	-0.00	-0.00	0.00
MJ EL MC scaling	0.53 -0.53	0.33 -0.33	0.15 -0.15	-0.01 0.01
MJ EL mixMET	2.27	1.92	0.14	-1.46
FSR	-0.37 -0.04	0.11 -0.04	0.23 -0.04	0.33 -0.06
$t\bar{t}$ $\mu_R = 2.0$, $\mu_F = 1.0$	-0.32	-0.22	-0.13	-0.04
$t\bar{t}$ $\mu_R = 0.5$, $\mu_F = 0.5$	0.63	0.39	0.20	0.02
$t\bar{t}$ hardscatter	2.87	-0.07	-1.93	-3.59
$t\bar{t}$ hadronisation	-0.43	-0.40	-0.60	-0.79
$t\bar{t}$ hdamp	-0.41	-0.48	-0.91	-1.31
$t\bar{t}$ NNPDF RMS	-0.13 0.13	-0.24 0.24	-0.19 0.19	-0.14 0.14

References

[1] J. J. Thomson, *Cathode Rays*, The London, Edinburgh, and Dublin Philosophical Magazine and Journal of Science **44** (1897) 293–316, https://doi.org/10.1080/14786449708621070.

[2] S. Weinberg, *A Model of Leptons*, Phys. Rev. Lett. **19** (1967) 1264–1266, https://link.aps.org/doi/10.1103/PhysRevLett.19.1264.

[3] S. L. Glashow, *Partial-symmetries of weak interactions*, Nuclear Physics **22** (1961) 579–588, https://doi.org/10.1016/0029-5582(61)90469-2.

[4] A. Salam, *Weak and Electromagnetic Interactions*, Conf. Proc. **C680519** (1968) 367.

[5] G. 't Hooft and M. J. G. Veltman, *Regularization and Renormalization of Gauge Fields*, Nucl. Phys. B **44** (1972) 189.

[6] O. S. Brüning, P. Collier, P. Lebrun, S. Myers, R. Ostojic, J. Poole, and P. Proudlock, *LHC Design Report*, https://cds.cern.ch/record/782076.

[7] ATLAS Collaboration, G. Aad et al., *The ATLAS Experiment at the CERN Large Hadron Collider*, JINST **3** (2008) S08003.

[8] CMS Collaboration, S. Chatrchyan et al., *The CMS Experiment at the CERN LHC*, JINST **3** (2008) S08004.

[9] LHCb Collaboration, A. A. Alves Jr. et al., *The LHCb Detector at the LHC*, JINST **3** (2008) S08005.

[10] ALICE Collaboration, K. Aamodt et al., *The ALICE experiment at the CERN LHC*, JINST **3** (2008) S08002.

[11] M. Farina, G. Panico, D. Pappadopulo, J. T. Ruderman, R. Torre, and A. Wulzer, *Energy helps accuracy: Electroweak precision tests at hadron colliders*, Physics Letters B **772** (2017) 210–215, http://dx.doi.org/10.1016/j.physletb.2017.06.043.

[12] LIGO Scientific Collaboration and Virgo Collaboration, B. Abbott et al., *Observation of Gravitational Waves from a Binary Black Hole Merger*, Physical Review Letters **116** (2016) .

[13] The ATLAS, CDF, CMS and D0 Collaborations, *First combination of Tevatron and LHC measurements of the top-quark mass*, 2014. https://arxiv.org/abs/1403.4427.

[14] ATLAS and CMS Collaboration, G. Aad et al., *Combined Measurement of the Higgs Boson Mass in pp Collisions at $\sqrt{s} = 7$ and 8 TeV with the ATLAS and CMS Experiments*, Physical Review Letters **114** (2015) 191803, http://dx.doi.org/10.1103/PhysRevLett.114.191803.

[15] Particle Data Group Collaboration, P. Zyla et al., *Review of Particle Physics*, PTEP **2020** (2020) 083C01.

[16] Super-Kamiokande Collaboration, Y. Fukuda et al., *Evidence for Oscillation of Atmospheric Neutrinos*, Physical Review Letters **81** (1998) 1562–1567, http://dx.doi.org/10.1103/PhysRevLett.81.1562.

[17] SNO Collaboration, Q. R. Ahmad et al., *Direct Evidence for Neutrino Flavor Transformation from Neutral-Current Interactions in the Sudbury Neutrino Observatory*, Physical Review Letters **89** (2002) 011301, http://dx.doi.org/10.1103/PhysRevLett.89.011301.

[18] S. L. Glashow, J. Iliopoulos, and L. Maiani, *Weak Interactions with Lepton-Hadron Symmetry*, Phys. Rev. D **2** (1970) 1285.

[19] C. S. Wu, E. Ambler, R. W. Hayward, D. D. Hoppes, and R. P. Hudson, *Experimental Test of Parity Conservation in Beta Decay*, Phys. Rev. **105** (1957) 1413–1415, https://link.aps.org/doi/10.1103/PhysRev.105.1413.

[20] J. H. Christenson, J. W. Cronin, V. L. Fitch, and R. Turlay, *Evidence for the* 2π *Decay of the* K_2^0 *Meson*, Phys. Rev. Lett. **13** (1964) 138–140, https://link.aps.org/doi/10.1103/PhysRevLett.13.138.

[21] M. Kobayashi and T. Maskawa, *CP Violation in the Renormalizable Theory of Weak Interaction*, Progress of Theoretical Physics **49** (1973) 652–657.

[22] A. Salam and J. C. Ward, *Electromagnetic and weak interactions*, Physics Letters **13** (1964) 168–171, https://doi.org/10.1016/0031-9163(64)90711-5.

[23] F. Englert and R. Brout, *Broken Symmetry and the Mass of Gauge Vector Mesons*, Phys. Rev. Lett. **13** (1964) 321.

[24] P. W. Higgs, *Broken Symmetries and the Masses of Gauge Bosons*, Phys. Rev. Lett. **13** (1964) 508.

[25] G. S. Guralnik, C. R. Hagen, and T. W. B. Kibble, *Global Conservation Laws and Massless Particles*, Phys. Rev. Lett. **13** (1964) 585.

[26] ATLAS Collaboration, *Observation of a new particle in the search for the Standard Model Higgs boson with the ATLAS detector at the LHC*, Phys. Lett. B **716** (2012) 1.

[27] CMS Collaboration, *Observation of a new boson at a mass of 125 GeV with the CMS experiment at the LHC*, Phys. Lett. B **716** (2012) 30.

[28] J. C. Collins, D. E. Soper, and G. F. Sterman, *Factorization of Hard Processes in QCD*, Adv. Ser. Direct. High Energy Phys. **5** (1989) 1–91, arXiv:hep-ph/0409313.

[29] R. P. Feynman, *Space-Time Approach to Quantum Electrodynamics*, Phys. Rev. **76** (1949) 769–789, https://link.aps.org/doi/10.1103/PhysRev.76.769.

[30] W. Stirling, *private communication*, http://www.hep.ph.ic.ac.uk/~wstirlin/plots/lhcgrid13.pdf.

[31] NNPDF Collaboration, R. D. Ball et al., *Parton distributions from high-precision collider data.*, Eur. Phys. J. C **77** (2017) 663. 95 p, arXiv:1706.00428.

[32] J. Haffner, *The CERN accelerator complex. Complexe des accélérateurs du CERN*, https://cds.cern.ch/record/1621894, General Photo.

[33] CERN, *High-luminosity LHC*, 08, 2017, http://hilumilhc.web.cern.ch/.

[34] G. Aad et al., *ATLAS pixel detector electronics and sensors*, JINST **3** (2008) P07007.

[35] ATLAS Collaboration, *Technical Design Report for the ATLAS Inner Tracker Pixel Detector*, CERN, Geneva, Sep, 2017. https://cds.cern.ch/record/2285585.

[36] ATLAS Collaboration, *Track Reconstruction Performance of the ATLAS Inner Detector at* $\sqrt{s} = 13$ *TeV*, http://cds.cern.ch/record/2037683.

[37] ATLAS Collaboration, M. Capeans et al., *ATLAS Insertable B-Layer Technical Design Report*, Sep, 2010. https://cds.cern.ch/record/1291633.

[38] ATLAS Collaboration, *ATLAS Insertable B-Layer Technical Design Report Addendum*, CERN, May, 2012. https://cds.cern.ch/record/1451888.

[39] ATLAS Collaboration, *ATLAS liquid argon calorimeter: Technical Design Report*, Dec, 1996. https://cds.cern.ch/record/331061.

[40] CERN, *Public Results LAr Calorimeter*, 08, 2020, http://twiki.cern.ch/twiki/bin/view/AtlasPublic/LArCaloPublicResultsDetStatus.

[41] ATLAS Collaboration, *ATLAS muon spectrometer: Technical Design Report*, 1997. https://cds.cern.ch/record/331068.

[42] ATLAS Collaboration, M. Aaboud et al., *Performance of the ATLAS trigger system in 2015*, The European Physical Journal C **77** (2017), http://dx.doi.org/10.1140/epjc/s10052-017-4852-3.

[43] S. D. Drell and T.-M. Yan, *Massive Lepton-Pair Production in Hadron-Hadron Collisions at High Energies*, Phys. Rev. Lett. **25** (1970) 902–902, https://link.aps.org/doi/10.1103/PhysRevLett.25.902.2.

[44] S. D. Drell and T.-M. Yan, *Massive Lepton-Pair Production in Hadron-Hadron Collisions at High Energies*, Phys. Rev. Lett. **25** (1970) 316–320, https://link.aps.org/doi/10.1103/PhysRevLett.25.316, Erratum.

[45] J. W. Kraus, *Measurement of the differential* $W \to \mu + \nu$ *cross section at high transverse masses at* $\sqrt{s} = 13$ *TeV with the ATLAS detector*, Nov, 2020. https://cds.cern.ch/record/2753249. Presented 24 Nov 2020.

[46] F. Ellinghaus et al., *Charged-current Drell-Yan cross sections at high transverse masses in pp collisions at* $\sqrt{s} = 13$ *TeV*, CERN, Geneva, Mar, 2020. https://cds.cern.ch/record/2711872.

[47] ATLAS Collaboration, G. Aad et al., *Search for a heavy charged boson in events with a charged lepton and missing transverse momentum from pp collisions at* $\sqrt{s} = 13$ *TeV with the ATLAS detector*, Phys. Rev. D **100** (2019) 052013, arXiv:1906.05609 [hep-ex].

[48] CMS Collaboration, *Search for new physics in the lepton plus missing transverse momentum final state in proton-proton collisions at* $\sqrt{s} = 13$ *TeV*, 2022. https://arxiv.org/abs/2202.06075.

[49] V. Blobel, *Unfolding*. John Wiley and Sons, Ltd, 2013. Data Analysis in High Energy Physics.

[50] CERN, *Proceedings of the PHYSTAT 2011 Workshop on Statistical Issues Related to Discovery Claims in Search Experiments and Unfolding: CERN, Geneva, Switzerland 17 - 20 Jan 2011. PHYSTAT 2011 Workshop on Statistical Issues Related to Discovery Claims in Search Experiments and Unfolding*. CERN, Geneva, 2011. https://cds.cern.ch/record/1306523.

[51] G. D'Agostini, *A multidimensional unfolding method based on Bayes' theorem*, Nuclear Instruments and Methods in Physics Research Section A: Accelerators, Spectrometers, Detectors and Associated Equipment **362** (1995) 487 – 498.

[52] ATLAS Collaboration, *Luminosity determination in pp collisions at* $\sqrt{s} = 13$ *TeV using the ATLAS detector at the LHC*, CERN, Geneva, Jun, 2019. https://cds.cern.ch/record/2677054.

[53] ATLAS Collaboration, *Luminosity Group*, https://twiki.cern.ch/twiki/bin/view/AtlasPublic/LuminosityPublicResultsRun2, (visited 12/07/2021).

[54] A. Buckley et al., *General-purpose event generators for LHC physics*, Physics Reports **504** (2011) 145–233.

[55] T. Gleisberg, S. Höche, F. Krauss, M. Schönherr, S. Schumann, F. Siegert, and J. Winter, *Event generation with SHERPA 1.1*, Journal of High Energy Physics **2009** (2009) 007–007, http://dx.doi.org/10.1088/1126-6708/2009/02/007.

[56] B. Andersson, G. Gustafson, G. Ingelman, and T. Sjöstrand, *Parton fragmentation and string dynamics*, Physics Reports **97** (1983) 31–145, https://www.sciencedirect.com/science/article/pii/0370157383900807.

[57] D. Amati and G. Veneziano, *Preconfinement as a property of perturbative QCD*, Physics Letters B **83** (1979) 87–92, https://www.sciencedirect.com/science/article/pii/0370269379908967.

[58] S. Agostinelli et al., *GEANT4: A simulation toolkit*, Nucl. Instrum. Meth. A **506** (2003) 250.

[59] E. Richter-Was, D. Froidevaux, and L. Poggioli, *ATLFAST 2.0 a fast simulation package for ATLAS*, CERN, Geneva, Nov, 1998. https://cds.cern.ch/record/683751.

[60] T. Sjöstrand, S. Mrenna, and P. Z. Skands, *A Brief Introduction to PYTHIA 8.1*, Comput. Phys. Commun. **178** (2008) 852.

[61] NNPDF Collaboration, R. D. Ball et al., *Parton distributions with LHC data*, Nuclear Physics B **867** (2013) 244–289, https://doi.org/10.1016/j.nuclphysb.2012.10.003.

[62] ATLAS Collaboration, *The Pythia 8 A3 tune description of ATLAS minimum bias and inelastic measurements incorporating the Donnachie-Landshoff diffractive model*, CERN, Geneva, Aug, 2016. https://cds.cern.ch/record/2206965.

[63] S. Alioli, P. Nason, C. Oleari, and E. Re, *A general framework for implementing NLO calculations in shower Monte Carlo programs: the POWHEG BOX*, JHEP **06** (2010) 043.

[64] S. Frixione, P. Nason, and C. Oleari, *Matching NLO QCD computations with Parton Shower simulations: the POWHEG method*, JHEP **11** (2007) 070.

[65] P. Nason, *A New method for combining NLO QCD with shower Monte Carlo algorithms*, JHEP **11** (2004) 040.

[66] H.-L. Lai et al., *New parton distribution functions from a global analysis of quantum chromodynamics*, Phys. Rev. D **82** (2010) 074024, arXiv:1007.2241 [hep-ph].

[67] T. Sjöstrand, S. Mrenna, and P. Z. Skands, *A brief introduction to PYTHIA 8.1*, Comput. Phys. Commun. **178** (2008) 852, arXiv:0710.3820 [hep-ph].

[68] ATLAS Collaboration, G. Aad et al., *Measurement of the Z/γ^* boson transverse momentum distribution in pp collisions at $\sqrt{s} = 7$ TeV with the ATLAS detector*, Journal of High Energy Physics **2014** (2014), http://dx.doi.org/10.1007/JHEP09(2014)145.

[69] J. Pumplin, D. R. Stump, J. Huston, H.-L. Lai, P. Nadolsky, and W.-K. Tung, *New Generation of Parton Distributions with Uncertainties from Global QCD Analysis*, Journal of High Energy Physics **2002** (2002) 012–012, https://doi.org/10.1088/1126-6708/2002/07/012.

[70] P. Golonka and Z. Was, *PHOTOS Monte Carlo: a precision tool for QED correctionsin Z and W decays*, The European Physical Journal C **45** (2006) 97–107, https://doi.org/10.1140%2Fepjc%2Fs2005-02396-4.

[71] S. Dulat, T.-J. Hou, J. Gao, M. Guzzi, J. Huston, P. Nadolsky, J. Pumplin, C. Schmidt, D. Stump, and C.-P. Yuan, *New parton distribution functions from a global analysis of quantum chromodynamics*, Physical Review D **93** (2016), http://dx.doi.org/10.1103/PhysRevD.93.033006.

[72] M. Bähr, S. Gieseke, M. A. Gigg, D. Grellscheid, K. Hamilton, O. Latunde-Dada, S. Plätzer, P. Richardson, M. H. Seymour, A. Sherstnev, and B. R. Webber, *Herwig++ physics and manual*, The European Physical Journal C **58** (2008) 639–707, http://dx.doi.org/10.1140/epjc/s10052-008-0798-9.

[73] J. Bellm et al., *Herwig++ 2.7 Release Note*, 2013. arXiv:1310.6877 [hep-ph].

[74] T.-J. Hou et al., *New CTEQ global analysis of quantum chromodynamics with high-precision data from the LHC*, Phys. Rev. D **103** (2021) 014013, arXiv:1912.10053 [hep-ph].

[75] E. Bothmann et al., *Event Generation with Sherpa 2.2*, arXiv:1905.09127 [hep-ph].

[76] R. D. Ball et al., *Parton distributions for the LHC run II*, Journal of High Energy Physics **2015** (2015), http://dx.doi.org/10.1007/JHEP04(2015)040.

[77] *ATLAS Run 1 Pythia8 tunes*, CERN, Geneva, Nov, 2014. https://cds.cern.ch/record/1966419.

[78] J. Alwall, R. Frederix, S. Frixione, V. Hirschi, F. Maltoni, O. Mattelaer, H.-S. Shao, T. Stelzer, P. Torrielli, and M. Zaro, *The automated computation of tree-level and next-to-leading order differential cross sections, and their matching to parton shower simulations*, Journal of High Energy Physics **2014** (2014), http://dx.doi.org/10.1007/JHEP07(2014)079.

[79] S. Frixione, E. Laenen, P. Motylinski, B. R. Webber, and C. D. White, *Single-top hadroproduction in association with a W boson*, JHEP **07** (2008) 029, arXiv:0805.3067 [hep-ph].

[80] ATLAS Collaboration, G. Aad et al., *Performance of electron and photon triggers in ATLAS during LHC Run 2*, The European Physical Journal C **80** (2020), http://dx.doi.org/10.1140/epjc/s10052-019-7500-2.

[81] ATLAS Collaboration, G. Aad et al., *Electron and photon performance measurements with the ATLAS detector using the 2015–2017 LHC proton-proton collision data*, http://dx.doi.org/10.1088/1748-0221/14/12/P12006.

[82] ATLAS Collaboration, M. Aaboud et al., *Electron reconstruction and identification in the ATLAS experiment using the 2015 and 2016 LHC proton-proton collision data at* $\sqrt{s} = 13$ *TeV*, Eur. Phys. J. C **79** (2019) 639. 40 p, arXiv:1902.04655.

[83] ATLAS Collaboration, G. Aad et al., *Electron and photon energy calibration with the ATLAS detector using LHC Run 1 data*, The European Physical Journal C **74** (2014), http://dx.doi.org/10.1140/epjc/s10052-014-3071-4.

[84] ATLAS Collaboration, M. Aaboud et al., *Electron efficiency measurements with the ATLAS detector using 2012 LHC proton–proton collision data*, The European Physical Journal C **77** (2017), http://dx.doi.org/10.1140/epjc/s10052-017-4756-2.

[85] ATLAS Collaboration, *Electron Performance Group*, https://twiki.cern.ch/twiki/bin/view/AtlasProtected/ElectronGamma, (visited 17/01/2022).

[86] ATLAS Collaboration, G. Aad et al., *Muon reconstruction performance of the ATLAS detector in proton–proton collision data at* $\sqrt{s}$ *=13 TeV*, http://dx.doi.org/10.1140/epjc/s10052-016-4120-y.

[87] J. Illingworth and J. Kittler, *A survey of the hough transform*, Computer Vision, Graphics, and Image Processing **44** (1988) 87–116.

[88] M. Cacciari, G. P. Salam, and G. Soyez, *The anti-k_t jet clustering algorithm*, Journal of High Energy Physics **2008** (2008) 063–063.

[89] ATLAS Collaboration, *Jet energy scale and resolution measured in proton-proton collisions at $\sqrt{s} = 13$ TeV with the ATLAS detector*, Eur. Phys. J. C **81** (2020) 689. 73 p, arXiv:2007.02645 [hep-ex].

[90] ATLAS Collaboration, G. Aad et al., *Topological cell clustering in the ATLAS calorimeters and its performance in LHC Run 1*, The European Physical Journal C **77** (2017).

[91] ATLAS Collaboration, M. Aaboud et al., *Jet reconstruction and performance using particle flow with the ATLAS Detector*, The European Physical Journal C **77** (2017).

[92] ATLAS Collaboration, G. Aad et al., *Performance of missing transverse momentum reconstruction for the ATLAS detector in the first proton-proton collisions at $\sqrt{s} = 13$ TeV*, CERN, Geneva, 7, 2015. https://cds.cern.ch/record/2037904.

[93] ATLAS Collaboration, *Expected performance of missing transverse momentum reconstruction for the ATLAS detector at $\sqrt{s} = 13$ TeV*, https://cds.cern.ch/record/2037700.

[94] M. K. Bugge et al., *Search for new particles in the charged lepton plus missing transverse energy final state using pp collisions at $\sqrt{s} = 13$ TeV in the ATLAS detector*, CERN, Geneva, Sep, 2018. https://cds.cern.ch/record/2640567.

[95] ATLAS Collaboration, *Electron identification efficiencies using the Zmass method*, CERN, Geneva, Mar, 2021. https://cds.cern.ch/record/2798044.

[96] ATLAS Collaboration, M. Aaboud et al., *Electron and photon energy calibration with the ATLAS detector using 2015–2016 LHC proton-proton collision data*, Journal of Instrumentation **14** (2019) P03017–P03017, http://dx.doi.org/10.1088/1748-0221/14/03/P03017.

[97] *Unfolding algorithms and tests using RooUnfold*. CERN, Geneva, 2011. arXiv:1105.1160 [physics.data-an].

[98] S. Schmitt, *Data Unfolding Methods in High Energy Physics*, EPJ Web of Conferences **137** (2017) 11008.

Acknowledgement

At this point, I would like to thank Prof. Dr. Christian Zeitnitz and Priv.-Doz. Dr. Frank Ellinghaus for the opportunity to visit the University of Wuppertal and work as a Ph.D. student. The two of you gave me the possibility to participate at several schools and conferences, where I was able to enhance my understanding of multiple topics.
In addition, I would especially like to express my gratitude to Priv.-Doz. Dr. Frank Ellinghaus for the extraordinary supervision and guidance. I am very grateful for his continuous support, all the time that we spend on discussions about physics and his advice as an expert, when there seemed to be no solution. Thanks a lot!
Next, I am very grateful to Prof. Dr. Eram Rizvi from the Queen Mary University of London. During my time as a Ph.D. student, we had the opportunity to discuss a lot in the regular meetings of the ATLAS analysis group and even met at the standard model conferences. In particular, I appreciate that he agreed to act as the second examiner of this thesis.

I owe many thanks to Johanna Wanda Kraus for the great last two years and all the time for discussions we spend during the work on *our amazing* measurement.
A special thanks to my colleagues Volker Andreas Austrup and Jens Roggel. Besides the great collaboration, we always had the opportunity to think through even the most obvious topics of physics again. Thanks a lot to both of you!
In addition, I would like to thank Dr. Dominic Hirschbühl for his technical support and advice. Without his help, it wouldn't have been possible to finalise the validation and generate the alternative signal MC sample so quickly.
Furthermore, I would like to thank all the other members of the chair, where I had a very pleasant time.

I am also grateful for the collaboration with all members of the ATLAS analysis group, the discussions we have had and the knowledge that you shared with me remain very useful.

For proofreading I would like to thank Johanna Wanda Kraus, Fatih Ertas, Volker Andreas Austrup, Jens Roggel and Karina Schröder. All of your comments and suggestions have been very useful and inspiring for me.

Finally, I would like to thank my wife, my family, and my friends for the continuous encouragement and huge support during the past years.